

UNIVERSITÀ
DEGLI STUDI
DI PADOVA

Sede Amministrativa: Università degli Studi di Padova

Dipartimento di Geoscienze

SCUOLA DI DOTTORATO DI RICERCA IN SCIENZE DELLA TERRA
VIA G. GRADENIGO 6, 35131 PADOVA
CICLO XXX

SEISMOGENIC CARBONATE-BUILT NORMAL FAULTS: STRUCTURE AND DEFORMATION PROCESSES

Tesi redatta con il contributo finanziario dell'European Research Council Consolidator Grant Project (NOFEAR) No 614705. Titolo intero del progetto: New Outlook on seismic faults: From EARthquake nucleation to arrest. Principal investigator: Giulio Di Toro.

Coordinatore: *Ch.mo Prof. Fabrizio Nestola*
Supervisore*: Ch.mo Prof. Giulio Di Toro*
Co-Supervisore*: Dr. Steven A. F. Smith*
Ph.D. Michele Fondriest

Dottorand*o: Matteo Demurtas*

2018

Abstract

Carbonate-built rocks are a widely recurrent lithology often involved in most of the present seismicity occurring in densely populated areas, such as the circum-Mediterranean area (e.g., L'Aquila 2009, M_W 6.1; Amatrice 2016, M_W 6.5). Earthquake and fault mechanics is controlled by several properties that are distributed over a wide range of scales, spanning from the tens of kilometers to the nanoscale. In this thesis, we propose to study the architecture and the rocks of an exhumed fault zone cutting carbonates (mainly dolostones and limestones) to investigate the fault-related deformation processes that can be active during the seismic cycle. Therefore, we used a multidisciplinary approach that included (i) detailed structural field surveys (including systematic rock sample collection), (ii) construction of digital outcrop models of fault zones, (iii) rock deformation experiments (i.e., rotary-shear experiments on gouges), (iv) microstructural and mineralogical investigations of natural and experimental fault products (optical- and scanning electron microscopy, X-ray energy dispersive spectroscopy, electron backscatter diffraction, EBSD, transmission Kikuchi diffraction, TKD).

As a case study for the field investigation, we selected the seismically active fault zone outcropping within carbonates in the Central Italian Apennines, namely the Vado di Corno Fault Zone (VCFZ), exhumed from < 3 km depth. The fault zone consists of a quite complicated network of faults and fractures and of a large variety of fault rocks (foliated cataclasites, gouges, *in-situ* shattered rocks, sheared veins, etc.). Based on the field description of the fault and fracture network and of the distribution of fault zone rocks, we suggested that the internal structure of the VCFZ strongly resembles the buried structures associated to the seismic sequences in the Central Apennines and highlighted by high resolution hypocentral distributions obtained from seismic inversion studies (e.g., L'Aquila 2009, M_W 6.1; Amatrice 2016, M_W 6.5). In particular, foreshocks, main shocks and especially aftershocks re-activate (mainly as low-angle normal faults) the inherited fault structures formed from compression during the Miocene-Pliocene and the high-angle normal faults associated to the present extension occurring in the mountain belt.

Motivated by their common occurrence in the fault network of the VCFZ, we investigated the frictional behavior and microstructural evolution of gouges composed of mixtures of calcite-dolomite. We performed low- to high velocity rotary-shear friction experiments (V = 30 μms^{-1} – 1 ms^{-1}) over a wide range of displacements (0.05-0.4 m), normal loads (17.5-26 MPa), deformation conditions (room-humidity vs. water-dampened) and slip histories (single slide vs. slide-hold-slide).

Most of these experimental conditions reproduced the deformation conditions occurred in the VCFZ. The development of a well-defined foliation in the gouge layers occurred only in the experiments performed at slip rates of 1 ms^{-1} and under room-humidity conditions. Consistent with previous studies, our observations support the notion that foliated gouges and cataclasites, especially in the absence of clay minerals in the matrix, may form during seismic slip in natural carbonate-bearing faults.

Further work was focused on the investigation, especially by means of EBSD analysis, of the physical processes associated to strain accommodation both in the slip zones (composed by aggregates of nanoparticles, grain size 20-2000 nm) and in the nearby and less deformed gouge layers of the experimentally sheared calcite-dolomite mixtures. This resulted in the surprising finding of the development of a crystallographic preferred orientation (CPO) in calcite in the less deformed gouges when sheared in the purely brittle regime (i.e., max T < 30 °C). Here, the formation of a CPO was suggested to be controlled by the strong anisotropy in calcite (cleavage planes), mechanical grain rotation towards the direction of the maximum compressive stress and subsequent fracturing. Moreover, the large differential stresses (ca. 170 MPa) estimated through calcite twin paleopiezometry were interpreted as a record of the local stress (*force chains*) carried by grain bridges during shearing.

The analysis of the experimental slip zones of calcite-dolomite gouge mixtures slid at seismic slip rate (i.e., 1 ms^{-1}) was carried out by the application of the novel micro-analytical technique, the TKD (this is one of the very first applications to geological materials). The main advantages of the TKD compared to standard techniques used to determine CPO in rocks, is the high spatial resolution (in our case we could use an analysis step size as small as 20 nm) and the large number of data collected, which allowed us to obtain a statistically significant CPO dataset. The presence of a very weak CPO in the nano-grains organized in a characteristic foam texture in the slip zone suggested that the main deformation mechanism during seismic slip was grain boundary sliding aided by diffusion creep.

In conclusion, based on the field, experimental and microstructural evidence reported in the thesis, earthquakes occurring in the shallow crust made of carbonate-built rocks are the result of a combination of elasto-frictional ("brittle") but especially viscous-plastic ("ductile") micro-processes.

Riassunto

Le rocce carbonatiche sono spesso interessate dall'attività sismica che caratterizza zone densamente popolate, come l'area Mediterranea (e.g., il terremoto de L'Aquila, 2009, M_W 6.1, e il più recente terremoto di Amatrice, 2016, M_W 6.5). La meccanica dei terremoti e delle faglie è controllata da una serie di proprietà geometriche e fisico-chimiche distribuite su una scala che si estende dalle decine di kilometri ai nanometri. L'obiettivo di questa tesi è di studiare l'architettura e le rocce di una zona di faglia esumata per individuare i processi deformativi che controllano il ciclo sismico nelle rocce carbonatiche (principalmente dolomie e calcari). A questo fine abbiamo adoperato un approccio multidisciplinare che ha compreso (i) rilievi geologico-strutturali di terreno (e relativo campionamento sistematico delle rocce di faglia), (ii) la costruzione di modelli digitali della zona di faglia, (iii) esperimenti di tipo *rotary* su polveri, e (iv) l'analisi microstrutturale e mineralogica dei prodotti di faglia naturali e sperimentali tramite l'utilizzo di microscopia ottica ed elettronica a scansione, spettroscopia EDX, diffrazione da elettroni retrodiffusi (EBSD) e diffrazione Kikuchi in trasmissione (TKD) elettronica.

Per il caso di terreno, abbiamo selezionato la zona di faglia di Vado di Corno (VCFZ) che è splendidamente esposta all'interno di carbonati dell'Appennino Centrale (Campo Imperatore, massiccio del Gran Sasso, Abruzzo), è sismicamente attiva ed è stata esumata da < 3 km di profondità. La zona di faglia si compone di un sistema articolato di faglie e fratture, e comprende una grande varietà di rocce di faglia (cataclasiti foliate, *gouge*, rocce frantumate *in-situ*, vene deformate in taglio, etc.). Sulla base delle evidenze di terreno del sistema di faglie e fratture e della distribuzione delle rocce di faglia, abbiamo interpretato la struttura della VCFZ come un analogo esumato delle strutture sepolte associate all'attività sismica negli Appennini Centrali. Queste ultime sono state "illuminate" dalla distribuzione ad alta risoluzione degli ipocentri (errori di localizzazione spesso inferiori ai 20 m e quindi comparabili con le osservazioni di terreno) grazie a studi di inversione sismica (e.g., L'Aquila 2009, M_W 6.1; Amatrice 2016, M_W 6.5). In particolare, eventi precursori, la scossa principale, e quelle successive, riattivano, come piani a basso angolo, il sistema di faglie ereditate dalla compressione Miocenico-Pliocenica, e soprattutto le faglie ad alto angolo associate con l'estensione Pleistocenica-attuale della catena Appenninica.

Motivati dalla loro presenza nel sistema di faglie della VCFZ, abbiamo studiato le proprietà frizionali e l'evoluzione microstrutturale di polveri composte da una mistura di calcite e dolomite. Abbiamo condotto esperimenti da basse- ad alte velocità di scivolamento (V = 30 μms^{-1} – 1 ms^{-1}) per

una varietà di rigetti (0.05-0.4 m), sforzi normali (17.5-26 MPa), condizioni di deformazione (umidità ambiente e presenza d'acqua) e storia di deformazione (esperimenti di tipo *single slide* e *slide-hold-slide*). La maggior parte delle condizioni sperimentali imposte hanno riprodotto condizioni deformative occorse nella VCFZ. In particolare, la formazione di una foliazione ben definita nei livelli di *gouge* è stata osservata solamente negli esperimenti eseguiti ad umidità ambiente e ad una velocità di 1 ms^{-1}. In accordo con studi precedenti, le nostre osservazioni supportano l'interpretazione che *gouge* e cataclasiti foliate, in particolar modo se in assenza di minerali delle argille nella matrice, possono formarsi durante la deformazione cosismica in faglie in carbonati.

Il lavoro successivo si è quindi focalizzato nello studio microstrutturale, specialmente mediante analisi EBSD, di faglie sperimentali composte da misture di calcite e dolomite per individuare i processi fisici associati alla intensa localizzazione della deformazione nelle zone di scivolamento (spessori < 0.1 mm) composte da aggregati di nanoparticelle con una granulometria compresa tra 20 e 2000 nm, che nel *gouge* adiacente e meno deformato (spessori ca. 2 mm). Un risultato sorprendente di questa analisi è stata la scoperta dello sviluppo di un'orientazione cristallografica preferenziale (CPO) nei granuli di calcite presenti nei livelli meno deformati. Infatti la mistura è stata deformata per taglio semplice in regime puramente fragile (massima temperatura < 30 °C). La formazione di una CPO è interpretata come conseguenza della forte anisotropia strutturale tipica della calcite (piani di clivaggio). Durante lo scivolamento per taglio, la rotazione meccanica dei grani fa sì che i piani di clivaggio risultino progressivamente circa paralleli alla direzione di massima compressione, comportando il cedimento fragile (fratturazione) del clasto. Inoltre, le alte stime di sforzo differenziale (ca. 170 MPa), ottenute attraverso il paleopiezometro per i geminati nella calcite, sono state interpretate come un'indicazione degli elevati sforzi locali (*force chains*) sperimentati dai grani durante la deformazione per taglio fino al cedimento per fratturazione.

L'analisi della zona di scivolamento (intensa localizzazione della deformazione) in polveri miste di calcite-dolomite deformate a velocità cosismiche (1 ms^{-1}) è stata effettuata tramite l'applicazione di una tecnica micro-analitica innovativa, la TKD (quella presentata nella tesi è stata una delle prime applicazioni di questa tecnica su materiali geologici). Il vantaggio principale nell'uso della TKD rispetto alle tecniche frequentemente impiegate per determinare la CPO nelle rocce, come l'EBSD, è l'alta risoluzione spaziale (nel nostro caso siamo riusciti ad usare un passo di campionamento fino a 20 nm) e la grande quantità di dati raccolta, statisticamente significativa per l'analisi della CPO rispetto, per esempio, all'impiego di microscopi a trasmissione elettronica. La

presenza di una CPO molto debole negli aggregati nanometrici di calcite, organizzati in una caratteristica microstruttura “a schiuma”, suggerisce che il principale meccanismo di deformazione durante la deformazione cosismica era *grain boundary sliding* assistito da meccanismi diffusivi.

In conclusione, sulla base delle evidenze di terreno, sperimentali e microstrutturali riportate nella tesi, i terremoti che occorrono della crosta superficiale caratterizzata dalla presenza di rocce carbonatiche sono il risultato di una combinazione di micro-processi elastico-frizionali (“fragili”) ma specialmente visco-plastici (“duttili”).

Table of contents

Abstract..... I

Riassunto..... III

Table of contents..... VI

General introduction..... 1

Chapter I

Structure of a normal seismogenic fault zone in carbonates: The Vado di Corno Fault, Campo Imperatore, Central Apennines (Italy)

Abstract..... 10

1. Introduction..... 11

2. Geological setting..... 14

2.1. The Gran Sasso Massif..... 14

2.2. The Vado di Corno Fault Zone..... 17

3. Methods..... 18

4. Cross-sectional structural architecture..... 23

5. Structural units..... 24

5.1. Low Strain Damage Zone..... 24

5.2. High Strain Damage Zone..... 27

5.3. Breccia unit..... 27

5.4. Cataclastic units..... 28

5.4.1. Cataclastic unit 2..... 31

5.4.2. Cataclastic unit 1..... 31

6. Microstructures of the slip zones..... 34

6.1. Highly localized sheared calcite veins..... 34

6.2. Non-foliated cataclasites..... 39

6.3. Foliated cataclasites..... 39

6.4. Deformation bands..... 40

7. Discussion..... 41

7.1. Structural complexity of the VCFZ..... 41
7.1.1. Origin of the CU..... 42
7.2. Evidence of coseismic slip..... 44
7.3. Implications for the interpretation of seismicity in the Central Apennines..... 46
8. Conclusions..... 49

Chapter II

Frictional properties and microstructural evolution of mixed calcite-dolomite gouges

Abstract..... 52
1. Introduction..... 53
2. Methods..... 58
2.1. Starting materials..... 58
2.2. Experimental setup..... 59
2.3. Deformation conditions..... 60
2.4. Analytical techniques..... 61
3. Results..... 61
3.1. Mechanical data..... 61
3.1.1. Friction evolution with slip rate..... 62
3.1.2. Gouge thickness evolution with slip rate..... 66
3.2. Temperature evolution..... 66
3.3. CO_2 emissions..... 73
3.4. Mineralogy of the deformed gouges..... 73
3.5. Microstructures of deformed gouge layers..... 74
3.5.1. Microstructures produced at low velocity ($V \leq 0.001$ ms^{-1}) 79
3.5.2. Microstructures produced in the intermediate velocity regime ($V = 0.01$-0.1 ms^{-1}) 80
3.5.3. Microstructures produced in the high velocity regime ($V = 1$ ms^{-1}) 86
3.5.4. Microstructures produced in slide-hold-slide experiments..... 87
3.5.4.1. Velocity step from 30 μms^{-1} to 1 ms^{-1}..... 87
3.5.4.2. Velocity step from 1 ms^{-1} to 30 μms^{-1}..... 88
4. Discussion..... 89
4.1. Strain localization and dynamic weakening mechanisms in calcite-dolomite mixtures..... 89

4.2. Coseismic foliations in calcite-dolomite gouges..... 94
4.3. Preservation potential of microstructures during overprinting slip events..... 98
4.4. Implication for natural faults in carbonates..... 99
5. Conclusions..... 100
6. Tables..... 102

Chapter III

Crystallographic controls on the textural evolution of carbonate gouges during cataclasis

Abstract..... 105
1. Introduction..... 106
2. Methods..... 107
2.1. Samples and sample preparation..... 107
2.2. Electron backscatter diffraction (EBSD) analysis..... 107
2.3. Data cleaning and texture analysis..... 108
2.4. Calcite twin piezometry..... 113
3. Results..... 114
3.1. Crystallographic preferred orientation in calcite and dolomite gouges..... 114
3.1.1. Static load (water dampened) 114
3.1.2. Deformed gouges..... 114
3.2. Fracturing and calcite twins analysis..... 121
4. Discussion..... 122
4.1. Mechanism for CPO development in a granular material..... 122
4.2. Applicability of paleopiezometry to granular materials..... 130
4.3. Implication for natural faults..... 133
5. Conclusions..... 134
6. Tables..... 135

Chapter IV

Transmission Kikuchi Diffraction nanoscale investigation of experimental seismic faults in carbonates

Abstract..... 138
1. Introduction..... 139
2. Methods..... 141
2.1. Starting materials and sample preparation..... 141
2.2. Transmission Kikuchi Diffraction analysis..... 145
2.3. Data cleaning and processing..... 146
3. Results..... 147
3.1. Grain size analysis of the experimental slip zone..... 147
3.2. Grain shapes..... 152
3.3. Chemical analysis..... 152
3.4. Crystallographic preferred orientation and intragranular misorientations..... 152
4. Discussion..... 153
4.1. Deformation mechanisms active in the PSZ..... 153
4.2. The role of nanoparticle in fault lubrication..... 159
5. Conclusions..... 160
6. Tables..... 162

Chapter V

Discussion and future work..... 163

References..... 167
Appendix A..... 190
Appendix B..... 196

Acknowledgements..... 220

General introduction

Carbonates are a widely recurrent lithology typically involved in crustal-scale deformation. Many seismically active areas worldwide, such as the Apennines (Italy), the Hellenides-Dinarides (Balkan Peninsula), the Himalayan-Tethyan mountain belt and the Canadian Rockies, are characterized by the occurrence of carbonate sequences that can be as thick as 4-10 km (e.g., Mirabella et al., 2008; Chiaraluce, 2012; Govoni et al., 2014). In particular, in the circum-Mediterranean area, moderate to large earthquakes (up to ca. M_W 7) and seismic sequences occurred within carbonate host rocks (i.e., limestones and dolostones) (e.g., Irpinia-Basilicata 1980, M_W 6.9; Bovec-Krn 1998, M_D 5.6; L'Aquila 2009, M_W 6.1; Amatrice 2016, M_W 6.5; Di Bucci and Mazzoli, 2003; Burchfiel et al., 2008). Although in the aforementioned seismic sequences it is still debated whether the mainshock nucleated within the crystalline basement or in the overlying carbonate sequences, most of the seismic ruptures propagated and most of the aftershocks nucleated in carbonates (e.g., Valoroso et al., 2014). Therefore, the study of fault zones hosted in carbonate sequences may yield a more sound understanding of earthquake mechanics.

Earthquake mechanics is controlled by several properties that are distributed over a wide range of scales (Scholz, 2002). On the high-end of this scale ($10^0 – 10^5$ m), is the architecture of fault systems (i.e., geometry of fault network and fault-related damage distribution). This scale is of great importance, for example, in reservoir exploration studies, where faults can act as conduits or seals for oil and gas migration (e.g., Al-Anzi et al., 2003). Fault architecture plays also a major role in controlling the propagation and arrest of an earthquake rupture (e.g., Sibson, 1985; Wesnousky, 1988, 2006). In particular, the relationship of the fault network with the regional stress field can strongly influence the distribution of the foreshock and aftershock activity within a seismic sequence. As an example, in the case of the Emilia (Northern Italy) 2012 seismic sequence (Lavecchia et al., 2012), the aftershocks that followed the mainshock M_W 6.1 of the 20th May, were mainly located on the frontal ramp of the Ferrara thrust and showed a progressive eastwards migration with time. Conversely, the aftershocks related to the mainshock M_W 6.0 of the 29th May occurred along the frontal ramp of the Mirandola thrust and migrated westwards with time. Both the eastwards and westwards migration of the seismicity was showed to be controlled by the frontal and lateral ramps of the main thrust (Lavecchia et al., 2012). Even though theoretical (e.g., Fang and Dunham, 2013) and seismological studies (e.g., Lavecchia et al., 2012) have found the fault zone

structure and fault network to play a key role in the evolution of a seismic sequence (e.g., Wesnousky, 1988, 2006), to date few attempts have been made to quantify the geometrical complexity and off-fault damage distribution of exhumed seismogenic fault zones (e.g., Faulkner et al., 2003; Tesei et al., 2014; Fondriest et al., 2015; Schröckenfuchs et al., 2015; Demurtas et al., 2016).

Modern advanced geophysical and seismological techniques (e.g., tomographic studies, trapped waves, double-difference method; Waldhauser and Ellsworth, 2000; Di Stefano et al., 2011; Allam and Ben-Zion, 2012) allow to image the geometrical complexity of active buried fault zones with high spatial resolution (i.e., tens of meters) (e.g., Schaff et al., 2002; Chiaraluce et al., 2011; Valoroso et al., 2013, 2014) comparable to the resolution of geological field observations (e.g., Collettini et al., 2014), and to retrieve parameters related to the seismic source (e.g., stress drop, radiated energy; Kanamori and Brodsky, 2004). Thus, the characterization of the internal structure of exhumed fault zones in the field is even more necessary both for the validation of the remotely acquired geophysical/seismological observations and for the investigation of the deformation processes active at smaller scale during the seismic cycle (e.g., Alvarez et al., 1978; Lavecchia, 1985; Wojtal and Mitra, 1986; Gratier and Gamond, 1990; Willemse et al., 1997; Faulkner et al., 2003; Agosta and Aydin, 2006; Mitchell and Faulkner, 2009; Bistacchi et al., 2010; Mitchell et al., 2011; Fondriest et al., 2012; Tesei et al., 2013; Bullock et al., 2014; Collettini et al., 2014; Tesei et al., 2014; Fondriest et al. 2015; Demurtas et al. 2016). In addition, the development of fault zones in carbonates has been demonstrated to be highly influenced by lithological heterogeneities (e.g., pure vs. marly limestone; Delle Piane et al., 2017) and inherited features, such as stylolites, bedding surfaces, joints and veins (e.g., Mollema and Antonellini, 1999; Billi et al., 2003; Agosta and Aydin, 2006; Hausegger et al., 2010).

In the first part of this thesis (Chapter I), we focused our attention to the characterization and quantification of the architecture and microstructures of an exhumed seismically active fault zone cutting through carbonate-built rocks in the Central Apennines (Italy), namely the Vado di Corno Fault Zone (VCFZ), by means of high resolution geological surveys, construction of digital outcrop models and optical- and scanning electron microscopy. Our results show that the internal structure of the VCFZ can be considered a good exhumed analog of the buried structures responsible for the seismic sequences in the Central Apennines (e.g., L'Aquila 2009, M_W 6.1; Amatrice 2016, M_W 6.5). Moreover, the finding, during the survey, of a large variety of fault zone features (mirror surfaces, damage zones, etc.) and rocks (foliated ultracataclasites and gouges, sheared veins, etc.)

motivated the following parts of the PhD thesis. In fact, the latter has been mainly addressed to understand what are the processes active during the seismic cycle associated to the formation of such a variety of fault rocks and geological features.

Earthquakes occur when faults lose their strength with increasing slip and slip rate (Scholz, 2002; Rice, 2006). The nucleation, propagation and arrest of an earthquake rupture are controlled by many factors, including the fault geometry, the frictional properties of the host rocks, the mechanical and chemical effects of fluids and the regional or local variation of the stress field (Sibson, 1973; Stein, 1999; Scholz, 2002; Miller et al., 2004). The frictional behavior of a fault during the nucleation phase is well described by the rate-and-state friction laws that were empirically derived from experiments performed at low slip rates ($V < 0.1$ ms^{-1}) and displacements (Dieterich, 1979; Ruina, 1983; Marone, 1998 and Scholz, 2002 for reviews). However, the rate-and-state is unable to describe the significant dynamic weakening observed in faults when slipping at seismic slip rates (estimated in about $V \sim 1$ ms^{-1} based on seismic inversion data, Heaton, 1990). Such frictional evolution with slip rate seems to be independent of the mineral assemblage involved in the deformation, but rather influenced by the significant amount of mechanical work rate dissipated on the fault during sliding (Di Toro et al., 2011). The energy budget of an earthquake or the conversion of the elastic strain energy stored in the wall rocks into gravitational work (if the faults are not strike-slip), radiated energy, on- and off-fault damage, frictional heating, etc., remains an open question both in the geological and seismological communities (e.g., Shipton et al., 2006; Kanamori and Rivera, 2006; Udías et al., 2014). However, most of field, theoretical and experimental observations suggest that the majority of the energy released during coseismic sliding is converted into heat along a thin band, probably < 10 mm thick, where coseismic slip is localized (e.g., Sibson, 2003; Rice, 2006; Pittarello et al., 2008). The temperature increase in the slip zone (and in the nearby wall-rocks) results from frictional heating during sliding. The temperature increase in the slip zone is thought to promote a wealth of potential weakening mechanisms such as flash heating and weakening at asperity contacts, frictional melting, thermal pressurization, dehydration or decarbonation reactions and activation of crystal-plastic strain accommodation mechanisms (e.g., Rice, 2006; Di Toro et al., 2011; Goldsby and Tullis, 2011; Violay et al., 2013; De Paola et al., 2015). The ability to understand how these processes influence or trigger dynamic weakening is still a matter of experimental and theoretical investigation. Moreover, the ability to recognize such processes in the fault record (e.g., Cowan, 1999; Niemeijer et al., 2012; Collettini et al., 2014; Rowe

and Griffith, 2015) is of primary importance both for field-based studies of exhumed fault zones addressed to contribute to the understanding of earthquake physics and for seismic hazard studies, especially in areas recently populated by man or with poor historical earthquake catalogues. To date, the occurrence of solidified frictional melts (*pseudotachylyte*) along exhumed fault zones seems to be the only unarguable evidence for seismic slip in the fault record (Sibson, 1975; Di Toro et al., 2005).

For carbonate-built rocks, where the mineralogy is relatively simple, with calcite and dolomite by far the main constituents of the rock, frictional melting is unlikely to occur due to the higher temperature required to produce melts with respect to the decarbonation reaction (i.e., ~ 550 °C for dolomite and ~ 800 °C for calcite; Samtani et al., 2002). In fact, the melting point for lime, the main decarbonation product of both calcite and dolomite (see below), is ~2500 °C at low partial pressure (P_{CO2}) of CO_2, since CO_2 is expected to escape from the slip zone during earthquakes (i.e., melting can occur in calcite at lower temperatures, ~1100 °C, only for very high P_{CO2}). Thus, rather than the occurrence of solidified (friction) carbonate melts (Viganò et al., 2011), other microstructural features were proposed as possible indicators for ancient seismic slip within carbonates. In fact, the temperature increase along the slip zone could promote decarbonation reactions, resulting in lower bounds for the maximum temperature achieved during earthquakes to be inferred. Typical reaction products are lime (CaO), periclase (MgO) and, in the presence of Fe-bearing minerals (e.g., siderite), magnetite (Fe_3O_4) or magnesioferrite ($MgFe_2O_4$) (Han et al., 2007a). However, lime is typically unstable and quickly reacts with water to form portlandite ($Ca(OH)_2$), thus its occurrence along natural faults is unlikely. Another important product of decarbonation is CO_2. The presence of particular ambient condition during deformation (e.g., anoxic conditions) might promote decomposition of CO_2 with the formation of amorphous carbon (Spagnuolo et al., 2015). The latter has been documented to own a very low friction coefficient (ca. 0.1) and act as an effective lubricant during fault slip. To date, the best evidence for thermal decomposition along a natural fault in carbonates (though with abundant clay content) was reported by Collettini et al. (2013), where they documented the occurrence of skeletal calcite crystals and an amorphous silica matrix interpreted as the result of a high-temperature pulse associated with the propagation of the seismic rupture.

Mirror-like slip surfaces are a common feature of faults exhumed from shallow depths, especially in limestones and dolostones. Within non-cohesive dolostones, mirror-like slip surfaces, have been demonstrated to form under seismic deformation conditions (i.e., slip rate ≥ 0.1 ms^{-1})

(e.g., Chen et al., 2013; Fondriest et al., 2013; Siman-Tov et al., 2013). However, shiny mirror-like patches developed also in calcite gouges sheared at sub-seismic slip rates (V ~ 1-10 μms^{-1}; Verberne et al., 2013a, 2014). Although these latter observations might undermine the restriction of the formation of mirror-like slip surfaces to seismic slip rates, it is worth noting that the presence of truncated clasts on the principal slip surface, suggesting indicating extreme and possibly fast strain localization, has been documented so far only in the case of experimental faults that underwent fast sliding (e.g., Fondriest et al., 2013).

Within carbonate natural fault gouges, mixtures of calcite and dolomite are typically observed (e.g., Schröckenfuchs et al., 2015; Demurtas et al., 2016), sometimes showing the development of a foliation (e.g., Demurtas et al., 2016). Foliated gouges and cataclasites are common fault rocks in the brittle upper crust (Chester et al., 1985; Snoke et al., 1998). Typically, they are interpreted as forming due to a combination of cataclasis and dissolution-precipitation reactions during aseismic fault creep (e.g., Rutter et al., 1986; Chester and Chester, 1998; Lin, 2001; Collettini and Holdsworth, 2004; Jefferies et al., 2006; De Paola et al., 2008; Wallis et al., 2013). Experimental observations have also confirmed this hypothesis, where a well-defined foliation was formed as a result of dissolution-precipitation reactions accompanied by granular flow and frictional sliding at low slip rates (V < 1 μms^{-1}) (Bos et al., 2000; Niemeijer and Spiers, 2006). Smith et al. (2017) investigated the possibility that some of the natural foliated fault rocks might have a coseismic origin. Rotary-shear experiments performed at V = 1.13 ms^{-1} on gouges with 50 wt.% calcite and 50 wt.% dolomite showed the development of a foliation defined by an organized banding of heavily fractured calcite and dolomite clasts (Smith et al., 2017). Consequently, Smith et al. (2017) suggested that some natural foliated rocks (i.e., compositional banding, grain size variations, and preferred particle or fracture alignments) could form by distributed brittle flow as strain localizes during coseismic shearing, especially if such foliations are found in proximity to other plausible evidences of coseismic slip (e.g. mirror-like slip surfaces). However, their interpretation was based exclusively on experiments performed at seismic slip rates (i.e., V = 1.13 ms^{-1}) and under room-humidity conditions. Therefore, motivated by the experimental and microstructural work conducted by Smith et al. (2017), the Chapter II of the thesis was dedicated to the investigation of the frictional and microstructural evolution (scale range 10^{-6}-10^{-2} m) of gouge mixtures of calcite-dolomite over a wider range of slip rate, displacement, normal stress and deformation conditions (room-humidity vs. water-dampened). In particular, foliated gouges formed only in the experiments performed at seismic slip rates and in the absence of water, at least for the max slip of about 0.4 m

investigated in the experiments which was consistent with the finding of foliated cataclasites in natural faults accommodating < 0.1 m of slip.

The investigation of the deformation mechanisms that are at the base of the frictional behavior and microstructural evolution that we observe in the laboratory, such as those documented in Chapter II, is important to the understanding of the different phenomena that control the fault slip behavior within the seismic cycle (e.g., Smeraglia et al., 2017b). Such mechanisms typically operate at scale lengths ranging 10^{-9}-10^{-2} m. Cataclasis is the primary mechanism for gouge formation, grain size reduction, and has a major influence on strain localization. The mechanical properties of gouges are a function of their composition, particle size distribution, grain shapes, etc. (e.g., Mair et al., 2002; Abe and Mair, 2009). Numerous microphysical models for cataclasis have been proposed to quantitatively describe and interpret certain characteristics of fault rocks such as the grain size distribution (e.g., Allègre et al. 1972, Turcotte, 1986; Sammis et al., 1987; Sammis and King, 2007) and frictional behavior (e.g., Bos and Spiers, 2002; Niemeijer and Spiers, 2007; den Hartog and Spiers, 2014; Chen and Spiers, 2016) as deformation proceeds. However, due to computing/technical limitations, such microphysical models are accompanied by quite strong assumption, like considering the sheared gouge to have isotropic properties and simple grain shapes (usually spherical or cylindrical). In the last decade, the development of three-dimensional (3D) numerical simulations of gouge evolution introduced a novel tool to study shear in granular materials (Abe and Mair, 2005; Mair and Hazzard, 2007; Mair and Abe, 2008; Abe and Mair, 2009). Some of the main results from the 3D modelling approach were: (1) the ability to image the formation, destruction and the overall geometries of grain bridges (also called *force chains*) acting between clasts during shear; (2) the reproduction of typical fractal grain size distributions found in natural gouges and cataclasites (e.g., Bili et al., 2003; Billi and Storti, 2004; Di Toro and Pennacchioni, 2005; Agosta and Aydin, 2006; Muto et al., 2015) and theorized in microphysical models (e.g., constrained comminution model, Sammis et al. 1987); (3) the reproduction of grain shapes that evolve with slip (Abe and Mair, 2009). However, natural fault gouges often contain minerals with strong anisotropies, such as cleavage planes in phyllosilicates, carbonates, feldspars and amphiboles (e.g., Faulkner et al., 2003; Rutter et al., 2007; Fondriest et al., 2012; Schröckenfuchs et al., 2015; Smeraglia et al., 2016). The role that such anisotropies might have during cataclasis has not been explored so far. The study presented in Chapter III focuses on the investigation of the deformation mechanisms active within the bulk gouge from experiments

performed on gouge mixtures of calcite and dolomite described in Chapter II (scale range 10^{-6}-10^{-3} m). Supported by detailed microstructural investigations (Field Emission Scanning Electron Microscopy and Electron Back Scattered Diffraction) we suggest that mineral anisotropy plays a pivotal role under the shallow deformation conditions leading, quite surprisingly, to the formation of a crystal preferred orientation in the cataclastic regime as a result of mechanical grain rotation and brittle fracturing.

For a complete characterization of the deformation mechanisms active during seismic slip in carbonate gouges, our analysis moved from the bulk gouge (Chapter III), where cataclasis was operating, to the principal slip zone (Chapter IV), where strain localization occurred and frictional heating and grain size reduction were intense (Smith et al., 2015). Here, the principal slip zone was mainly composed by nanogranular (<< 1 μm) aggregates. Principal slip zones with such characteristics have being widely reported both in natural fault zones (e.g., Chester et al., 2005; Wilson et al., 2005; Ma et al., 2006; Pittarello et al., 2008; Siman-Tov et al., 2013; Fondriest et al., 2015; Demurtas et al., 2016; Smeraglia et al., 2017a) and experimental faults (e.g., Han et al., 2007b, 2010; Reches and Lockner, 2010; De Paola et al., 2011b; Han et al., 2011; Tisato et al., 2012; Chen et al., 2013; Verberne et al., 2013b, 2014; De Paola et al., 2015; Green et al., 2015; Spagnuolo et al., 2015; Yao et al., 2016; Aretusini et al., 2017; Smeraglia et al., 2017b). Although very common, the mechanism of formation of nanograins remains debated (Wilson et al., 2005; Han et al., 2007b; Sammis and Ben-Zion, 2008; Siman-Tov et al., 2013; Green et al., 2015; Spagnuolo et al., 2015) and so is their mechanical role during frictional sliding (Han et al., 2010; Reches and Lockner, 2010; De Paola et al., 2015; Green et al., 2015; Spagnuolo et al., 2015). This is mainly due to the diversity of factors that can control the influence of nanograins on the fault mechanical behavior and the inability of current common microanalytical techniques to properly investigate them. Some authors have ascribed a “mechanical” influence of the nanoparticle to the dynamic weakening observed concomitant to their production during experimental faulting (Han et al., 2011). More recently, experimental studies performed at low- and high-velocity (slip rate V = 1 μms^{-1} to 1 ms^{-1}) have explored the possibility that nanoparticles could influence fault rheological properties due to the activation of “viscous” deformation mechanisms, with efficient strain accommodation through grain-size sensitive deformation mechanisms like grain boundary sliding aided by dislocation- or diffusion creep (e.g., Verberne et al., 2013b, 2014; De Paola et al., 2015; Green et al., 2015; Spagnuolo et al., 2015). To date, the investigation of deformation mechanisms active within

nanoparticle aggregates has been performed mainly by SEM and TEM analyses. However, the resolution of the SEM is too low and the volumes investigated with TEM too small to yield statistical significant dataset (e.g. nanograin orientation) to constrain the deformation mechanism operating at the nanoscale. Here, in Chapter IV, we test a newly developed technique (Transmission Kikuchi Diffraction, TKD; Trimby, 2012) that allowed us to obtain the same type of information as in conventional electron backscatter diffraction analysis, but with the advantage of a significantly higher spatial resolution (i.e., 1-2 nm; Trimby, 2012). Our results report a new type of observation (e.g., crystallographic preferred orientation, lattice distortion, grain boundary misorientation) on the properties of nanoparticles and nanogranular aggregates and show the great potential of TKD to the study of ultrafine geological materials.

Chapter I

Structure of a normal seismogenic fault zone in carbonates: The Vado di Corno Fault, Campo Imperatore, Central Apennines (Italy)

This study was performed with the collaboration of Michele Fondriest, Giulio Di Toro, Fabrizio Storti, Fabrizio Balsamo, Luca Clemenzi and Andrea Bistacchi. I was assisted in the field by Michele Fondriest, Giulio Di Toro, Fabrizio Storti, Fabrizio Balsamo, Luca Clemenzi and Andrea Bistacchi. I was assisted (but not continuously) during microstructural analysis by Michele Fondriest and Giulio Di Toro. The material presented here was discussed with Michele Fondriest, Giulio Di Toro, Fabrizio Storti, Fabrizio Balsamo, Luca Clemenzi and Andrea Bistacchi. This chapter was published as the following paper: Demurtas, M., Fondriest, M., Balsamo, F., Clemenzi, L., Storti, F., Bistacchi, A., Di Toro, G., 2016. Structure of a normal seismogenic fault zone in carbonates: The Vado di Corno Fault, Campo Imperatore, Central Apennines (Italy). J. Struct. Geol. 90, 185–206. doi:10.1016/j.jsg.2016.08.004. Part of the data it this chapter were also used in the following paper: Pischiutta, M., Fondriest, M., Demurtas, M., Magnoni, F., Di Toro, G., Rovelli, A., 2017. Structural control on the directional amplification of seismic noise (Campo Imperatore, central Italy). Earth Planet. Sci. Lett. 471, 10–18. doi:10.1016/j.epsl.2017.04.017.

Abstract

The Vado di Corno Fault Zone (VCFZ) is an active extensional fault cutting through carbonates in the Italian Central Apennines. The fault zone was exhumed from ~2 km depth and accommodated a normal throw of ~2 km since Early-Pleistocene. In the studied area, the master fault of the VCFZ dips N210/54° and juxtaposes Quaternary colluvial deposits in the hangingwall with cataclastic dolostones in the footwall. Detailed mapping of the fault zone rocks within the ~300 m thick footwall-block evidenced the presence of five main structural units (Low Strain Damage Zone, High Strain Damage Zone, Breccia Unit, Cataclastic Unit 1 and Cataclastic Unit 2). The Breccia Unit results from the Pleistocene extensional reactivation of a pre-existing Pliocene thrust. The Cataclastic Unit 1 forms a ~40 m thick band lining the master fault and recording in-situ shattering due to the propagation of multiple seismic ruptures. Seismic faulting is suggested also by the occurrence of mirror-like slip surfaces, highly localized sheared calcite-bearing veins and fluidized cataclasites. The VCFZ architecture compares well with seismological studies of the L'Aquila 2009 seismic sequence (mainshock M_W 6.1), which imaged the reactivation of shallow-seated low-angle normal faults (Breccia Unit) cut by major high-angle normal faults (Cataclastic Units).

1. Introduction

Thick carbonate sedimentary sequences (4–10 km) are common within the shallow crust of many seismically active areas worldwide, including the circum-Mediterranean mountain belts. In most of these belts (e.g., the Apennines, Italy; the Hellenides-Dinarides, Balkan Peninsula; the Maghrebides, Algeria–Tunisia) moderate to large earthquakes nucleate and propagate within carbonate host rocks (i.e., limestones and dolostones) (e.g., Di Bucci and Mazzoli, 2003; Burchfiel et al., 2008). Modern advanced geophysical and seismological techniques (e.g., tomographic studies, trapped waves, double-difference method; Waldhauser and Ellsworth, 2000; Di Stefano et al., 2011; Allam and Ben-Zion, 2012) allow to image the geometrical complexity of active buried fault zones with high spatial resolution (i.e., tens of meters) (e.g., Schaff et al., 2002; Chiaraluce et al., 2011; Valoroso et al., 2013, 2014) comparable to the resolution of geological field observations (e.g., Collettini et al., 2014). Therefore, the characterization of the internal structure of exhumed fault zones in the field is even more necessary both for the validation of the remotely acquired geophysical/seismological observations and for the investigation of the deformation processes active at smaller scale during the seismic cycle (e.g., Alvarez et al., 1978; Lavecchia, 1985; Wojtal and Mitra, 1986; Gratier and Gamond, 1990; Willemse et al., 1997; Faulkner et al., 2003; Agosta and Aydin, 2006; Mitchell and Faulkner, 2009; Bistacchi et al., 2010; Mitchell et al., 2011; Fondriest et al., 2012; Tesei et al., 2013; Bullock et al., 2014; Collettini et al., 2014). Regarding the deformation processes, clues can arise from laboratory experiments conducted both on cohesive and non-cohesive rocks (e.g., Paterson, 1958; Rutter, 1983; Verberne et al., 2010; De Paola et al., 2011a; Di Toro et al., 2011; Smith et al., 2013) and from detailed microstructural investigations of both natural and experimental fault rocks through different techniques, such as cathodoluminescence (e.g., Clemenzi et al., 2015), electron back scatter diffraction (e.g., Smith et al., 2013), optical-, electron- and atomic force-microscopy (e.g., Siman-Tov et al., 2013; Tesei et al., 2013; Viti et al., 2014), water- and laser-granulometry (e.g., Billi and Storti, 2004; Storti et al., 2007).

Based on these studies, simplified models of fault zones have been developed to describe the architecture and permeability of fault zones. In particular, they consist of a fault core, where most of the strain is accommodated, surrounded by an intensely deformed damage zone, which grades into a host rock with background deformation level (Chester and Logan, 1986; Caine et al., 1996; Shipton et al., 2006; Childs et al., 2009; Faulkner et al., 2010). The fault core is characterized by intense faulting and includes fault products like gouges, ultracataclasites, cataclasites and

breccias (Sibson, 1977). The damage zone generally comprises most of the fault zone volume (up to hundreds of meters in thickness) and includes rocks that underwent fault-related fracturing, veining and subsidiary faulting, but maintain their primary features (Caine et al., 1996; Wibberley et al., 2008). Though this model describes fairly well a number of fault zones in different tectonic settings and lithologies (Faulkner et al., 2003; Wibberley and Shimamoto, 2003; Agosta and Aydin, 2006; Micarelli et al., 2006), it may result oversimplified when the presence of inherited structures developed through different times and kinematics results in complex spatial relationships between high- and low-strain compartments (e.g., Fagereng and Sibson, 2010). This point is of paramount importance in carbonates, which are frequently affected by the presence of joints, pressure solution seams, veins and faults derived from sequential deformation events (e.g., Agosta and Aydin, 2006; Aydin et al., 2010). Moreover, carbonates rocks are frequently characterized by compositional and facies heterogeneities (e.g., bedding thickness variation, laminations, grain size, presence of marl layers) that have a strong influence on rock mechanical and transport properties (Billi et al., 2003; Bonson et al., 2007; Tesei et al., 2013; Bullock et al., 2014; Michie et al., 2014; Tesei et al., 2014).

The carbonate-dominated sequences of the Apennines have experienced the alternation of extensional and compressional deformation regimes since Jurassic times, resulting in a complex structural setting on which the Quaternary extension is superposed (Elter et al., 1975). In particular, the Apennines expose the sedimentary sequences of the passive margin associated with the opening of the Alpine Tethys, subsequently involved in the westward subduction of the African plate underneath Eurasia (Boccaletti et al., 1971; Patacca et al., 1990) starting from the Eocene and the build-up of the collisional chain (fold-and-thrust belt) from Pliocene onwards (Malinverno and Ryan, 1986; Buiter et al., 1998; Jolivet and Faccenna, 2000; Vezzani et al., 2010; Molli and Malavieille, 2011; Carminati et al., 2012; Cardello and Doglioni, 2014). Since late Tortonian-Messinian times, the eastward rollback of the subducting plate (Malinverno and Ryan, 1986) resulted in a progressive eastward migration of the fold-and-thrust belt and backarc extension started affecting the upper plate. As a consequence, the former compressional domains in the hinterland of the Apennine belt have been progressively subjected to extension coaxial with compression (Elter et al., 1975; Ghisetti and Vezzani, 1981; Patacca et al., 1990; Jolivet et al., 1998; Rosenbaum and Lister, 2004).

In the Central Apennines, the main topographic divide is located within the Gran Sasso Massif (GSM, the Corno Grande, 2912 m a.s.l. is the highest peak of the Apennines), which marks the eastern limit where active extension occurs (D'Agostino et al., 1998). The GSM is located at the transition between the Mesozoic Latium-Abruzzi carbonate platform and the Umbria-Marche

pelagic domain (e.g. Parotto and Praturlon, 1975). The inherited paleogeography influenced both the construction of the thrust belt and the subsequent extension, leading to the formation of a complex array of non-cylindrical thrusts, folds and normal faults whose interpretation is still largely debated (D'Agostino et al., 1998; Calamita et al., 2003a; Speranza, 2003; Speranza et al., 2003; Vezzani et al., 2010; Santantonio and Carminati, 2011; Cardello and Doglioni, 2014). Indeed different authors described the same structural framework as the result of (i) out-of-sequence thrusting with the formation of duplex structures eventually cut by normal faults due to eastward migration of extensional domains (Ghisetti and Vezzani, 1991; Sani et al., 2004; Vezzani et al., 2010), (ii) postorogenic normal faulting due to gravitational collapse of the orogen (D'Agostino et al., 1998), or (iii) alternation of positive and negative stress inversions and subsequent rotation and folding of preexisting faults during the evolution of the belt (Calamita et al., 2003a, 2003b, 2008; Cardello and Doglioni, 2014).

Extension in the GSM and surrounding areas occurred since late Pliocene-Early Pleistocene and led to the formation of a series of seismically active extensional fault zones striking NW-SE, which are responsible for major earthquakes in the Central Apennines. A major recent seismic sequence that hit the area was associated with the L'Aquila earthquake (M_W = 6.1, April 6th, 2009, Chiarabba et al., 2009; Chiaraluce, 2012). There are still uncertainties whether the main shock of the seismic sequence was localized within the crystalline basement or in the overlying ultra-thick (up to 8 km) carbonate succession (Chiaraluce, 2012; Speranza and Minelli, 2014), but it is certain that the mainshock rupture propagated through the carbonate sequence, and that some of the foreshocks and most aftershocks nucleated within and propagated through it (Chiaraluce, 2012). Focal mechanism solutions of the seismic events were mostly normal dip-slip, consistent with the mainshock (strike = 140°±5°, dip angle = 52°±5°; rake = 97°±10°; Chiaraluce, 2012), and just a few focal mechanism solutions showed strike-slip kinematics (Valoroso et al., 2013, 2014).

In this study, we describe the architecture of the Vado di Corno Fault Zone (VCFZ), an extensional fault cutting through a dolomitized carbonate platform sequence in the GSM area, which is a segment of the Campo Imperatore Fault System (CIFS) (Vezzani et al., 2010). Field surveys were performed in the fault footwall block, which is excellently exposed due to the occurrence of a well-developed badland morphology. Several structural units were recognized within the fault zone. The mapped structural units allowed us to document the evidence for a Pliocene dolomitized thrust zone and determine its crosscutting relationships with the Quaternary extensional structures of the VCFZ. Microstructural and field observations suggest that most of the slip surfaces within the VCFZ

experienced coseismic deformation. Therefore, the VCFZ can be considered as an exhumed analogue of seismogenic sources active in the Central Apennines. Based on this assumption we finally compare the overall geometry and kinematics of the exposed section of the VCFZ (footwall block) with the geophysically imaged structures of the L'Aquila fault system activated during the April 2009 seismic sequence.

2. Geological setting

2.1. The Gran Sasso Massif

The GSM is one of the principal structural features of the Central Apennines and formed during Late Messinian, Early-Middle Pliocene orogenic contraction (Ghisetti and Vezzani, 1991). The main thrust and related anticline display an arcuate geometry that consists of two main segments striking ca. E-W and N-S, respectively (Fig. 1a). The E-W striking segment is characterized by an overturned anticline in the hangingwall, cut by out-of-sequence dip-slip thrusts (e.g., Ghisetti and Vezzani, 1991). The N-S striking segment shows both dip-slip and right-lateral strike-slip components (Speranza et al., 2003; Vezzani et al., 2010). The GSM consists of an array of six major thrust faults crosscutting each other in an out-of-sequence geometry (Ghisetti and Vezzani, 1991) with the uppermost thrust faults outcropping in the Vado di Corno area (i.e., the Omo Morto thrust fault; Ghisetti and Vezzani, 1991, Fig. 1b). Early Pleistocene to Present extension within the GSM is testified by the presence of a well-developed system of active extensional fault zones including the VCFZ described in this study (e.g., D'Agostino et al., 1998; Galadini, 1999).

In the study area, the VCFZ is developed mostly within the same lithostratigraphic unit, namely the *Calcare Massiccio Fm.* (Lower Jurassic; e.g. Adamoli et al., 2012, Fig. 1b and c), which consists of an up to 600 m thick sequence of whitish to brownish limestones with beds (5–50 cm thick) and intervals (1–5 m thick) organized in cyclothems. The ciclothems comprise grainstones, packstones and wackestones with oolites, oncolites, intraclasts, peloids and trails of birdeyes and *fenestrae* (Adamoli et al., 2003). The occurrence of dolostones is frequent. This is the case of the studied outcrops, which are located within a wide band (up to 300 m thick) of intensely deformed dolostones. Exposures of undeformed dolostones are not observed within the study area. Nevertheless, the primary sedimentary and diagenetic features of the dolostones are preserved within low-strain domains embedded within the fault footwall damage zone (see section 5.1 and

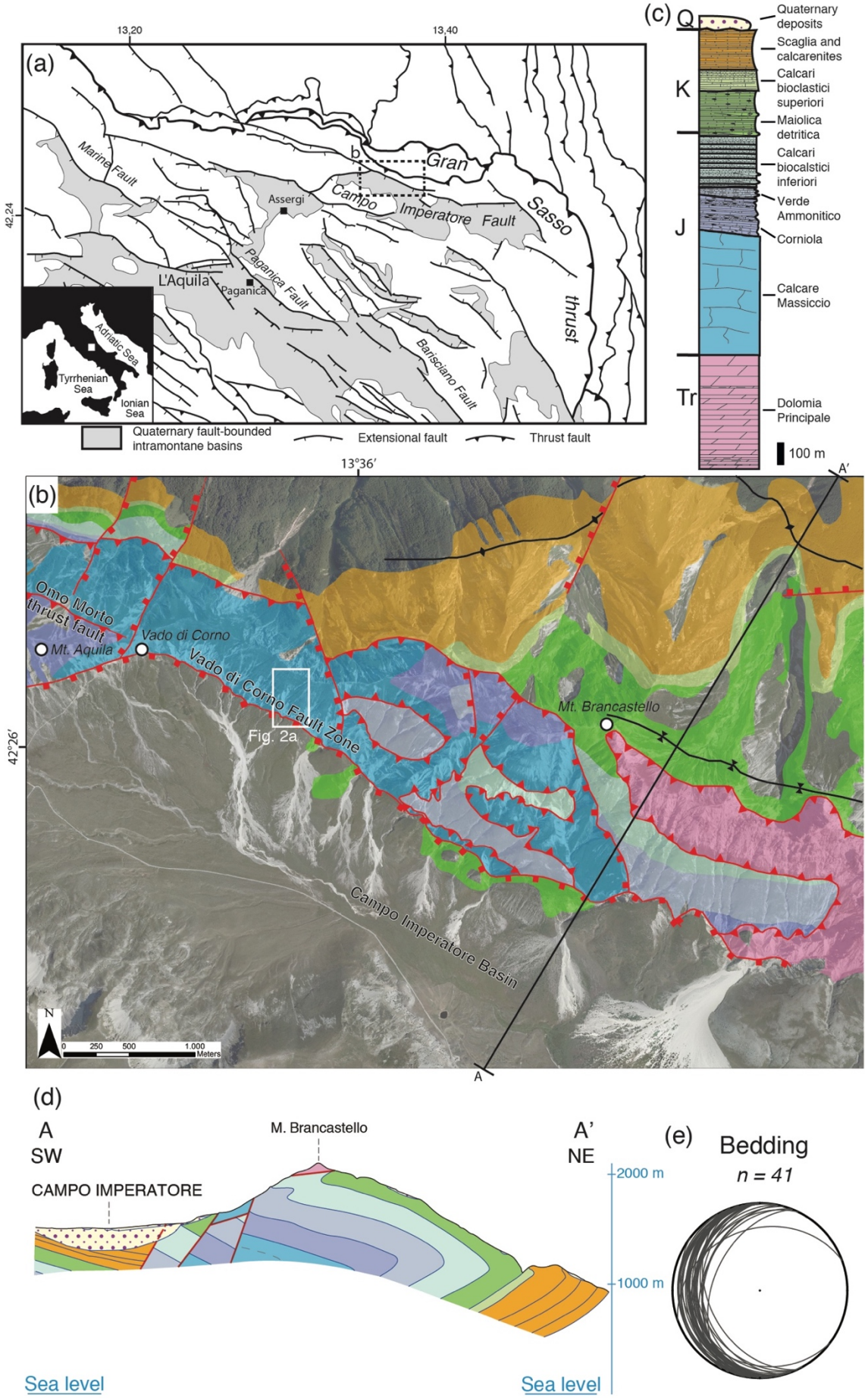


Fig. 1. See next page for caption.

Fig. 1. (previous page) Geological setting of the Campo Imperatore area. (a) Structural map of the Gran Sasso area (modified after Storti et al., 2013). (b) Geological map of the study area simplified after the published Foglio 349 "Gran Sasso d'Italia" (Ispra, 2012). Quaternary colluvial deposits are the infilling of the Campo Imperatore intramontane basin and correspond to the non-colored areas. NNE-SSW striking normal faults dissect and displace the thrust system. The Omo Morto thrust fault runs on the northern side of Mt. Aquila and disappears before Vado di Corno, where the fault zone (VCFZ) is exposed within badlands. (c) Stratigraphic column of the Campo Imperatore area (modified after Cardello and Doglioni, 2014). (d) Geological cross section across the Campo Imperatore intramontane basin (modified after Ispra, 2012). To the NE of the Mt. Brancastello strata at the hangingwall of the thrust are overturned, while in the Campo Imperatore plain normal faults cut and dislocate the thrust system. (e) Stereographic projection of bedding surfaces measured within the VCFZ result in a monocline with constant attitude of N270/20° (stereographic projection in the figure is equal area, lower hemisphere).

Fig. 4). At least two dolostone facies were distinguished: (i) dolomicrite to dolomitic packstone-wackestones with stromatolitic laminations and preserved original microfabric (i.e., allochems of limestone precursor) and (ii) crystalline dolostones with coarser average crystal/grain size, which locally are nodular and porous (*fenestrae*, etc.). The two facies are in stratigraphic continuity or are separated by irregular boundaries (e.g., rock lenses), and are interpreted as the product of different diagenesis (i.e., timing and intensity of dolomitization).

Other lithologies outcropping along the fault zone adjacent to the study area consist of the slope and basinal deposits of the *Corniola* (mudstone, Lower Jurassic), *Verde Ammonitico e Calcari e Marne a Posidonia* (micritic limestone, Lower-Middle Jurassic), *Calcari Bioclastici Inferiori* (breccias and megabreccias Middle-Upper Jurassic) and *Maiolica Detritica* (micritic limestone, Upper Jurassic-Lower Cretaceous) formations (Adamoli et al., 2012). The *Verde Ammonitico e Calcari e Marne a Posidonia Fm.*, hereby simply indicated as *Verde Ammonitico Fm.*, consists of green to dark grey micrite, locally intercalated with marly layers and levels rich in dark chert. To the east of the study area, the *Verde Ammonitico Fm.* is overthrusted by the *Calcare Massiccio Fm.* (e.g., Ghisetti and Vezzani, 1991; Adamoli et al., 2012, Fig. 1b–d). In the footwall of the VCFZ, we found local occurrences of strongly dolomitized *Verde Ammonitico Fm.* and associated dark chert remnants, typically underlying the dolomitized *Calcare Massiccio Fm*. This indicates that the stacking exposed to the east, actually occurs also in the footwall of the VCFZ, in the study area, where both units underwent severe dolomitization preceding Quaternary extensional faulting. Small outcrops of the *Maiolica Detritica Fm.* occur in the hangingwall of the fault zone near Mt. Brancastello (Fig. 1d).

The Campo Imperatore intramontane basin, in the hanging wall of the VCFZ, is characterized by glacial, alluvial and colluvial deposits. The former are related to Late Pleistocene glacial events (Giraudi and Frezzotti, 1995, 1997; Adamoli et al., 2012); the latter are Holocene in age and derived from weathering of the exposed carbonate rocks. These loose deposits feed well-developed alluvial fan systems (Adamoli et al., 2012 and references therein). In this study all these deposits will be comprehensively referred to as *Quaternary deposits*.

2.2. The Vado di Corno Fault Zone

The VCFZ outcrops continuously for ca. 5 km bordering the northern part of the Campo Imperatore intramontane basin (Fig. 1b). The VCFZ belongs to a larger fault system (the so called Campo Imperatore Fault System – CIFS) which runs for ~ 20 km in the Gran Sasso Massif and is

thought to have accommodated a cumulative throw of 2000–3000 m (Ghisetti and Vezzani, 1991, 1999; D'Agostino et al., 1998). The exposed fault zone was exhumed from ca. 1–2 km depth starting from Early-Pleistocene (Agosta and Kirschner, 2003).

Between Vado di Corno and Mt. Brancastello, the VCFZ outcrops almost continuously along about 20 sub-parallel creeks oriented orthogonal to the average strike of the fault zone. The creeks are affected to fast erosion and the resulting badland topography offers a unique three-dimensional view into the fault zone footwall block. With the aim of describing the internal structure of the VCFZ, we performed a detailed survey along the strike of the fault zone and selected a creek (UTM coordinates, zone 33N WGS84, 385611 E, 4700440 N, white arrow in Fig. 1b) that provided a representative cross-section of the fault. Measurements of bedding surfaces (dip azimuth/dip angle N270/20°, Fig. 1e) in the fault zone show a gently W-dipping monocline at the hangingwall block of the GSM thrust.

The seismic activity of the CIFS is documented both by paleoseismological studies and instrumental seismicity (Giraudi and Frezzotti, 1995; Galli et al., 2002; Galadini et al., 2003; ISIDe Working Group, 2010). Trenches dug in the Campo Imperatore basin highlighted at least three main surface ruptures since Late Pleistocene; an earthquake with magnitude up to M_W = 6.95 was estimated to be produced in case of activation of the entire extensional Campo Imperatore Fault System (Galli et al., 2002; Galadini et al., 2003). Current seismicity is documented in the GSM; in particular, the CIFS is characterized by relatively continuous microseismicity with M_L < 2.5 (ISIDe Working Group, 2010).

3. Methods

The footwall block of the VCFZ was mapped at 1:500 scale in a selected creek and the adjacent areas (mapped area c. 0.2 × 0.4 km2; Fig. 2a) using, as a topographic basis, orthorectified aerial photographs (spatial resolution 0.2 m, courtesy of the Regione Abruzzo: www.regione.abruzzo.it/xcartografia). The resulting structural map of the exposed fault zone is shown in Fig. 2a. The map shows (i) the principal fault strands and (ii) the spatial distribution of fault zone structural units, i.e. rock volumes affected by distinct bulk deformation intensity and, likely, deformation processes. Fault zone structural units were defined on the base of a series of mesoscale observations such as:

- spacing of fractures and subsidiary faults (i.e., faults with outcrop continuity less than 5 m);

- relative abundance and geometry of veins and sealed fractures;
- clast/matrix proportion in the fault rocks;
- color of non-weathered rocks;
- preservation of primary sedimentary features.

In particular, we identified five main structural units within the VCFZ (Fig. 2a): (i) the Low Strain Damage Zone (LSDZ), (ii) the High Strain Damage Zone (HSDZ), (iii) the Breccia Unit (BU), (iv) the Cataclastic Unit 1 (CU1) and (v) the Cataclastic Unit 2 (CU2). In the exposed footwall, the CU1 and CU2 represent the fault core, while the LSDZ, HSDZ and BU represent the damage zone. These data were digitized using ArcGIS© and Move© software.

Structural data, such as attitude of bedding, joints, and veins, orientation and kinematics of faults, and fracture frequency in damage zones, were collected at sites evenly distributed across the outcrops and located using a handheld GPS (accuracy typically ± 2 m) and along scan-lines oriented perpendicular to the master fault.

Fracture abundance (i.e., areal fracture density and intensity, P_{20} and P_{21} respectively, *sensu* Dershowitz and Herda, 1992) was computed in both the LSDZ and the HSDZ to quantify fault-related damage at increasing distance from the master fault of the VCFZ. The areal fracture density (P_{20}) is defined as number of trace centers per unit sampling area [m^{-2}], while the areal fracture intensity (P_{21}) is defined as length of fracture traces per unit sampling area [m^{-1}]. Since both P_{20} and P_{21} are orientation-dependent, they were measured perpendicular to the principal fracture/fault systems of the structural domain. To prevent bias due to the resolution of the techniques (i.e., data truncation) and the finite size of the sampled domain (i.e., data censoring), measurements were performed on a selected range of fracture length. The upper and lower cutoff were specifically chosen to consider only the linear interval of the trace length distribution in a logarithmic plot (i.e., 0.407–1.125 m and 0.01–0.1 m for the LSDZ and HSDZ respectively). Truncation and censoring take place since the lower cutoff usually exceeds the resolution of the images (typically ≤ 1 cm) and the upper cutoff is smaller than the dimension of the sampled domain. Since the selected range for computing fracture abundance was limited up to two orders of magnitude, we used this data only for comparison between the damage intensity in the LSDZ and HSDZ. For the LSDZ, fracture traces were digitized in Move© on a vertical section oriented perpendicular to the master fault (strike N30°) obtained from a georeferenced photogrammetric model. Traces were then exported in GoCAD© to compute trace properties (centroid distance from the master fault, trace length, trend and plunge). Finally, fracture statistics were computed with an ad-hoc Matlab© script. For the HSDZ,

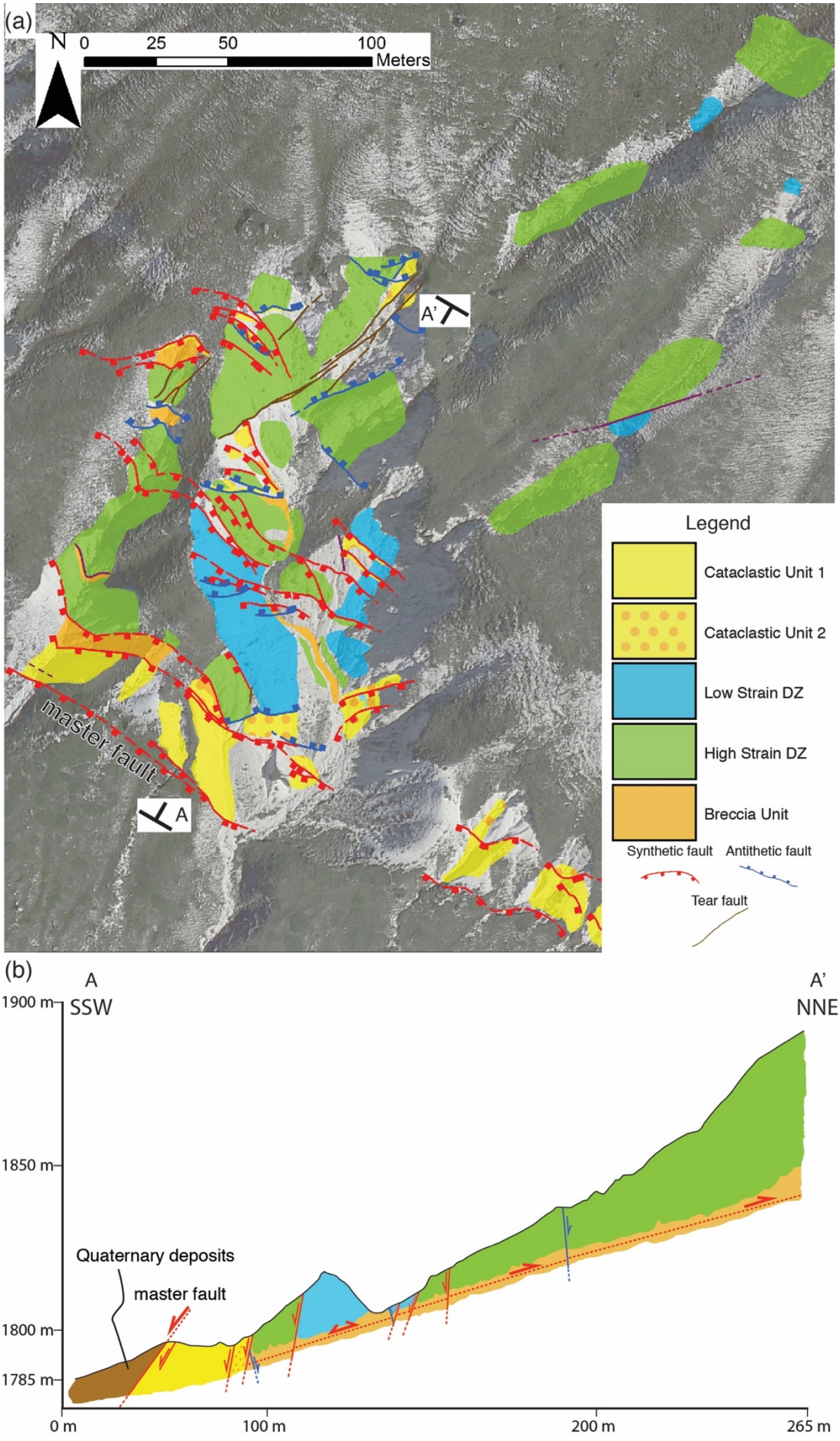


Fig. 2. See next page for caption.

Fig. 2. (previous page) Structural map and geological section of the study area. (a) The structural map shows the distribution of principal fault strands (ticks on faults are drawn on the downthrown side) and structural units distinguished within the footwall block of the Vado di Corno Fault Zone. The base of the creek is marked by the master fault, which is lined by the cataclastic units. A tens of meters thick lithon of Low Strain Damage Zone is found at about 50 m from the master fault. The Breccia Unit outcrops both at the bottom of the creek in the center of the map and in contact with the Cataclastic Unit 1 to the SW. The High Strain Damage Zone comprises most of the fault zone in terms of rock volumes. (b) A geological section oriented orthogonal to the master fault (N30°E) shows how the structural units are typically associated and bounded by the normal faults with the exception of the Breccia Unit, which dips at low angle and outcrops where the creek is more eroded. The axes are in scale X:Y = 1:2.

Fig. 3. (next page) Core of the Vado di Corno Fault Zone. (a) The structural units distinguished in the footwall block of the VCFZ show a great variability in appearance due to changes in the bulk deformation intensity and deformation processes. (b) The base of the badlands is marked by the contact between the Quaternary deposits in the hangingwall (reddish in color) and the cataclasites in the footwall (white in color) along the master fault. (c) The core of the master fault is < 20 cm thick and exhibits an alternation of reddish Quaternary deposits and whitish cataclastic layers with irregular borders resembling fluidization textures typical of sedimentary flame structures. (d) Stereoplots of both non- and lineated fault and joints across the studied creek. Thick great circles are mean attitude of principal synthetic and antithetic fault strands, while dashed great circles represent mean orientation of the NE-SW striking tear faults (stereographic projection in the figure is equal area, lower hemisphere).

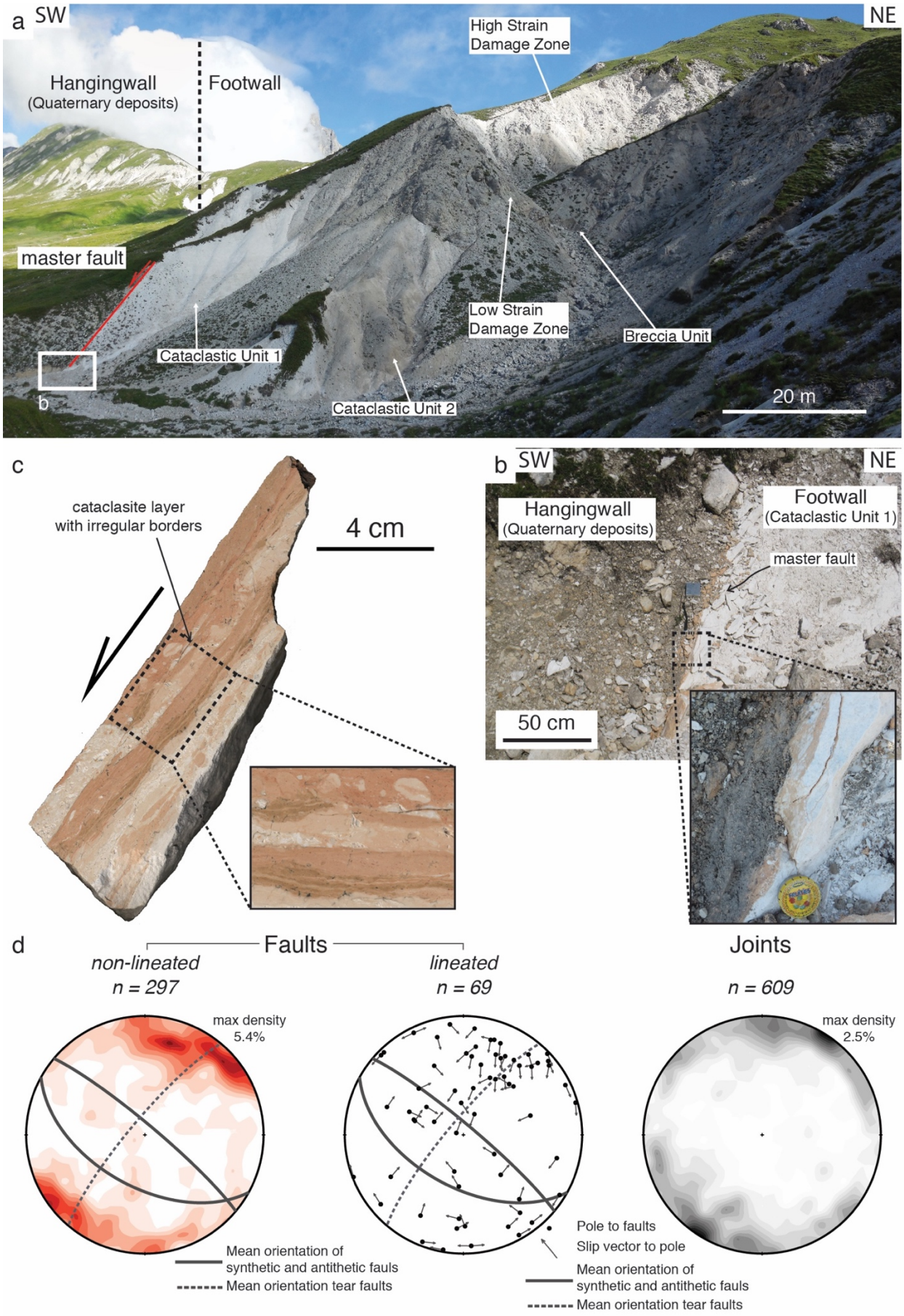


Fig. 3. See previous page for caption.

traces were mapped in ArcGIS© on smaller image frames oriented both parallel and perpendicular to the master fault (window sampling dimension 60 × 40 cm, photo resolution < 1 mm). Fracture statistics were then calculated using the same Matlab© script as for the LSDZ.

The acquisition of structural data (n = 965) was coupled with the collection of oriented fault rock samples (n = 87) to characterize the microstructures and mineralogy of the host rock, veins and slip zones. Microstructural observations were conducted on polished thin sections (n = 40) cut perpendicular to the veins and the slip surfaces and oriented either parallel or perpendicular to fault lineations, using transmitted-light optical microscopy (OM), field emission scanning electron microscopy (FE-SEM), and optical microscopy cathodoluminescence (OM-CL). Mineral phase identification and elemental analysis were performed through energy dispersive spectroscopy (EDS) at the FE-SEM, while bulk mineralogy was derived from X-ray powder diffraction (XRPD) analyses. Analyses were conducted at the Department of Geoscience in Padua (Italy) and at HT-HP laboratories at the Istituto Nazionale di Geofisica e Vulcanologia (INGV) in Rome (Italy).

4. Cross-sectional structural architecture

The VCFZ in the mapped creek consists of an array of ~ NW-SE striking, mostly SW dipping, fault surfaces. The major ones can be easily followed in the field for distances of 20–30 m and are characterized by strong shear strain localization within layers of cataclasite with thickness up to 30 cm. They bound different structural units both in the fault core and in the damage zone (Fig. 2a–b). At the base of the badlands, the contact between the cataclastic rocks and the hangingwall Quaternary deposits is marked by a polished fault slip surface with average dip azimuth/dip of N209/54° and average pitch of 80° to the E (Fig. 3a). The fault is assumed to be the master fault because (i) it marks the major discontinuity between the Quaternary alluvial deposits of the Campo Imperatore intramontane basin in the hangingwall block and the Jurassic carbonates in the footwall block (Fig. 3b) and, (ii) it is associated with a ~ 40 m thick cataclastic fault core (CU1) in the footwall block. The master fault principal slip zone consists of a ~ 20 cm thick cataclastic layer with mixed hangingwall and footwall materials, characterized by up to two-centimeter-thick, cohesive injections of reddish and whitish ultracataclasites (Fig. 3c). The boundaries of the injected ultracataclasites are wavy and resemble fluidization features (e.g., Brodsky et al., 2009). Moreover, they are truncated by sharp slip surfaces (Fig. 3c) (e.g., Siman-Tov et al., 2013).

A representative cross-section of the VCFZ footwall is provided in Fig. 2b. The CU1 lines the master fault forming a continuous ~ 40 m thick band. Moving to the NE, the CU1 grades into the CU2, which crosscuts the BU along a SW dipping major synthetic normal fault. The BU is the lowermost structural unit, which outcrops along the bottom of the creek, with the mean attitude of a gently SW dipping flat (Fig. 2a). The BU is embedded within the damage zone units (LSDZ and HSDZ) (Fig. 2a–b), which show a sharp fault contact with the cataclastic rocks (CU1 and CU2). Most of the damage zone volume consists of HSDZ, while the LSDZ represents a ca. 20 m thick isolated block (in direction orthogonal to the Vado di Corno master fault) embedded within the HSDZ. Bands of cataclastic rocks (mostly CU1) up to few meters thick were also documented along major fault strands in the outer part of the VCFZ up to distances of hundreds of meters from the master fault. Smaller volumes of LSDZ occur also in the northernmost outer portion of the creek towards the mountain ridge.

The faults in the footwall damage zone typically show high dip angles (>70°) and are organized in two main sets synthetic and antithetic with respect to the master fault. A third set striking NE-SW is also present (Fig. 3d). Synthetic faults include two subsets with attitude (dip azimuth/dip angle) N195/75° and N225/80°, while the average orientation of antithetic faults is N50/85°. NE-SW striking faults control the topography in the upper part of the creek (usually at distance greater than 100 m from the master fault) and dip both towards SE and NW. Grooves and fault lineations are generally dip-slip for synthetic faults, while antithetic- and NE-SW striking faults exhibit both dip-slip and left- (rarely right-) lateral slip kinematics. The absence of clear markers makes difficult to estimate the amount of offset accommodated by individual faults. Poles to joints (opening mode fractures) are at high angle and show different orientations with clustering around the orientations of the faults (Fig. 3d).

5. Structural units

5.1. Low Strain Damage Zone

The Low Strain Damage Zone (LSDZ) consists of relatively poorly deformed rock volumes, where sedimentary features of the host rocks such as bedding surfaces, stromatolitic lamination, planar trails of fenestrae and “burial” stylolites/pressure solution seams are well recognizable (Fig. 4a and b). In the selected creek, the LSDZ outcrops as a ca. 20 m thick block (measured orthogonal

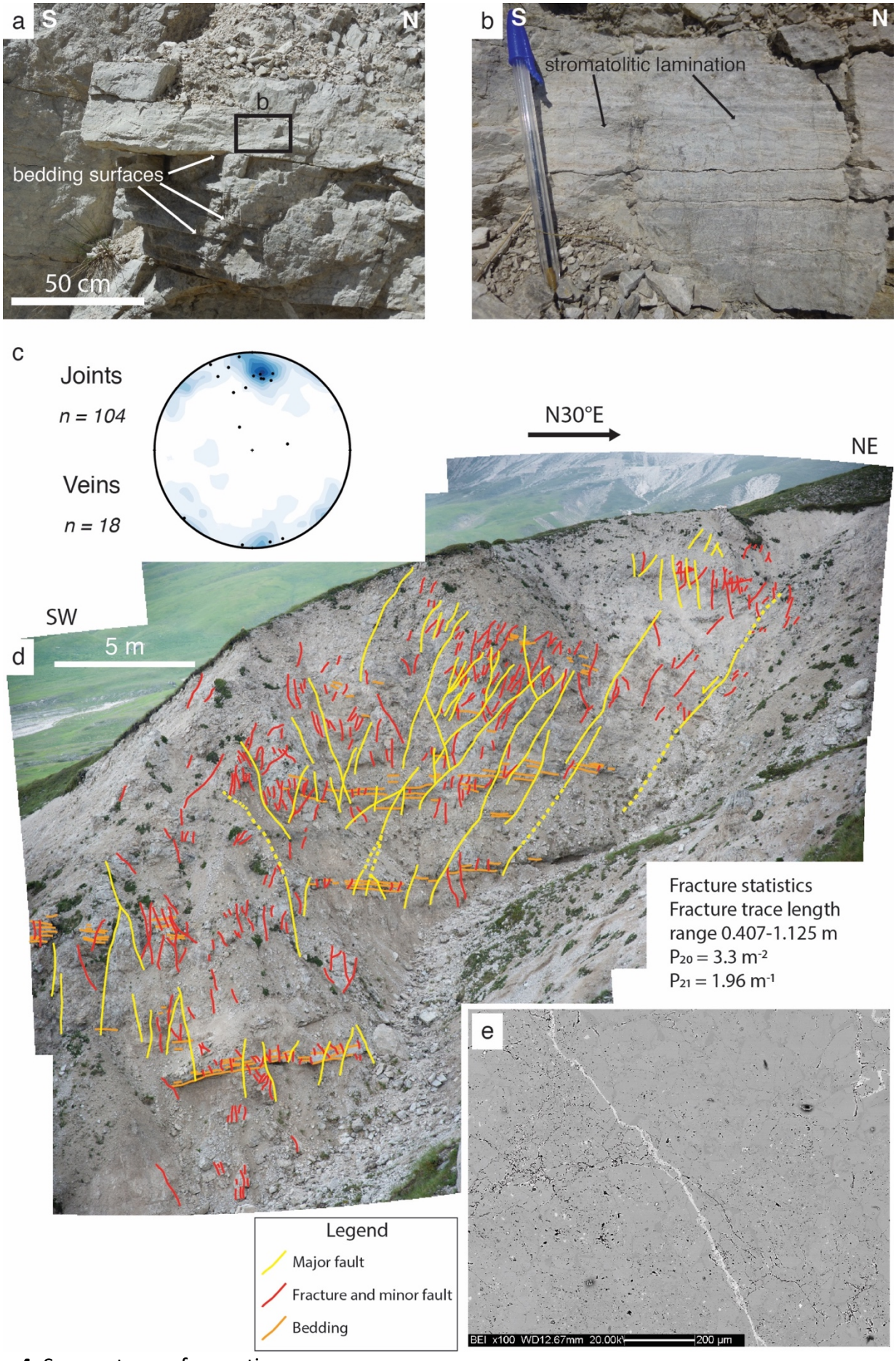


Fig. 4. See next page for caption.

Fig. 4. (previous page) The Low Strain Damage Zone. (a-b) Typical field appearance of the Low Strain Damage Zone. This structural unit is affected mainly by fracturing, veining and subsidiary faulting. Original sedimentary features such as laminations, bedding surfaces and stylolites are easily recognizable. (c) Stereoplot of veins (poles) and joints (contours) in the Low Strain Damage Zone (stereographic projection in the figure is equal area, lower hemisphere). Here, deformation features are organized in sets typically synthetic and antithetic to the master fault. (d) Photomosaic in Move© of the main outcrop of the Low Strain Damage Zone in the study area with line drawing of fractures and minor faults (red), major faults (yellow) and bedding (orange). (e) A large dolomite vein ~ 1 mm thick (grey at BSE-SEM image) is cut by a 10 µm thick calcite vein (white in color in the BSE-SEM image).

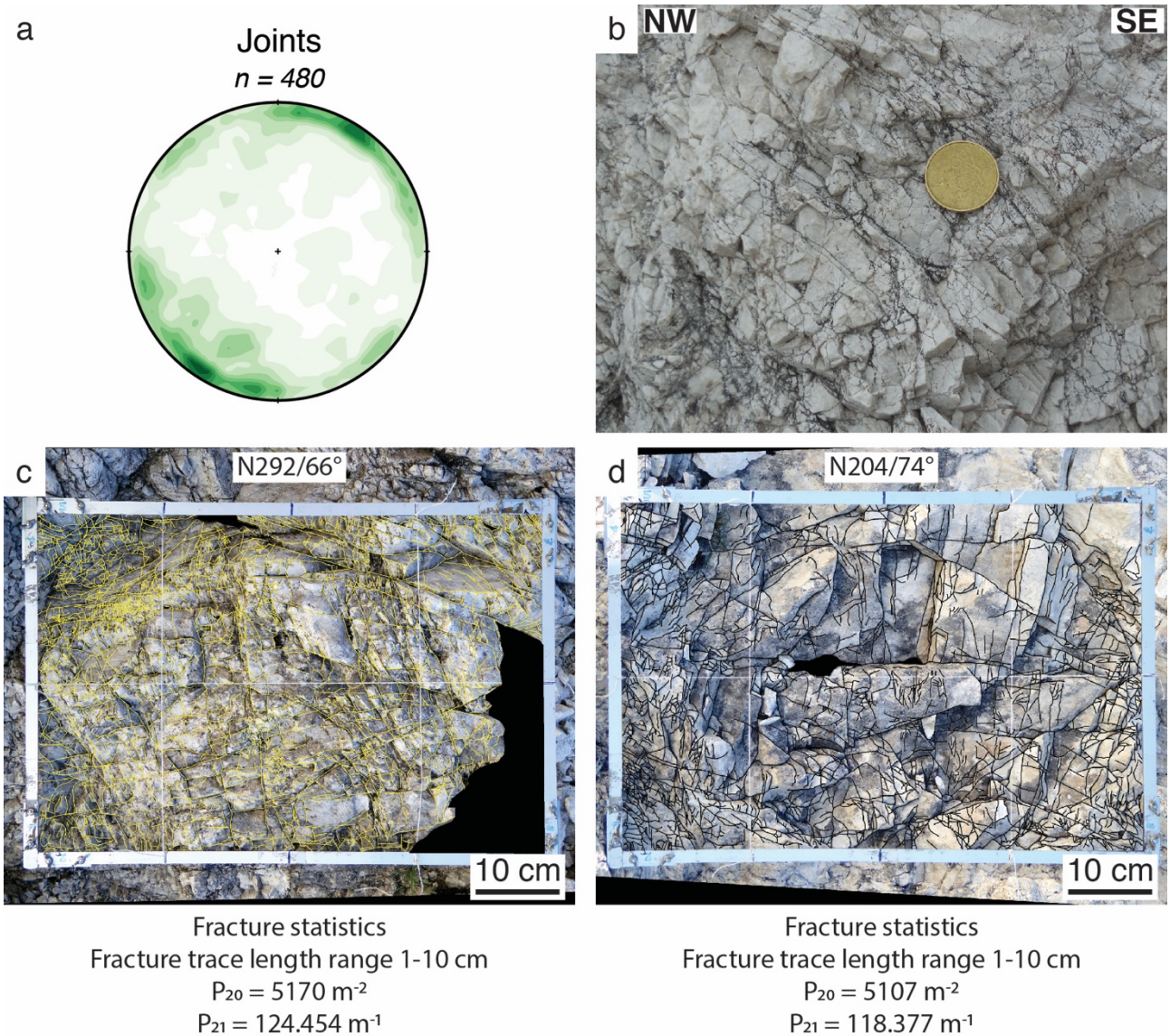


Fig. 5. The High Strain Damage Zone. (a) Stereoplot of poles of joints in the High Strain Damage Zone shows fracturing related both to synthetic and antithetic faults and NE-SW striking faults (stereographic projection in the figure is equal area, lower hemisphere). (b) The presence of fracture sets closely spaced (< 1 cm) typically isolates rock fragments of 1-2 cm in size. (c) Fracture traces perpendicular to the master fault. The frame dimension is 40 x 60 cm and its attitude is N292/66°. (d) Fracture traces parallel to the master fault. The frame dimension is 40 x 60 cm and its attitude is N204/74°.

to the master fault, Fig. 2a). Smaller volumes of LSDZ, less than 15 m thick, are found in the upper part of the mountain ridge (i.e., upper right part in Fig. 2a). Faults within LSDZ are spaced 1–15 m apart and dislocate strata with normal separation (i.e., displacement) < 1 m. Joints are the most abundant deformation features, with minor strata-bound calcite and dolomite veins, and subsidiary faults (Fig. 4a and b). Since most faults and fractures in this area are synthetic and antithetic to the master fault (Fig. 4c), areal fracture density and intensity were calculated on a continuously exposed outcrop oriented at high angle to the master fault that have been projected in Move© on a vertical cross section perpendicular to the master fault (Fig. 4d). Fracture abundance was computed for fracture traces with length in the range 0.407–1.125 m and resulted in P_{20} = 3.3 m^{-2} and P_{21} = 1.96 m^{-1}. Veins are typically arranged perpendicular to pressure solution seams and have aperture up to 0.2 mm for calcite and 2–3 mm for dolomite veins. Calcite veins have a lateral continuity typically <10 cm, while dolomite veins have lateral continuity usually 10–15 cm and are spaced up to few centimeters apart. Systematic cross-cutting relationships suggest that calcite-filled veins are younger than the dolomite-filled ones (Fig. 4e).

5.2. High Strain Damage Zone

The High Strain Damage Zone (HSDZ) consists of fractured rock volumes with significantly higher fracture density/intensity with respect to the LSDZ. The HSDZ is the structural unit that occupies the largest volume within the VCFZ (thickness of 150–300 m measured orthogonal to the master fault). Faults are few and spaced 5–15 m apart. Fracturing is pervasive and typically results from the intersection of three to five sets of joints isolating rock fragments down to 1–2 cm in size (Fig. 5b). In this structural unit, fracture attitude is scattered and is associated to synthetic, antithetic and NE-SW striking faults (Fig. 5a). Veins are less frequent. Here, the higher fracture intensity makes the recognition of primary sedimentary features much more difficult compared to LSDZ. Quantitative scan areas were performed on image frames oriented both parallel and perpendicular to the master fault (frame attitudes were N204/74° and N292/66°, respectively). For sampling windows oriented perpendicular to the master fault, P_{20} = 5170 m^{-2} and P_{21} = 124.454 m^{-1} (fracture trace length range 0.01–0.1 m, Fig. 5c). For sampling windows oriented parallel to the master fault, P_{20} = 5107 m^{-2} and P_{21} = 118.377 m^{-1} (fracture trace length range 0.01–0.1 m, Fig. 5d).

5.3. Breccia unit

The BU consists of rocks that show evidence of pervasive secondary dolomitization of the host rock and dolomite veining. This structural unit is strictly related to areas where the *Verde Ammonitico Fm.* is exposed and at the outcrop scale it mainly consists of grey, green to brownish in color fault rocks (Fig. 6a), which can be classified mostly as cohesive crush breccias (Sibson, 1977). Following the classification proposed by Mort and Woodcock (2008) the breccias should furthermore be classified as "mosaic-crackle breccias" (i.e., clast concentration > 60%, clast rotation < 20%). The BU typically outcrops (i) at the bottom of the creeks, (ii) associated with NNE-SSW striking low-angle (dip angle 20–40°) oblique faults with contractional S-C cleavages and R-shear fractures (Riedel fractures) or (iii) related with low-angle normal faults characterized by an older-on-younger "stratigraphy" (Fig. 6b and c). The transition to the less deformed structural units of the damage zones is typically gradational, i.e. characterized by progressively decreasing vein intensity, while the transition to the cataclastic rock is generally sharp and fault-bounded (e.g., Fig. 6b). Faults inside the BU are few and have polished to mirror-like slip surfaces associated with very localized cataclastic to ultracataclastic brownish slip zones with thickness up to 5–10 cm. Major faults (i.e., fault that can be followed in the field for more than 10 m) within the BU are usually lined by < 50 cm thick fault cores.

Dolomite veins in less brecciated areas have large lateral continuity (up to few meters), planar geometries and large aperture (2–3 cm at maximum, 5–6 mm on average). They are typically found in conjugate sets dipping perpendicular (NW-SE and NE-SW striking with dip angle 75–85°) and parallel to low-angle bedding surfaces (Fig. 6d and e); however, when approaching subsidiary faults, veins are arranged in chaotic networks that overprint tectonic brecciation. Breccia clasts (up to tens of centimeters in size) are generally angular but locally show irregular cuspate-lobate boundaries related to a diffuse presence of dolomite veins (Fig. 6f).

5.4. Cataclastic units

The cataclastic structural units include mainly fault rocks of the "cataclasite series" according to the definition by Sibson (1977) (i.e., volumetric matrix content of 10–50% for a protocataclasite, 50–90% for a cataclasite and 90–100% for an ultracataclasite); therefore, we called it "cataclastic unit" (CU). At the outcrop scale, depending of the grade of cataclasis and preservation of the protolith, two subunits of the CU, called cataclastic unit 1 (CU1) and cataclastic unit 2 (CU2) respectively, were identified. The contact between CU1 and CU2 can be both sharp (i.e., marked by

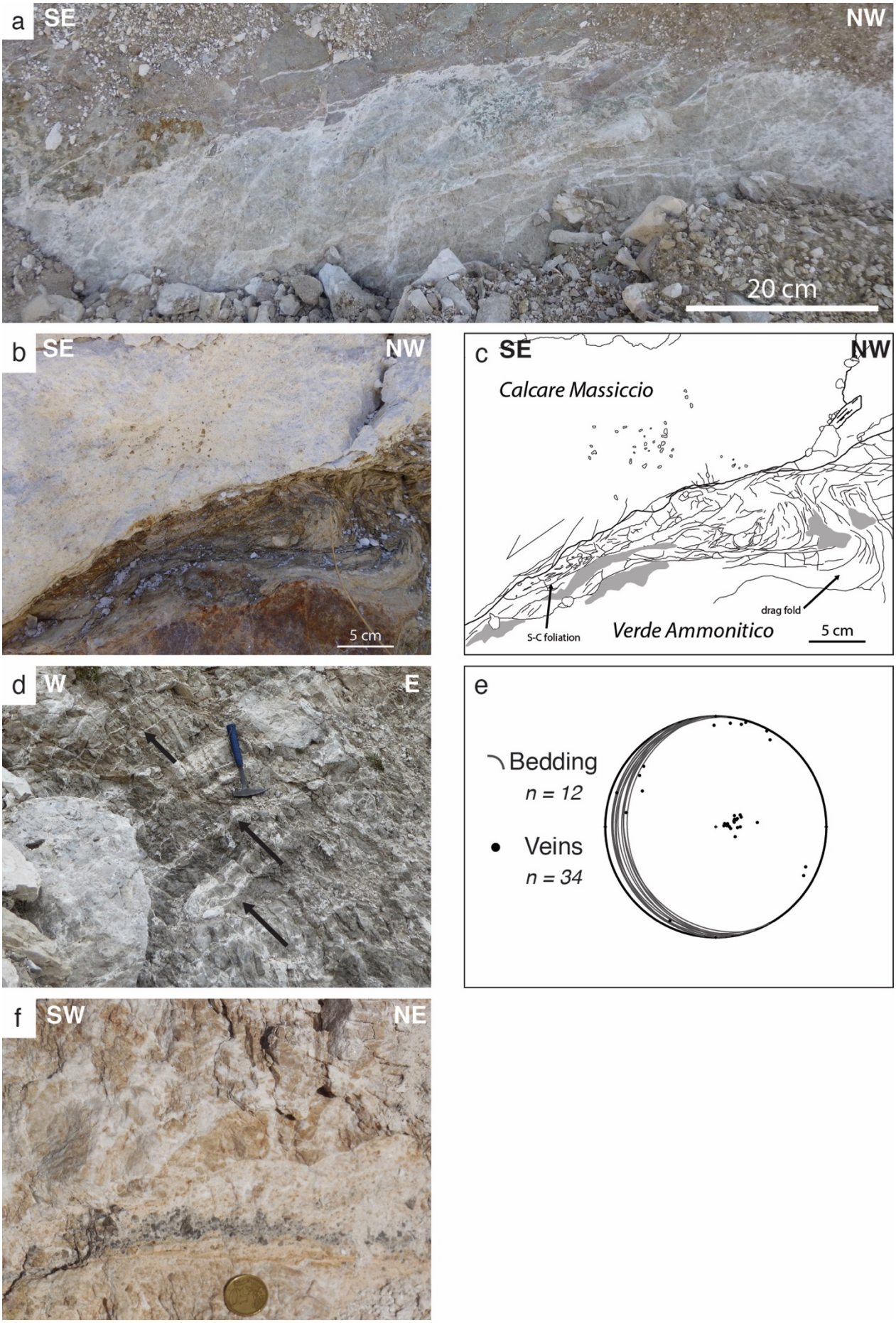


Fig. 6. See next page for caption.

Fig. 6. (previous page) The Breccia Unit. (a) Near faults the dolomite vein network becomes chaotic. Veins are up to 3-4 cm thick and have < 1 m lateral continuity. Minor faults cut through the breccia unit exploiting and dislocating the dolomite veins. (b) Inherited thrust fault juxtaposing the Calcare Massiccio Fm. onto the Verde Ammonitico Fm. exhibits reactivation as normal fault with fault-drag-fold (on the right part) and development of S-C foliation bounding the fault plane (bottom left part). (c) Line drawing of (b). (d) Dolomite veins exploit preexisting discontinuities in the protolith, such as bedding surfaces (black arrows). (e) Stereoplot of veins (poles) and bedding (great circles) in the breccia unit (stereographic projection in the figure is equal area, lower hemisphere). (f) Where dolomite veining becomes pervasive, breccia clasts have irregular boundaries.

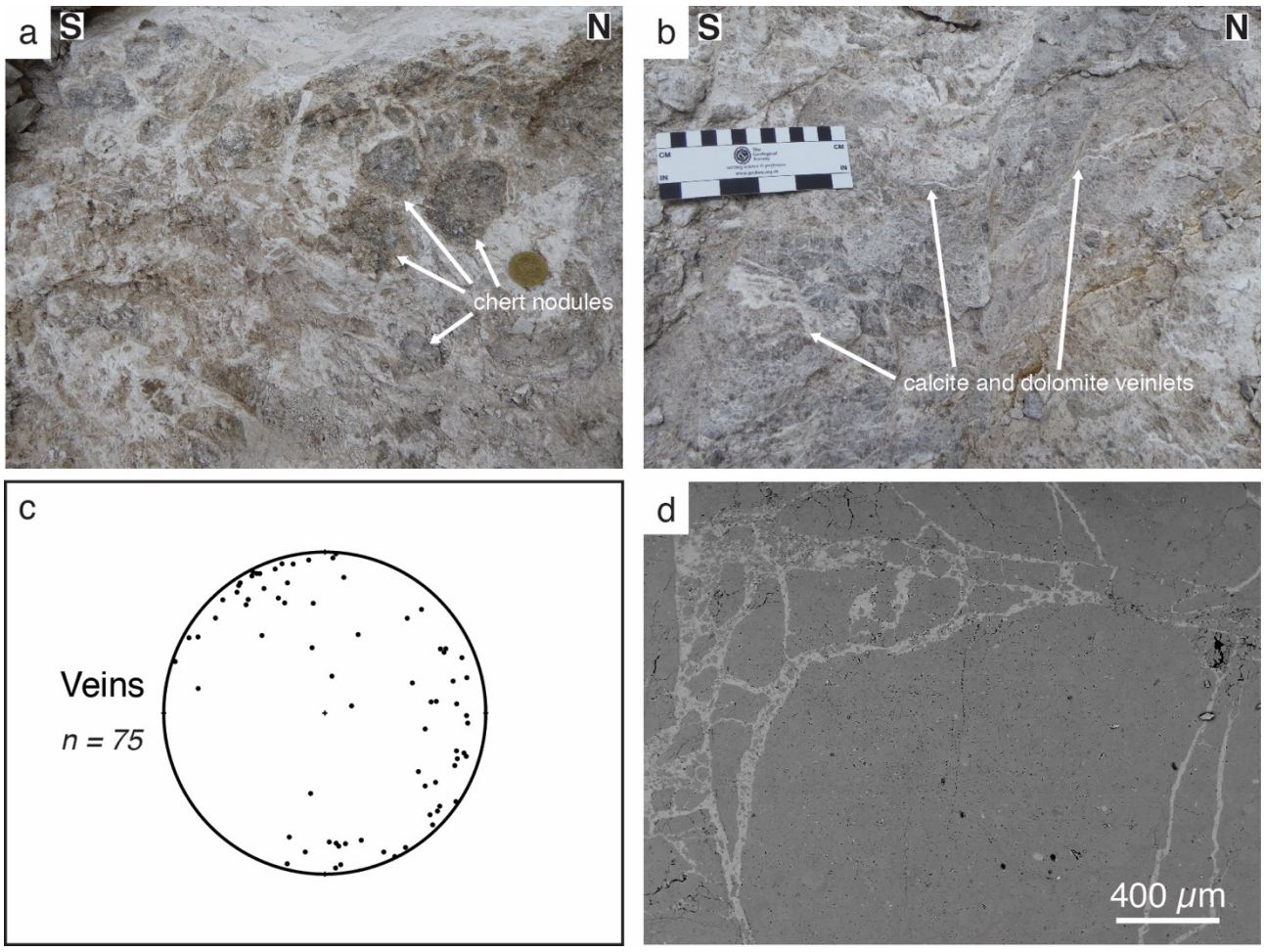


Fig. 7. The Cataclastic Unit 2. (a) Typical field appearance of the Cataclastic Unit 2 with relicts of the protolith that are preserved (i.e., Verde Ammonitico Fm.). (b) Diffuse presence of dolomite and calcite veinlets in the Cataclastic Unit 2 with lateral continuity up to ten cm and aperture of about 5 mm. (c) Stereoplot of poles to veins in the Cataclastic Unit 2. Veins have typically high dip angle (> 70°) and are slightly clustered around a dip of N0°, N140° and N270° (stereographic projection in the figure is equal area, lower hemisphere). (d) Microbreccias occur locally at the intersection of veins and consist of dolomite clasts embedded in a calcite matrix 5-10 µm in size (BSE-SEM image).

faults) or transitional (i.e., gradual change in fabric from CU1 to CU2). In the latter case, the contact between the CU1 and CU2 is usually mapped where one subunit becomes dominant in terms of volume with respect to the other one.

5.4.1. Cataclastic unit 2

The CU2 comprises brownish proto-cataclasites and cataclasites where the original fabric of the protolith is still recognizable (Fig. 7a). Clasts (cm-to tens of cm in size) are pervasively fractured *in-situ* down to the millimeter scale (*in-situ* shattering *sensu* Brune, 2001). At the outcrop scale, the CU2 exhibits great variability in the fabric depending on the source rock (e.g. *Calcare Massiccio* rather than *Verde Ammonitico*). In particular, the occurrence of heterogeneities in the protolith, such as the alternation of facies in the *Calcare Massiccio Fm.* or chert nodules in the *Verde Ammonitico Fm.*, typically result in a lower intensity of deformation of these features and their preservation within the CU2.

At the outcrop scale, the CU2 is cut by a relatively dense network of dolomite- and calcite-bearing veins and veinlets (maximum aperture 1 cm), which contribute to seal the entire fragmented rock volume (Fig. 7b). Most of the veins have scarce lateral continuity (up to few 10s cm for dolomite veins and <10 cm for calcite veins) and irregular shape possibly due to subsequent shearing/rotation and complex cross-cutting/abutting relationships among the different sets of veins and faults. Their attitude distribution is scattered though veins have often high dip angles (i.e., >70°, Fig. 7c). Pockets of “microbreccias” (clasts size less < 1 mm) are observed within the CU2 as consequence of the complex intersection of branching of larger veins (Fig. 7d). The “microbreccia” clasts are typically separated by microcrystalline calcite-filled veins (crystal size 5–10 μm) and often seem to be not in contact.

5.4.2. Cataclastic unit 1

The CU1 consists of a white in color, fine-grained (average grain size < 1–2 mm) and calcite cemented ultracataclasite (Fig. 8a). Well-rounded “survivor” clasts in the cataclasite are few and usually small in size (usually <1–2 cm). Locally, the CU1 includes lithons of the CU2 up to tens of meters in size (Fig. 8b), which are bounded or cross-cut by minor faults, or are in contact with the surrounding cataclasite through irregular wavy contacts.

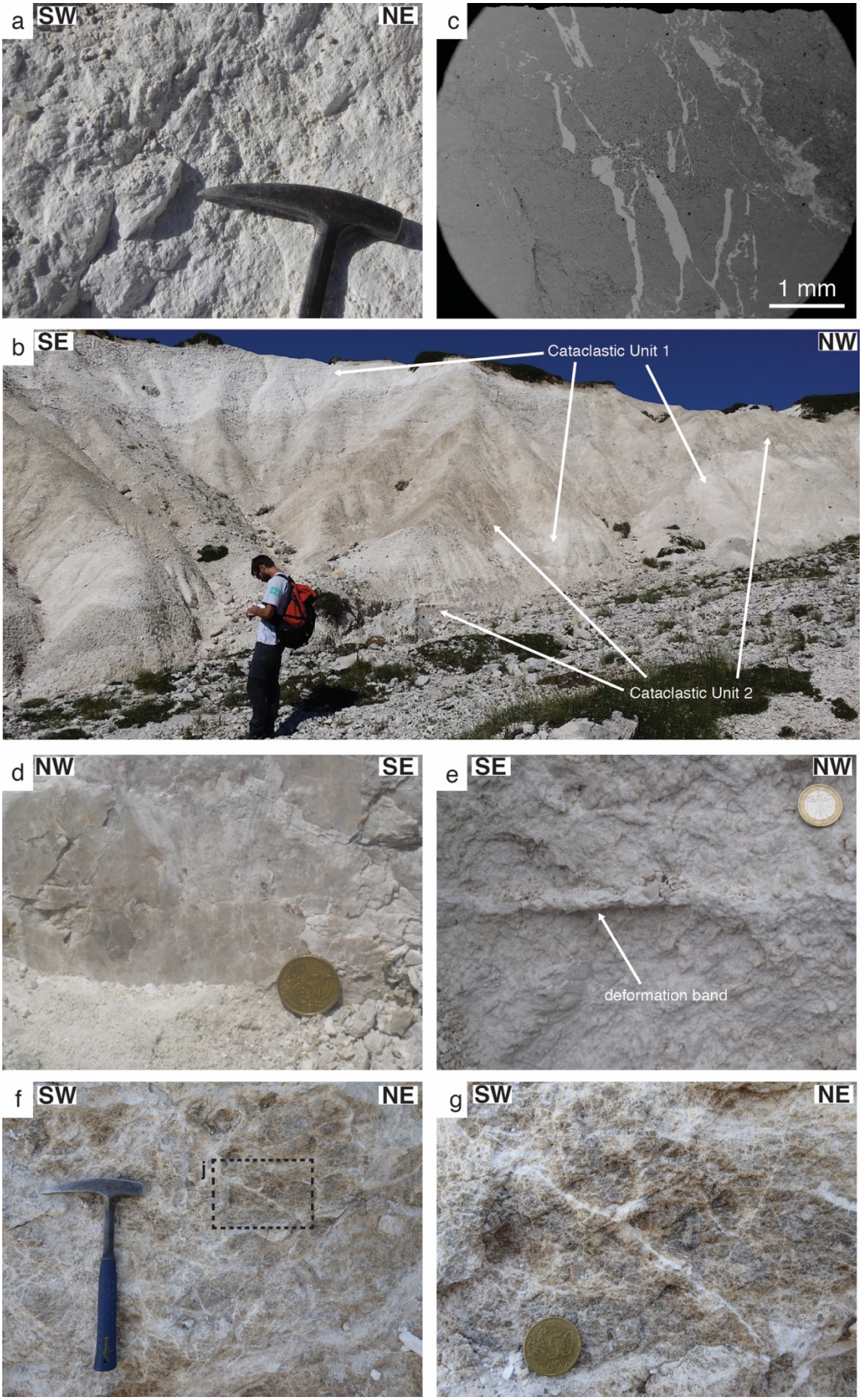


Fig. 8. See next page for caption.

Fig. 8. (previous page) The Cataclastic Unit 1. (a) The Cataclastic Unit 1 is typically well cemented and cut by hundreds of minor faults with thin (< 2 cm) ultracataclastic layers. (b) Decametric lithons of the CU2 embedded in the CU1. (c) Minor calcite veins (white at BSE-SEM image) cross-cut by Riedel shear fractures with low displacement (< 1 mm). (d) Lineated mirror-like slip surfaces. (e) Deformation bands are sometimes observed within more granular cataclastic units. (f-g) Small rock volumes embedded within the CU1 are affected by intense fracturing (fracture spacing < 1 mm) but lack significant shear deformation.

At the microscale, calcite veins have sharp boundaries, are arranged in en-echelon or branching arrays and are often cross-cut and displaced by shear fractures with an offset typically <1 mm (Fig. 8c). Small calcite veins with fuzzy boundaries, irregular geometries and lateral continuity of few millimeters are also frequent. Veins are filled by blocky calcite crystals with average size of 10–50 μm. The CU1 typically contains polished (i.e., mirror-like) slip surfaces (Fig. 8d) associated with cataclastic and ultracataclastic bands with foliated and non-foliated fabric (see section 6 for an extensive description of the slip zones). The mirror-like slip surfaces sharply truncate dolostone and small calcite clasts (grain size < 10 μm) (Fig. 8d) and are often decorated by iron oxides and hydroxides. Fault spacing is usually less than 10 cm. In places, mm-to cm thick deformation bands (i.e., narrow tabular structures with limited shear offset, Fossen et al., 2007) were found in the granular cataclastic unit (Fig. 8e).

6. Microstructures of the slip zones

The five structural units of the VCFZ are cut by faults with different types of slip zones including: (1) highly localized sheared calcite veins, (2) non-foliated cataclasites to ultracataclasites, (3) foliated ultracataclasites with flow structures, and 4) deformation bands. Slip zones (1), (2) and (3) are often bounded by mirror-like principal slip surfaces. Here we define the slip surface as the fault surface itself, sometimes containing slip direction indicators such as slickenlines and surface grooves (Smith et al., 2011). The slip zone, up to several centimeters thick, develops beneath the slip surface and consists of variously developed fault rocks described following the classification of Sibson (1977). Together, the slip surface and the slip zone are thought to accommodate the bulk of displacement during seismic faulting (Sibson, 2003). In addition, we define the principal slip surface (PSS) as the slip surface on which the majority of the displacement is thought to be accommodated.

6.1. Highly localized sheared calcite veins

Locally within the CU1 shear deformation is accommodated within up to 200 μm thick slip zones exploiting preexisting calcite veins. The latter are up to 300–500 μm thick and sealed by undeformed polygonal calcite crystals with an average size of ca. 50–100 μm (Fig. 9a). Instead, slip zones contain fine-grained calcite crystals 50 nm to 1 μm in size rimming sub-angular to

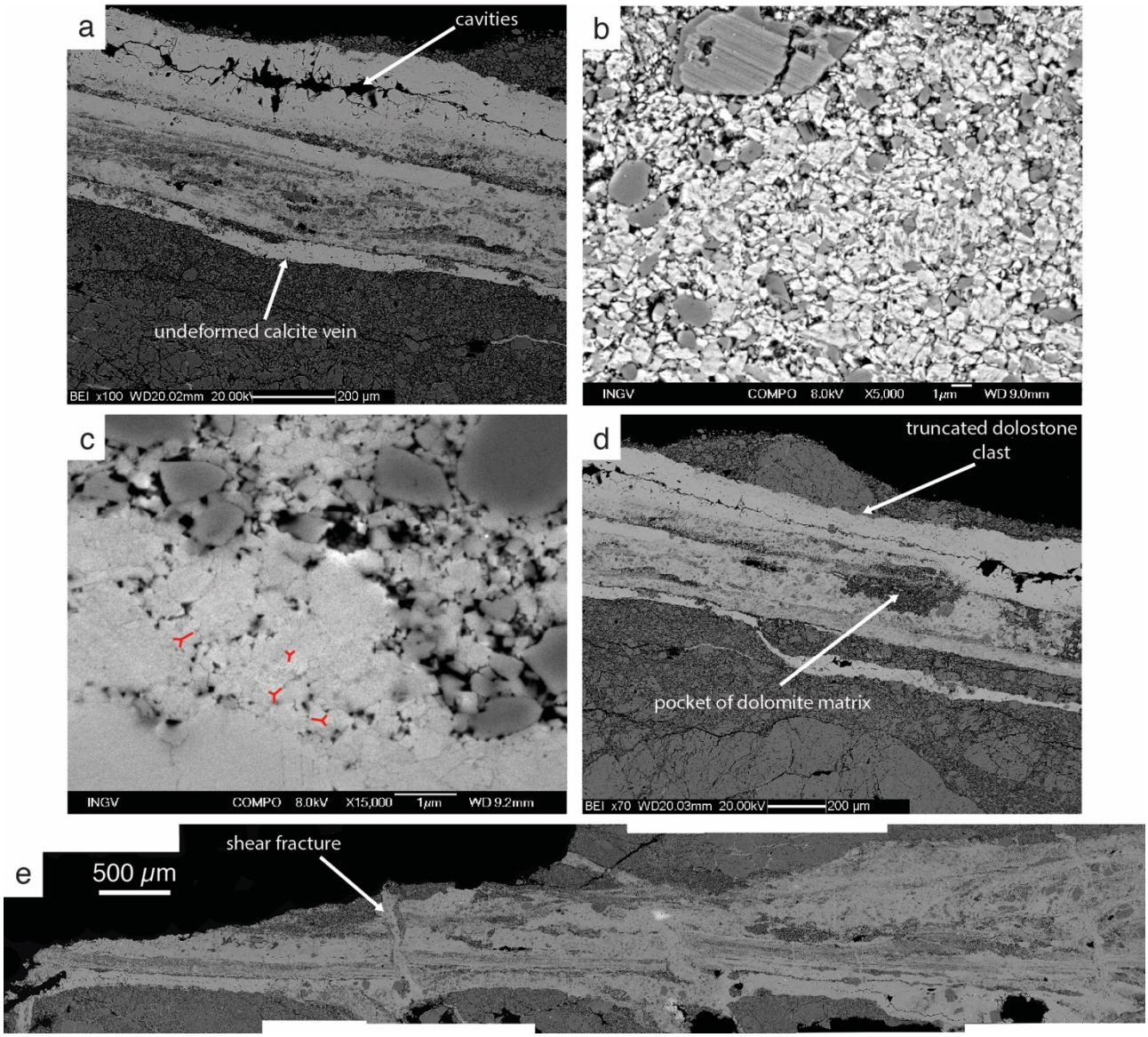


Fig. 9. Microstructures of the highly localized sheared calcite veins. (a) The slip zone records a succession of multiple vein deposition and then shearing, testified by calcite levels with different proportion of embedded dolomite matrix and internal microstructure. These has been interpreted as likely the expression of different strain accommodated by each calcite level. Here, the last vein precipitation event is preserved and characterized by polygonal calcite crystals up to 150 µm in size and the presence of cavities. (b) Ultrafine grained calcite crystals (typical size of 1 µm) surround rounded micrometric dolomite clasts in high strain domains within sheared calcite veins. (c) The calcite matrix exhibits a foam texture. Calcite crystals have straight boundaries and triple junctions (some highlighted in red) are decorated by pores with size << 1 µm. (d) Calcite veins in the slip zone sharply truncating large dolomite clasts (see arrow). Occasionally, pockets of dolomite matrix are found preserved within the slip zone. (e) Minor conjugate high-angle sheared fractures cut and dislocate the PSS. All images are BSE-SEM.

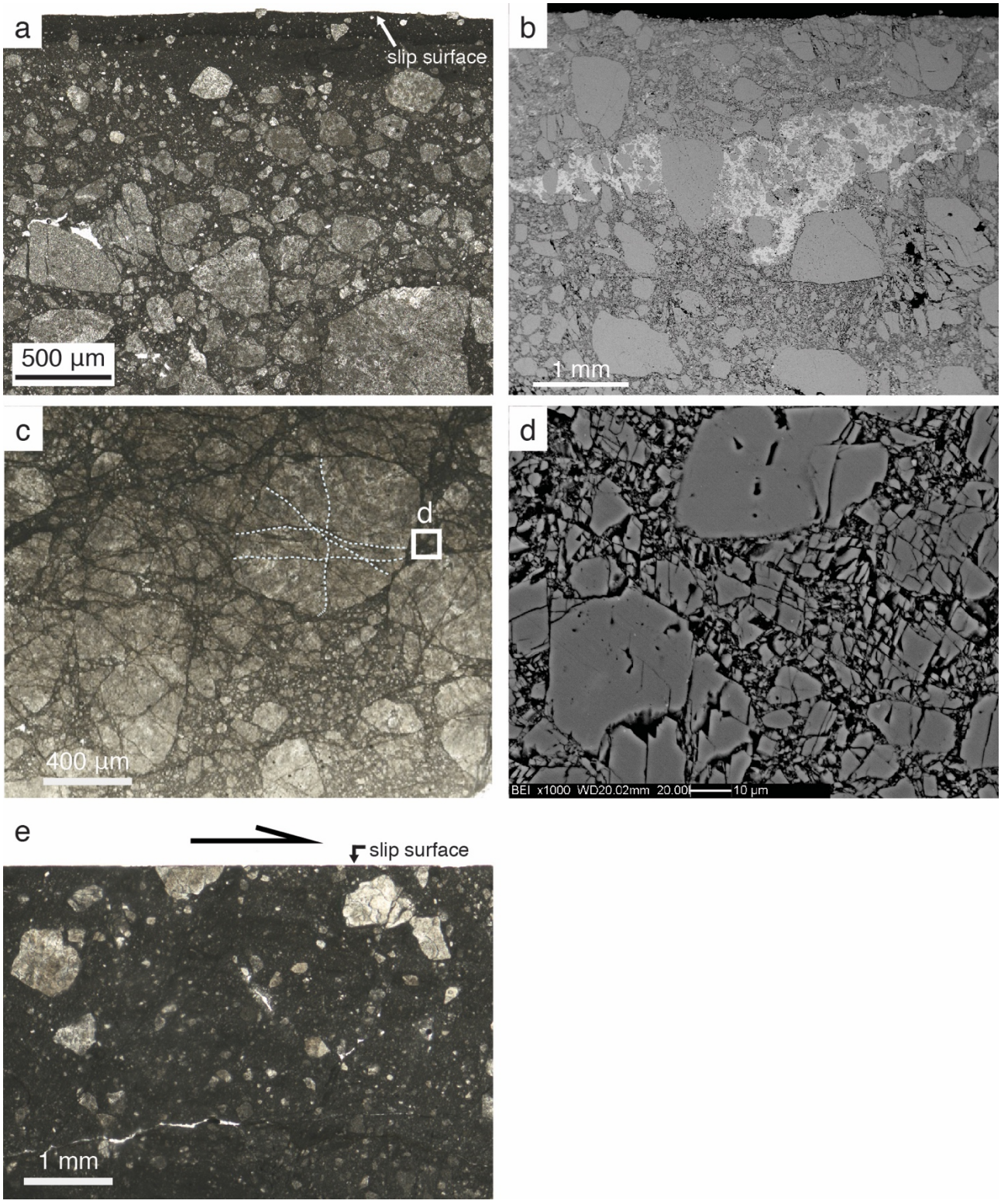


Fig. 10. Microstructures of non-foliated cataclasites. (a) Slip zone grading from cataclasite to ultracataclasite towards the slip surface (top of the image, OM). (b) Extended plagues of calcite cement may occur as infilling of pores within the dolomite matrix (BSE-SEM image). (c) In-situ shattering in the VCFZ. Dolomite clasts are radially fractured and lack of evidence of shearing; they are interpreted as "exploded" (OM image). (d) In the in-situ shattered rocks, the dolomite matrix consists of angular clasts, less than 10 µm in size, which underwent grain size reduction by splitting (BSE-SEM image). (e) Mirror-like slip surface truncating dolostone clasts embedded in a very fine dolomite matrix (OM image).

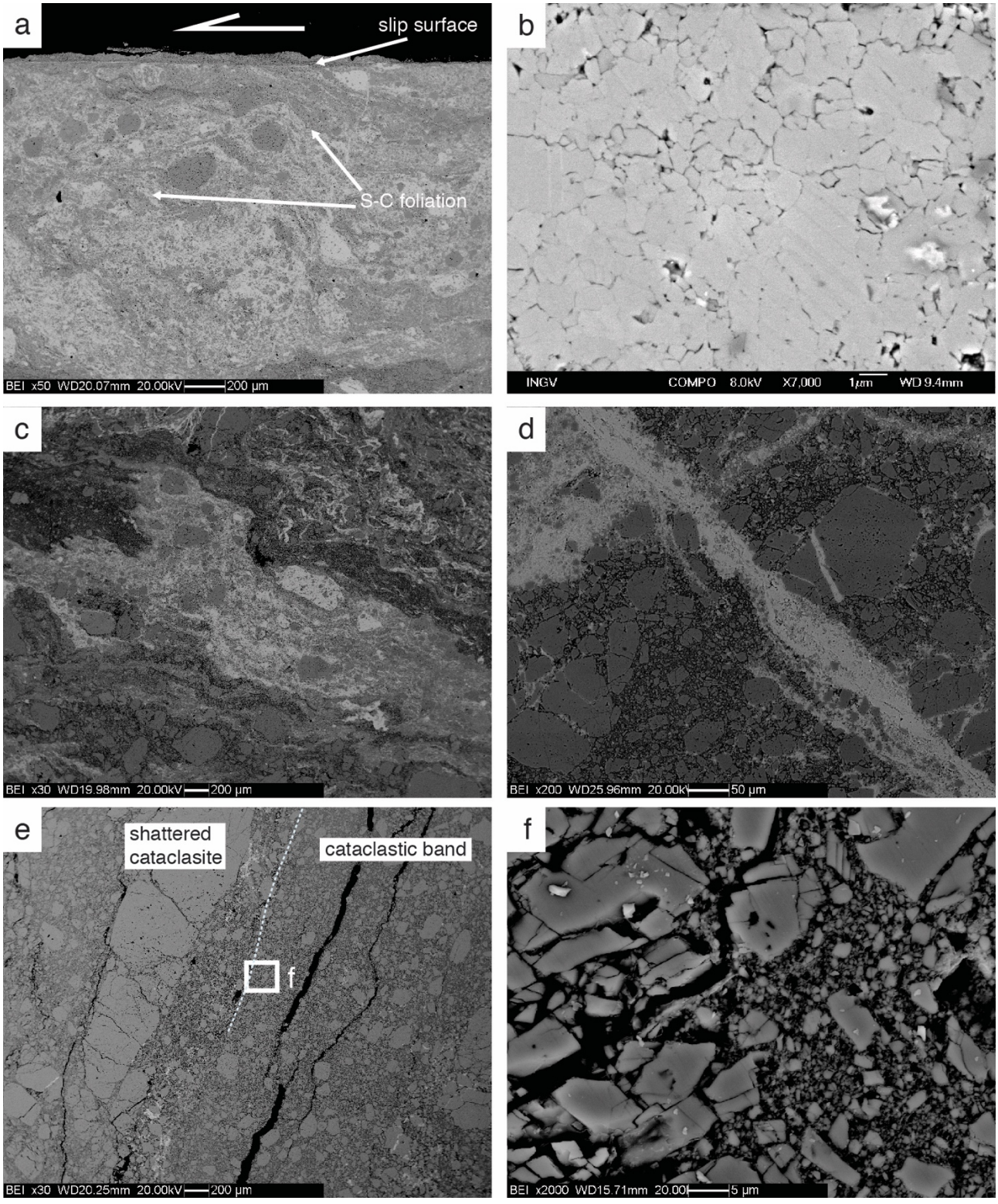


Fig. 11. See next page for caption.

Fig. 11. (previous page) Microstructures of foliated cataclasites and cataclastic bands. (a) Foliated cataclasite with layering of calcite- and dolomite-rich bands. Layers are organized in a S-C type foliation, consistent with the direction of shear. Elongated “tails” of fine dolomite and calcite crystals are observed around big dolomite and calcite clasts (about 200 µm in size). The slip surface cuts abruptly the foliated cataclasite. (b) Foam texture in the deformed calcite matrix, similar to the one observed in the highly localized sheared calcite veins (Fig. 9c). (c) Irregular wavy boundaries between the calcite-rich domains and dolomite dominated areas in the foliated ultracataclasites. (d) Injection of calcite cement-supported ultracataclasite (comprising mostly grains from the Quaternary deposits) in the dolomite-rich ultracataclasite (i.e., CU1). (e-f) The contact between the shattered cataclasite and the cataclastic band is sharp and characterized by an increase in the fine part in the matrix. All images are BSE-SEM.

rounded micrometer in size dolomite grains (Fig. 9b). The calcite grains are often euhedral and with straight boundaries terminating in triple junctions decorated by nanometric in size pores (foam texture, Fig. 9c). The sheared calcite veins are cut by sharp, ultra-smooth slip surfaces truncating larger dolostone grains (>100 μm in size) (Fig. 9d). The sheared veins record multiple cycles of fracture opening – calcite deposition – shearing, as suggested by the occurrence, within the same slip zone, of multiple slip surfaces and deformed veins (Fig. 9e). Both undeformed veins and sheared veins sub-parallel and at high angle to the principal slip surface are observed, with the high angle sheared veins frequently dislocating the subparallel ones (Fig. 9a–e).

6.2. Non-foliated cataclasites

Most slip zones of the CU1 and CU2 – and few of the BU – are 5 cm–30 cm thick and consist of dolomite-built cataclasites grading into ultracataclasites (Sibson, 1977) (Fig. 10a). The non-foliated cataclasites consist of angular to sub-rounded dolostone clasts (size < 1 cm) immersed in a matrix of sub-angular dolostones grains (size below 50 μm down to 1 μm). Extended areas and bands of calcite cement with 10–20 μm in size polygonal crystals occur locally as infilling of pores in the dolomite matrix (Fig. 10b). Moving towards the principal slip surface, the volume of matrix increases and the cataclasite grades into ultracataclasites. Both cataclasites and ultracataclasites contain reworked clasts derived from fragments of older slip zones or from the fragmentation of the calcite cement. Both synthetic and antithetic Riedel shear fractures and stylolites are occasionally found within the ultracataclasites.

Some of the cataclasites include up to 1 cm in size radially fragmented dolostone clasts immersed in a matrix made of angular dolostone clasts with evidence of splitting down to the micrometer scale (Fig. 10c–d). These fault rocks lack clear evidence of shear strain accommodation and are interpreted as the result of *in-situ* shattering (Fondriest et al., 2015; Schröckenfuchs et al., 2015). Minor faults cutting the LSDZ and HSDZ are usually associated with slip zones with a proto-cataclastic fabric (volumetric matrix content < 20%). Most of the slip zones described above and in particular those associated to cataclasites, ultracataclasites and in-situ shattered fault rocks, are cut by polished and ultra-smooth mirror-like slip surfaces truncating large dolostones clasts (Fig. 10e).

6.3. Foliated cataclasites

Some of the dolomite-rich cataclasites with the highest content (>30% in volume) of calcite as cement-rich areas or bands display a peculiar “foliated” fabric. These “foliated cataclasites” consist of bands of fragmented dolomite clasts (grey in BSE-SEM images) alternating with either patchy or more continuous layers of sheared calcite matrix (white in BSE-SEM images) (Fig. 11a). The calcite layers contain clasts from few to hundreds of micrometers in size arranged in a S- or C-type foliation consistent with the shear sense of the slip zone (Fig. 11a). Elongated “tails” of fine-grained dolomite and calcite matrix (down to few micrometers in size) wrap larger dolomite and calcite clasts. Similar microstructures have been documented by Smith et al. (2016) in rotary shear experiments performed at seismic slip velocity in mixed calcite/dolomite gouges and resemble porphyroclastic systems in mylonites (e.g., Passchier and Trouw, 2005) or rigid grains suspended in foliated clay-rich fault gouges (Cladouhos, 1999). The foliated calcite-rich matrix is microstructurally similar to the one found in sheared calcite veins (see Figs. 11b and 8c).

Foliated cataclasites and ultracataclasites made of dolomite/calcite mixtures are frequent within the CU1 and CU2 and decorate the faults marking the contact between the two structural units. Moreover, the pluri-centimeter thick slip zone associated with the master fault and bordering the Quaternary deposits consists of reddish and whitish foliated ultracataclasites (Fig. 3c). Here, ultracataclasites consist of dolomite and calcite (reddish in color ultracataclasite) or dolomite (whitish ultracataclasite) clasts < 200 μm in size immersed in an ultra-fine grained (<1 μm) foliated dolomite matrix with calcite cement (Fig. 11c). Rounded clasts of microcrystalline chert (up to hundreds of micrometer in size) and fine-grained iron oxides suggest mixing of quaternary-derived material within the slip zone.

The occurrence of fluidization structures such as (i) cataclastic to ultracataclastic layers with irregular cuspate-lobate boundaries (Fig. 11c), and (ii) injection veins filled with micrometric calcite crystals or cement-supported ultracataclasites (Fig. 11d), is widespread in the slip zones lining the master fault and also within some of the foliated cataclasites of the CU and BU. In addition, many of the dolomite-calcite foliated cataclasites and ultracataclasites are cut by mirror-like surfaces with truncated grains.

6.4. Deformation bands

Few-millimeters-thick deformation bands are observed to cut through the CU1 in areas where the cataclasites appear less cemented or even loose (Fig. 8e). These granular bands are found

in the footwall within a maximum distance of 10–20 m from the master fault. According to Fossen et al. (2007), these features can be classified as cataclastic bands since they cut through relatively high porosity cataclastic material and are characterized by a less porous core, which has undergone grain size reduction by cataclasis and pore-space collapse. The cataclastic bands are up to 2–3 mm thick, consist of fine-grained comminuted dolomite (average grain size < 10 μm) with some larger dolomite clasts up to 300–500 μm in size and very rare calcite cement (Fig. 11e and f). The latter occurs in areas with crystals that are usually 10–20 μm in size. The core of the cataclastic bands is typically 200–400 μm thick and exhibits a grain-size reduction that goes down to less than 1 μm (Fig. 11f). Clasts with size >10 μm often have an angular shape, with fracturing occurring along cleavage surfaces; conversely, clasts <5 μm in size are rounded and may form intra-clast bridges. Due to lack of structural markers in the walls, offset cannot be calculated, though it is likely that cataclastic bands accommodated some shear strain other than only compaction.

7. Discussion

7.1. Structural complexity of the VCFZ

The spatial distribution of the mapped structural units and the orientation of joints and subsidiary faults in the damage zone, support their genetic link with the activity of the VCFZ (e.g., Destro, 1995; Bai and Pollard, 2000). The occurrence of the LSDZ as an isolated fault bounded block adjacent to the fault core is interpreted as the expression of differences in the protolith (bed thickness, grain size, presence of fenestrae, etc.), which have resulted in a minor overall deformation. However, the limited three-dimensional exposure of this block in the field inhibits a more comprehensive understanding of the spatial relationship with the surrounding structural units. The strike-slip kinematics of NE-SW striking high-angle faults in the upper part of the creek are interpreted as tear faults likely accommodating lateral variations in displacement within the VCFZ. The occurrence and geometry of secondary dolostones and related veins (i.e., BU), developed in the *Calcare Massiccio* and *Verde Ammonitico* formations raises the question whether this major dolomitization pulse was triggered by thrusting or Quaternary extension. The evidence that secondary dolostone pervasively occurs along a shallow-dipping zone involving both protolith lithologies implies that dolomitization exploited the thrust damage zones, thus being synchronous to or postdating the contractional event responsible for the tectonic juxtaposition of the *Calcare*

Massiccio onto the *Verde Ammonitico*, well preserved to the East (Fig. 1b). On the other hand, secondary dolostones are systematically crushed within fault rocks of the CU1, unequivocally associated with the Quaternary master fault, indicating that dolomitization preceded extensional faulting. Moreover, cataclasites are cemented by calcite veins. The latter have also been involved in the deformation, thus providing another indirect evidence for the different environmental conditions during extension. It follows that the relative timing of the major dolomitization pulse can be constrained as syn-to post-thrusting in the area, but still in the contractional tectonic regime (Middle to Late Pliocene). A detailed study of the evolution of dolomitization is out of our purposes in this study and is the subject of specific ongoing research.

In the study area, the presence of the thrust did not affect the extensional fault geometry, which cuts through the pre-existing structural fabric, but the related dolomitization is inferred to have influenced both the width of the footwall damage zone and the frequency and density of fracturing within the high- and low-strain structural units.

7.1.1. Origin of the CU

Field and microstructural observations, including fragmentation in the cataclasites locally showing lack of shearing, suggest that *in-situ* shattering (equivalent to rock pulverization in crystalline lithologies), played a major role in the early stages of formation of the CUs. Pulverized fault rocks are rock volumes that appear to have been shattered *in-situ*; they typically have very fine grain size (i.e., <1 mm) and lack of evidence of significant shearing. *In-situ* shattering has been already reported both in crystalline (Brune, 2001; Dor et al., 2006a, 2006b; Mitchell et al., 2011) and carbonate fault zone rocks (Agosta and Aydin, 2006; Fondriest et al., 2015; Schröckenfuchs et al., 2015).

Both theoretical and experimental investigations (e.g., Ben-Zion and Shi, 2005; Dor et al., 2006a, 2006b; Doan and Gary, 2009; Yuan et al., 2011) suggest a coseismic origin for pulverized rocks, and interpret rock pulverization as a consequence of high strain rate dynamic loading associated with the propagation of single or multiple earthquake ruptures along faults with different geometries and kinematics. More recently Doan and d'Hour (2012), Aben et al. (2016) demonstrated that multiple milder dynamic loadings can lead to the development of pulverization

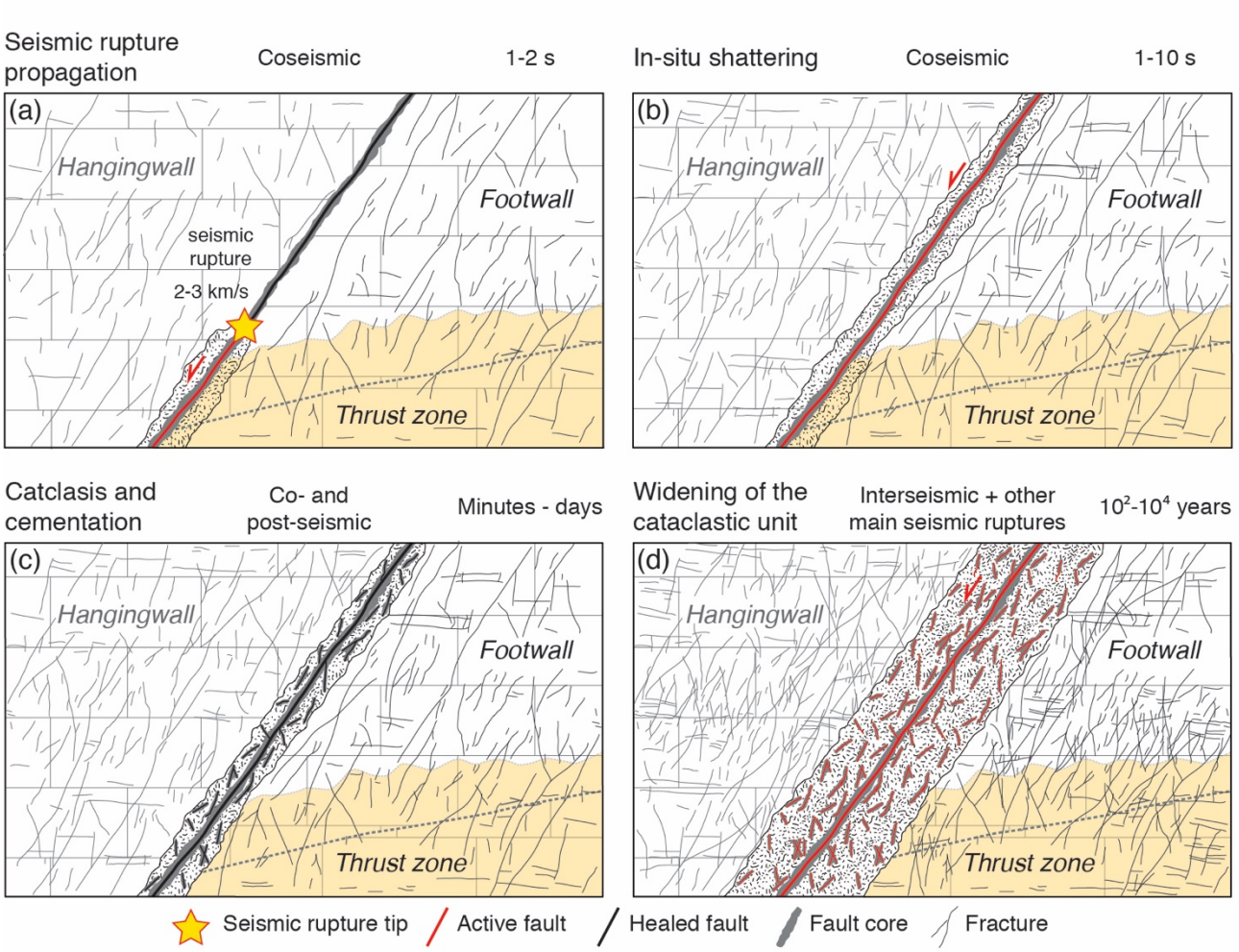


Fig. 12. Conceptual model for the formation of the cataclastic unit. (a-b) The propagation of seismic ruptures along the master fault result in the formation of a comminuted in-situ shattered dolostone band. The presence of a host rock already damaged allows in-situ shattering to occur at lower strain rates to those expected for the same intact rock (Doan and d'Hour, 2012). (c) Localization in the in-situ shattered dolostone along the master fault and subsidiary faults leads to grain rotation, matrix development and obliteration of the host rock original sedimentary features. Eventually calcite-rich fluids percolate and cement the cataclastic band. (d) The cataclastic unit widens as it records multiple cycles of seismic rupture propagation – in-situ shattering – localization – cementation. The conceptual model is based on the interpretation of the exposures of the footwall of the VCFZ. Given the absence of outcrops of the hangingwall, the deformation has only been inferred and colored in light gray.

bands up to hundreds of meters thick without invoking the large scale propagation of supershear rupture fronts, which are generally infrequent rupture modes (i.e, reported for straight and long boundary faults; e.g., Bouchon and Vallee, 2003). In the VCFZ the CU1 forms a continuous band almost 40 m thick lining the master fault and is characterized by a rather homogeneous cataclastic fabric with a very fine grain size (<1–2 mm). Minor faults within the CU1 are associated with thin ultracataclastic layers that cross-cut each other but do not affect the entire cataclastic rock volume. Small rock volumes (few meters at maximum) affected by intense fracturing but lacking significant shear deformation are embedded within the CU1 (Fig. 8f and g). Moreover, looking at the microscale within the cataclastic rocks, exploded clasts and relics of older *in-situ* shattered microstructures were often observed. This suggests that the propagation of multiple seismic ruptures (see section 7.2) might have produced *in-situ* shattering up to several meters from the master fault (Fig. 12a–d). During each shattering event, coseismic strain localization along multiple slip surfaces evenly distributed in the fractured rock mass was likely to be activated (Ma and Andrews, 2010; Fondriest et al., 2015). Further displacement and strain (i.e., widening of the single cataclastic bands) were then accumulated during post-seismic and interseismic stages (Fig. 12c and d). Therefore, the occurrence of multiple shattering episodes which produced thick bands of intensely fragmented rocks, subsequently affected by shear strain localization, can explain the development of a 40 m thick homogeneous CU1 which would be difficult to develop only by cataclasis.

7.2. Evidence of coseismic slip

Field and microstructural observations of faults and fault zone rocks suggest the propagation of seismic ruptures within the VCFZ. Faults are typically characterized by the presence of polished (i.e. mirror-like) slip surfaces associated with ultracataclastic and cataclastic slip zones. Mirror-like slip surfaces are common in faults cutting carbonates (Fondriest et al., 2012; Siman-Tov et al., 2013; Tesei et al., 2013) and are described as naturally polished fault surfaces with high visible-light reflectivity, which implies an extreme smoothness at the microscale, below the wavelength of visible light (e.g., Siman-Tov et al., 2013). Recent experimental studies on both dolomite and calcite gouges and solid rocks (Fondriest et al., 2013; Smith et al., 2013, 2015; Siman-Tov et al., 2015) show that mirror-like slip surfaces form at seismic slip rate (~0.1–1 ms^{-1}) and are associated with strong dynamic weakening and shear strain localization. Conversely to mirror-like surfaces formed at sub-seismic slip rates (~10 μms^{-1}) in calcite gouges (Verberne et al., 2013a), mirror-like surfaces

produced at seismic slip rates (~1 ms^{-1}) sharply truncate large grains (hundreds of micrometers in size) and cover most of the experimental fault surface (Fondriest et al., 2013; Siman-Tov et al., 2015). Therefore, the occurrence within the VCFZ of mirror-like fault surfaces truncating mm-to cm-in size grains (e.g., Figs. 8d and 9e) is a potential indicator of seismic rupture propagation.

A further possible evidence of seismic slip along the studied faults is the presence of sub-micrometric calcite euhedral grains organized in a foam texture in the sheared calcite veins (Figs. 8c and 10b). Similar microstructures were produced in experiments simulating seismic slip in calcite and dolomite gouges (De Paola et al., 2011a; Fondriest et al., 2013; Smith et al., 2013; De Paola et al., 2015; Green et al., 2015; Mitchell et al., 2015; Smith et al., 2015). These foam-like textures were associated with grain-size dependent (grain boundary sliding aided by diffusion creep) fault weakening mechanisms activated during seismic slip (De Paola et al., 2015), possibly followed by sintering processes occurring at the end of seismic slip (Di Toro et al., 2015; Green et al., 2015). Moreover, these microstructures were found to be spatially related to both sheared and undeformed calcite veins sub-parallel to fine-grained ultracataclastic principal slip zones. This and the above observations are in good agreement with microstructures from other carbonate-bearing faults, in which a close association of mirror-like slip surfaces, ultracataclasites, principal slip zone veins and fluidized cataclasites was also observed (e.g., Tesei et al., 2013). The sequential opening and shearing of veins sub-parallel to localized slip zones suggest the cyclic build-up of fluid overpressure during deformation through a fault-valve mechanism, which is thought to be associated with seismic slip events (Sibson, 1981, 1990).

The cataclastic units and the slip zones therein include exploded clasts up to 1–2 cm in size with radial fractures embedded in a micrometric in size matrix composed of angular clasts with no evidence of shearing (Fig. 9c and d). This occurrence within dolostones has been already reported by Fondriest et al. (2015) and interpreted as the result of in-situ shattering due to the propagation of seismic ruptures along neighbor faults. In the VCFZ these features are typically associated with mirror-like slip surface suggesting a related seismic origin.

The possibility to relate the occurrence of foliation in mixed calcite-dolomite gouges and cataclasites to coseismic sliding has been recently investigated by Smith et al. (2017) by performing high-velocity (imposed slip rate $V < 1.13$ ms^{-1}) shear experiments on mixtures of calcite-dolomite gouges. Their results show that a well-organized foliation can develop quickly from an initial random distribution as displacement is distributed along a shear band before dynamic weakening occurs. When the latter takes place, deformation is localized to a discrete slip surface, which cuts sharply

the foliated gouge and accommodates most of the strain. The described microstructures exhibit striking similarities with the foliated cataclasites documented in the VCFZ (Fig. 11a) suggesting a common seismic origin.

A feature that has been documented both at the meso- and microscale related to the master fault and some foliated cataclasites within the VCFZ is the presence of “fluidization textures”. These fluidized layers develop up to 5 cm away from the slip surface and include wavy borders and injection of material in the surrounding cataclasite (e.g., Fig. 11c). In the Kodiak accretionary complex (Alaska, USA), Brodsky et al. (2009) described cuspate-lobate, locally intrusive, contacts between black in color aphanitic rocks with flame-like and laminar to convolute flow structures interpreted as pseudotachylytes and foliated illite-rich cataclasites. Similar fluidal structures were described in slip zones cutting carbonates and were tentatively associated with seismic faulting (Smith et al., 2011; Fondriest et al., 2012; Rowe et al., 2012). The formation of fault rocks with intrusive geometry (e.g., pinch out terminations) and laminar-to turbulent-like flow structures plus, in some cases, cuspate-lobate contacts with the wall rocks, is thought to be the result of fluidization of the slip zone material. Triggering mechanisms may be thermal decomposition (e.g., Collettini et al., 2013), pressurization of fluids trapped in the pore spaces of the gouge (e.g., Rowe et al., 2012) or focused injection of pressurized fluids from the fault surroundings during rupture propagation (e.g., Sibson, 1990; Fondriest et al., 2012). The fluidized features in the VCFZ compare well with laminar grain flow layers characterized by grain preferred orientation parallel to the fault surface (Rowe and Griffith, 2015). Consequently, the presence of calcite-cemented cataclasite and the occurrence of laminar grain flow structures in the slip zones along the master fault suggest the presence of pressurized fluids during seismic faulting along the VCFZ.

7.3. Implications for the interpretation of seismicity in the Central Apennines

In the previous sections, we documented the evidence of seismic rupture propagation within the footwall of the VCFZ and the occurrence of both inherited compressional- and present active extensional-structures. Here we relate these structural features to the active fault network inferred from high-precision hypocenter relocations for the L'Aquila 2009 seismic sequence by Valoroso et al. (2013, 2014).

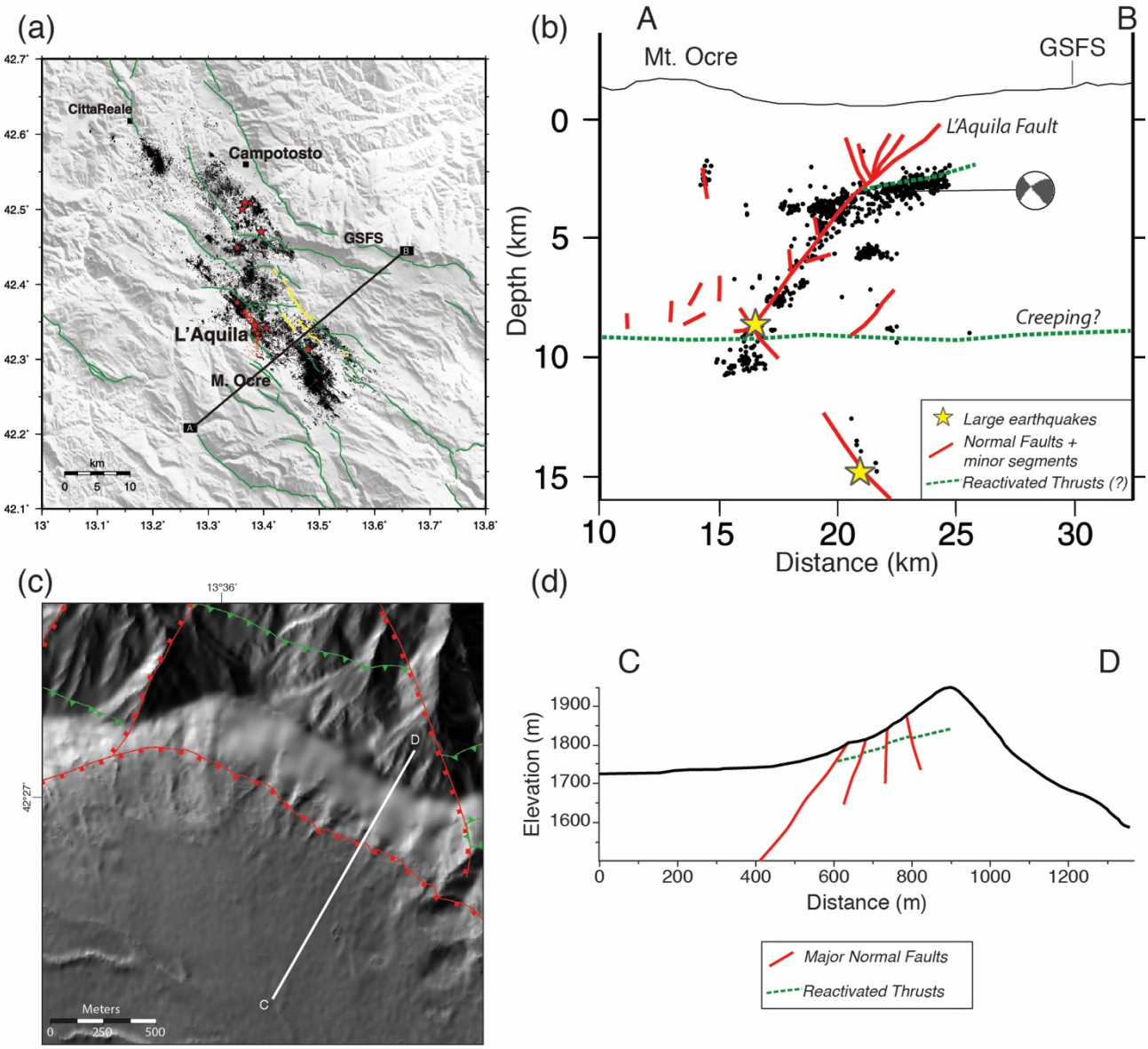


Fig. 13. Earthquake distribution in the L'Aquila 2009 seismic sequence. (a) Map of the relocated earthquakes for the L'Aquila 2009 seismic sequence (modified after Valoroso et al., 2013). Red dots: foreshocks; black dots: aftershocks; red stars: main earthquakes; green lines: active mapped faults; yellow lines: co-seismic surface ruptures. GSFS is Gran Sasso Fault System. (b) Vertical section of aftershocks distribution at depth with seismotectonic model of the area (modified after Valoroso et al., 2013). The low-angle plane was interpreted as a shallow flat portion of a thrust reactivated as normal fault during the seismic sequence. (c) Map of lineaments from the geological map in Fig. 1b in the study area. (d) Simplified geological section from Fig. 2b evidencing the major faults within the studied creek. Note the similarity of the fault network, at smaller scale, with the vertical cross section shown in Fig. 12b.

In the case of the L'Aquila 2009 earthquake sequence (mainshock MW 6.1 April 6, 2009), Valoroso et al. (2013, 2014) depicted the seismic faults of the area by means of high-precision relocation of ~64,000 events, both foreshocks and mostly aftershocks during 2009, with a completeness magnitude of 0.7 (Fig. 13a). The relative hypocenter location precision was smaller than the dimension of seismic ruptures (e.g., ~30 m for M_L = 1.0, Sibson, 1989) with a precision ranging from few meters to tens of meters. The L'Aquila Fault, responsible for the mainshock, was described as a fault striking NW-SE and dipping 50° towards SW for a length of about 18 km (Valoroso et al., 2013). In particular, in its central sector the L'Aquila Fault is imaged as a fault zone dipping at high angle (~55°) towards SW and cutting at 3–5 km depth a well-defined fault structure dipping at low angle (~15°) (i.e., the dashed green line in Fig. 13b) towards SW (Fig. 13a and b). The possible focal mechanism solutions on the low-angle structure are consistent either with a low-angle plane dipping towards SW or with a series of closely spaced high-angle planes dipping towards NE. Some authors (Chiaraluce et al., 2011; Valoroso et al., 2013) interpreted the low-angle planes as the shallow flat portions of a thrust inherited from the Miocene-Pliocene compressional phase. The thrust has been reactivated as a low-angle extensional fault during the Present extension (Speranza et al., 2003). Moreover, the projection of this plane to the surface, coincides with the central sector of the GSM (Chiaraluce et al., 2011). This fault network imaged by seismic inversion compares well with the structural setting that we described in the VCFZ, where low-angle thrusts are reactivated as (minor, at least in terms of displacement) extensional faults (Fig. 6b and c) and a major extensional Andersonian-type fault cuts the older thrust zone (Fig. 13c and d).

Another important comparison with the L'Aquila seismic sequence regards the kinematics of focal mechanism solutions for both foreshocks and aftershocks. Chiaraluce et al. (2011) documented a strong predominance of extensional solution (i.e., normal and transtensional, 82%), with strike-slip focal mechanism solutions (13%) typically located at linkage areas between fault segments. A minor occurrence of compressive earthquakes (i.e., thrust and transpressive, 5%) is dispersed in the fault system. This distribution compares well with the kinematics measured on fault surfaces in the VCFZ. Although evidence of extension-related thrust kinematics was not found, extensional and transtensional faults were the most recurrent structures. Moreover, strike-slip kinematics were associated with faults interpreted as kinematic tears.

Therefore, all the documented similarities between the VCFZ and the buried structures activated during the L'Aquila 2009 seismic sequence described through seismological techniques

(Chiaraluce et al., 2011; Valoroso et al., 2013, 2014) allow the VCFZ to be considered a valid exhumed analog of the structures responsible for the present seismicity in the Central Apennines.

8. Conclusions

The active Campo Imperatore Fault System (CIFS) cuts the dolostones bounding the inner part of the Gran Sasso Massif in the Italian Central Apennines. The exposed segment of the VCFZ strikes about SE-NW (i.e., sub-parallel to the main seismogenic faults of the Central Apennines), cuts through dolostones and limestones, accommodated about 2 km of maximum vertical throw and was exhumed from about 2 km depth since the Early Pleistocene.

Within the VCFZ we mapped five main structural units based on fault zone rocks and damage intensity: namely they are the Low Strain Damage Zone, the High Strain Damage Zone, the Breccia Unit, the Cataclastic Unit 1 and the Cataclastic Unit 2. At the base of the badlands the master fault (attitude of N209/54°) juxtaposes the Quaternary deposits in the hangingwall with the cataclastic dolostones in the footwall. Faults in the footwall are mainly synthetic and antithetic to the master fault, but a set of NE-SW trending strike-slip faults are well exposed in the upper part of the creek and interpreted as kinematic tears. The spatial distribution of the fault and fracture network affecting the VCFZ suggest a close relationship between these structural units and extensional deformation active in the area since Early Pleistocene times. However, dolomitization in the Breccia Unit occurred along the damage zone of a shallow-dipping thrust juxtaposing the Lower Jurassic *Calcare Massiccio Fm.* onto the Middle Jurassic *Verde Ammonitico Fm*. The same thrust zone, not affected by dolomitization, is exposed immediately to the East of the VCFZ. This evidence, coupled with the attitude parallel to low-angle bedding surfaces of dolomite veins in the Breccia Unit, and the systematic deformation of Breccia Unit rocks by cataclasis on the extensional master fault and subsidiary ones, indicate that dolomitization was syn- or post-thrusting, but occurred still during the contractional regime, before regional extension affected the area. The presence of a continuous ~40 m thick band of Cataclastic Unit 1 lining the master fault is interpreted as the result of in-situ shattering due to the propagation of multiple seismic ruptures and subsequent slip localization and cementation along a multitude of subsidiary faults. Past seismic behavior of the exposed faults is suggested by the occurrence of mirror-like slip surfaces truncating dolomite grains, foam-like textures in the sheared calcite-bearing veins and in-situ shattering associated with mirror-like slip surfaces and fluidized cataclasites.

For the L'Aquila 2009 seismic sequence, high-precision hypocenter relocation imaged a fault network characterized by a principal high-angle fault cutting a low-angle plane at shallow depth (3–5 km). The low-angle plane was interpreted as a flat portion of a thrust inherited from the compressional phase during Miocene-Pliocene and exploited as low-angle extensional fault during Present extension. This structural setting compares well with the reactivation of thrust-related features and fault network geometry described in the VCFZ. Therefore, the VCFZ provides a suitable exhumed analog of seismically active buried fault zones in the Central Apennines, such as those that caused the L'Aquila 2009 seismic sequence.

Chapter II

Frictional properties and microstructural evolution of mixed calcite-dolomite gouges

This study was performed with the collaboration of Steven A.F. Smith, Elena Spagnuolo, Stefano Aretusini, Michele Fondriest and Giulio Di Toro. I performed all the work described in this chapter except for the experiments at different calcite/dolomite content performed by Steven A.F. Smith and Michele Fondriest. I was assisted during laboratory work by Elena Spagnuolo. I was assisted (but not continuously) during microstructural analysis by Steven A.F. Smith and David J. Prior. The material presented here was discussed with Steven A.F. Smith, Michele Fondriest, Elena Spagnuolo and Giulio Di Toro.

Abstract

Carbonate-built rocks are a common lithology involved in crustal-scale deformation. Calcite and dolomite are the most common minerals found in carbonate-bearing faults and shear zones. Although similar in chemical composition, the mechanical behavior of calcite and dolomite shows important differences, with calcite accommodating deformation by crystal-plastic mechanisms at relatively very low temperatures (< 100 °C) and dolomite exhibiting brittle behavior up to ~ 700 °C. To date only a small number of studies have focused on the mechanical behavior and microstructural evolution of calcite-dolomite mixtures.

Rotary-shear experiments were performed on a gouge mixture consisting of 50 wt.% calcite and 50 wt.% dolomite. The gouge was sheared for slip rates ranging from 30 μms^{-1} to 1 ms^{-1}, displacements up to 0.4 m, normal load of 17.5-26 MPa and under both room-humidity and water-dampened conditions. Slide-hold-slide experiments were performed with velocity steps from 30 μms^{-1} to 1 ms^{-1} and vice-versa. The frictional behavior of the gouge was strongly influenced by the presence of water: under room-humidity conditions, slip-strengthening behavior was observed up to a velocity of ca. 0.1 ms^{-1}, above which dynamic weakening occurred. In water-dampened conditions, the gouge showed dynamic weakening only at a slip rate of 1 ms^{-1}. These mechanical differences observed under room-humidity and water-dampened conditions were associated with a wealth of newly-formed microstructures. In particular, the development of a well-defined foliation in the gouge layers occurred only in the experiments performed at slip rates of 1 ms^{-1} and under room-humidity conditions. Consistent with previous studies, our observations support the notion that some foliated gouges and cataclasites may form during seismic slip in natural carbonate-bearing faults. Lastly, during the slide-hold-slide experiments, microstructures associated with particular deformation conditions (e.g., seismic slip rates) were preserved only in the room-humidity case.

1. Introduction

Calcite and dolomite are the most common minerals in carbonate-bearing faults and shear zones (e.g., Busch and Van Der Pluijm, 1995; Snoke et al., 1998; Bestmann et al., 2000; De Paola et al., 2006; Molli et al., 2010; Tesei et al., 2014; Fondriest et al., 2015; Delle Piane et al., 2017). Carbonates are a widely recurrent lithology typically involved in crustal-scale deformation. The distribution of dolomitic rocks in respect to more calcitic ones often play an important role in controlling where localization might occur. As an example, in the Naukluft Nappe Complex (central Namibia), the distribution of variably dolomitized rocks, likely played a significant role in the structural evolution (Viola et al., 2006; Miller et al., 2008), with ductile deformation localized along calcite-mylonites and the main Naukluft Fault occurring within dolomitized layers (Miller et al., 2008). In the South Tibetan Detachment System, part of the > 100 km inferred total displacement was ductily accommodated within calcitic- and dolomitic marbles (e.g., Cottle et al., 2007).

Although similar in chemical composition, the mechanical behavior of calcite and dolomite during fault-related deformation shows important differences. The rheology, deformation mechanisms and frictional behavior of calcite have been investigated under a wide range of deformation conditions, including experiments performed at (relatively) high temperature-high pressure (e.g., Rutter, 1972; Schmid et al., 1980, 1987; de Bresser et al., 1990; Rutter, 1995; Kennedy and Logan, 1997; Paterson and Olgaard, 2000; Kennedy and White, 2001; Liu et al., 2002; Bestmann et al., 2006; Molli et al., 2011;) and experiments at low temperature and low pressure (Smith et al., 2013; Verberne et al., 2014; De Paola et al., 2015; Smith et al., 2015; Rempe et al., 2017; Tesei et al., 2017). Comparatively, the rheology and frictional behavior of dolomite is relatively poorly understood, although dolomite has received an increasing amount of attention in recent years thanks to an increasing number of studies showing its occurrence both in sedimentary and metamorphic setting, typically together with calcite (e.g., Barber et al., 1981; Weeks and Tullis, 1985; Austin and Kennedy, 2005; Delle Piane et al., 2007, 2008; Davis et al., 2008; De Paola et al., 2011a, 2011b; Fondriest et al., 2013; Holyoke et al., 2014). At low strain rates dolomite exhibits brittle behavior up to ~ 700 °C (Kushnir et al., 2015), while calcite can deform plastically at temperatures of 150 – 200 °C (Kennedy and White, 2001). This pronounced difference in the deformation style under similar ambient conditions can affect the rheology of shear zones in which the two phases occur. For example, the occurrence of patches or dispersed grains of dolomite

within calc-mylonites can result in enhanced strain localization (Oesterling et al., 2007; Kushnir et al., 2015).

To date, only a small number of studies have focused on the experimental investigation of the mechanical behavior and microstructural evolution of calcite-dolomite mixes. Experiments have been performed to study the high pressure and high temperature rheological behavior of mixes (e.g. torsion experiments of Delle Piane et al., 2009; Kushnir et al., 2015), as well as the frictional behavior of mixes at room temperature over a wide range of strain rates (e.g. room temperature rotary-shear experiments: Mitchell et al., 2015; Smith et al., 2017). In the first case, torsion experiments (performed at confining pressures up to 300 MPa, temperatures of 700-800 °C, shear strain rate $\dot{\gamma}$ of 1-3*10^{-4} s^{-1} and finite shear strain γ < 11) showed that minor quantities of dolomite (e.g., 25 wt.%) in a sintered calcite-rich sample increased the yield strength with respect to pure calcite samples. Under such experimental conditions, two main deformation mechanisms were observed: brittle fracturing in the dolomite grains and ductile flow in calcite, possibly as a result of grain boundary sliding assisted by diffusion creep and dislocation glide (Kushnir et al., 2015). Strain hardening observed in these experiments was interpreted to be due to dolomite grains interrupting more continuous calcite-rich layers and acting as stress concentrators. Brittle failure of dolomite grains eventually allowed the calcite-rich layers to become continuous and to continue deforming by superplastic flow. Electron Backscattered Diffraction (EBSD) analysis on both calcite and dolomite grains showed the development of a crystallographic preferred orientation (CPO). The CPO was typically more intense in calcite and directly related to the total strain accommodated.

The experimental studies conducted by Mitchell et al. (2015) and Smith et al. (2017) focused on the frictional behavior and microstructural evolution of gouge mixtures composed of 50 wt.% dolomite and 50 wt.% calcite under low normal stresses (σ_n ≤ 17.5 MPa), high slip rates (V ≥ 0.01 ms^{-1}) and large displacements (d = 0.03 – 3 m), reproducing the conditions encountered at the base of fast-moving landslides and during the seismic cycle in shallow-crustal faults. At a slip velocity of 1 ms^{-1}, dynamic weakening (up to 60% of the initial friction coefficient) was associated with grain size reduction and decarbonation of dolomite within a thin (< 100 μm) slip zone and in the nearby gouge, as attested by the detection of CO_2 during the experiments and the formation of “degassing” microstructures in dolomite clasts (i.e., enhanced internal porosity and vesicular

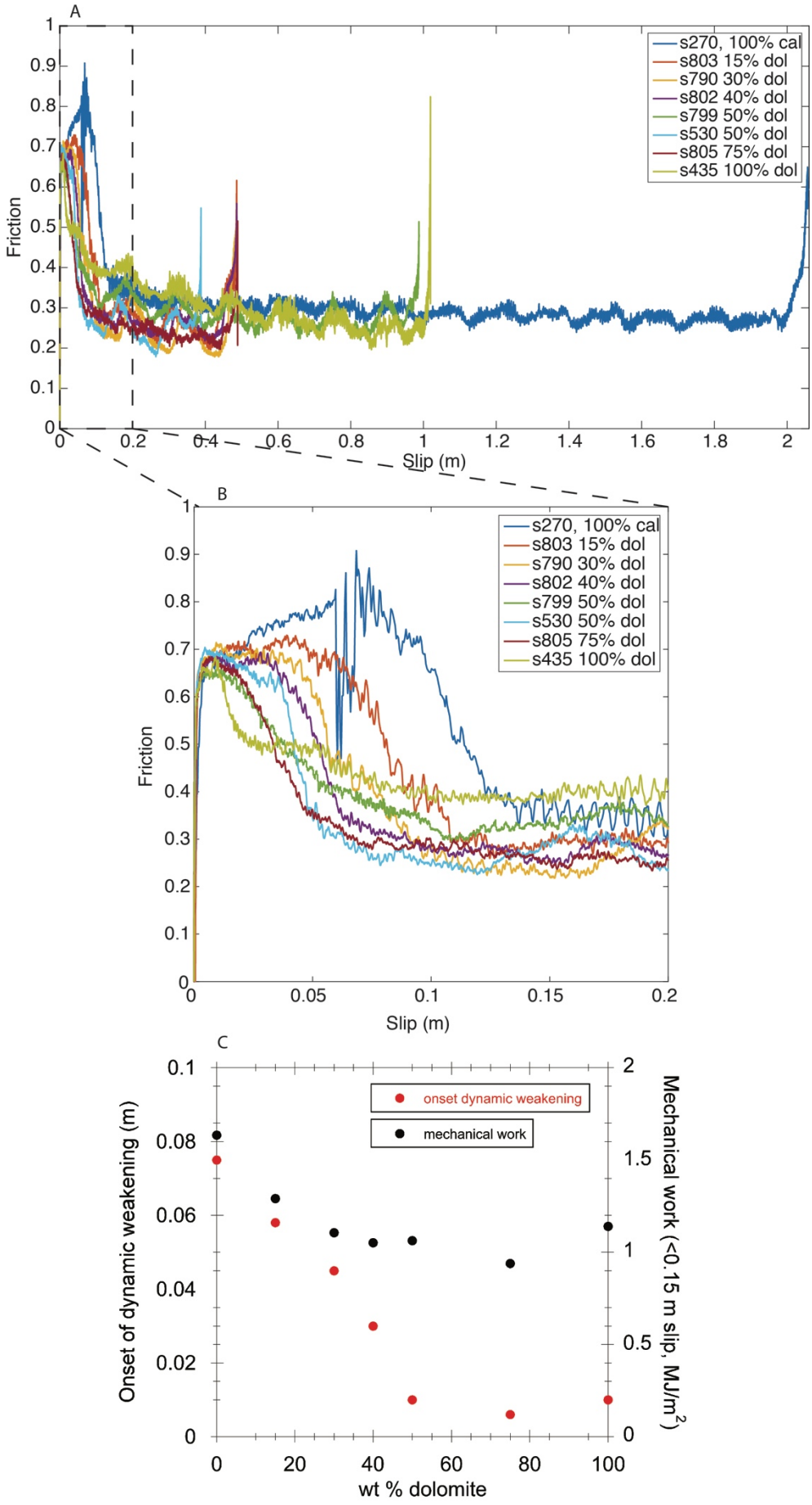


Fig. 1. See next page for caption.

Fig. 1. (previous page) Mechanical data from rotary-shear experiments conducted on pure calcite and dolomite gouges and calcite-dolomite mixtures with between 15-75 wt % dolomite (Smith and Fondriest, unpublished). a) Friction coefficient vs. slip for all experiments. b) Detail of the first 0.2 m of slip, showing that the friction coefficient during the early stages of sliding is sensitive to variations in dolomite content with contents as low as 15 wt%. When the dolomite content is 40-50 wt.%, the gouge mixture shows a similar evolution to the pure (100 wt.%) dolomite gouge. All experiments performed under room humidity conditions at 17.4 MPa normal stress and 1 m/s target slip rate. c) Slip required to reach the onset of dynamic weakening and mechanical work in the first 0.15 m of slip in function of the dolomite content.

Fig. 2. (next page) Rotary-shear experimental setup. a) Detectors assemblage in the sample chamber. Gas emission, room humidity and room temperature detectors were placed at < 1 cm from the sample holder. Four thermocouples were placed on the stationary side at increasing distance from the gouge layer. Note: the position of the thermocouple nearest to the gouge layer is not visible here and is illustrated in b). b) Diagram of the gouge holder with the location of the nearest thermocouple to the gouge layer (modified after Smith et al., 2015). c) Mirror-like slip surface formed in an experiment performed at V = 0.1 ms^{-1} on a mixed calcite-dolomite gouge layer. d) Diagram showing the location of the recovered and analyzed gouge layer after the experiment (after Smith et al., 2017). e) SEM backscattered (SEM-BSE) image of the starting material. Crushed calcite (white in color) and dolomite (gray in color) powder was passed through a 250 µm sieve prior mixing.

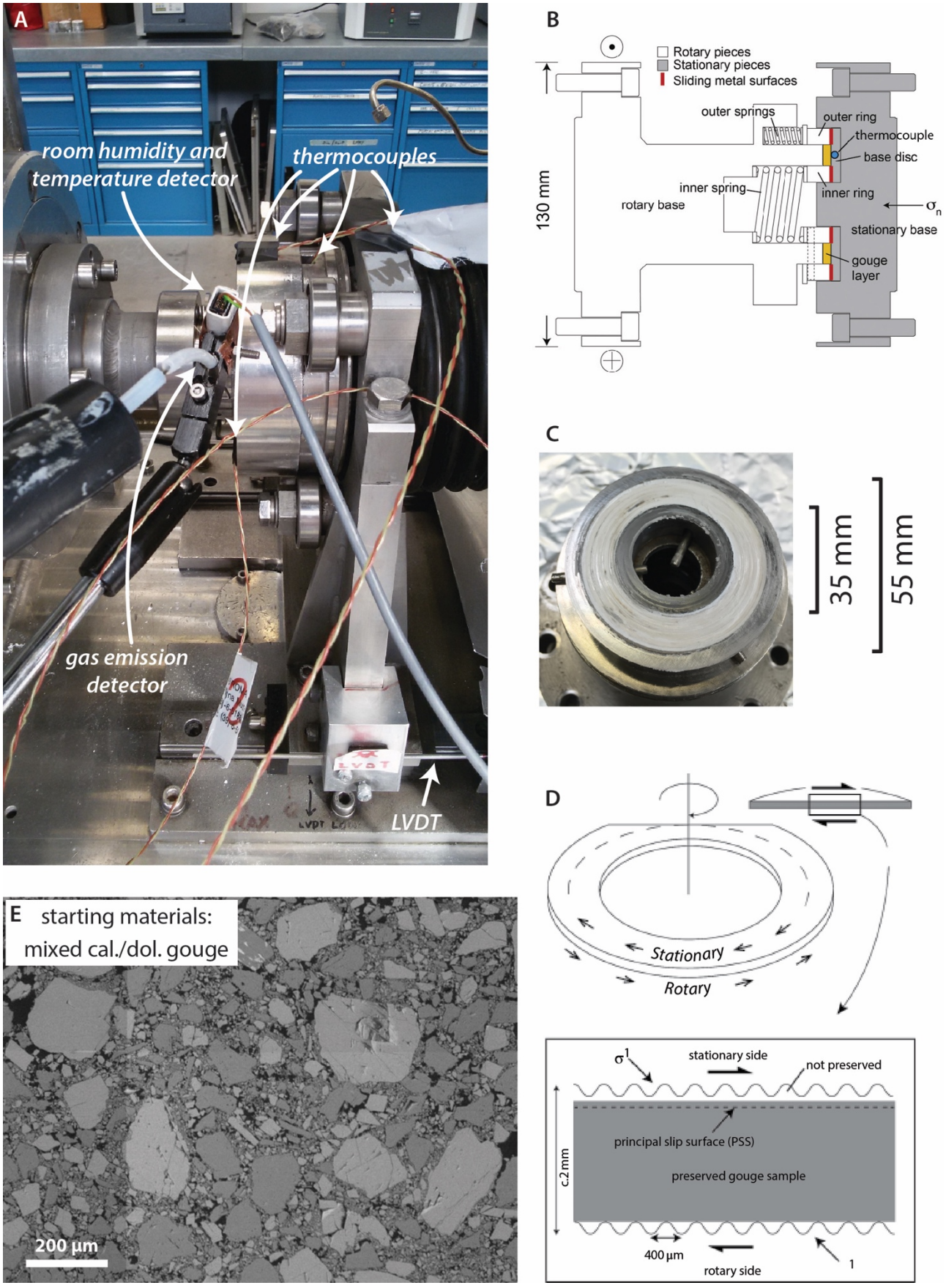


Fig. 2. See previous page for caption.

rims) up to 100 µm from the slip zone. During the early stages of these high-velocity experiments, prior to the onset of dynamic weakening, a well-defined foliation developed within the gouge mixtures due to brittle fracturing of calcite and dolomite grains and shearing of the fractured material in to compositional bands (Mitchell et al., 2015; Smith et al., 2017). These observations indicate that some examples of foliated gouge and cataclasite could form during coseismic shearing (Smith et al., 2017), challenging the common interpretation that fault rock foliations result from slow aseismic sliding (e.g., Rutter et al., 1986; Chester and Chester, 1998; Lin, 2001; Jefferies et al., 2006).

Motivated by microstructural observations of natural calcite-dolomite gouges (e.g., Demurtas et al., 2016), Steven Smith and Michele Fondriest (unpublished data) performed preliminary rotary-shear experiments under room humidity conditions to quantify the effect of dolomite on the frictional behavior of calcite-dolomite gouges during seismic slip ($V = 1\ ms^{-1}$) (Fig. 1). Pure calcite gouges show a prolonged strengthening phase (up to 0.1 m of slip under 17.4 MPa normal stress) prior the onset of dynamic weakening (Smith et al., 2015; Fig. 1a-b, blue curve). For the same deformation conditions (acceleration, target slip rate, normal stress, gouge thickness, ambient conditions, etc.) pure dolomite gouges show a much shorter ($d \leq 0.01$ m) strengthening phase before dynamic weakening occurs (Fig. 1a-b, snot green curve). For dolomite contents between 15-40 wt%, there is a linear decrease in the slip distance before dynamic weakening occurs (Fig. 1). At dolomite contents >50 wt%, the mechanical behavior of the gouge mixtures was similar to pure dolomite gouges (Fig. 1c).

The aims of this study are: (1) to expand on the preliminary experiments of Smith and Fondriest (unpublished) to better understand how the presence of dolomite influences the mechanical behavior of carbonate gouges during faulting; (2) identify any diagnostic microstructures in mixed carbonate gouges that could be associated with seismic and/or aseismic slip and; (3) to perform slide-hold-slide experiments to investigate the preservation potential of coseismic microstructures in the geological record.

2. Methods

2.1. Starting materials

The gouges were prepared by mixing 50 wt.% calcite and 50 wt.% dolomite. The calcite-dolomite ratio in the experimental mixture was similar to that found in natural fault gouges and cataclasites from the Vado di Corno Fault Zone (VCFZ, Italian Central Apennines; Demurtas et al., 2016) (see microstructures in Chapter I). The calcite gouge was derived by crushing Carrara marble with a modal composition of 98.8 wt.% calcite and < 1 wt.% of dolomite and muscovite (see Appendix A for XRPD analysis). The dolomite gouge was derived by crushing the Calcare Massiccio Fm. outcropping in the High Strain Damage Zone of the VCFZ (Demurtas et al., 2016). In this area, the Calcare Massiccio Fm. was entirely "dolomitized" (100 wt.% dolomite according to XRPD analysis, see Appendix A; this composition was confirmed by scanning electron microscope investigations performed on the gouges). The crushed gouges were passed through a 250 μm sieve and then mixed together by slowly tumbling for ca. 30 minutes (Fig. 2e). The XRPD semi-quantitative analysis performed at the Department of Geoscience (Padova) on the resulting two batches of mixtures (CDM1 and CDM2) yielded calcite = 47.2 wt.% and dolomite = 52.8 wt.% for CDM1 and calcite = 42.9 wt.% and dolomite = 57.1 wt.% for CDM2 (see Appendix A).

2.2. Experimental setup

Twenty-eight experiments were performed at slip rates ranging from 30 μms^{-1} (slow; Rowe and Griffith, 2015) to 1 ms^{-1} (seismic) with SHIVA (Slow- to HIgh-Velocity rotary-shear friction Apparatus) installed at the Istituto Nazionale di Geofisica e Vulcanologia (INGV) in Rome (Di Toro et al., 2010; Niemeijer et al., 2011). Rotary motion is controlled by two brushless electric motors and an air actuator applies the normal force. By means of a lever, a maximum thrust of up to 5 tons can be applied (Di Toro et al., 2010; Niemeijer et al. 2011). The small motor can dissipate up to 5.15 kW on the samples and imposes, for standard in size samples (see below) equivalent slip rates ranging from 1.0 10^{-5} to 3.0 10^{-3} m/s, while the second and bigger motor dissipates up to 280 kW and imposes slip rates ranging from 1.0 10^{-3} to 9 m/s. The gouges were deformed inside a metal holder specifically designed for incohesive materials (Fig. 2; Smith et al., 2013, 2015). The gouge sample assembly includes rotary and stationary pieces (in the latter, only the "axial" movements were allowed). The rotary side of the gouge holder consists of a base plate and inner and outer rings (int./ext. diameters of 35/55 mm) that prevent gouge extrusion and allow sliding over a base disc located in the stationary base plate. The thickness of the gouge layer at the initiation of the

experiment was ca. 3 mm. Mechanical data (i.e., axial load, torque, axial displacement, angular rotation) were acquired at a frequency up to 25 kHz, and determination of (equivalent) slip rate (defined as $v_e = \left(4\pi R(r_i^2 + r_i r_o + r_o^2)\right)/\left(3(r_i + r_o)\right)$, with r_i and r_o being the inner and outer radius of the sample, respectively, and R the number of revolutions per minute; Hirose and Shimamoto, 2005), total (equivalent) slip (defined as $d_e = v_e t$) and shear stress followed the methods outlined in Di Toro et al. (2010). The gouge mechanical behavior was expressed by the effective friction coefficient, μ, defined as the ratio between the shear stress (τ) and the effective normal stress (σ') - note that the pore fluid pressure was not measured in the experiments: $\mu = {}^{\tau}/_{\sigma'}$, Horizontal displacements of the axial column were measured using a direct current differential transformer (DCDT, 50 mm range and ~ 50 µm resolution) and a linear variable differential transformer (LVDT, 3 mm range and ~ 0.03 µm resolution). For further details about the data acquisition system and the characteristics, location and calibration of the load cells, detectors and devices, see Niemeijer et al. 2011 and Smith et al. (2013) for calibration of the gouge sample holder.

Measurements of room humidity and room temperature were collected at a distance of < 1 cm from the gouge holder before and during the experiments (Fig. 2a). Temperature variations during deformation in the gouge were measured at an acquisition rate of 2.5 Hz by four K-type thermocouples (Nickel-Alumel) installed on the stationary side (Fig. 2a-b). One thermocouple was positioned at ~ 200 µm from the gouge layer (Fig. 2b), where temperature increase is typically expected. The other three thermocouples where located on the sample holder and stationary column to detect temperature variations due to heat conduction in the sample apparatus (Fig. 2a). CO_2 emissions were monitored using an OmniStar™ GSD 301 O mass spectrometer designed for gas analysis at atmospheric pressure.

2.3. Deformation conditions

Table 1 lists the experiments performed in this study. Experiments were performed at both room-humidity and water-dampened conditions with the normal stress held constant at 17.4 ± 0.1 MPa, with the exception of experiment s1324 performed at 26 MPa normal stress (Table 1). Room humidity varied between 41% and 62% and room temperature between 19 and 22°C. In water-dampened conditions, ca. 2 ml of deionized water was added to the gouge in the sample holder using a pipette before applying the normal stress. Experiments were performed at target slip rates

ranging from 30 μms^{-1} to 1 ms^{-1} with the same acceleration of 6 ms^{-2}. Total displacements ranged from 0.05 m to 0.4 m.

Two types of experiments were performed: single-slide and slide-hold-slide. Single-slide experiments consisted of a single pulse of acceleration → constant sliding velocity → deceleration. In velocity step experiments the total displacement of 40 cm was attained with two consecutive slip pulses. Between the two pulses a hold time of 300 seconds was applied during which the normal stress was held constant at 17.3 MPa. One slide-hold-slide experiment was performed as follows: the first pulse at 30 μms^{-1} for 10 cm of displacement and the second pulse at 1 ms^{-1} for 30 cm of displacement. Another slide-hold-slide experiment was performed as follows: first pulse at 1 ms^{-1} for 30 cm of slip and the second pulse at 30 μms^{-1} for 10 cm of slip.

2.4 Analytical techniques

After every experiment, the gouge layer was recovered and impregnated in a low-viscosity epoxy (Araldite 2020) for microstructural analysis. Polished petrographic thin sections were cut perpendicular to the slip surface and both parallel (i.e., tangential cut) and perpendicular (i.e., radial cut) to the slip direction (Fig. 2). Detailed microstructural investigation was performed with a Zeiss Sigma VP Field-Emission Scanning Electron Microscope (SEM) installed at the Otago Centre for Electron Microscopy (University of Otago) operating in backscattered mode (acquisition conditions: accelerating voltage 15 kV, working distance 6-7 mm). Energy-dispersive X-ray spectroscopy (EDS) in the SEM was used to produce elemental maps showing the distribution of calcium and magnesium, hence calcite and dolomite, in the gouge layer. Possible mineralogical changes that occurred during the experiments were determined by semi-quantitative X-ray powder diffraction (XRPD) analysis conducted in the Department of Geoscience, Padova. Two types of XRPD analysis were performed: (i) on the bulk gouge (after being crushed in an agate mortar), and (ii) on small intact chips of the localized slip surface that formed in the experiments.

3. Results

3.1. Mechanical data

3.1.1. Friction evolution with slip rate

Under room-humidity conditions and slip rates $\leq$ 0.01 ms^{-1}), the gouge mixtures exhibited comparable mechanical behavior (Fig. 3a). The initial peak of the friction coefficient was followed by a small decrease ($\Delta\mu$ < 0.03) in the first ~ 0.02 m of slip and then by a slow and progressive increase with slip (slip-strengthening behavior) until a steady state friction coefficient (averaged between 0.15-0.38 m of slip) of μ = 0.75-0.8 was attained after 0.1-0.25 m (Fig. 3a). At a slip rate of 0.1 ms^{-1} (Fig. 3a; only one experiment was performed under this deformation conditions), the gouge had a rather long initial strengthening phase that lasted for ca. 0.062 m of slip up to a peak friction coefficient of μ = 0.68 (Fig. 3a-b); then the effective friction coefficient progressively decreased with slip (slip-weakening behavior) until a steady state value of μ = 0.55 was attained (green curve in Fig. 3a). At higher slip rates (V = 1 ms^{-1}), after a short initial strengthening phase of ~ 0.005 m of slip, the effective friction coefficient decreased over a slip weakening distance (D_w) of ~ 0.14 m until a steady state value of μ = 0.28 was achieved (light blue curve in Fig. 3a-b). At the end of the experiment, during the deceleration phase, the friction coefficient increased up to μ ~ 0.56 (Fig. 3a). At the same high slip rates (V = 1 ms^{-1}), but under 26 MPa normal stress, the mechanical behavior of the gouge mixture was similar to the one observed in the experiments performed at lower normal stress (i.e., 17.5 MPa): dynamic weakening initiated after 0.008 m of slip, with the friction coefficient decreasing to a steady state value of μ = 0.25 after 0.16 m of slip, followed by re-strengthening during sample deceleration up to μ = 0.59 (orange curve in Fig. 3a-b).

Under water-dampened conditions at slip velocities of $\leq$ 0.1 ms^{-1} the experiments showed similar mechanical data (Fig. 3c). Some of the gouges exhibited slight slip-strengthening, achieving the steady state friction coefficient within the first 0.1 m of slip (Fig. 3c). The steady state friction coefficient was slightly lower than in room-humidity conditions, but the gouges still had a friction coefficient (μ = 0.62-0.70) in the Byerlee range (Fig. 3c). At higher imposed slip rates (V = 1 ms^{-1}), the evolution of the friction coefficient was similar to the room-humidity experiments. However, the onset of dynamic weakening occurred in ca. 0.003 m of slip rather than ca. 0.008 m (Fig. 3c-d). A shorter strengthening phase in water-dampened conditions was also reported by Rempe et al. (2017) for pure calcite gouges.

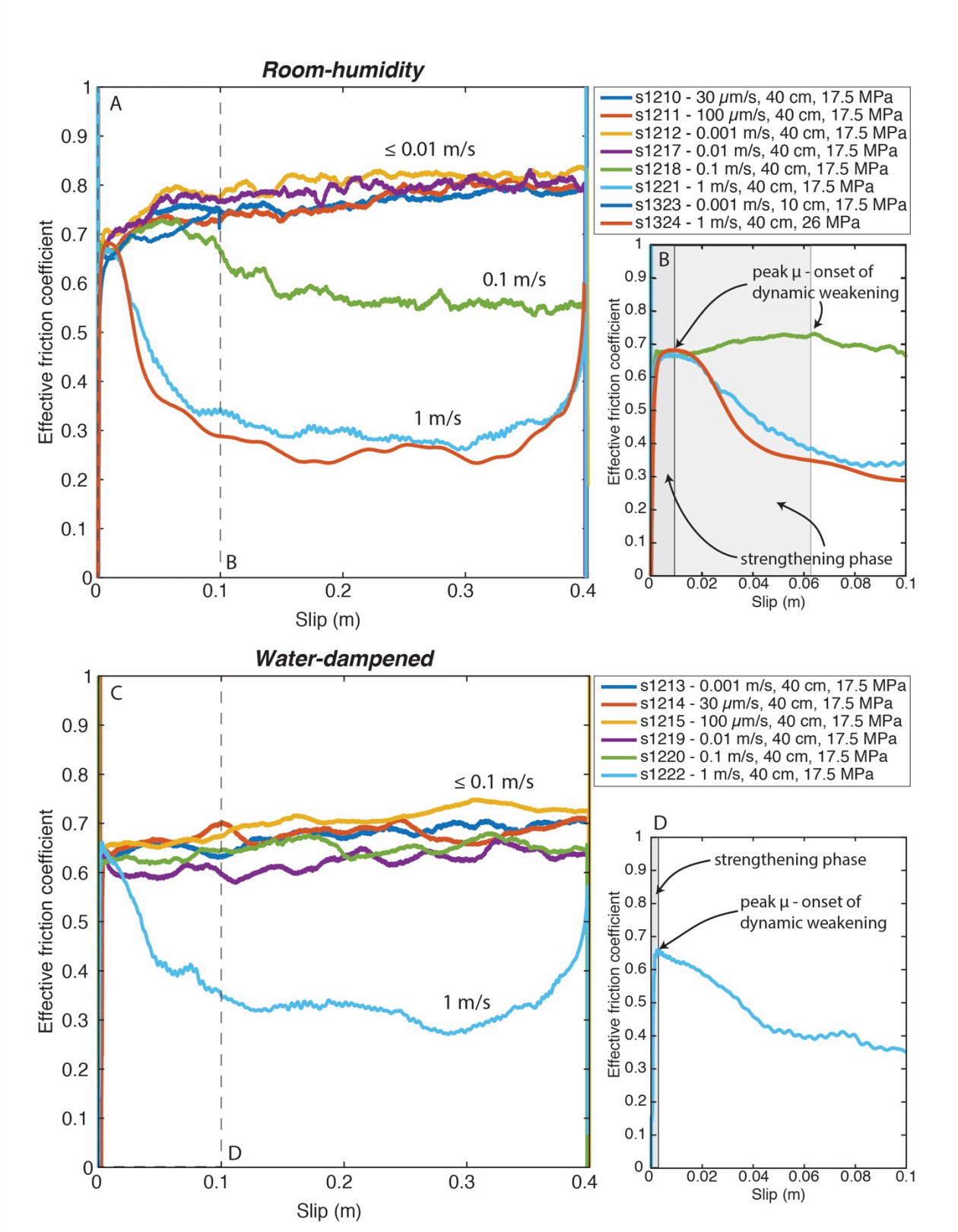


Fig. 3. Continues next page.

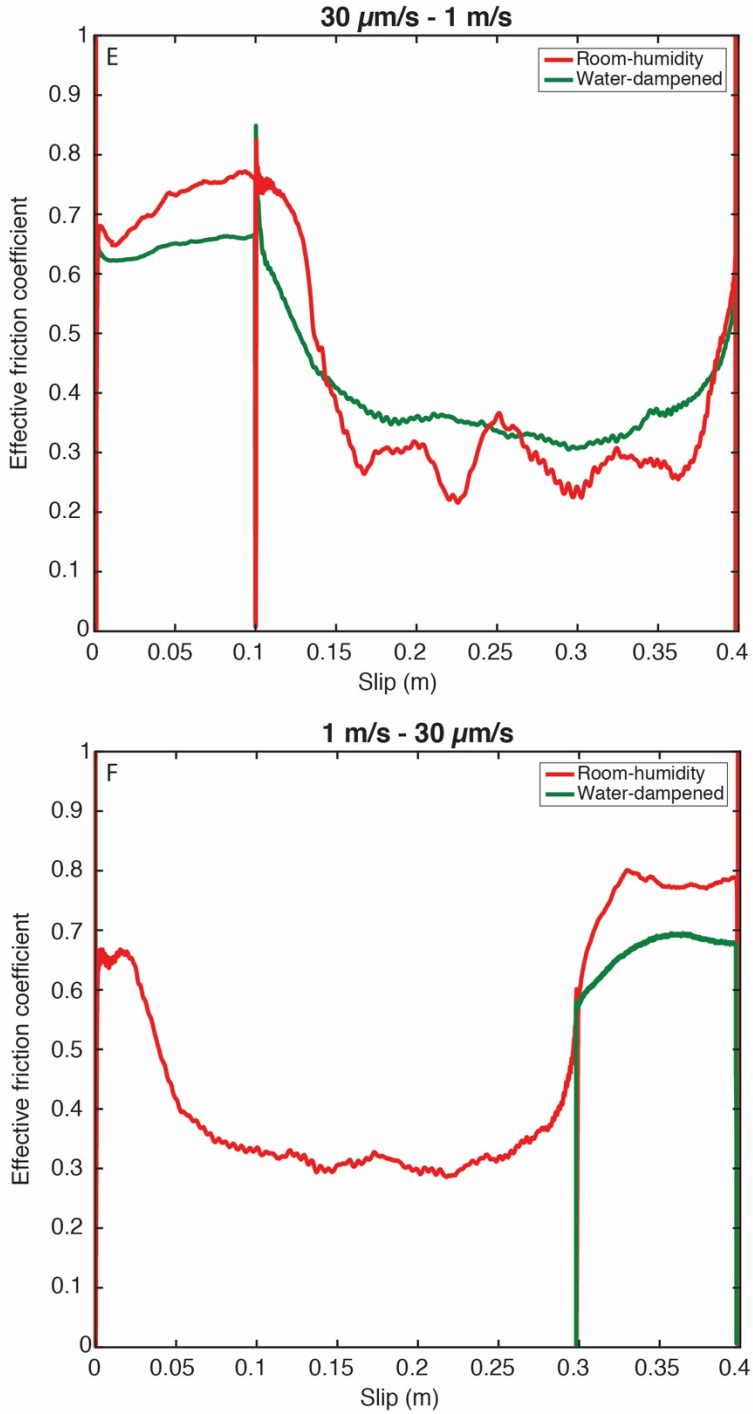


Fig. 3. (see previous page for a-d) Mechanical data of rotary-shear experiments on calcite-dolomite mixtures. a-c) Effective friction coefficient evolution with slip under room-humidity and water-dampened conditions, respectively. In room-humidity conditions, the gouge showed slip-strengthening behavior up to slip rate of 0.01 ms^{-1}. For $V \geq 0.1$ ms^{-1}, slip-weakening was observed. Conversely, in water-dampened condition, slip-strengthening/neutral evolution of the effective friction coefficient was observed up to a slip rate of 0.1 ms^{-1}. Weakening was observed only when slip rate reached 1 ms^{-1}. c-d) Detail of effective friction coefficient evolution for slip ≤ 0.1 m in experiments where slip-weakening was observed in room-humidity and water-dampened conditions, respectively. e-f) Effective friction coefficient evolution for the two types of slide-hold-slide experiments. Mechanical data of the first slip in water-dampened condition in f) is missing due to problems during data acquisition (i.e., data acquisition rate was mistakenly set too low for the 1 ms^{-1} slip pulse).

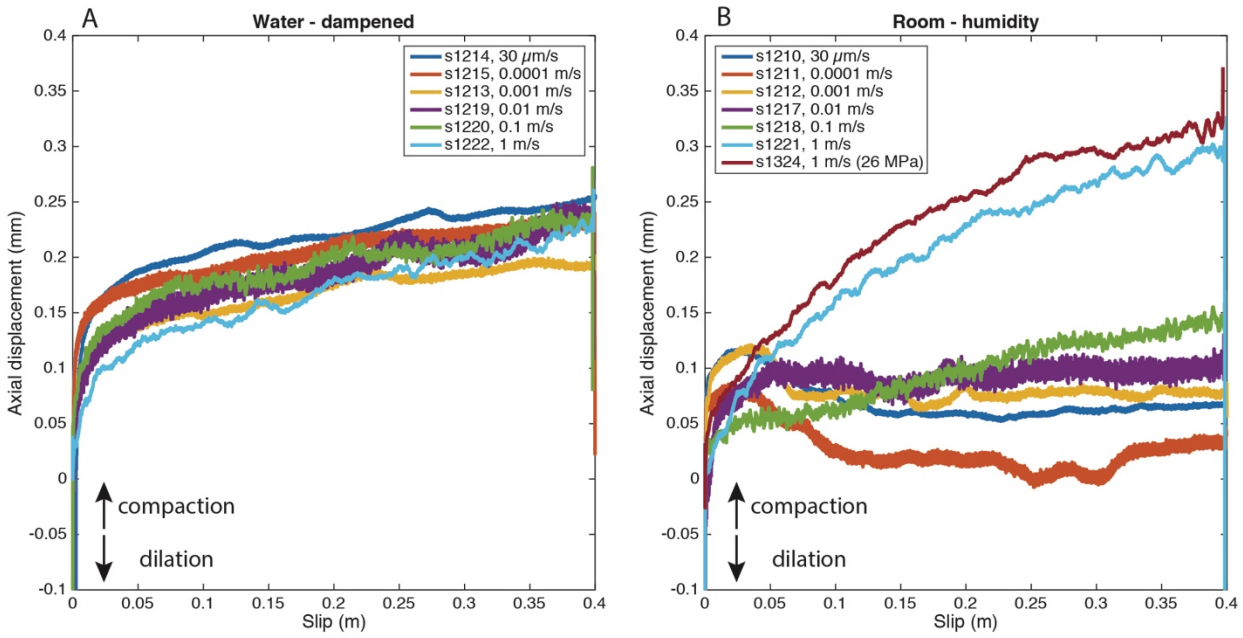


Fig. 4. Gouge thickness evolution with slip rate. a) Under water-dampened conditions, the gouge compacted at all investigated slip rates. An initial fast compaction is followed by a slower constant compaction during steady-state friction. b) Under room-humidity conditions, for slip rates of V ≤ 0.01 ms^{-1}, after a transient dilation phase lasting the first 0.1-0.15 m of slip, no clear compaction or dilation was observed. Instead, at higher slip rates (V ≥ 0.1 ms^{-1}), the gouge compacted constantly throughout the whole experiment, with compaction rate increasing with slip rate.

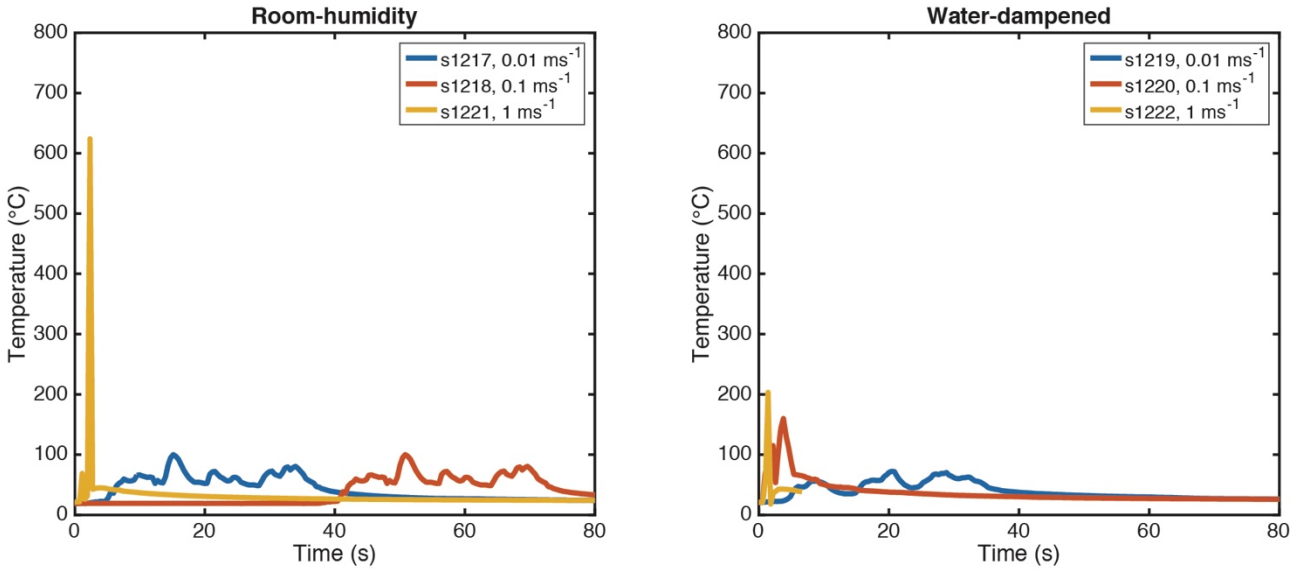


Fig. 5. Experimental measure of temperature evolution. Temperature measurements were collected as near as ca. 200 µm from the localized volume within the gouge by means of thermocouples with an acquisition rate of 2.5 Hz. The use of K-type thermocouples, with relative low acquisition rate (i.e., 2.5 Hz), typically results in an underestimation of the real temperature achieved on the slip surface. However, such temperatures can be used as a lower bound.

In the slide-hold-slide experiments performed in room-humidity and water-dampened conditions, the evolution of the friction coefficient during the first slip pulse was consistent with the single-slide experiments (Fig. 3e-f). Note that mechanical data for the first pulse in experiment s1226 are missing due to problems during data acquisition (i.e., data acquisition rate was mistakenly set too low for the 1 ms^{-1} slip pulse). At the beginning of the second velocity step (after the first slide event at 30 μms^{-1} and the 300 s long hold time), our preliminary data indicate that the peak friction coefficient (μ = 0.8-0.85) was slightly higher than in the single pulse experiments, and that it was reached after a shorter amount of slip (0.002 m, Fig. 3e). Once the peak friction coefficient was overcome, the friction coefficient evolved towards steady state conditions similar to the single-pulse experiments.

3.1.2. Gouge thickness evolution with slip rate

Since no significant gouge losses were observed in the experiments, the axial displacement evolution with slip is interpreted to be due to dilation and compaction within the gouge layers, which varied as a function of the deformation conditions. In water-dampened conditions, the gouges exhibited continuous compaction during the experiments (Fig. 4a). Compaction was initially rapid and then reached a constant rate once steady state friction was achieved. In total, ca. 200-250 μm of compaction was measured and this did not vary with slip rate (Fig. 4a).

Under room-humidity conditions, the gouge thickness evolution varied with slip rate (Fig. 3b). At 30 $\mu ms^{-1} \leq V \leq 0.001\ ms^{-1}$, the gouge layer thickness showed a three-stage evolution: (i) compaction of ~90-120 μm at the initiation of sliding when the friction coefficient slightly decreases, (ii) dilation of ~50-70 μm during slip-strengthening behavior, and (iii) overall neutral behavior once steady state friction coefficient is reached with final total compaction of ~30-60 μm. At V = 0.01 ms^{-1}, after an initial compaction of 100 μm, there is no evidence of compaction or dilation within the gouge layer (Fig. 4b). At high slip rates ($V \geq 0.1\ ms^{-1}$), continuous compaction is observed throughout the duration of the experiment (up to ca. 300 μm of axial shortening at V = 1 m/s) (Fig. 4b).

3.2. Temperature evolution

Temperature variations were measured with four thermocouples positioned at increasing distance from the slip surface, with the nearest one installed ca. 200 µm away from where strain localizes (Fig. 2a-b). In Fig. 5, temperature measurements from the thermocouple nearest to the gouge layer (Fig. 2b) are shown for experiments with a slip rate ≥ 0.01 ms^{-1}. The higher temperature increase was seen in the room-humidity experiment that slid at 1 ms^{-1}, with a measured temperature of ca. 610 °C. At the same slip rate, but in the presence of fluid water (experiment s1222 in Fig. 5), that maximum temperature measured was of 210 °C. However, due to the low acquisition rate of the thermocouples (i.e., 2.5 Hz) and the high thermal conductivity of the metal gouge holder, temperatures were likely underestimated (Fig. 5).

Therefore, the bulk temperature rise during the experiments was estimated using (Rice, 2006):

$$\Delta T = \frac{\mu \sigma_n \sqrt{vd}}{\rho c_p \sqrt{\pi \kappa}}$$

where μ is the friction coefficient (measured throughout the whole experiment), σ_n is the normal stress, v the slip rate, d the displacement, ρ is the density, c_p is the specific heat capacity and κ the thermal diffusivity of the gouge. Since the experiments were performed on mixtures of 50/50 wt.% of calcite/dolomite, the above thermal and physical properties were averaged in a way that the temperature rise accounted for the presence of both minerals in the gouge (Table 2). Therefore, the equation to estimate the bulk temperature rise in the gouge mixture is (the suffixes cal and dol stand for calcite and dolomite, respectively):

$$\Delta T = \frac{\mu \sigma_n \sqrt{vd}}{2} \left(\frac{1}{\rho^{cal} c_p^{cal} \sqrt{\pi \kappa^{cal}}} + \frac{1}{\rho^{dol} c_p^{dol} \sqrt{\pi \kappa^{dol}}} \right).$$

For experiments performed under water-dampened conditions, the presence of water must also be accounted for in the bulk temperature rise. Based on the water quantity added at the beginning of the experiment, and considering minor losses during the setup of the experiment (e.g., installation of the gouge holder, application of the normal stress), the water content was estimated to be around 20 wt % of the gouge material. Hence, the temperature rise was estimated to be:

$$\Delta T = \frac{\mu \sigma_n \sqrt{vd}}{5} \left(\frac{2}{\rho^{cal} c_p^{cal} \sqrt{\pi \kappa^{cal}}} + \frac{2}{\rho^{dol} c_p^{dol} \sqrt{\pi \kappa^{dol}}} + \frac{1}{\rho^{water} c_p^{water} \sqrt{\pi \kappa^{water}}} \right).$$

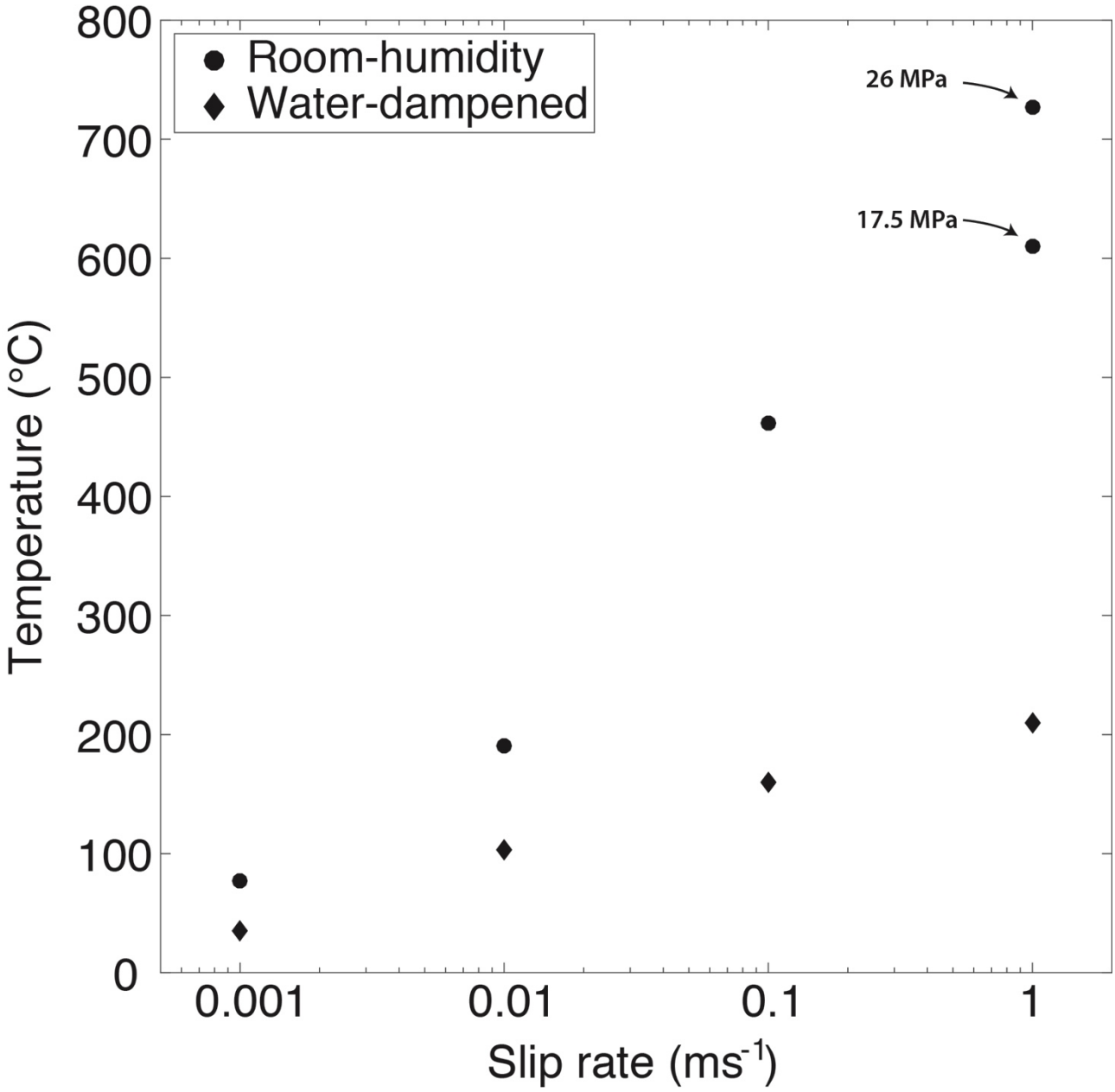


Fig. 6. Estimate of the maximum temperature rise achieved in the slip zone with slip rate. Temperature rise was calculated for experiments at slip rate V ≥ 0.01 ms^{-1} both in room-humidity and water-dampened conditions. In the presence of fluid water, due to the continuous changes of the physical properties of water with temperature and pressure, the temperature rise estimate is underestimated and does not relate to microstructure observations at high slip rates (V = 1 ms^{-1}). Therefore, the calculated temperature can be used as a lower bound.

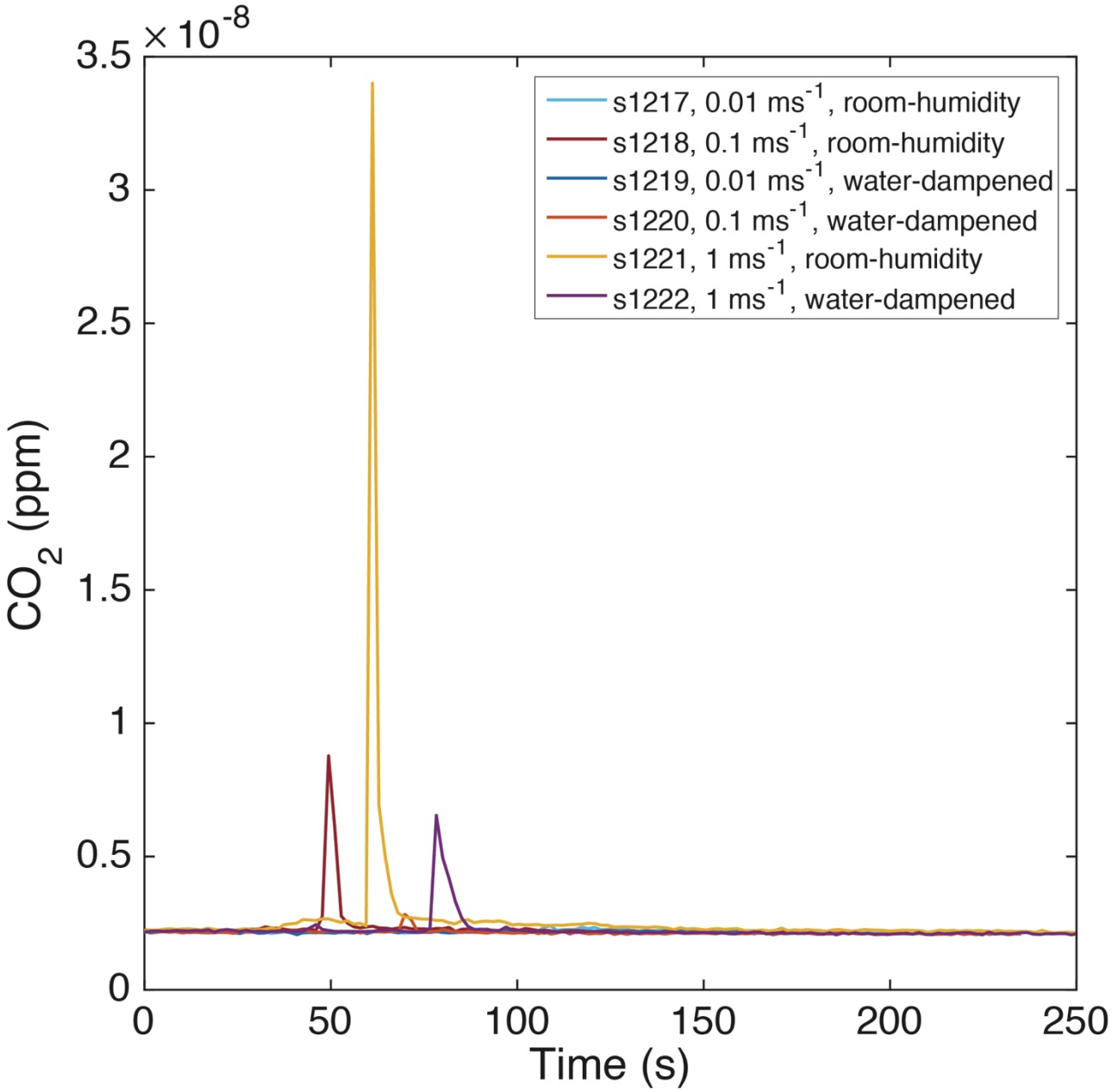


Fig. 7. Gas emission data for intermediate and high slip rate experiments. CO_2 emission data for experiments at 0.01 $ms^{-1} \leq V \leq 1$ ms^{-1} and room-humidity and water-dampened conditions. Although the data can be interpreted only in a qualitative way, CO_2 emissions under room-humidity conditions are larger than in the experiments performed in the presence of water, probably indicating a larger gouge volume undergoing decarbonation due to the temperature rise.

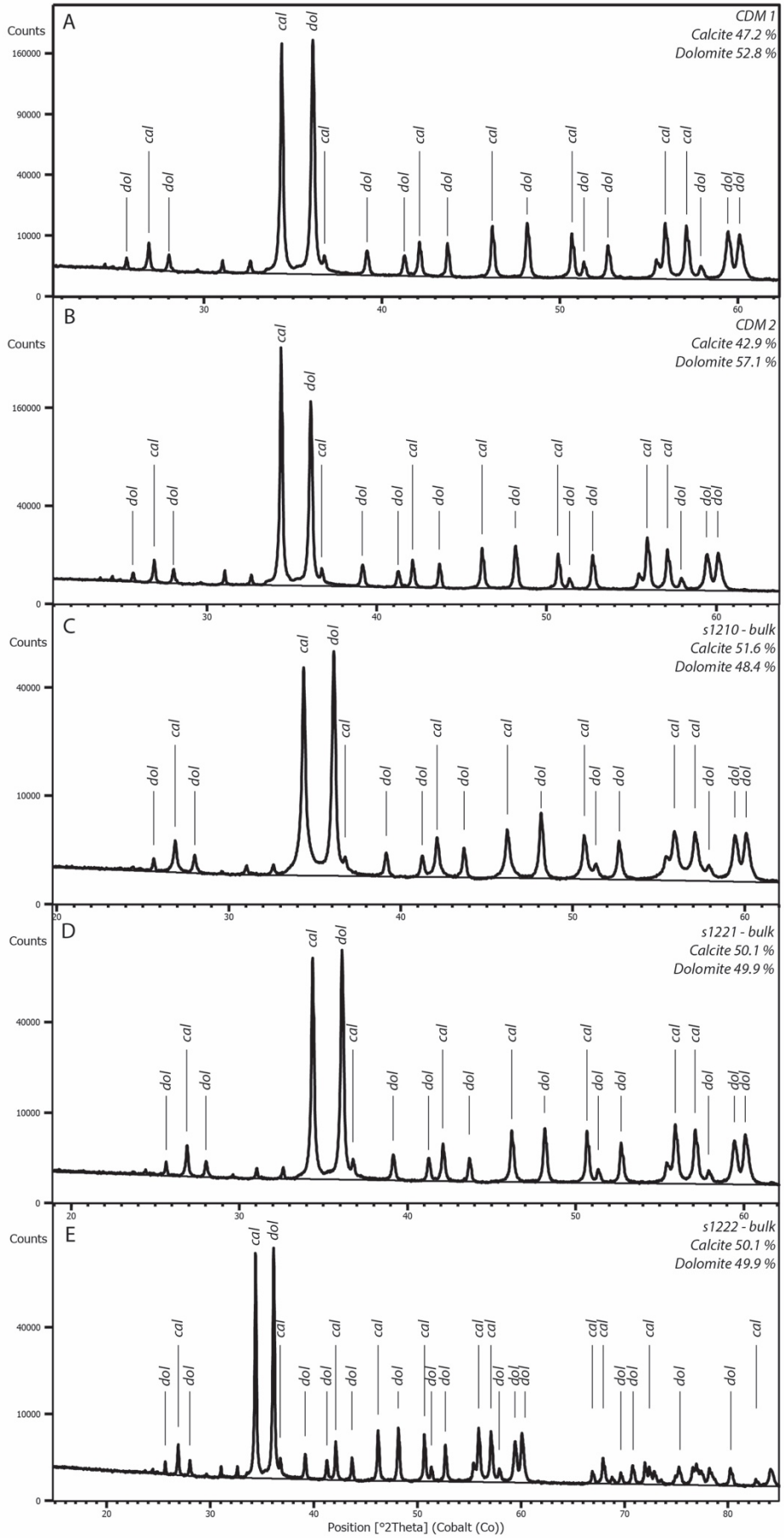


Fig. 8. Continues next page.

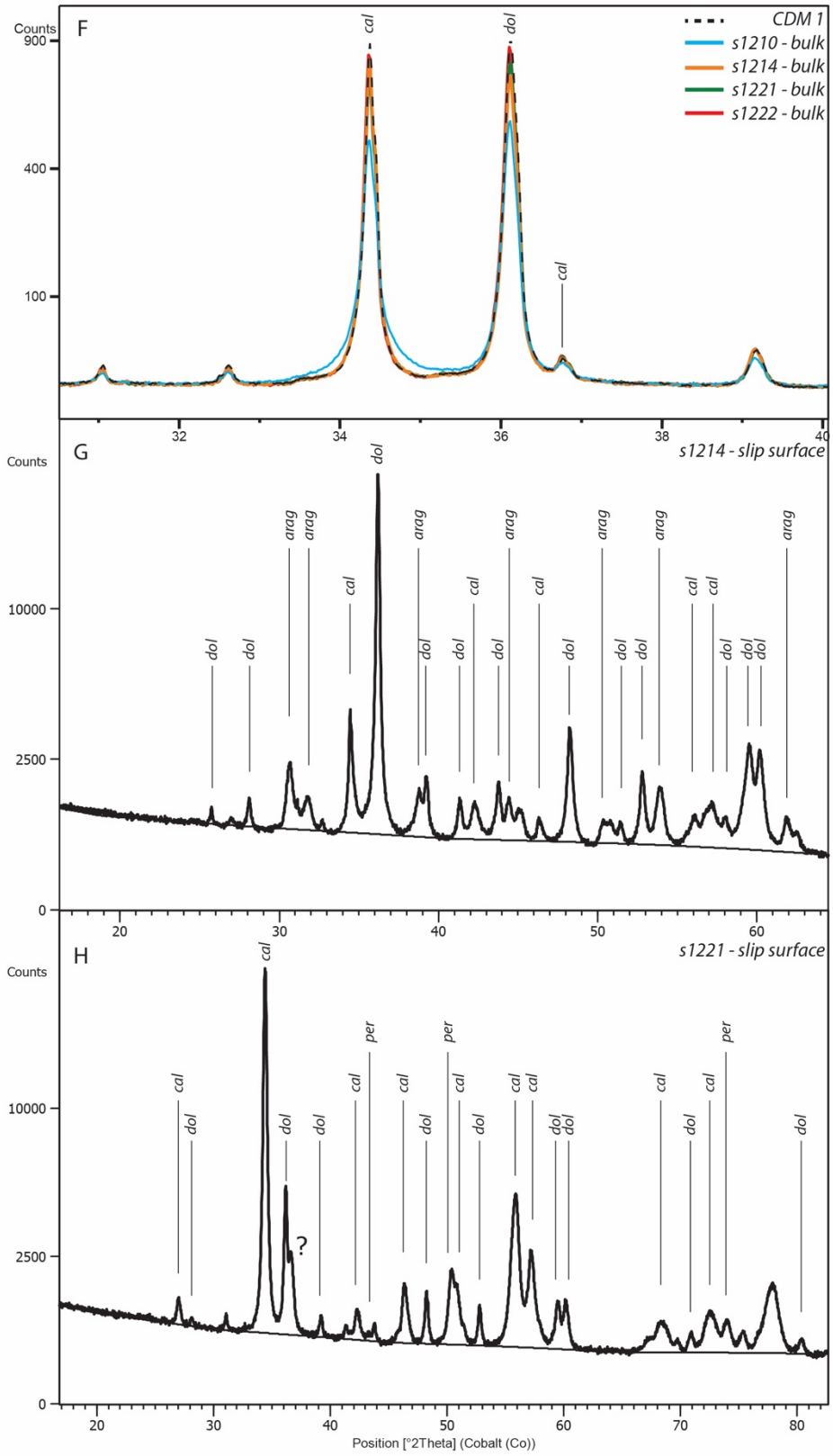


Fig. 8. See next page for caption.

Fig. 8. (previous page) X-ray powder diffraction analysis of experimental bulk gouge and slip surfaces. a) – b) XRPD analysis of CDM1 and CDM2, respectively. c) – d) – e) No mineralogical variations were detected in the bulk gouge for experiments s1210, s1221 and s1222, respectively. f) In experiment s1210, the main calcite peak showed a Lorentzian profile, which corresponds to a large crystallite distribution. This suggests that intense comminution occurred in the gouge. g) At 30 μms^{-1} in water-dampened conditions, traces of aragonite along with calcite and dolomite are found on the slip surface. Transformation of calcite into aragonite has been documented as a consequence of dry mechanical grinding by Lin et al. (2014). This raises either the possibility of the presence of dry patches during deformation or that such transformation can occur also in the presence of water. b) At 1 ms^{-1} in room-humidity conditions, production of periclase (MgO) is observed. Periclase is a one of the reaction products of the decarbonation of dolomite, along with carbon dioxide (CO_2) and Mg-calcite. The presence of these newly formed minerals allows us to estimate a minimum temperature of ~550°C in the slip surface during slip.

Finally, contribution also of flash heating to the temperature rise estimate in the bulk gouge was not taken into account. Estimates of the maximum temperature achieved during intermediate- and high-velocity experiments are shown in Fig. 6. The maximum estimated T was 727°C for experiment s1324 (i.e., 1 ms^{-1} at 26 MPa) (Fig. 6).

In the case of water-dampened experiments, simplifications on the physical properties of water (i.e., constant physical properties throughout the experiment independent of variation of ambient condition) were taken given the difficulty of considering the continuous changes in ρ, c_p and κ with temperature and pressure due to experimental limitations on pore pressure calculations. Moreover, the latent heat of vaporization that would buffer the temperature increase was not included in the calculations (Chen et al., 2017). In any case, the maximum temperature rise estimates in the presence of water (Fig. 6) were of the order of 35-210 °C (for the case of 0.001 and 1 ms^{-1}, respectively).

3.3. CO_2 emissions

CO_2 emissions were only detected for experiments performed at slip rates $\geq$ 0.1 ms^{-1} (Fig. 7). Since there was no calibration of the mass spectrometer, the data collected can only be used in a qualitative way. The amount of detected CO_2 increased with slip rate and was higher for the room-humidity experiments. This is consistent with previous experiments performed on pure calcite gouges and rocks (Smith et al 2013; Violay et al., 2013).

3.4. Mineralogy of deformed gouges

X-ray powder diffraction (XRPD) analysis was performed both on the bulk gouge and on small intact chips of the slip surface (the latter was not reduced into powder). No mineralogical variations were detected in the bulk gouge (= entire recovered gouge layer) of any of the analyzed experiments (s1210, s1214, s1218, s1221, s1222). Observation of the main peaks of calcite and dolomite suggested a reduction in the crystallite (defined as single particle/grain that contributes to the diffractogram) size in the room-humidity experiment at 30 μms^{-1} (Fig. 8c-f). Moreover, the main calcite peak showed a Lorentzian profile, which corresponds to a large crystallite size distribution (Fig. 8f). This decrease in the crystallite size is consistent with microstructural observations that shows the development of a thick slip zone where intense comminution occurred (see Fig. 11b).

XRPD analysis of the chips of recovered slip surfaces shows the presence of aragonite in water-dampened experiment s1214 performed at V = 30 μms^{-1}. Given that aragonite was not present in the starting material (Fig. 8a-g, Table 1 and Appendix A), the transformation of calcite into aragonite due to mechanical grinding is a possibility (Li et al. (2014). However, Li et al. (2014) investigated the polymorphic transformation only under room-humidity conditions. This could imply that in our experiments there were either dry patches where the calcite to aragonite transformation occurred, or that such transformation is also possible under water-saturated conditions. Further investigation to address this matter is required because aragonite could be a useful marker of such a phase transformation in natural fault zones. Under room-humidity conditions at V = 1 ms^{-1}, the slip surface consists of dolomite, Mg-calcite and periclase (MgO) (Fig. 8b), the latter being one of the products of the (first) decarbonation reaction of dolomite at 550°C, $MgCa(CO_3)_2 \implies MgO + (Ca, Mg)CO_3 + CO_2$ (Samtani et al., 2002).

3.5. Microstructures of deformed gouge layers

Figure 9 summarizes the range of microstructures that developed in room-humidity and water-saturated conditions at different slip rates (for a more complete illustration of the microstructures found in all the experiments see Appendix B). As in previous work (e.g., Kitajima et al., 2010; Smith et al., 2017) several distinct microstructural domains were developed, defined by variations in grain size, fabric and the presence of localized slip surfaces. In the present experiments, the microstructural domains varied in thickness and occurrence at different slip rates (Fig. 9).

In the descriptions below, we define the experimental slip surface as the fault surface itself, sometimes containing slip direction indicators such as slickenlines and surface grooves (Smith et al., 2011). Instead, the slip zone, up to tens of centimeters thick in nature, develops beneath the slip surface and consists of variously developed fault rocks (see classification by Sibson, 1977). Together, the slip surface and the slip zone are thought to accommodate the bulk of displacement during seismic faulting (Sibson, 2003). In addition, we define the principal slip surface (PSS) as the slip surface on which most of the displacement is thought to be accommodated and the principal slip zone (PSZ) as its related slip zone.

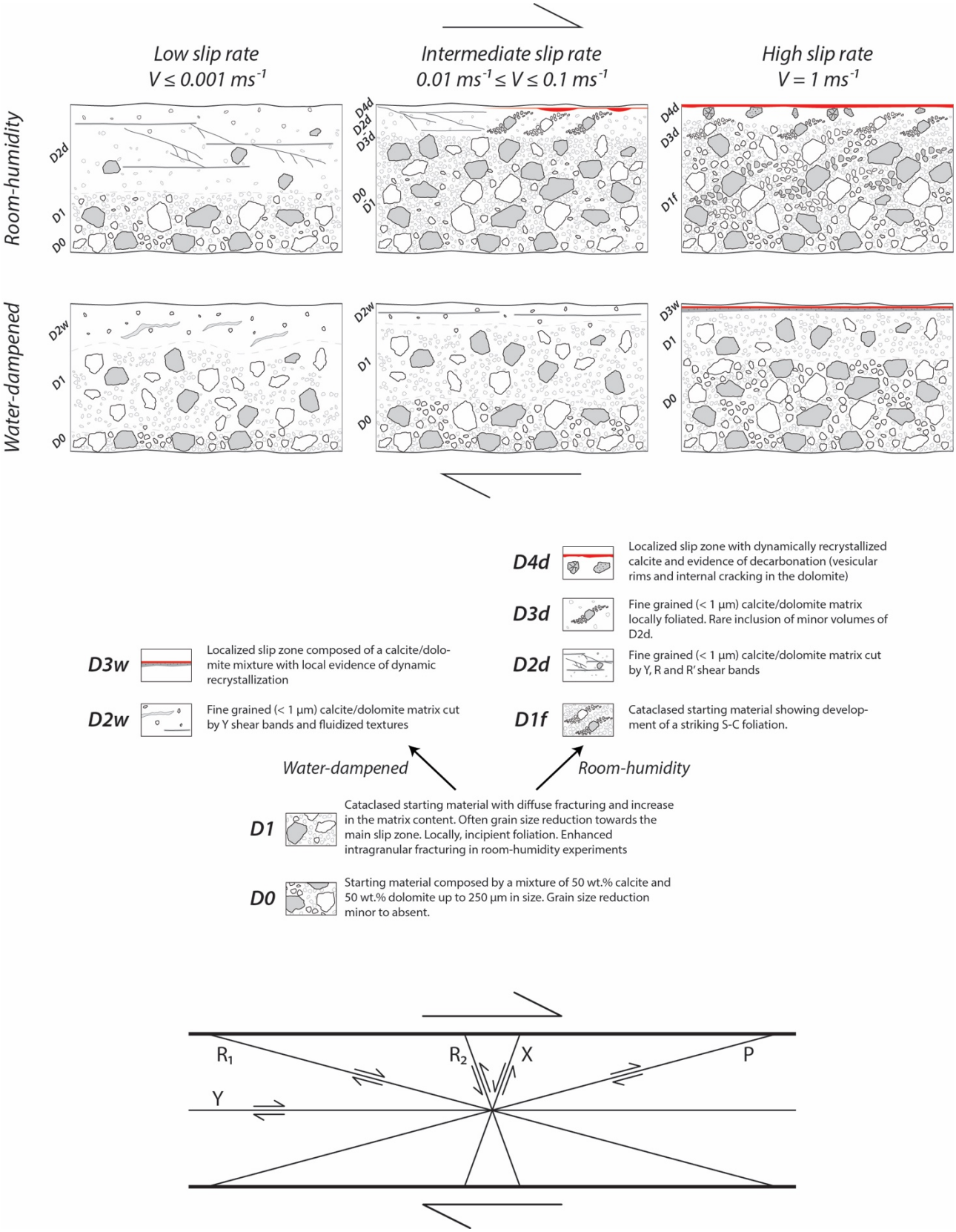


Fig. 9. Diagram of microstructural evolution with slip rate and deformation condition. Major microstructural changes have been subdivided in domains (D) and drawn in function of slip rate and the presence of fluid water during deformation. Room-humidity experiments are characterized by a wider spectrum of microstructures that progressively evolve.

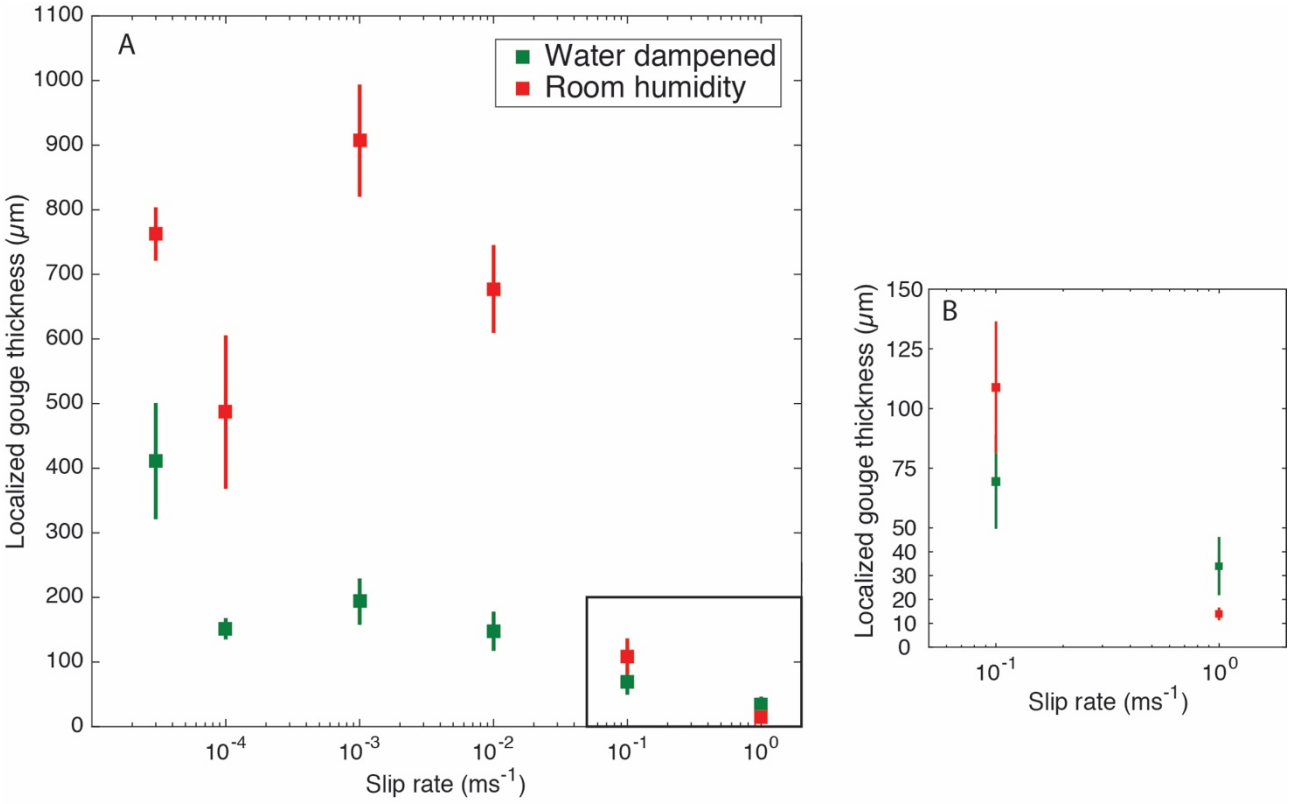


Fig. 10. Average slip zone thickness with slip rate and ambient conditions. a) The thickness of the localized gouge decreases almost linearly with log(V) in both room-humidity and water dampened experiments. For water-dampened experiments, the localized gouge thickness corresponds to the microstructural unit 3 (see description in section 3.4.1.). Apparently, the out-of-trend data regarding the slip zone thickness of experiments s1210, s1211 and s1215 (i.e., 30 μms^{-1} room-humidity, 0.0001 ms^{-1} room-humidity and 0.0001 ms^{-1} water-dampened, respectively) are due to partial sample loss during recovery at the end of the experiment. Under room-humidity conditions and $V \leq 0.1$ ms^{-1}, the localized gouge thickness is larger compared to the water-dampened case. For $V = 1$ ms^{-1}, the average thickness of the gouge layer is slightly smaller in the room humidity experiment due to the more efficient strain localization process than in water dampened conditions. b) Magnification of inset in a) for localized gouge thickness at slip rates $V \geq 0.1$ ms^{-1}.

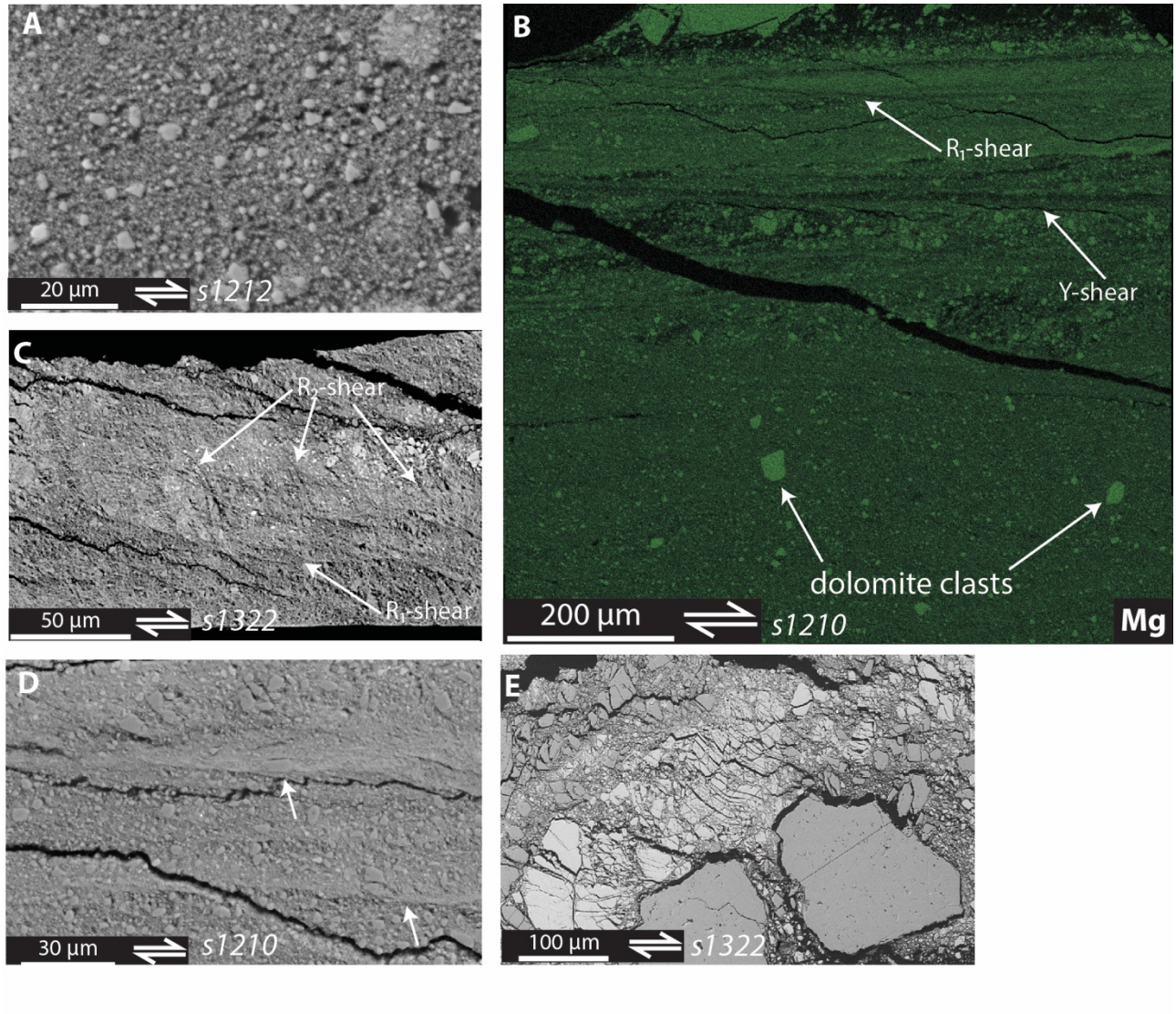


Fig. 11. Microstructures of room-humidity experiments in the low velocity regime ($V \leq 0.001$ ms^{-1}). a) The matrix in the slip zone consisted of a fine-grained (< 1 µm) mixture of calcite and dolomite with surviving sub-rounded dolomite clasts up to few tens of micrometers in size. b) The fine-grained slip zone is cut by Y-, R- and R'-shear bands crosscutting each other. c) Detail on R-shears cutting R'-shears. d) Asymmetric grain size grading along lighter R-shear bands, probably indicating an higher calcite content or reduced micro-porosity. e) The underlying gouge shows pervasive fracturing, typically exploiting crystallographic anisotropies (e.g., cleavage planes in calcite).

Fig. 12. (next page) Microstructures of water-dampened experiments in the low velocity regime ($V \leq 0.001$ ms^{-1}). a) Microstructural domain D0. b) Microstructural domain D1. c) Microstructural domain D2w. d) Y-shears cutting the microstructural domain D2w. e) and g) show the progressive thickening of domains D1 and D2w at the expenses of D0, with displacement after 0.05 m (e) and 0.4 m (g). f) and h) are cartoons of e) and g), respectively. Dark gray = microstructural domain D0; gray = microstructural domain D1; light gray = microstructural domain D2w.

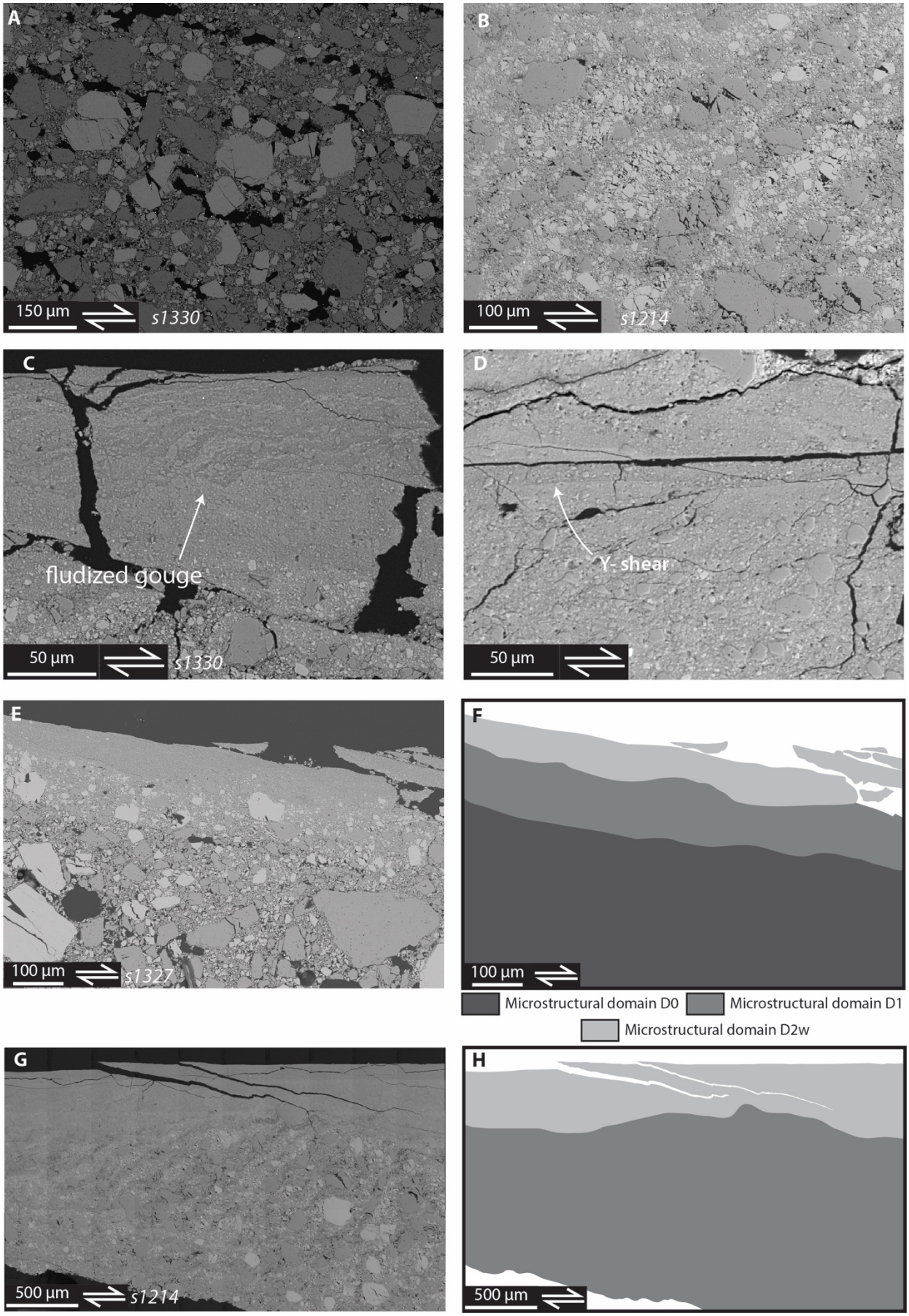


Fig. 12. See previous page for caption.

3.5.1. Microstructures produced at low velocity ($V \leq 0.001$ ms^{-1})

Room-humidity experiments

Room-humidity experiments were characterized by the formation of a 750-1000 μm thick (Fig. 10) slip zone (D2d) made of fine-grained matrix (grain size ca. 1 μm) cut by sub-parallel 10-30 μm thick Y, R_1 and R_2 type shear bands (using the terminology of Logan et al., 1979; Figs. 10 and 11). Each individual shear band includes a very fine grained matrix (grain size < 1 μm) of calcite and dolomite (Fig 11a), commonly too fine grained to be resolved at the SEM, embedding a few grains of sub-rounded dolomite up to few tens of micrometers in size (Fig. 11a-b). Multiple shear bands contribute to a boundary-parallel foliation (Fig. 11b-c). The shear bands were typically slightly brighter at the SEM, probably implying a higher abundance of calcite grains and perhaps reduced porosity (Fig. 11d). Given the same normal stress, slip rate and ambient conditions, experiments performed with increasing displacement (i.e., s1322 and s1210, see Table 1) suggest that calcite grains required less slip than dolomite ones to decrease their grain size (see less presence of surviving calcite grains in respect to dolomite ones in Fig. 11b-d and Appendix B; Smith et al., 2017). The transition to the underlying highly fractured gouge (D1) was sharp (Fig. 9). In domain D1, calcite commonly exhibited pervasive cleavage-controlled fracturing (Fig. 11e).

Water-dampened experiments

In water-dampened conditions, the area furthest from the slip zone was composed of unaffected starting material (D0; Fig. 12a). Most the gouge was composed of domain D1 in which the overall grain size decreased and the matrix content increased compared to the starting materials. In experiment s1214 at 30 μms^{-1} this domain also contained a foliation defined by compositional banding Fig. 12b). Both calcite and dolomite clasts in D1 are angular to sub-angular. A few intensely fractured large clasts (~ 100 μm in size) of calcite were found (Fig. 12b). The boundary between D0 and D1 was gradational and not always distinct. The thickness of D1 decreased with increasing slip rate (from 1500 μm thick at 30 μms^{-1} to 150 μm thick at 1 ms^{-1}). The main slip zone (D2w) consisted of an ultrafine matrix (grain size < 1 μm) composed of a mixture of calcite and dolomite with a few well-rounded dolomite grains up to 20-30 μm in size (Fig. 12c). This domain typically exhibited fluidized structures and the border with the underlying D1 domain was well-defined and irregular (Fig. 12c). The matrix was cut by discrete slip surfaces oriented parallel

to the boundaries of the gouge (Fig. 12d). The thickness of D2w decreased linearly with slip rate from ~410 μm thick at 30 μms^{-1} to ~200 μm thick at 0.001 ms^{-1} (Fig. 10).

Experiments performed at 30 μms^{-1} and increasing displacement (s1327, s1329, s1328, s1330-s1214 with displacement of 0.05 - 0.1 - 0.2 - 0.4 m, respectively) showed that the three microstructural domains develop after <5 cm of slip (Fig. 12e-f). As slip increased, D1 and D2w progressively became thicker at the expense of D0 (Fig. 12e-h).

3.5.2. Microstructures produced in the intermediate velocity regime (V = 0.01-0.1 ms^{-1})

Room-humidity experiments

At room humidity and a slip rate of 0.01 ms^{-1} the gouge showed distributed deformation in an ultrafine-grained (grain size < 1 μm) slip zone composed of calcite and dolomite (D2d; Fig. 13a) containing sub-rounded dolomite grains up to 20 μm in size. D2d was ~700 μm thick (Fig. 10) and cut by Y- and R_1-shear bands, with R_2-shear bands being less common than in the low velocity experiments (Fig. 13b). At this slip rate (0.01 ms^{-1}), D1 had the highest intensity of cataclasis of all the deformation conditions explored, with widespread intragranular fracturing dominated by clast impingement and fracturing along cleavage planes (Fig. 13c). At a slip rate of 0.1 ms^{-1}, the gouge showed the transition from D0-D1, to D3d showing the development of a subtle foliation, to a well localized slip zone with a thickness of ~110 μm (D4d; Fig. 9). The foliation consisted of an alternation of calcite and dolomite domains inclined at about 25-30° from the PSS and derived from the disaggregation and shearing of calcite and dolomite grains (Fig. 13d). The transition from D0-D1 to D3d was gradational and characterized by a decrease in the mean grain size. Up to 100 μm from the PSS, the slip zone consisted of sub-angular dolomite clasts up to 5-10 μm in size embedded in a fine-grained homogeneous matrix (grain size < 1 μm) composed of both calcite and dolomite (Fig. 13e). Locally, the PSS cuts discontinuous and lens-shaped patches, up to 15-20 μm thick, of calcite micro-aggregates with irregular borders (Fig. 13f). These patches had little to no porosity and resemble those documented by Smith et al. (2013) in calcite gouges and interpreted as evidence of incipient localization and dynamic recrystallization during seismic slip ($V \geq 0.01$ ms^{-1}).

Water-dampened experiments

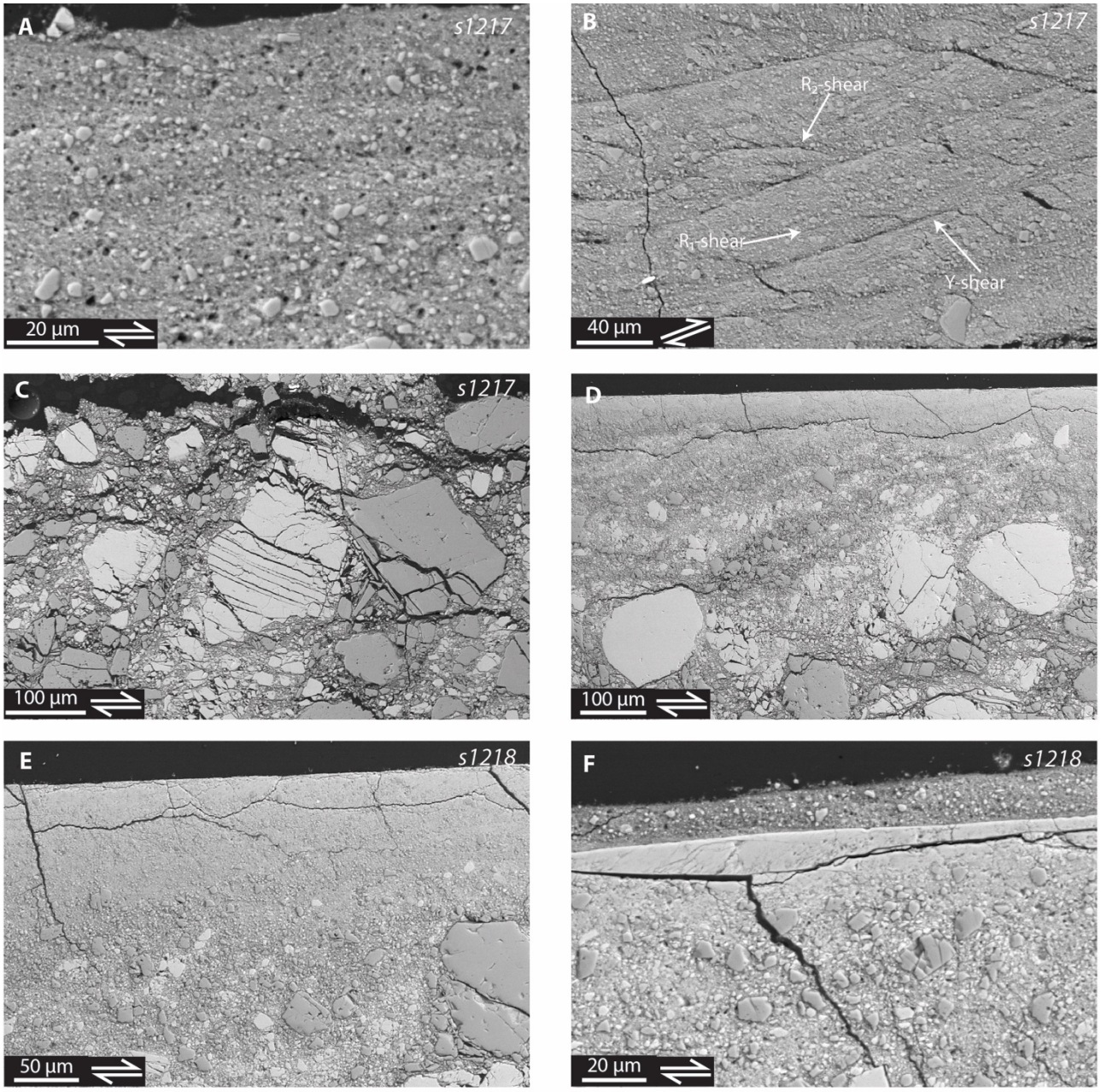


Fig. 13. Microstructures of room-humidity experiments in the intermediate velocity regime (V = 0.01-0.1 ms^{-1}). a) Fine-grained matrix, b) Y-, R- and R'-shear bands cutting the slip zone and c) fracturing in the underlying gouge for slip rates of 0.01 ms^{-1}. d) Development of a slight foliation in a highly comminuted layer beneath the PSS. e) The PSZ is characterized by a very fine-grained matrix (< 1 µm) and sub-angular dolomite clasts up to 10 µm in size. f) Decarbonation patches of dynamically recrystallized calcite line the PSS.

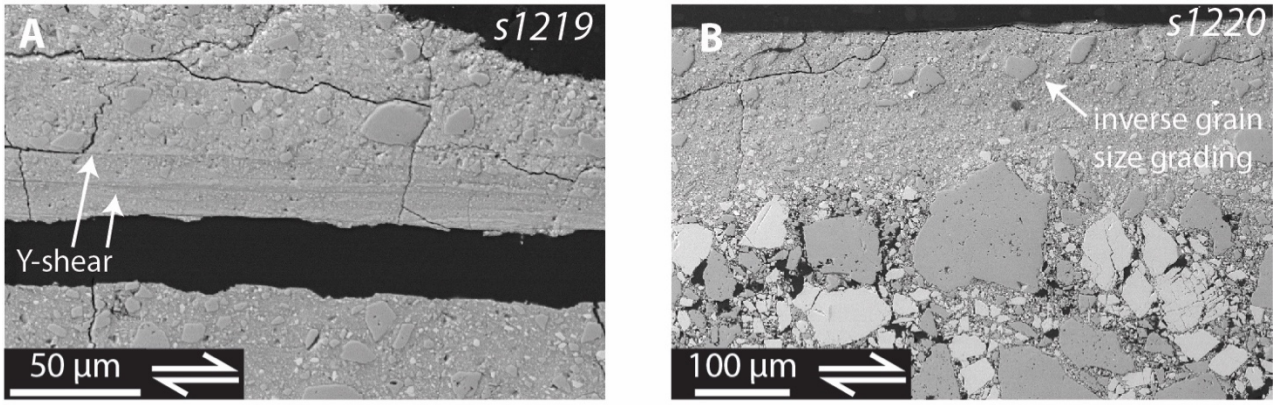


Fig. 14. Microstructures of water-dampened experiments in the intermediate velocity regime (V = 0.01-0.1 ms^{-1}). a) The microstructural unit 3 is typically cut by Y-shears. b) At V = 0.1 ms^{-1} the slip zone shows inverse grain size grading, resembling the Brazil nut effect.

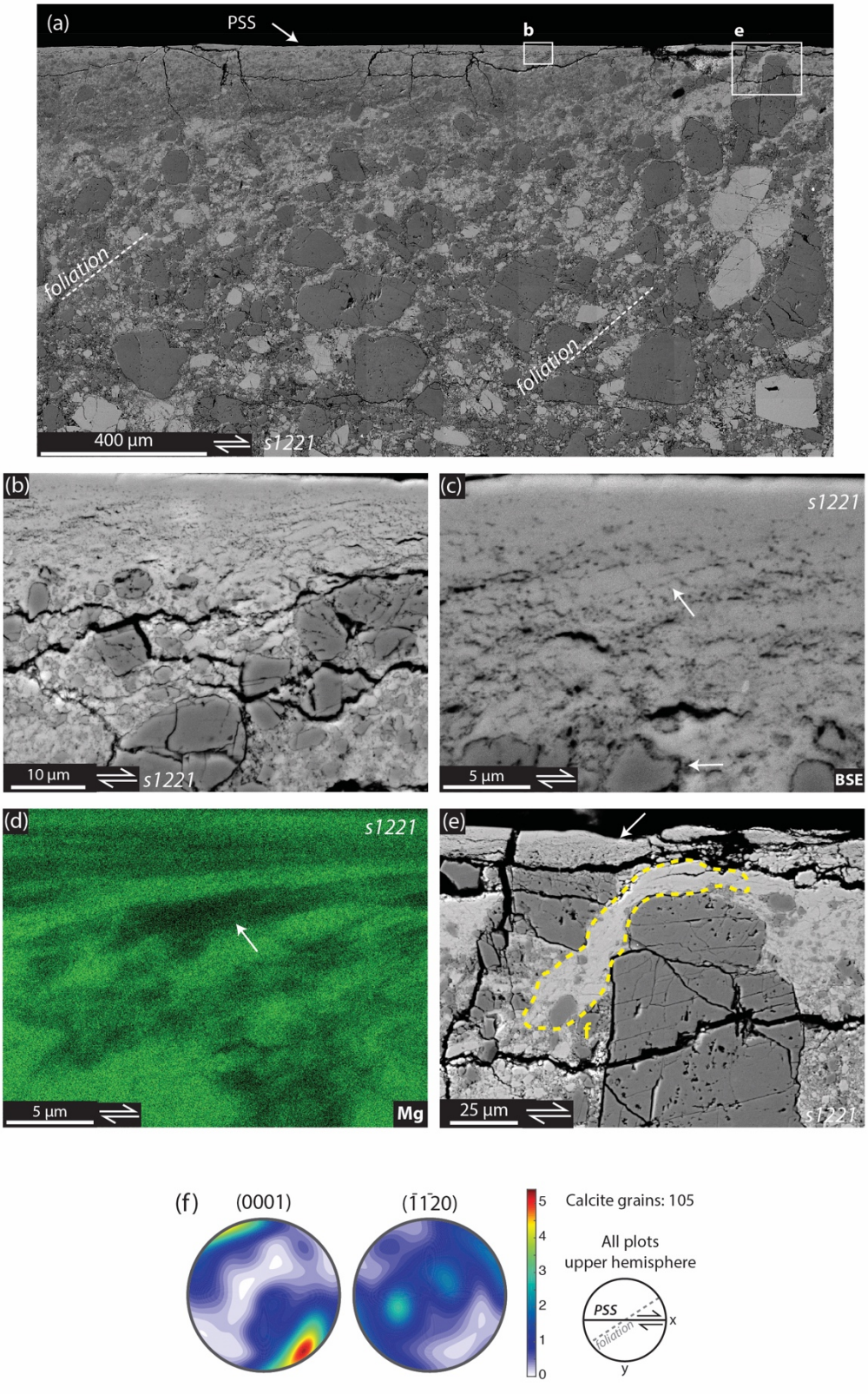


Fig. 15. Continues next page.

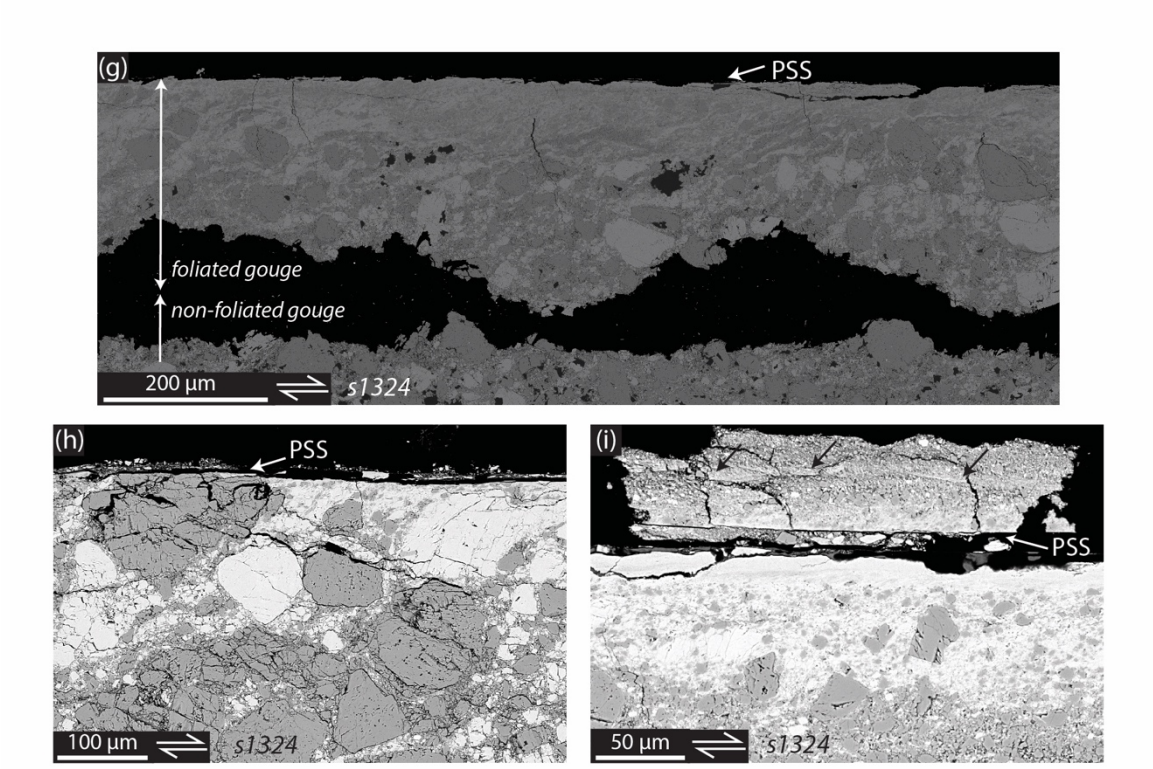


Fig. 15. (see previous page for a-f) Microstructures of room-humidity experiments in the high velocity regime (V = 1 ms^{-1}). a) The gouge show the development of a striking foliation consisting in alternation of calcite- and dolomite-rich domains. Foliation is typically antithetically inclined ~ 40° from the PSS and becomes subparallel to gouge boundaries when approaching the PSS. Larger dolomite (and when present calcite) clasts have tails of fine-grained material, resembling mantled porphyroclasts in mylonites. b) Dolomite clasts beneath the PSS are typically characterized by internal small holes and vesicular rims interpreted as due to degassing during dolomite decarbonation reactions. c) The PSS is characterized by banding of ultra-fine (<< 1 µm) porous material made of dolomite and its decarbonation products, alternated with calcite ribbons showing a shape preferred orientation up to 10 µm in size. d) EDS map of c) showing chemical banding inside the decarbonated volume. e) The PSS is characterized by a 15 µm thick decarbonated volume undergoing dynamic recrystallization. Dynamically recrystallized calcite exhibiting development of a crystallographic preferred orientation (CPO) can be seen up to ~ 70 µm from the PSS (yellow-contoured area). f) Orientation data for calcite in area highlighted in e). Calcite shows the development of a clear CPO with the c-axes oriented roughly sub-parallel to the instantaneous shortening direction. g) At higher normal loads (26 MPa) the thickness of the foliated gouge decreases to ~ 400 µm. h) The PSS truncates sharply dolomite clasts up to 150 µm in size, similar to those observed by Fondriest et al., 2013. i) The PSS is composed by a calcite-rich layer with negligible porosity. Slip surfaces interpreted as older localization features are locally observed.

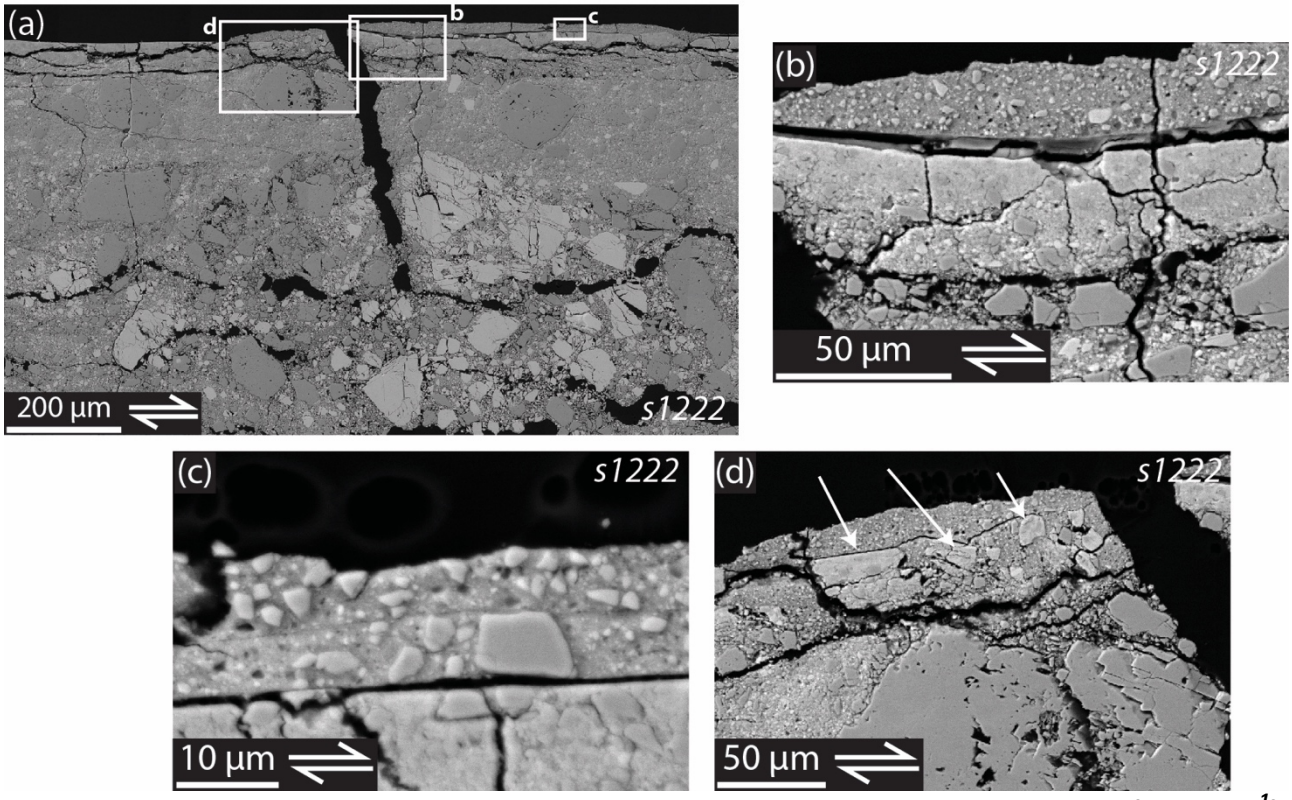


Fig. 16. Microstructures of water-dampened experiments in the high velocity regime (*V = 1 ms*$^{-1}$). a) At 1 ms^{-1} the development of a PSS is observed within the microstructural domain D2w. The gouge is mainly composed by microstructural domain D0, with D1 being ~ 400 µm thick. b) One side of the PSS consists in lens-shaped calcite-rich domains showing little to negligible porosity. c) The other side of the PSS is characterized by a very fine grained matrix (<< 1 µm) cut by discrete slip surfaces parallel to the PSS. d) Fragments of the PSS are locally found reworked in the PSZ.

In water-dampened conditions in the intermediate velocity regime, the deformed gouge exhibited similar microstructures (Fig. 14a) to those in the low velocity regime (Fig 12). As slip rate increased from 0.01 to 0.1 ms^{-1}, strain appears to become more localized, resulting in a progressive decrease in the thickness of domains D1 and D2w, with D2w becoming 70 μm thick at a slip rate of 0.1 ms^{-1}. At a slip rate of 0.1 ms^{-1} domain D2w was characterized by inverse grain-size grading (Fig. 14b), characterized by an abundance of relatively large and angular dolomite particles immediately adjacent to the PSS and an absence of such particles in the distal slip zone. These microstructures resembles the Brazil nut effect, a phenomenon observed when a homogeneously distributed mixture of large and small particles is vertically shaken in a container, such that large particles migrate towards the top (Ciamarra et al., 2006). Similar microstructures were observed by Boullier et al. (2009) in the principal slip zone of the 1999 Chi-Chi earthquake and by Boulton et al. (2017) in rotary-shear friction experiments on drill cuts from the Alpine Fault (New Zealand).

3.5.3. Microstructures produced in the high velocity regime (V = 1 ms^{-1})

Room-humidity experiments

At room-humidity and a normal stress of 17.4 MPa, the gouge developed a well-defined foliation consisting of alternating calcite- and dolomite-rich domains dipping at ~40° to the principal slip surface (microstructural domain D1f; Fig. 15a). The foliation rotated progressively approaching the PSS. Large remnant grains (up to 200 μm in size) in the gouge were often rimmed by tails of fine grained material (grain size < 10 μm), likely derived from the disaggregation of surrounding grains, resembling mantled porphyroclasts in mylonites (e.g., Snoke et al., 1998; Trouw et al., 2009). At < 400 μm from the principal slip surface, the mean grain size decreased, with very few surviving large grains (up to ~ 100 μm) and an overall high degree of mixing between calcite and dolomite (D3d; Fig. 9). The PSZ (D4d; Fig. 9) consisted of a 15-20 μm thick and fine-grained layer (<< 1 μm in size) composed of calcite, Mg-calcite and periclase grains (EDS and XRPD analysis) (Fig. 15b-d). Calcite (Mg-poor areas in EDS map; Fig 15d) had larger grain size (up to 5 μm), formed elongated aggregates with shape preferred orientation with the long axis sub-parallel to the foliation and negligible porosity (Fig. 15c). Instead, Mg-calcite rich domains had higher porosity and finer grain size (Fig. 15c). Electron backscattered diffraction (EBSD) analysis on the calcite domains showed the development of a distinct crystallographic preferred orientation (CPO) with the c-axes inclined perpendicular to the instantaneous shortening direction (Fig. 15e-f; see also Smith et al., 2013).

Adjacent to the PSZ, a ~30-40 μm thick layer included dolomite grains with diffuse internal cracking, clusters of small holes and vesicular rims interpreted as due to degassing during dolomite decarbonation reaction (Fig. 15b-c; Mitchell et al., 2015). Locally, trails of small well-rounded dolomite grains, less than 2 μm in size, were observed to depart from the parent grain and included in the porous-rich bands (Fig. 15b-c). At higher normal stress (experiment s1324 performed at 26 MPa) but identical slip rate of 1 ms^{-1}, D1f was found only in the first 400 μm from the PSS (Fig. 15g). Large clasts of dolomite (up to 150 μm in size) were sharply cut by the PSS (Fig. 15h) while the slip zone was composed, as in the lower normal stress experiments, by a calcite-rich recrystallized layer, with reduced porosity and few micrometer in size and well-rounded "survivor" clasts of dolomite (Fig. 15i).

Water-dampened experiments

Under water-dampened conditions, the gouge had an intensely comminuted ~300-400 μm thick domain D1 bordering the principal slip zone (Fig. 16a). In the matrix (grain size < 1 μm), mixing between calcite and dolomite occurred and surviving dolomite clasts were as large as 100 μm (Fig. 16a). The border of D1 with the underlying D0 was sharp, with an irregular geometry and characterized by a net increase in the mean grain size, especially within the matrix (Fig. 16a). The PSZ was sharply cut by the PSS and exhibits remarkable differences between the two sliding blocks (Fig. 16b-c). On one side, the PSZ consisted of lens-shaped patches of a calcite-rich and fine grained (grain size ~ 1 μm) layer ~ 30 μm thick with negligible porosity (D3w; Fig. 16b). Small dolomite clasts up < 10 μm in size were typically well-rounded and cut by the principal slip surface. Locally, these well-compacted calcite-rich patches were found broken and reworked in the underlying D1 (Fig. 16d). On the other side of the principal slip surface, the principal slip zone was composed of an ultrafine matrix (grain size << 1 μm) of calcite and dolomite with surviving dolomite clasts up to 5 μm in size (Fig. 16c), resembling D2w. Small discrete slip surfaces cut this layer (Fig. 16c). Here, the porosity was mainly derived from the removal of small grains during sample preparation (i.e., pores have an angular shape). However, some of them might be related to CO_2 emission during deformation.

3.5.4. Microstructures produced in slide-hold-slide experiments

3.5.4.1. Velocity step from 30 μms^{-1} to 1 ms^{-1}

Room-humidity experiments

Under room-humidity conditions, microstructures characteristic of both slip velocities are well preserved at the end of the slide-hold-slide experiments. Towards the PSS, the sample was composed of an undeformed gouge resembling the starting material (D0; Fig. 17a), grading into a gouge layer with a well-developed foliation (D1f) containing calcite and dolomite clasts rimmed by tails of fine-grained material (Fig. 17a). Here, D1f was typically 400-500 μm thick and the foliation was orientated at ~ 30° from the PSS, becoming progressively parallel to the Y- and R_1-shear bands that characterize the transition to the adjacent ultrafine (grain size << 1 μm) ~ 500 μm thick foliated gouge (D2d). Locally, the foliation wrapped around large (up to 70-80 μm) dolomite grains and exhibited an anastomosing style (Fig. 17b). The transition to the PSZ (D4d) was gradational and characterized by an increase in the calcite content, with dolomite grains being smaller (< 10 μm), well rounded and wrapped by trails of smaller grains oriented consistently with the sense of shear (Fig. 17c). The PSZ itself consisted of a continuous 15 μm thick layer of fine-grained calcite (< 1 μm) with little porosity (Fig. 17d). Although some calcite grains can be identified under high-resolution SEM investigation, there was no evident development of a grain shape preferred orientation in the PSZ.

Water-dampened experiments

In water-dampened conditions, the gouge preserved the typical microstructure of the slow slip pulse (i.e., 30 μms^{-1}). The PSZ was composed of a ~100 μm thick D2w, which was cut by Y- and R_1-oriented discrete slip surfaces (Fig. 17e). The PSS cut sharply through D2w, although without showing any evidence of strain localization as in s1222 (i.e., single slide experiment performed at 1 ms^{-1}, see Fig. 16).

3.5.4.2. Velocity step from 1 ms^{-1} to 30 μms^{-1}

Room-humidity experiments

Under room-humidity conditions, the gouge layer was characterized by diffuse fracturing with incipient foliation development and P- and Y-shear bands cutting through the gouge volume (D2d; Fig. 18a). The microstructure of the PSZ records both slip events. The localized slip zone active during the fast slip event (i.e., 1 ms^{-1}) was preserved near the “teeth” of the sample holder and consisted of sharply truncated dolomite clasts up to 10 μm in size embedded in an ultrafine (grain

size << 1 μm) calcite matrix (Fig. 18b). Locally, the PSS faded into multiple Y- and R_1- shear bands (Fig. 18b). The rest of the PSZ is made of an ultrafine mixture of calcite and dolomite cut by multiple Y-, R_1- and R_2-shear bands. Clasts are sub-rounded and composed of dolomite grains of reworked older slip zones (Fig. 18c).

Water-dampened experiments

Under water-dampened conditions (s1226), the microstructures resemble those found in experiment s1222 (i.e., 1 ms^{-1} and water-dampened conditions). Here, the PSZ (D3w) was 30-40 μm thick and characterized by a continuous layer with negligible porosity, composed of both calcite and dolomite (Fig. 18d). Locally, patches with a higher content in calcite were present. Small clasts (up to 5 μm) of reworked older slip surfaces were also observed (Fig. 18e). The PSS was cut by equally spaced injection veins (Fig. 18f). These injection veins probably developed during the second slip pulse (i.e., 0.1 m at 30 μms^{-1}) given their well-defined geometry and spacing. Another possibility on their origin is due to sample preparation.

4. Discussion

4.1. Strain localization and dynamic weakening mechanisms in calcite-dolomite mixtures

The microstructures and mechanical behavior of calcite-dolomite gouge mixtures show significant differences between the room-humidity and water-dampened cases (Figs. 9 to 18). Under room-humidity conditions, the slip zone was composed of a fine-grained (i.e., < 1 μm) mixture of calcite and dolomite with sharp boundaries to the underlying fractured gouge (so called D1). For slip rates between 30 μms^{-1} and 0.01 ms^{-1} dilation was commonly observed during the slip-strengthening phase prior to the achievement of steady state friction (Fig. 4b). This was associated with the development of R_2-shear bands in the slip zone (Figs. 9-11). These observations have previously been explained as due to the development and broadening of a distributed zone of deformation during strain-hardening (e.g., Marone et al., 1990; Beeler et al., 1996; Rathbun and Marone, 2010). In addition, Smith et al. (2015), observed a short-lived transitional dilatancy phase during the strengthening phase prior the onset of dynamic weakening in high-velocity (V = 1 ms^{-1}) rotary-shear experiments. Our microstructural and experimental

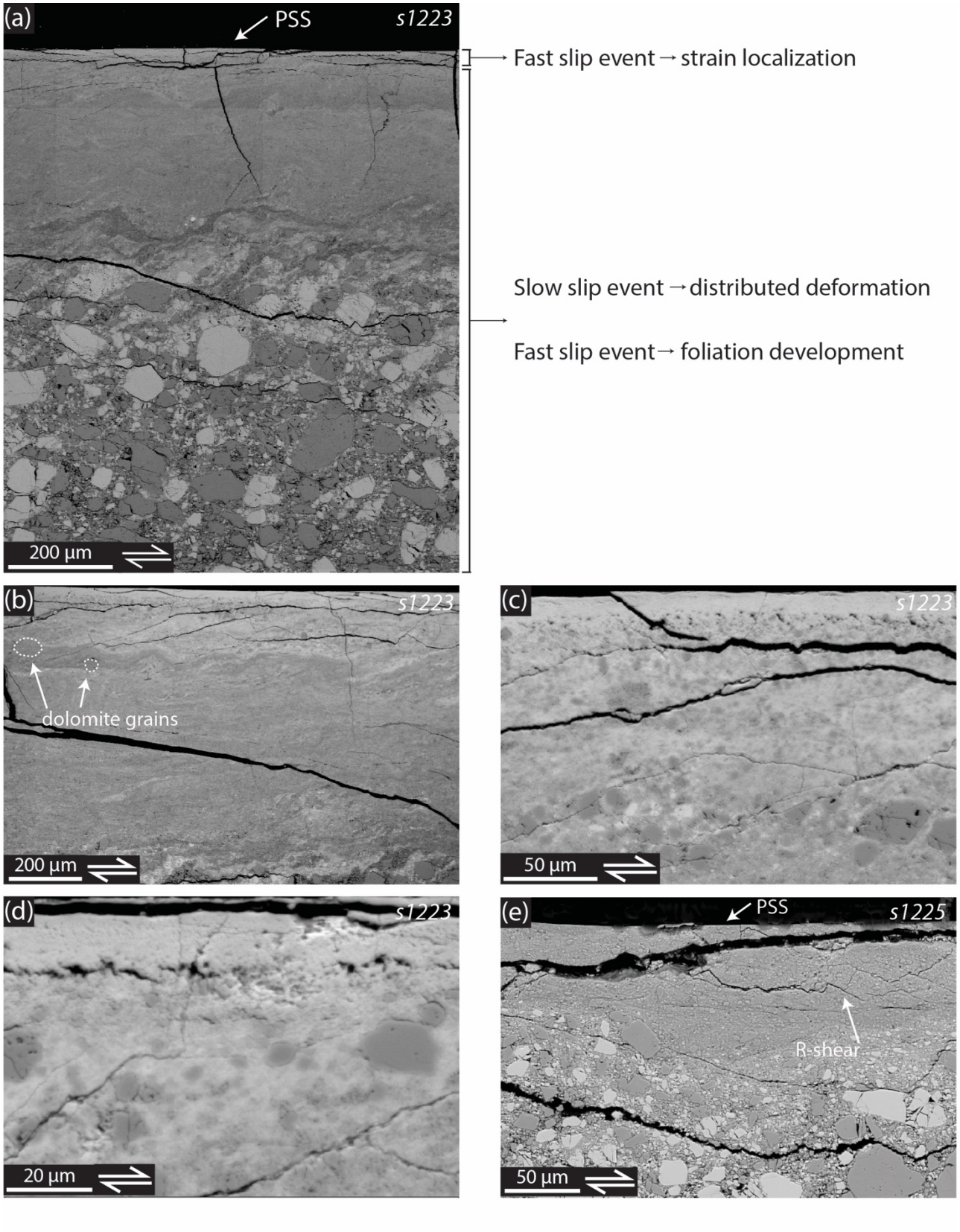


Fig. 17. See next page for caption.

Fig. 17. (previous page) Microstructures produced in the 30 µms^{-1} to 1 ms^{-1} velocity step experiments. a) to d) room humidity conditions; e) water-dampened conditions. a) Characteristic microstructures of both slip events are well preserved. The slow slip event is recorded by the development of a ~500 µm thick ultra-fine layer, while the fast slip event by the development of a foliation in the lowermost part of the gouge, and strain localization in the PSS with evidence of decarbonation and dynamic recrystallization. b) In the ~500 µm thick ultra-fine layer, surviving dolomite clasts up to 50 µm in size typically act as centers for the development of a S-C' foliation. c) Moving towards the PSS, the calcite content increases considerably, with dolomite clasts typically having a well-rounded shape and shady borders. d) The PSS consists of a 10 µm thick calcite-rich layer, with very small grain size (< 1 µm) and little porosity. e) In water-dampened conditions, microstructural unit 3 is ~100 µm thick and is cut by Y- and R-shear bands.

Figure. 18. (next page) Microstructures produced in the 1 ms^{-1} to 30 µms^{-1} velocity step experiments. a) to c) s1224, room humidity conditions; d) to f) s1226, water-dampened conditions. a) The underlying gouge shows intense fracturing and development of P- and R- shear bands. b) Locally, the PSS of the fast slip event is still preserved. The underlying slip zone of the slow event consists of a fine-grained gouge (< 1 µm) cut by multiple Y- and R-shear bands. c) Fragments of the fast slip PSS are found reworked within the gouge. d) The PSS is composed of a mixture of calcite and dolomite with very little porosity. The thickness of the localized layer is about 30-40 µm. e) Reworked clasts up to 5 µm in size consisting of older slip surfaces are typically found near the PSS. f) Injection veins of gouge cut the PSS at high angle and evenly distances. Such veins are interpreted as due to cracking of the PSS during cooling at the end of the first slip event and subsequent injection during the slow slip event.

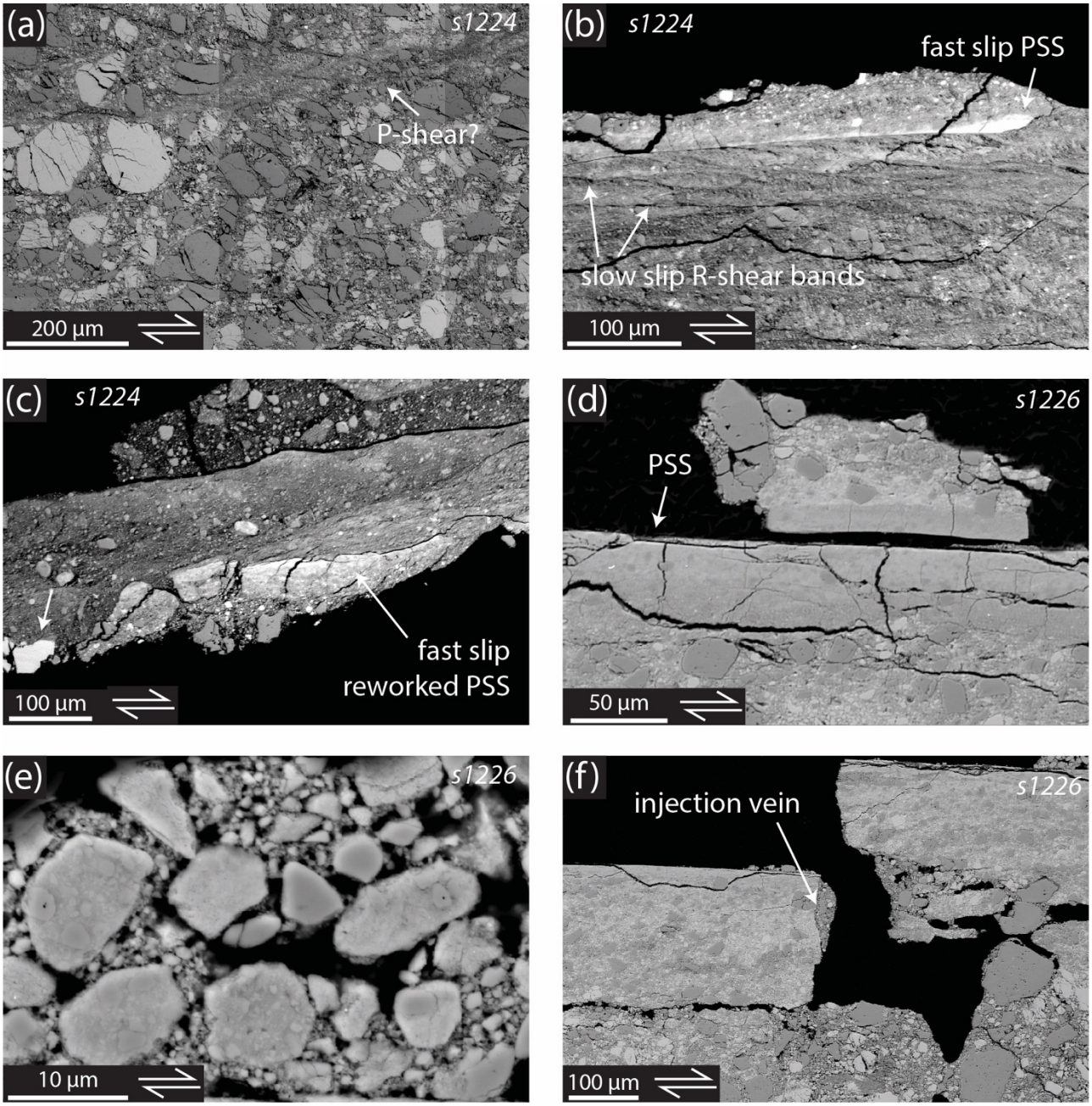


Fig. 18. See previous page for caption.

observations seem to validate this interpretation (Figs. 11c and 13b). The disappearance of a prolonged dilatancy phase is concomitant with the transition for $V \geq 0.1$ ms^{-1} to a slip-weakening evolution of the friction coefficient and the development of a PSZ that likely accommodated most of the strain (Fig. 15; Han et al., 2007a; Fondriest et al., 2013; Smith et al., 2013,2015; Green et al., 2015; De Paola et al., 2015; Mitchell et al., 2015; Rempe et al., 2017). Such strain localization is accompanied by detection of CO_2 emissions (Fig. 7) and the presence of recrystallized calcite grains on the PSZ (Figs. 13,15,17; Smith et al., 2013).

In water-dampened conditions, the slip zone was composed of well-rounded dolomite clasts embedded in a very fine-grained (i.e., << 1 μm) matrix of calcite and dolomite (microstructural domain D2w). Evidence for layer fluidization is observed within domain D2w (Fig. 12c). Moreover, the boundary with the underlying domain (D1) has an irregular geometry with characteristic wavelength, suggesting a viscosity difference between the fluidized D2w domain and the cataclastic D1 domain (Brodsky et al., 2009). Fluidized gouges and cataclasites have been documented in active seismic faults (e.g., Monzawa and Otsuki, 2003; Rowe et al., 2005; Boullier et al., 2009; Brodsky et al., 2009; Boulton et al., 2017). Different mechanisms have been proposed to account for fluidization of granular materials, including (i) frictional heating and thermal pressurization (Boullier et al., 2009), (ii) dilation limiting grain-grain contacts (Borradaile, 1981, Monzawa and Otsuki, 2003) or (iii) interconnection of phyllosilicate minerals providing mechanical weaknesses (Ujiie et al., 2011; Bullock et al., 2015). At the slip velocity at which we documented the occurrence of fluidization (i.e., 30 μms^{-1}), frictional heating and thermal pressurization is unlikely to play a major role. Water-dampened experiments were characterized by continuous compaction throughout the entire run. A possibility is that the absence of transient dilation might be an effect of the experimental configuration, with water partly extruded from the gouge holder. Finally, no phyllosilicates were present in the starting material. In the case of our experiments, fluidization might be caused by the presence of patches with slightly different composition (e.g., higher content in calcite) within the ultrafine D2w. Such patches would be characterized by different properties from the surrounding matrix (e.g., density) eventually leading to fluidization of such layers.

Although there is a general trend in the decreasing thickness of the slip zone with increasing slip rate, water-dampened experiments are characterized by a higher degree of localization and smaller grain size compared to room-humidity experiments (Fig. 10). These differences result in a lower steady state friction coefficient observed for $V < 1$ ms^{-1} and can be explained by a lower

surface fracture energy for calcite in the presence of water, resulting in faster crack propagation and comminution (Røyne et al., 2011).

At high slip rates ($V \geq 0.1$ ms^{-1}), dynamic weakening in carbonate gouges under room-humidity conditions has been explained by local flash heating within incipient slip surfaces (Goldsby and Tullis, 2011; Tisato et al., 2012), which eventually coalesce into a localized and through-going shear band (Smith et al., 2015). Further slip will increase the bulk temperature due to frictional heating in the PSZ, resulting in gouge recrystallization (Smith et al., 2015) and strain accommodation by diffusion-assisted grain boundary sliding (Green et al., 2015; De Paola et al., 2015). Temperature rise calculations show that in the case of limited dynamic weakening (i.e., experiment s1218 at V = 0.1 ms^{-1}; Fig. 3c), the average temperature (T ~ 460°C) in the PSZ remains below that required for decarbonation for dolomite (~550 °C; Samtani et al., 2002). However, gas emission data show some CO_2 production during shearing (Fig. 7a) and microstructural observations indicate that, at least locally, temperatures were high enough for dolomite to decarbonate and calcite to recrystallize. This discrepancy between temperature estimates and microstructural observation is clearer when considering the experiment performed at 1 ms^{-1} under water-dampened conditions. Here, the calculated (and observed) temperature rise was ca. 200 °C. However, the PZS was characterized by the presence of micropores (some of them probably formed by the decarbonation reaction of dolomite) and dynamically recrystallized calcite. Moreover, production of CO_2 was observed, suggesting that, at least locally, temperatures of ~550 °C were achieved. Therefore, temperature rise calculation can be used as a lower bound to temperature achieved on the slip surface during deformation.

4.2. Coseismic foliations in calcite-dolomite gouges

Foliated gouges and cataclasites are common fault rocks in the brittle upper crust (Snoke et al., 1998). Typically, they are interpreted as forming due to a combination of cataclasis and dissolution-precipitation reactions during aseismic fault creep (e.g., Rutter et al., 1986; Chester and Chester, 1998; Lin, 2001; Collettini and Holdsworth, 2004; Jefferies et al., 2006; De Paola et al., 2008; Wallis et al., 2013). Experimental observations have also confirmed this hypothesis, where a well-defined foliation was formed as a result of dissolution-precipitation reactions accompanied by granular flow and frictional sliding at low slip rates ($V < 1$ μms^{-1}) (Bos et al., 2000; Niemeijer and

Spiers, 2006). Following the documentation of natural foliated fault rocks closely associated with possible evidence of seismic sliding (e.g., mirror-like slip surfaces with truncated clasts; e.g., Demurtas et al., 2016), Smith et al. (2017) investigated the possibility that some observed natural foliated fault rocks might have a coseismic origin. Rotary-shear experiments performed at V = 1.13 ms^{-1} on gouges with 50 wt.% calcite and 50 wt.% dolomite showed the development of a foliation defined by an organized banding of heavily fractured calcite and dolomite clasts (Smith et al., 2017). These foliations documented by Smith et al (2017) broadly correspond to the foliated microstructural domain D1f discussed here. Experiments performed at increasing displacement in Smith et al (2017) showed that such foliations form during the initial strengthening phase, during which distributed deformation in the bulk gouge causes grain pulverization and shearing. Once dynamic weakening occurs, strain progressively localizes into a single continuous slip zone. Once dynamic weakening is achieved, strain is mainly localized on the PSZ and the foliation in the bulk gouge does not show any further microstructural changes. Based on their observations, Smith et al. (2017) suggested that some natural foliated rocks characterized by compositional banding, grain size variations, and preferred particle or fracture alignments could form by distributed brittle flow as strain localizes during coseismic shearing, especially if such foliations are found in proximity to other evidence of coseismic slip (e.g. solidified frictional melts). However, their interpretation was based exclusively on experiments performed at seismic slip rates (i.e., V = 1.13 ms^{-1}) and under room-humidity conditions.

In the experiments presented here, we documented microstructural changes over a wider range of slip rates (i.e., from 30 μms^{-1} up to 1 ms^{-1}) and deformation conditions (i.e., room-humidity vs. water-dampened). The formation of a well-defined foliation throughout the bulk gouge was observed only in two cases: (1) at high slip rates (i.e., V = 1 ms^{-1}) under room-humidity conditions (in microstructural domain D1f), corresponding to the conditions imposed by Smith et al. (2017), and, (2) at low slip rates (i.e., V = 30 μms^{-1}) under water-dampened conditions (in microstructural domain D1). Local foliation development (microstructural domain D3d) was also observed in low velocity experiments in the room-humidity case (Fig. 13d), but was restricted to small areas at less than 400 µm from the PSS.

In case (1), the overall foliated microstructure is consistent with observation from Smith et al. (2017) (Fig. 15). However, in case (2) at 30 μms^{-1} in water-dampened conditions, significant microstructural differences in the geometry of the foliations were noted. Although the foliation

resulted from fracturing and shearing of calcite and dolomite clasts, individual calcite- and dolomite-rich domains are relatively continuous and characterized by straight boundaries (Fig. 12b). No development of peculiar microstructures such as tails around larger clasts observed in the gouges sheared at high velocity (compare microstructural domain D1 formed at low slip rate and wet condition, with microstructural domain D1f formed at high slip rate and room humidity conditions). Moreover, the transition from D1 to the localized gouge (microstructural domain D2w) is not defined by a progressive decrease in the mean grain size and change in the foliation angle towards parallelism with the PSS, but by a sharp transition with wavy geometry with D2w (Fig. 12f).

One main problem that arises from the interpretation of the microstructures in the experiment at 30 μms^{-1} and water-dampened conditions is due to the sample assembly configuration. The sample holder used for these experiments does not seal the gouges perfectly, allowing small quantities of water (usually few drops) to be expelled during sample loading and shearing. Small misalignments of the sample holder could significantly enhance water and gouge loss during the experiment. For this reason, at very low velocity (i.e., 30 μms^{-1}) and moderate displacements (i.e., 0.4 m), the duration of the experiment (about four hours) might result in partial drying of the gouge. Therefore, the presence of "dry" patches could create instabilities within the gouge, promoting the development of the observed foliation within D1. Experiments s1214 and s1330 were performed under identical deformation conditions. While foliation in D1 is documented in sample s1214, it is absent in sample s1330. Although no significant water and material loss were observed in either of the two experiments, this microstructural difference seems to validate our hypothesis that drying out of the gouge sample may have occurred in the relatively long-duration experiments at 30 μms^{-1}. Further investigation under controlled pore fluid (drained and undrained) conditions will be necessary to understand the development of a foliation at low slip velocities.

Finally, our microstructural investigations across a wider range of slip rates and ambient conditions with respect to the work by Smith et al. (2017) seems to validate their initial hypothesis that well-defined foliations can form in mixed calcite-dolomite gouges at high slip-velocities (microstructural domain D1f). The slowest velocity investigated here (i.e., 30 μms^{-1}) is still too high

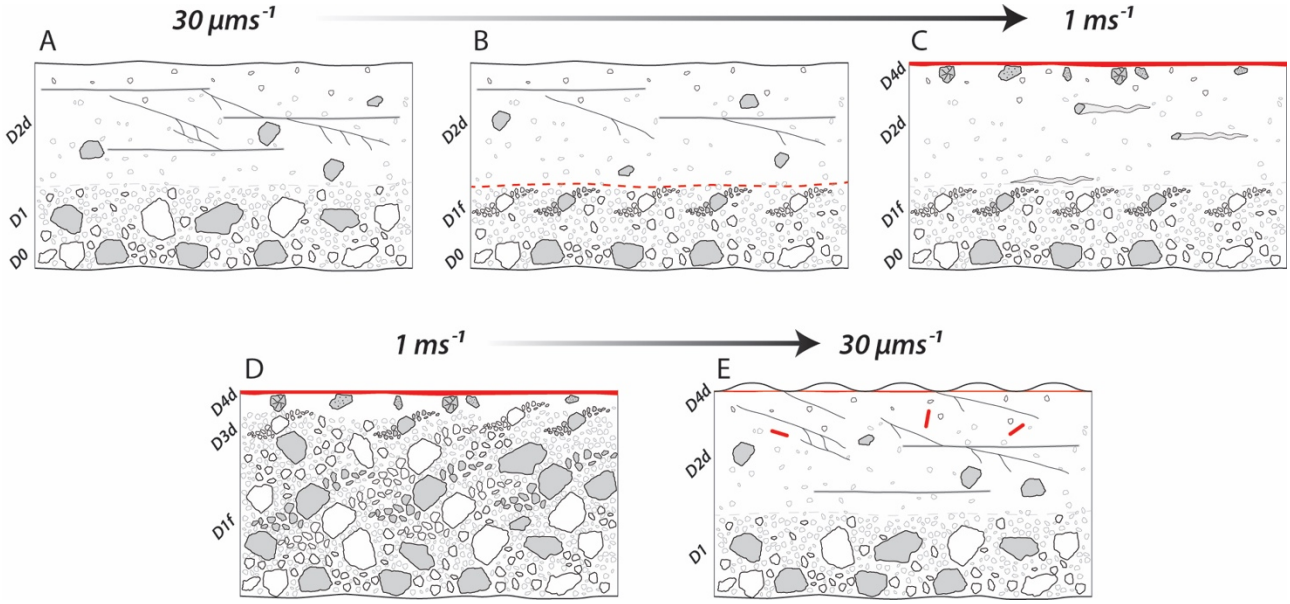


Figure. 19. Microstructure preservation during slide-hold-slide experiments in room-humidity conditions. a) – b) – c) Slow to high velocity step. The microstructure developed during the first slide event (a) is the same as the one produced during single slide experiments. When the slip rate is stepped up to 1 ms^{-1}, at first strain tends to localize at the interface between the microstructural domains D1 and D2d (b), which acts as a rheological boundary. During this phase, a foliation is developed in the lower part of the gouge. However, due to the sample holder and apparatus configuration, strain is forced to localize near the gouge holder teeth, resulting in the development of a PSS (D4d). d) – e) High to slow velocity step. During the fast slip event, a foliation in the gouge and a PSS are formed. During the successive slow slip event, the PSS is progressively dismembered and reworked in a thick slip zone (D2d). Locally, intact pieces of D4d are found preserved in between the gouge holder teeth. For a description of the microstructural domains, see legend in Fig. 9.

for pressure-solution to be efficient in calcite or dolomite (Aretusini pers. comm.). The activity of such deformation mechanisms might lead to similar foliations as those observed in the presence of phyllosilicates (e.g., Bos et al., 2000; Niemeijer and Spiers, 2006). Further experimental work is needed to constrain foliation development in carbonate gouges over a wider slip rate spectrum that covers the aseismic/creeping part of the seismic cycle.

4.3. Preservation potential of microstructures during overprinting slip events

During the seismic cycle a fault may experience episodes of slow, aseismic creep and faster, seismic slip, as well as a wide range of intermediate slip velocities (e.g., Edwards and Ratschbacher, 2005; Smeraglia et al., 2017b). Seismological, geodetic and theoretical investigations show that during the nucleation, propagation and arrest of an earthquake rupture, the slip rate at a point on a fault evolves continuously and non-linearly (e.g., Scholz, 2002; Heaton, 1990; Tinti et al., 2005). Most rotary-shear experiments to date have been performed by imposing constant slip rates between phases of acceleration and deceleration (e.g. trapezoid velocity functions: e.g., Han et al., 2010; Di Toro et al., 2011; Proctor et al., 2014; De Paola et al., 2015; Smith et al., 2015; Aretusini et al, 2017). Velocity-step experiments have allowed investigation of the mechanical response of a fault during sudden acceleration and/or deceleration (Sone and Shimamoto, 2009; Fukuyama and Mizoguchi, 2010; Chen et al., 2013; Ma et al., 2014; Proctor et al., 2014). However, these studies did not focus on the preservation of microstructures formed at different slip rates in the experiments (Sone and Shimamoto, 2009; Fukuyama and Mizoguchi, 2010; Ma et al., 2014; Proctor et al., 2014).

In the slide-hold-slide experiments presented here, the slip rate stepped from 30 μms^{-1} to 1 ms^{-1} or *vice-versa*, representing a magnitude change of ~ $3*10^4$. Since continuous slip during the slide-hold-slide was not possible, a preset hold time of 300 seconds was imposed. The friction evolution in the first slip pulse was consistent with single-slide experiments performed to larger total displacements (Fig. 3c-f). After the hold time, the peak friction coefficient showed a notable increase with respect to the single slide experiments. For experiments with velocity steps from low to high slip rate (i.e., 30 μms^{-1} to 1 ms^{-1}), such an increase in the peak friction can be explained through the initial tendency of localizing the coseismic strain along a rheological interface in the gouge, as the boundary between the microstructural domain D1 and D2w (Fig. 19b). However, due to the apparatus and sample holder configuration, strain was forced to localize adjacent to the

holder “teeth” on the stationary side (Fig. 19c; Rempe, 2015). This “forced” localization mechanism could in part explain the observed higher peak friction coefficient. Another, more intuitive, explanation can derive from the duration of the hold time and subsequent healing processes, consisting in a progressively more effective adhesion between the asperities within the gouge (Marone et al., 1998; Scholz, 2002). Microstructural evidence seems to validate this interpretation. In room-humidity conditions (experiment s1223), a well-developed foliation underlies a ~ 600 µm thick ultrafine layer that formed during the first slow slip velocity (Fig. 17a; Fig. 19b). However, strain is mainly localized within a c.15 µm thick PSS. The foliation in the gouge was absent in single slide experiments under the same deformation conditions. Therefore, it is likely to have formed concomitant to the short strengthening phase (Smith et al., 2017) during the high-velocity step, prior to strain localization on the PSS.

In the case of experiments with slip rate stepping from fast to slow (1 ms^{-1} to 30 μms^{-1}), the higher peak friction coefficient in room-humidity conditions can be intuitively explained by the initial tendency of reactivating the dynamically recrystallized slip surface developed during the first high slip-velocity event (Smith et al., 2015). However, such a mechanism in not efficient at slow slip rates and therefore the PSS is progressively dismembered and reworked within a distributely deformed slip zone (Fig. 18a-c; Fig. 19e).

4.4. Implication for natural faults in carbonates

A major difference is observed in the preservation of microstructural evidence of both slip events between room-humidity and water-dampened experiments. In the room-humidity case, characteristic microstructures of both slip events are typically preserved, thus allowing the “reconstruction” of a deformation history in the gouge (Fig. 19). In the water-dampened case, the first deformation event typically forms key microstructures in the gouge that are preserved and only slightly altered during further slip events. This could suggest that in natural faults, the overprinting of microstructures related to different slip events might be more likely in relatively dry conditions. However, a major limitation with this current interpretation is the fact that we performed only one velocity step, interpreted as one possible “seismic cycle”. In nature, large faults experience many sequences of alternating seismic and aseismic sliding. Further experimental work focused on the microstructural evolution of gouges during multiple velocity steps (i.e., seismic cycles) is needed.

Experiments show that in calcite-dolomite mixtures deformed at V < 1ms^{-1}, weakening is easier in the presence of water (i.e., lower peak and steady state friction coefficient). This is consistent with previous experimental observations on calcite gouges (Rempe et al., 2017) and solid rocks (Violay et al., 2014) and suggests that natural carbonate-bearing faults at shallow depths will be more prone to slip in the presence of small quantities of water. Nevertheless, slip-weakening behavior in room-humidity conditions occurs at lower velocity (i.e., V = 0.1 ms^{-1}) than under water-dampened conditions, suggesting that the presence of water might have a "stabilizing" effect on the friction evolution at intermediate slip rates.

Mixtures of calcite and dolomite in natural carbonate-bearing faults is common (e.g., Schröckenfuchs et al., 2015; Demurtas et al., 2016). Patchy development of dolomitized limestones surrounding basin-bounding faults suggests that fluid circulation in such settings is both episodic and heterogeneous. This is also suggested by geophysical data including variations of V_p/V_s with time. In the case of the 2009 L'Aquila seismic sequence, such variations prior the main shock were associated with the entry and disappearance of fluid in the fault zone during foreshock activity (e.g., Chiaraluce, 2012).

Recognition of microstructures that form at different slip rates in "wet" and "dry" conditions (e.g., development of a foliation, preservation of microstructures within the seismic cycle) could help in reconstructing fluids pathways in exhumed fault zones (e.g., Demurtas et al., 2016), as well as the distribution of aseismic and seismic slip within fault zones.

5. Conclusions

Rotary-shear experiments were performed on gouges composed of 50 wt.% calcite and 50 wt.% dolomite over a range of slip rates (30 µms^{-1} to 1 ms^{-1}), ambient conditions (room-humidity vs. water-dampened), total displacements (0.05 to 0.4 m) and normal loads (17.5 to 26 MPa).

The evolution of the friction coefficient was strongly influenced by the presence of water: under room-humidity conditions, slip-strengthening behavior was observed (with friction between 0.7-0.8) up to a velocity of c. 0.1 ms^{-1}, above which dynamic weakening occurred, consistent with previous studies performed on cohesive and non-cohesive rocks (Di Toro et al., 2011; Goldsby and Tullis, 2011; De Paola et al., 2015; Smith et al., 2015). Under water-dampened conditions, the friction coefficient was between 0.6-0.7 at slip velocities up to 0.1 ms^{-1}. Dynamic weakening

occurred at a slip rate of 1 ms^{-1}. As reported in previous studies, the initial strengthening phase was shorter in water-dampened conditions and, once dynamic weakening was triggered, the friction drop was quite abrupt. The above mechanical differences observed in room-humidity and water-dampened conditions were also reflected in the microstructures of the deformed gouge layers. Under water-dampened conditions, the slip zone preserved evidence of fluidization within an ultrafine-grained layer. Development of the PSS along with recrystallization of calcite was observed when the slip rate approaches 1 ms^{-1}. Under room-humidity conditions and slip rates of < 0.1 ms^{-1}, slip-strengthening behavior was associated with the development of a slip zone cut by Y-, R_1- and R_2-shear bands. For slip rates ≥ 0.1 ms^{-1}, strain was localized within a thin shear band in which dolomite experienced decarbonation and recrystallization.

The development of a well-defined foliation in the gouge layers occurred only in the experiments performed at slip rates of 1 ms^{-1} and under room-humidity conditions, consistent with the previous work of Smith et al. (2017). The foliation observed under water-dampened conditions and slip rate of 30 μms^{-1} appeared not to be reproducible and probably due to the experimental setup, resulting in partial drying of the sample during long experiments. These observations support the notion that some foliated gouges and cataclasites may form during seismic slip in natural carbonate-bearing faults.

Finally, in the case of the slide-hold-slide experiments, microstructures characteristic of each slip event were preserved only in the room-humidity case. Therefore, the presence of fluids in natural faults might prevent a complete record of the slip (-rate) history in nature.

6. Tables

	Experiment	*Experimental conditions*	*Target slip rate* ms^{-1}	*Displacement* m	*Normal stress* MPa	*Mixture batch*
Single slide						
	s1210	Room-humidity	0.00003	0.4	17.4	CDM1
	s1322	Room-humidity	0.00003	0.1	17.4	CDM2
	s1211	Room-humidity	0.0001	0.4	17.4	CDM1
	s1212	Room-humidity	0.001	0.4	17.4	CDM1
	s1323	Room-humidity	0.001	0.1	17.4	CDM2
	s1217	Room-humidity	0.01	0.4	17.4	CDM1
	s1218	Room-humidity	0.1	0.4	17.4	CDM1
	s1221	Room-humidity	1	0.4	17.4	CDM1
	s1324	Room-humidity	1	0.4	26	CDM2
	s1327	Water-dampened	0.00003	0.05	17.4	CDM2
	s1329	Water-dampened	0.00003	0.1	17.4	CDM2
	s1328	Water-dampened	0.00003	0.2	17.4	CDM2
	s1214	Water-dampened	0.00003	0.4	17.4	CDM1
	s1330	Water-dampened	0.00003	0.4	17.4	CDM2
	s1215	Water-dampened	0.0001	0.4	17.4	CDM1
	s1213	Water-dampened	0.001	0.4	17.4	CDM1
	s1219	Water-dampened	0.01	0.4	17.4	CDM1
	s1220	Water-dampened	0.1	0.4	17.4	CDM1
	s1222	Water-dampened	1	0.4	17.4	CDM1
Velocity-step						
	s1223	Room-humidity	0.00003 – 1	0.1 – 0.3	17.4	CDM2
	s1224	Room-humidity	1 – 0.00003	0.3 – 0.1	17.4	CDM2
	s1225	Water-dampened	0.00003 – 1	0.1 – 0.3	17.4	CDM2
	s1226	Water-dampened	1 – 0.00003	0.3 – 0.1	17.4	CDM2
Static load						
	sld	Room-humidity			17.4	CDM1
	slw	Water-dampened			17.4	CDM2

Table 1. Experiments presented in this chapter.

Phase	*ρ (kgm^{-3})*	*c_p ($Jkg^{-1}K^{-1}$)*	*κ (m^2s^{-1})*	*Reference*
Calcite	2700	700	$1{,}48 * 10^{-6}$	De Paola et al., 2015
Dolomite	2840	1072	$1{,}15 * 10^{-6}$	
Water	939 (400 K)	4260 (400 K)	$2{,}338 * 10^{-5}$ (400 K)	

Table 2. Mineral properties used to calculate the temperature increase during experiments.

Chapter III

Crystallographic controls on the textural evolution of carbonate gouges during cataclasis

This study was performed with the collaboration of Steven A.F. Smith, Elena Spagnuolo, David J. Prior, Michele Fondriest and Giulio Di Toro. I performed all the work described in this chapter. I was assisted (but not continuously) during microstructural analysis by Steven A.F. Smith and David J. Prior. The material presented here was discussed with Steven A.F. Smith, Michele Fondriest, Elena Spagnuolo and Giulio Di Toro.

Abstract

Gouges and cataclasites are a common product of grain comminution associated to faulting in the brittle upper crust. The investigation of the processes controlling grain comminution and wear is a key step towards a better understanding of the evolution of fault frictional properties during the seismic cycle. Although microphysical and numerical models reproduced and predicted certain characteristics of sheared gouges (e.g., grain size distribution, frictional behavior), they typically assume that the deformed material has isotropic properties and simple grain shapes (usually spherical or cylindrical). But natural fault gouges often contain minerals with strong anisotropies, such as cleavage planes in phyllosilicate, carbonates, feldspars and amphiboles. The role that such anisotropies might have during cataclasis has still not been explored so far.

Here we present results of electron backscatter diffraction analysis performed on the bulk gouge recovered from rotary-shear experiments carried out on a mixture of 50 wt.% calcite and 50 wt.% dolomite. The gouges were sheared on a wide range of slip rates (30 μms^{-1} to 1 ms^{-1}), displacements (0.05 to 0.4 m) and deformation conditions (room-humidity vs. water-dampened). At all investigated deformation conditions, calcite develops a crystallographic preferred orientation (CPO) on the (0001) plane, with the c-axes inclined subparallel to the instantaneous shortening direction and the poles to the a-axes direction and forming a girdle perpendicular to it. Eigenvalue analysis on the calcite orientation data shows that the CPO is typically stronger in experiments performed under room-humidity conditions. Misorientation analysis conducted on the calcite grains suggests twinning as the principal crystallographic active deformation mechanism. No CPO is observed to form in the dolomite. Intragranular microfractures are closely spaced, mainly oriented subparallel to the principal stress and rarely exploit calcite twin planes. The latter typically occur at high angle with respect to fractures, are oriented consistently with the sense of shear and almost orthogonal to the principal stress. Calcite twin paleopiezometry results in differential stresses almost an order of magnitude higher with respect to the applied stress.

Since there is no evidence for dislocation motion activity, the formation of a CPO in the cataclastic regime is interpreted to be the result of mechanical grain rotation and subsequent fracturing along cleavage planes oriented sub-parallel to the instantaneous shortening direction. Finally, the very high differential stress magnitudes estimated with calcite twin paleopiezometry are interpreted as the maximum local stress carried by grain bridges that formed within the gouge during cataclasis.

1. Introduction

Gouges and cataclasites are a common product of faulting in the brittle upper crust. An investigation of the processes controlling cataclasis by grain comminution is a key step towards a better understanding of the evolution of fault frictional properties during the seismic cycle. Numerous microphysical models for cataclasis have been proposed to quantitatively describe and interpret certain characteristics of fault rocks such as the grain size distribution (e.g., Allègre et al. 1972, Turcotte, 1986; Sammis et al., 1987; Sammis and King, 2007) and frictional behavior (e.g., Bos and Spiers, 2002; Niemeijer and Spiers, 2007; den Hartog and Spiers, 2014; Chen and Spiers, 2016) as deformation proceeds. However, such microphysical models typically assume the deformed material to have isotropic properties and simple grain shapes (usually spherical or cylindrical). In the last decade, the development of three-dimensional (3D) numerical simulations of gouge evolution introduced a novel tool to study shear in granular materials (Abe and Mair, 2005; Mair and Hazzard, 2007; Mair and Abe, 2008; Abe and Mair, 2009). For example, the 3D modelling approach allowed Mair and Hazzard (2007) to image the formation, destruction and the overall geometries of grain bridges (also called *force chains*) during shear of granular materials. Moreover, typical fractal grain size distributions found in natural gouges and cataclasites (e.g., Billi et al., 2003; Billi and Storti, 2004; Di Toro and Pennacchioni, 2005; Agosta and Aydin, 2006; Muto et al., 2015) possibly resulting from specific microphysical processes (e.g., constrained comminution model, Sammis et al. 1987) were successfully reproduced in the 3D numerical simulations. An important improvement of the 3D numerical simulations with respect to previous microphysical models was the introduction of an evolving grain shape with slip (Abe and Mair, 2009). The utilization of realistic grain shapes resulted in a modelled friction coefficient consistent with the one measured in laboratory experiments. However, natural fault gouges often contain minerals characterized by strong anisotropies, such as cleavage planes in phyllosilicates, carbonates, feldspars and amphiboles (e.g., Faulkner et al., 2003; Rutter et al., 2007; Fondriest et al., 2012; Schröckenfuchs et al., 2015; Smeraglia et al., 2016). The role that such anisotropies might have during cataclasis has not been explored so far.

Therefore, the main focus of this study is the investigation of deformation mechanisms and fracturing processes that are active in gouges composed of minerals with strong anisotropies (i.e., cleavage in calcite and dolomite). This is achieved by application of electron backscatter diffraction (EBSD) analysis to study granular carbonate gouges deformed experimentally in rotary-shear. Surprisingly, systematic microstructural analysis revealed that the calcite-dolomite gouges

developed a weak crystallographic preferred orientation (CPO) when sheared under very shallow crustal conditions (ambient temperature and normal stress < 20 MPa), even for small finite strains, and over the entire investigated range of slip velocities. The weak CPO is interpreted to form by grain rotation in the gouge layers followed by crystallographically-controlled intragranular fracturing.

2. Methods

2.1. Samples and sample preparation

The CPO analysis was performed on samples obtained from the rotary-shear experiments performed on calcite-dolomite mixtures described in Chapter II. The samples here analyzed cover a wide range of deformation conditions, with slip rates ranging from 30 μms^{-1} to 1 ms^{-1}, displacements being between 0.05-0.4 m, presence or absence of fluid water (water-dampened vs. room-humidity conditions), single slide and slide-hold-slide experiments. Table 1 lists the samples described in Chapter II and here analyzed. The EBSD analysis was carried out on petrological thin sections cut perpendicular to the gouge layer and parallel to the velocity vector (i.e., tangential cuts, Fig. 2d from Chapter II) thinned to a thickness of ~ 30 μm and successively SYTON®-polished (Fynn and Powell, 1979). The last step was crucial in order to obtain high-quality diffraction patterns (Prior et al., 1999).

2.2. Electron backscatter diffraction (EBSD) analysis

Images and orientation data were collected with a Zeiss Sigma VP Field-Emission-Gun Scanning Electron Microscope equipped with a NordlysF EBSD camera from Oxford Instruments, located at the Otago Centre for Electron Microscopy, University of Otago (New Zealand). Raw diffraction data and EDS spectra were acquired and processed using AZtec software (Oxford Instruments).

Calcite and dolomite are characterized by a similar crystal structure (crystal symmetry: $\bar{3}m$ and $\bar{3}$, respectively). This commonly causes systematic misindexing between the two phases during data acquisition, resulting in low quality EBSD maps. The AZtec software has a built-in function, named “True Phase”, which allows the EDS spectra to be used to identify the correct phase during the analysis, when the results for the diffraction patterns are not unique. The implementation of

the “True Phase” option in the EBSD analysis routine allowed me to significantly improve the quality of the raw EBSD data, reducing the misindexing. However, the quality of the coupled EDS-EBSD analysis was highly sensitive to the position of the sample with respect to the detectors. Therefore, before each analysis, *ad-hoc* regulations of the sample working distance (i.e., distance of the analyzed sample from the field-emission-gun) and of the position of the EDS and EBSD detectors were made to ensure the highest possible quality of the acquired data.

The EBSD data were collected with a 1 μm step size and the working distance was usually between 15 and 19 mm. The combined use of EDS-EBSD allowed high indexing rates (up to 70-75%). Such indexing rate is a remarkable achievement considered the nature of the analyzed sample (i.e., very fine-grained fault gouge with significant porosity). EBSD analysis was conducted on the bulk gouge, corresponding to the microstructural domains D0, D1 and D1f described in Chapter II. These microstructural domains were found typically at distances greater than 400-500 μm from the principal slip surface (Fig. 2d from Chapter II). In fact, recent studies have demonstrated that in the case of a rotary-shear configuration, the bulk gouge of domains D0, D1 and D1f accommodates relatively low finite strains (γ < 2-2.5: Smith et al., 2015; Rempe et al., 2017).

2.3. Data cleaning and texture analysis

Given (1) the difficulty of the analyzed material (i.e., fine-grained porous fault gouge) with respect to those typically used for standard EBSD analysis and (2) the systematic misindexing that occurred between calcite and dolomite, the standard data cleaning and processing routine with the CHANNEL5 software (from HKL Technology, Oxford Instruments) was unable to yield accurate crystallographic orientation data. Therefore, data cleaning and processing was carried out with MTEX (Bachmann et al., 2010). MTEX is a free MATLAB toolbox developed for analyzing and modelling crystallographic textures by means of EBSD or pole figure data. One of the main advantages in the use of MTEX is its open access structure allowing the operator to further develop the processing capabilities of the software.

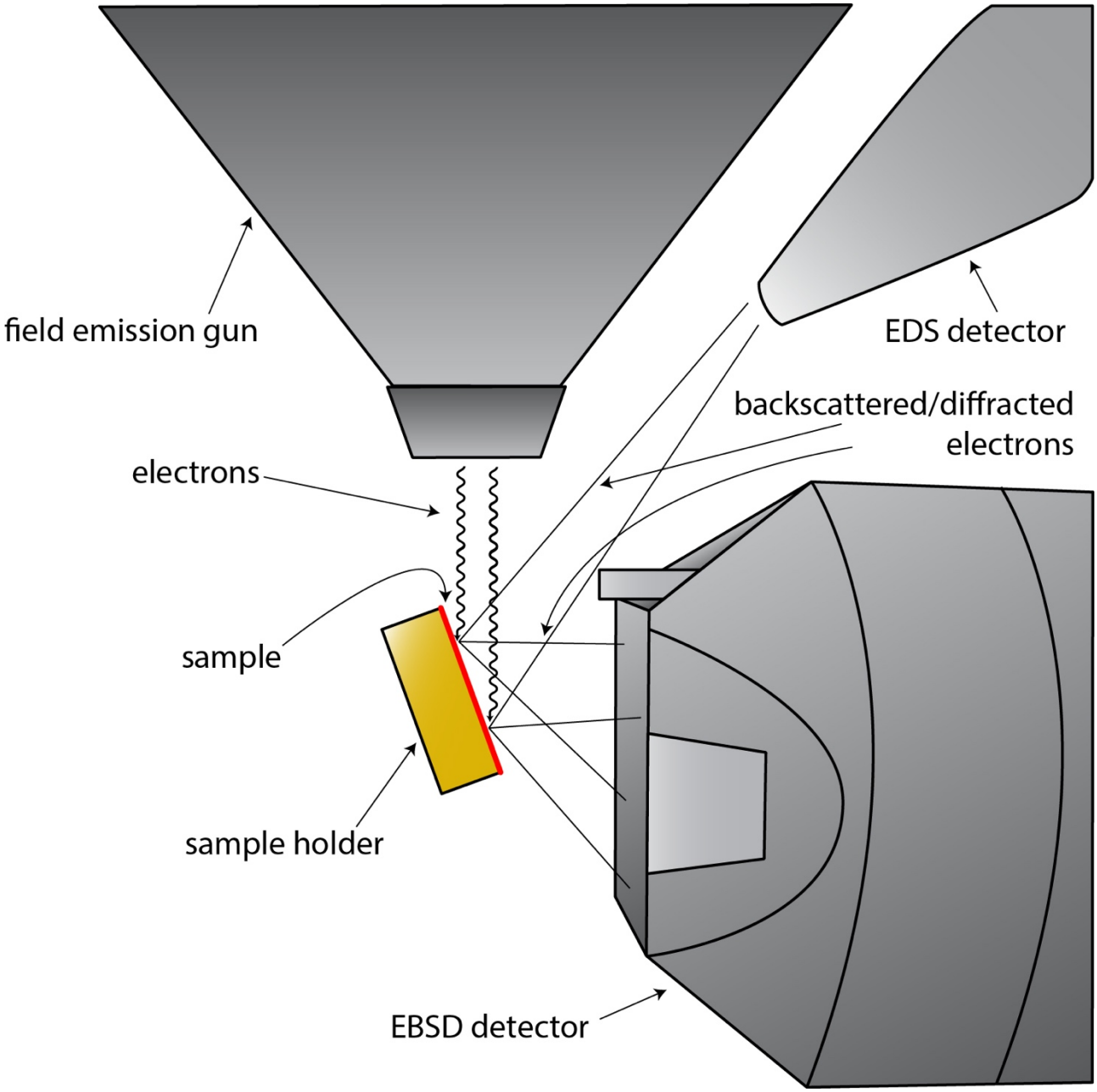


Fig. 1. Electron Backscattered Diffraction (EBSD) – X-ray Energy Dispersive Spectroscopy (EDS) coupled analysis setup. As in standard EBSD analysis, the sample (here depicted as a red line) is inclined of 70° towards the EBSD detector. The working distance was usually kept between 15 and 19 mm, depending on sample assembly (i.e., how the sample was inserted on the sample holder). During the analysis, the EBSD detector was held at a position at 207 mm, while the position of the EDS detector varied for each analysis according to the area analyzed on the sample and the working distance.

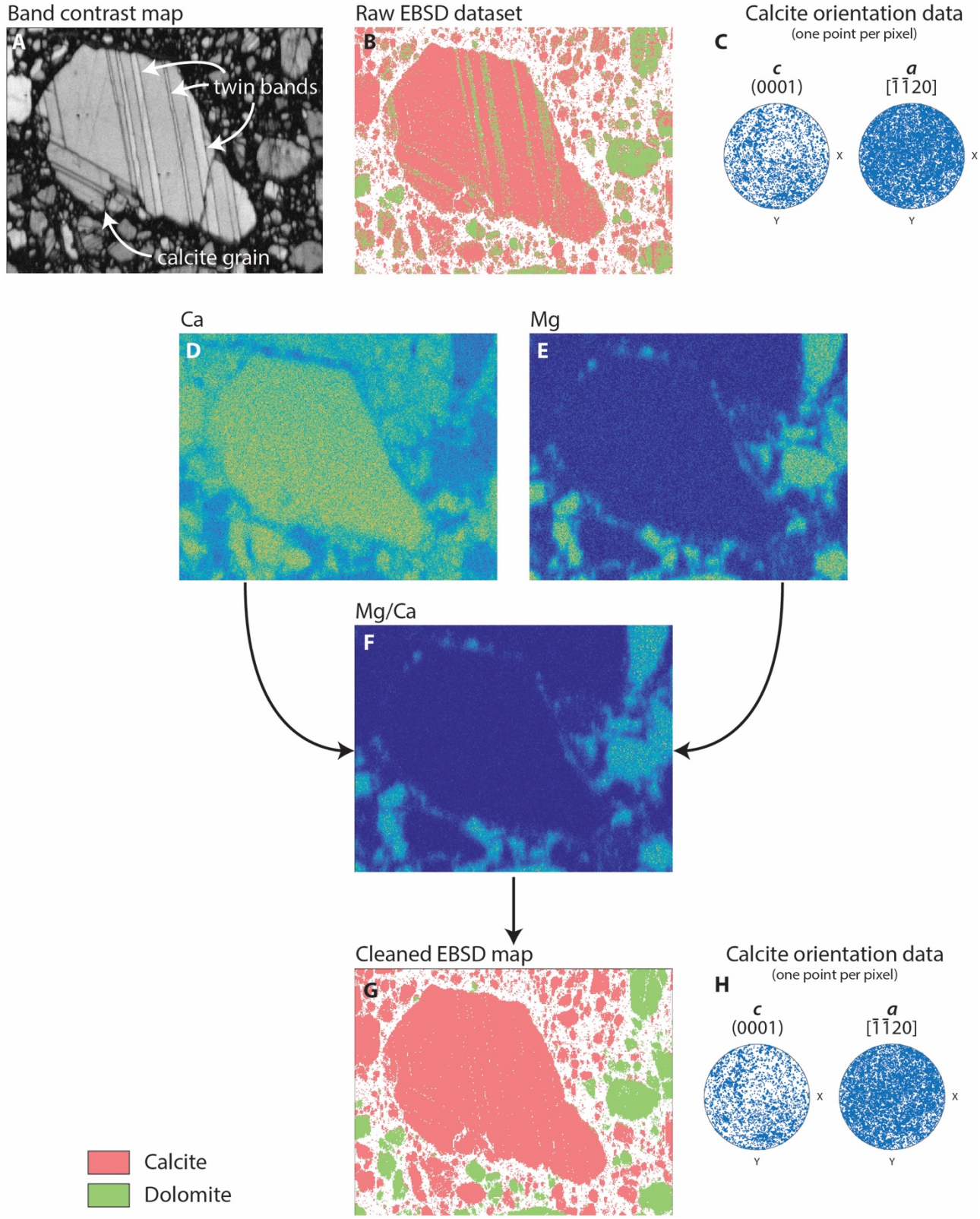


Fig. 2. See next page for caption.

Fig. 2. (previous page) Cleaning EBSD dataset workflow. a) Detail of a band contrast map from an EBSD map on sample s1217. b) Phase map of the raw EBSD dataset showed in a) evidencing typical misindexing between calcite and dolomite. In this case, misindexing occurred along the twin bands in the calcite grain and at the border of dolomite grains. The use of EDS spectra to identify the correct mineral phase improved significantly the amount of correct interpretation during the analysis. c) Scatter plot of orientation data for calcite from the raw EBSD dataset. d) EDS map for Ca. e) EDS map for Mg. f) Map of the Mg/Ca ratio. Dolomite was typically identified with a ratio > 0.2, while calcite with a ratio < 0.15. g) Phase map of the cleaned EBSD dataset. Voids within the grains were filled later in the data processing procedure by controlled grain "growth". h) Scatter plot showing orientation data for calcite (one point per pixel) after the "cleaning" procedure. No sensible variation in the orientation was detected.

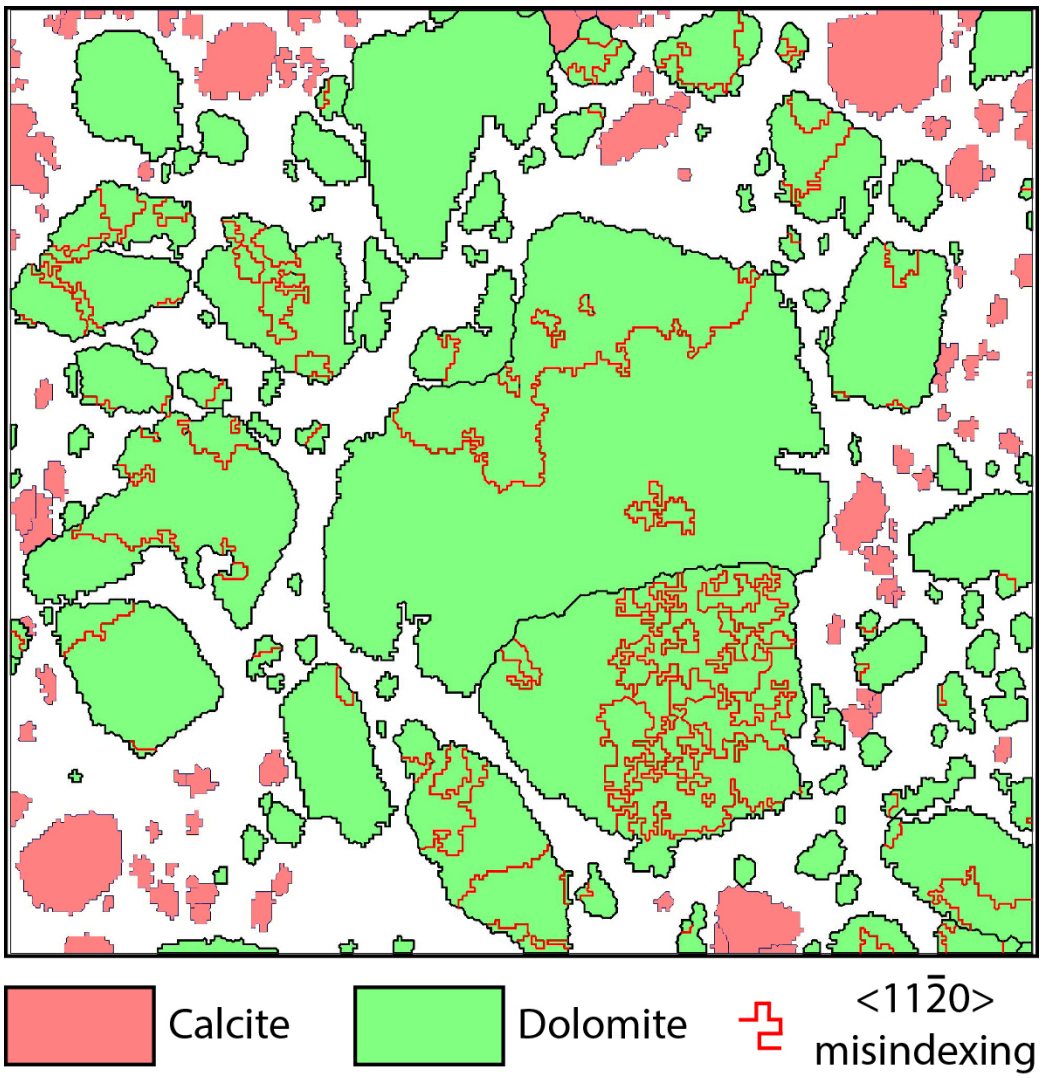


Fig. 3. Systematic misindexing occurring in dolomite grains. Dolomite is characterized by a systematic misindexing of 180° around $\langle 11\bar{2}0 \rangle$ (a-axis; Pearce et al., 2013). Black lines define grain boundaries in dolomite, while red lines represent misorientations corresponding to misindexing on the a-axis.

For our analysis, a new workflow was created to clean the systematic calcite/dolomite misindexing in the raw EBSD data by using EDS maps (Fig. 2). Since the EDS analysis does not yield quantitative element analysis of the investigated mineral phase, the elemental maps did not allow me to recognize immediately the mineral phase. Therefore, the reassignment of the correct phase to the misindexed pixel was done by setting a threshold for each phase on a Mg/Ca map, with ratios of $Mg/Ca \geq 0.2$ for dolomite and $Mg/Ca \leq 0.15$ for calcite (note: ratios used here were not stoichiometric; Fig. 2 d-f). During this step, non-indexed pixels remained unchanged. For each indexed pixel, depending on the Mg/Ca ratio, only the property called "phase" (or mineral) was changed, without changing the original crystal orientation. Before continuing with the data processing, tests were made that the above operation did not introduce errors in the crystal orientations (compare Fig. 2c and Fig. 2h).

Dolomite is commonly characterized by systematic misindexing of 180° around the a-axis direction (i.e., $\langle 11\bar{2}0 \rangle$; Fig. 3) due to the pseudosymmetrically equivalent patterns that are sufficiently similar and only differ by one or two, often weak, diffraction bands (Pearce et al., 2013). Such systematic misindexing is typically overcome by mapping dolomite as Mg-calcite, which has a higher crystal symmetry. In our case, this solution would have introduced further errors during acquisition, due to the difficulty of clearly discerning the diffraction patterns of low-Mg calcite and dolomite. Consequently, in our analysis dolomite systematic misindexing was corrected during data processing. However, the error introduced during the correction of the misindexing was significant and thus dolomite orientation data were not judged reliable. In order to have an insight regarding the possible textural evolution of dolomite grains during deformation, EBSD analysis was also performed on pure dolomite gouges deformed with a rotary shear machine at similar conditions as those imposed to the calcite/dolomite gouge mixtures (see Table 1). In this case, the systematic misindexing issue was resolved by indexing dolomite as Mg-calcite, and thus orientation data obtained were reliable.

Grains were reconstructed from processed orientation data following the procedure described by Bachmann et al. (2011). Grain boundaries were defined for a misorientation angle between neighboring pixels ≥ 10°. Grains that were made of ≤ 5 pixels, hence having an equivalent diameter of ca. ≤ 2.5 μm, were deleted. Orientation data were plotted both as scatter points and Orientation Density Functions (ODFs, after Bunge, 1982). Contouring in the latter corresponds to

value of 0 to maximum multiples of a uniform distribution (MUD) for each sample, to evidence the shape of the CPO. All pole figures were plotted as equal area and upper hemisphere in the stereograms (e.g., Fig. 4).

To quantify the strength of the CPOs, the eigenvalues orientation tensor (Woodcock, 1977) was determined. Eigenvalues S_1, S_2 and S_3 (where $S_1 > S_2 > S_3$) are related to the shape and the strength of the CPO. Here, we used the normalized form, so that $S_1 + S_2 + S_3 = 1$. In a log-log diagram, where the x-axis is $\ln(S_2/S_3)$ and the y-axis is $\ln(S_1/S_2)$, CPOs characterized by $S_1 > S_2 \approx S_3$ are clusters and CPOs with $S_1 \approx S_2 > S_3$ are girdles (see Fig. 1 in Woodcock, 1977). The strength of the texture is given by the parameter C, defined as $\ln(S_1/S_3)$, and ranges from 0 to infinite.

Fracture and twin orientation analysis was performed on the band contrast (also called pattern quality) maps collected during EBSD analysis. The band contrast map gives an indication of the quality of the diffraction patterns: high quality patterns would result in bright areas, whilst dark or black pixels would indicate low quality pattern (e.g., grain boundaries or pores). Here, fracture and twin planes were individually hand-traced in ArcGIS and their orientation was plotted in an 180° rose diagram.

2.4. Calcite twin piezometry

Calcite twins are the result of intracrystalline crystal-plastic deformation and have been used to constrain both paleostresses and temperatures during deformation (e.g., Rowe and Rutter, 1990; Burkhard, 1993; Ferrill et al., 2004; Rybacki et al., 2011, 2013). Twinning occurs when a critical resolved shear stress (CRSS) along a determined crystallographic plane is overcome. In the case of twinning in calcite, the planes responsible for twin formation are typically the faces of the rhomb (the most common are the *e*-planes) and the temperature range at which such deformation mechanism is efficient is commonly restricted to less than 400 °C (Turner, 1953; Carter and Raleigh, 1969; Groshong, 1988; De Bresser and Spiers, 1997). In this study, calcite paleopiezometry was applied on four samples to test the potential of this type of analysis to infer local stresses experienced in granular materials during shearing. Differential stress ($\Delta\sigma$) was calculated following the twin density paleopiezometer from Rowe and Rutter (1990):

$$\Delta\sigma = -52.0 + 171.1 \log D \quad \text{[MPa]} \qquad \text{(Eq. 1)}$$

where *D* is twin density, defined as the number of twins per millimeter. This paleopiezometer has an estimated error of ± 43 MPa. Alternatively, $\Delta\sigma$ was calculated with the revised paleopiezometer by Rybacki et al. (2013):

$$\Delta\sigma = 10^{1.29\pm0.02}\rho_{twin}{}^{0.50\pm0.05} \quad \text{[MPa]} \qquad \text{(Eq. 2)}$$

where ρ_{twin} is the twin density (same definition as in Rowe and Rutter, 1990). Here, the errors in the estimate were ca. ± 35-40 MPa.

3. Results

3.1. Crystallographic preferred orientation in calcite and dolomite gouge

3.1.1. Static load (water-dampened)

As a reference (= starting material) for the experiments where shear was also imposed, we determined the orientation data of the calcite-dolomite mixtures after the application of a static normal load of 17.5 MPa for 300 s (experiment *slw* in Table 1 and the two pole figures at the top of Fig. 4). Calcite grains in the starting material showed no CPO (Fig. 4) and had no significant intracrystalline distortion (Fig. 5a), with the parameter *C* = 0.45 (dashed line in Fig. 7b). Misorientation analysis on the starting material for correlated and uncorrelated grains (Wheeler et al., 2001) showed a misorientation angle distribution similar to the random misorientation distribution (Mackenzie and Thompson, 1957), with the exception of a clear peak at ca. 70° for the uncorrelated grains (Fig. 8a). This peak is related to the development of *e*-twins in calcite.

3.1.2. Deformed gouges

The calcite CPOs that developed over a wide range of slip velocities in room-humidity and water-dampened conditions are reported in Fig. 4. In all of the sheared gouges, independent of the loading conditions, calcite grains showed a texture characterized by a prominent cluster of the c-axes (i.e., (0001)) inclined c. 40-50° clockwise from the shear zone boundaries. This orientation is sub-parallel to the instantaneous shortening direction predicted during simple shear (Fig. 4). A girdle arrangement is present in the a-axis direction (i.e., $\langle 11\bar{2}0\rangle$) with an orientation

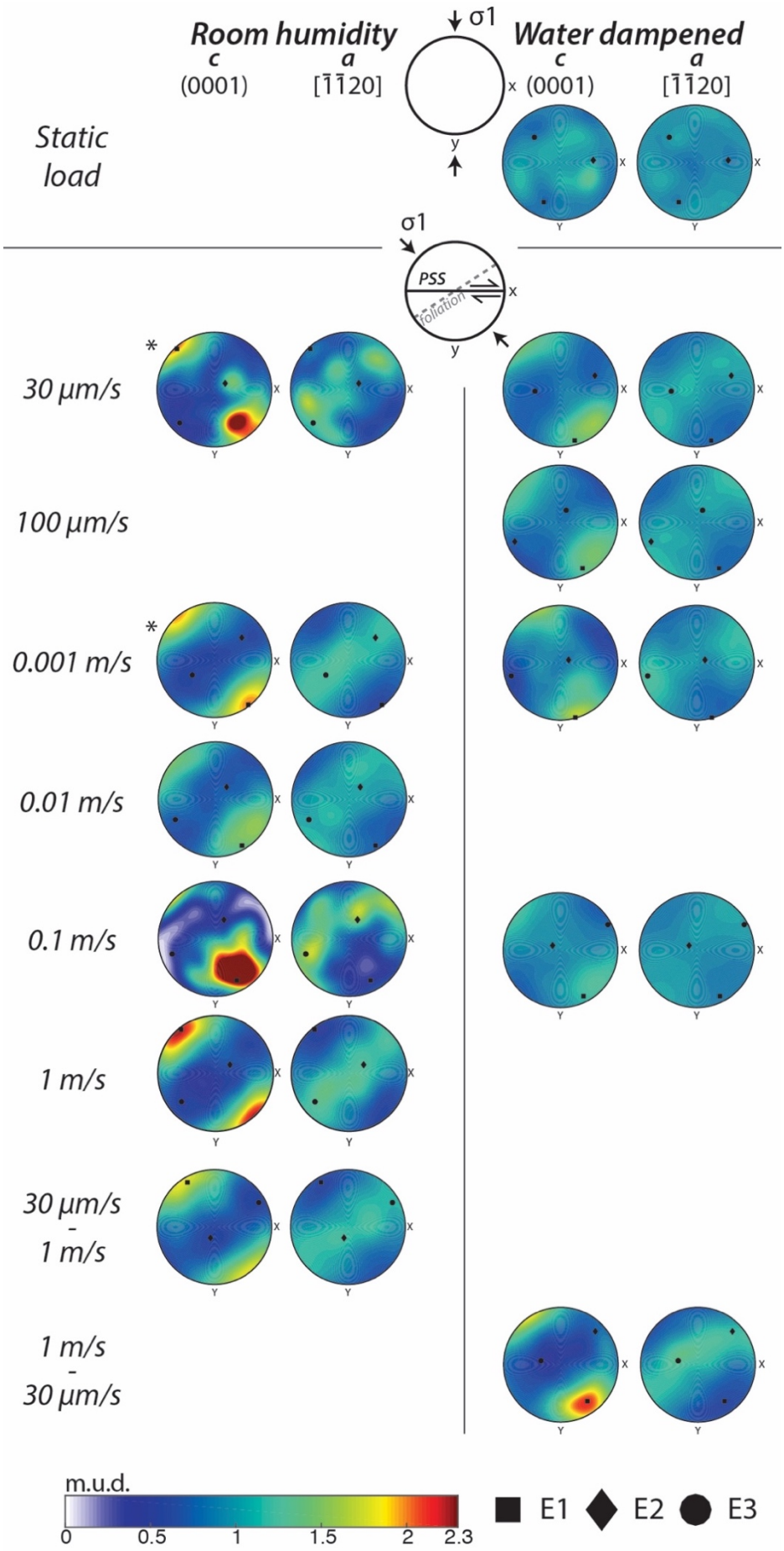


Fig. 4. See next page for caption.

Fig. 4. (previous page) Orientation data for calcite grains over a wide range of experimental conditions. Values have been scaled around the maximum density value for experiment at 1ms^{-1} in room-humidity conditions (i.e., 2.3) to highlight cluster density variations with deformation conditions. In the starting material, no clear CPO development was observed (calcite grains were randomly oriented). Development of a texture consisting in the c-axes planes clustered around 40-50° to the y-axis and sub-parallel to the instantaneous shortening direction was observed throughout all the imposed deformation conditions. Room-humidity experiments were typically characterized by a higher density around c-axis cluster in respect to the water-dampened case. The a-axis was oriented along a girdle perpendicular to the c-axis maxima. When a foliation was observed in the gouge, the a-axis girdle was typically oriented subparallel. All CPO data were collected from experiments were the gouge was slid for 0.4 m with exception of experiments performed at 30 μms^{-1} (s1322), 0.001 ms^{-1} (s1323) that were sheared for 0.1 m (see asterisks) and, of course, the static load case.

Fig. 5. (next page) Calcite intracrystalline misorientation. a) Under static load conditions, the calcite grains show little to negligible internal misorientation. b)-c) During shearing, internal misorientation in the calcite grains increases as a result of mechanical twinning and fracturing with lack significant shear within the grains. During data processing and grain reconstruction, the latter results in construction of a single grain composed by fractured domains that only slightly moved relative to each other. Therefore, that is seen displayed as an increase in intragranular misorientation.

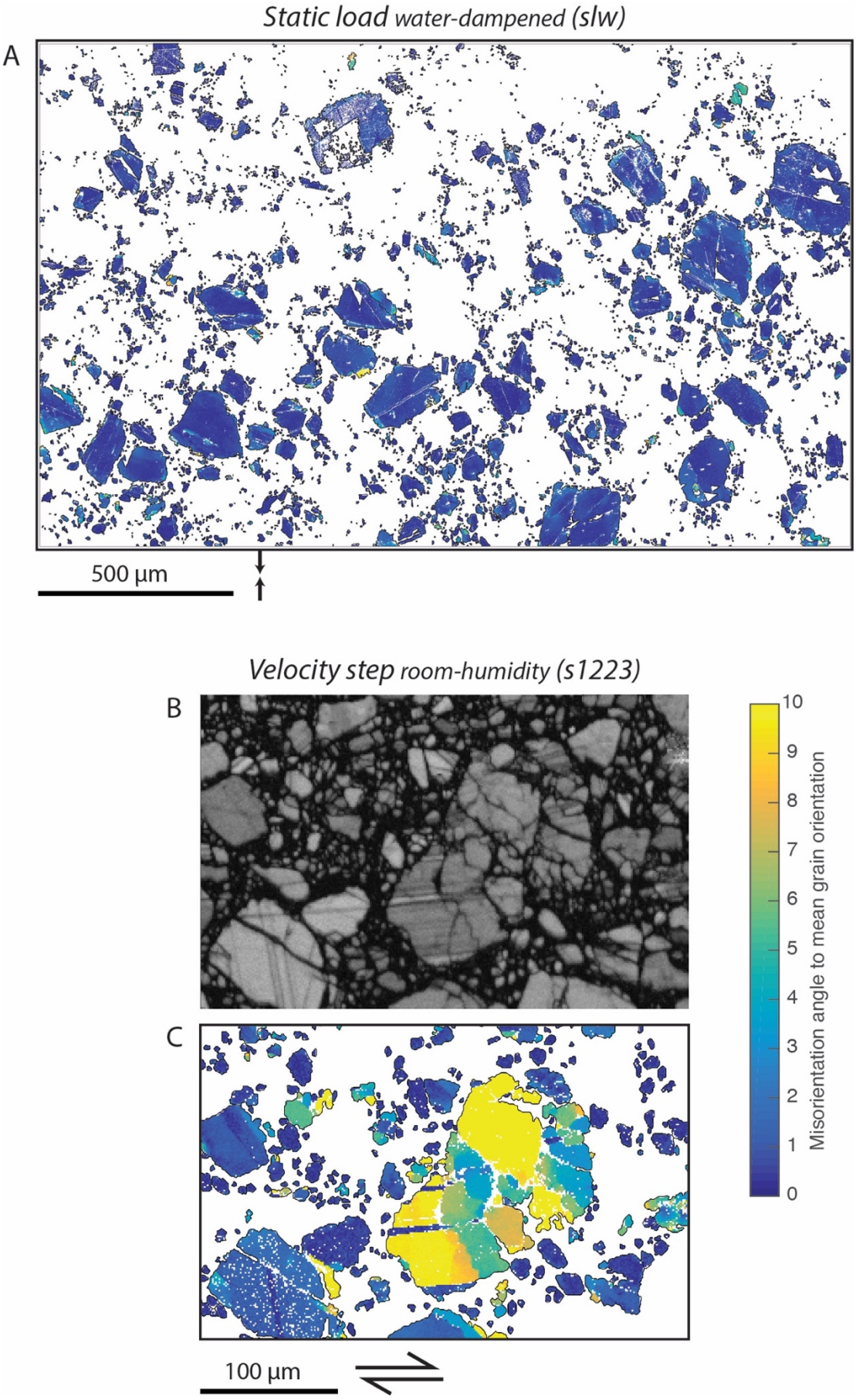


Fig. 5. See previous page for caption.

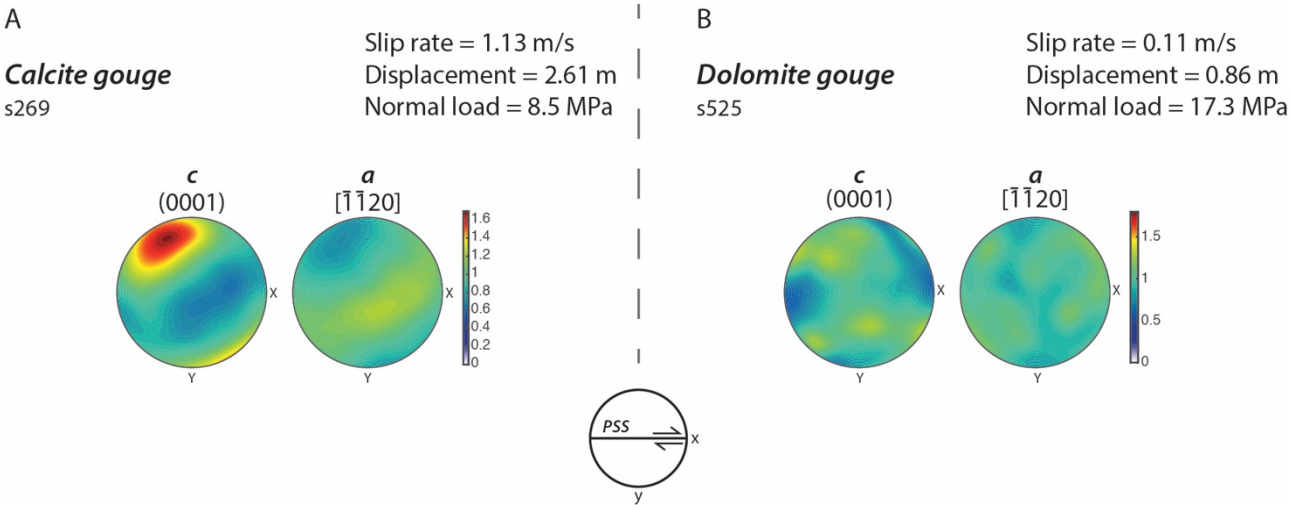


Fig. 6. Pure calcite and dolomite (= endmembers) orientation data. a) EBSD analysis on pure calcite gouges sheared at similar conditions to those imposed to the calcite-dolomite mixtures presented in this chapter, show the development of a CPO with the c-axis clustered sub-parallel to the instantaneous shortening direction. This CPO was consistent with the one observed in calcite in mixture experiments (Fig. 4). b) On the other hand, in experiments conducted on pure dolomite gouges, the development of a CPO was not observed, with grains being typically randomly oriented.

Fig. 7. (next page) Eigenvalues texture analysis. a) Two-axis logarithmic plot of ratios of normalized eigenvalues S1, S2 and S3, following the method outlined in Woodcock (1977). Most of the data plotted on the left side of the girdle/cluster transition, indicating the development of a cluster texture. b) Plot of C (i.e., the logarithm of the ratio between the largest and smallest eigenvalues, used to quantify the strength of the fabric) vs. slip rate. Velocity step experiments and starting material were plotted with a 1 ms^{-1} slip rate value. Room-humidity experiments were characterized by a higher C value in respect to the water-dampened case. As already observed in the calcite/dolomite gouge mixtures, also in the case of pure dolomite experiments (s525), there is no strong CPO development.

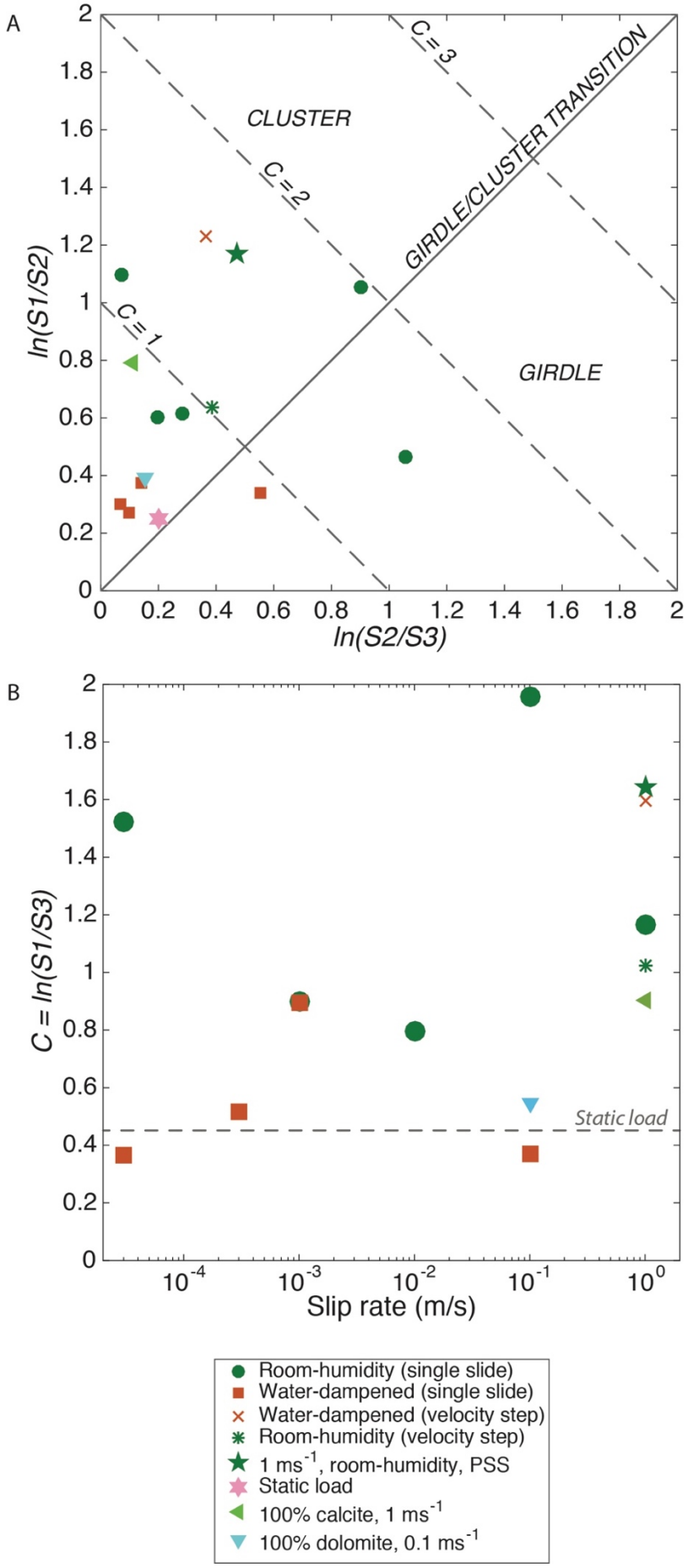


Fig. 7. See previous page for caption.

perpendicular to the c-axis (Fig. 4). In the case of samples showing the development of a foliation in the bulk gouge (i.e., experiments s1214 and s1221: see Chapter II for a comprehensive characterization of the microstructures), the c-axis and a-axis are oriented, respectively, at high angles and sub-parallel to the gouge foliation. Calcite CPOs under room-humidity conditions were characterized by substantially higher density of the c-axes clusters with respect to the water-dampened experiments.

EBSD analysis conducted in pure calcite gouges (experiment s269 in Table 1), sheared under room-humidity and similar deformation conditions (i.e., V = 1.13 m/s and $\sigma 1$ = 8.5 MPa), highlighted the development of a CPO like the one observed in the calcite-dolomite mixtures (Fig. 6a). Conversely, in the case of pure dolomite gouges (experiment s525 in Table 1), orientation data in the bulk gouge showed a random distribution (Fig. 6b), which was consistent with orientation data from dolomite for EBSD maps were there was minor systematic misindexing.

Following Woodcock (1977), the eigenvalue analysis of the CPOs resulted in most of the data plotting on the left side of the girdle/cluster transition in the two-axis logarithmic plot (Fig. 6a), confirming a cluster distribution for the calcite c-axes. The sheared gouges from water-dampened experiments typically had *C* values for calcite similar to the static load experiment (ca. 0.45), with only a couple of samples resulting in higher values (ca. 0.9 and 1.6). Conversely, gouges sheared under room-humidity conditions were characterized by relatively high *C* values for calcite, commonly > 0.9 and up to ca. 2. These *C* values were similar to those found in pure calcite gouges (Figs. 6 and 7) sheared under similar deformation conditions (i.e., V = 1.13 m/s and $\sigma 1$ = 8.5 MPa). As was already clear from the orientation data, in the pure dolomite experiments the CPO was very weak, with *C* value similar to the one of the static load and of the water-dampened cases (Fig. 7a).

The observed bulk calcite CPO (Fig. 9a) was formed by ~ 10 % of all calcite grains, which were composed of both twinned and non-twinned grains (Fig. 9b). Such grains contributing to the CPO were defined as being within a 30 degree cone of orientation from the mode of the CPO for the whole set of calcite grains (red and yellow star in pole figures in Fig. 9). However, since each twinned band within an individual calcite grain was counted as a separate grain, the CPO was recalculated for non-twinned calcite grains, thus excluding any possible bias derived from the way grains were constructed in MTEX. The resulting CPO was identical to the one that comprised both twinned and non-twinned grains (compare pole figures in Fig. 9a and Fig. 9c). Here, the grains that contributed to the CPO within a 30 degree cone from the mode were mainly part of the matrix, with grain sizes

ranging from ~ 3 to ~ 70 µm. No preferred alignment of those grains was observed, as well as no development of a significant shape preferred orientation (SPO).

Misorientation angle distribution analysis on the sheared gouges confirmed the occurrence of a random grain distribution (Fig. 8b-c), as described by Mackenzie and Thompson (1957), but with a strong misorientation angle peak associated to the formation of twins in the calcite grains at 75-80°. Sheared calcite grains had higher values of internal misorientation with respect to those from the static loading case (Fig. 5b-c). Higher internal strain was typically associated with grain fracturing and slight rotation of fractured clasts, resulting in domains with slightly different orientation within the same grain.

3.2. Fracturing and calcite twin analysis

In the static load experiment, there were relatively few equally distributed between calcite and dolomite grains (Fig. 10a). No significant evidence of grain-grain interaction was detected. Moreover, fractures were typically oriented parallel to the shortening direction, that in the case of the static load sample was vertical (Fig. 10a). Calcite twins showed a large spread in orientations, probably reflecting twinning within a gouge with random CPO (Fig. 10a). In the deformed gouges, the density of fractures and twins increased significantly with respect to the static load case (Fig. 10b-e). Fractures were more common in calcite and preferentially oriented, typically exploiting cleavage planes, and on average sub-parallel to the instantaneous shortening direction (Fig. 11a). However, a higher scattering with respect to the mean orientation was observed, with the presence of a vertically oriented fracture subset (Fig. 10b-e).

Under static load conditions, twinning in calcite was not common. When twinned, calcite grains were characterized by a single set of straight twins, where bending would imply the activity of dislocation slip (e.g., Burkhard, 1993), and relatively low twin density (45 ± 23 mm^{-1}; Fig. 9a and Table 2). After the classification of Burkhard (1993), twins were typically type II (twins 1-5 µm thick) with type I twins (≤ 1 µm thick) being less common. Similar to fractures, in sheared gouges twin planes in calcite had a preferred orientation. In this case twins were typically inclined of ca. 30-40° anticlockwise to the gouge layer boundaries (Fig. 11b), sub-perpendicular to the instantaneous shortening direction. Although the orientation of the twins had some scattering with different

deformation conditions and within the same sample, the general trend was constant and independent of the loading conditions. Again, twins were mostly type II with few type I, and had straight, rarely slightly bent, borders. Twin density was higher than in the static loading case (60-78 mm^{-1}; Table 2).

Paleopiezometry analysis resulted in estimated differential stresses significantly higher than those applied during the experiments (i.e., normal load was kept at 17.5 MPa and the measured shear stress was always below 15 MPa, see Chapter II). Under static load conditions, calcite twin analysis resulted in a $\Delta\sigma$ of 129 ± 30 MPa (using the Rybacki et al. paleopiezometer). In the case of the sheared gouges, estimated $\Delta\sigma$ were higher, comprised between 152 ± 37 MPa and 175 ± 45 MPa. Even if, given the large errors, the estimates may seem comparable, a general trend of higher $\Delta\sigma$ was observed in the case of sheared gouge. The $\Delta\sigma$ estimates made with the Rowe and Rutter paleopiezometer resulted in larger stresses, typically above 240 MPa.

Along with twin density, twin incidence was also measured. Twin incidence, defined as the ratio between the number of twinned grains with respect to the total number of grains (for a single mineral phase), is largely independent of temperature and strain rate, but depends mainly on stress. Rowe and Rutter (1990) defined another paleopiezometer that accounted for twin incidence and grain size. However, the estimates would be reasonable only in the case of samples loaded in a single, coaxial, strain-inducing event, which is not the case for experiments in rotary shear apparatuses. Other than that, stresses will be overestimated. For our samples, twin incidence was plotted as a function of slip rate, to test whether the higher torque applied for high slip rate experiments resulted in a change of the twin incidence in the gouge (Fig. 12). For samples deformed both under room-humidity and water-dampened conditions, no clear systematic variation of the twin incidence in function of the slip rate was observed (Fig. 12).

4. Discussion

4.1. Mechanism for CPO development in a granular material

The CPO development in mylonites has been widely studied, where it typically results from crystal plasticity associated with the motion of dislocations, involving processes such as dislocation

creep, grain boundary migration, grain boundary sliding aided by dislocation creep and dynamic recrystallization (e.g., Poirier, 1985, and references therein; Karato, 2008; Hansen et al., 2011). Another mechanism likely to form a CPO is the oriented growth of crystals in veins along specific crystal directions (e.g., the c-axis for quartz; Bons et al., 2012, and references therein).

Recently, some studies reported the formation of a CPO in both natural cataclasites exhumed from shallow crustal depths (e.g., Smith et al., 2011) and experiments performed on granular materials at room temperature and high slip velocity (e.g., Smith et al., 2013). A clear fabric was observed to develop close to the PSS of calcite gouges sheared at seismic slip rates (V = 1.13 ms^{-1}), with the calcite c-axes clustered at high angles to the principal slip surface and antithetic with respect to the shear sense (Smith et al., 2013). The CPO was also associated with a shape preferred orientation (SPO) of the calcite grains that were interpreted to have deformed by dynamic recrystallization in a thin layer of plastically-deformed calcite. The development of a CPO was also observed in calcite gouges sheared at sub-seismic velocity (V = 0.1 – 10 μms^{-1}; Verberne et al., 2013b). In this case, extreme comminution (grain size ~ 5-20 nm) localized along Riedel and boundary shear bands, along with an ambient T of c. 80 °C, promoted deformation of calcite nanograins by dislocation glide along the rhomb *r*-planes (Verberne et al., 2013b). Their results showed that the increase of ambient temperature resulted in the activation of dislocation glide in the shear bands, alongside with cataclasis, promoting the transition from stable velocity strengthening to (unstable) velocity weakening at ~ 80 °C (Verberne et al., 2013b).

In this study, we focused on the deformation mechanisms that are active in the bulk calcite-dolomite gouges during cataclasis. Recent studies investigated the strain distribution in rotary-shear type experiments, and showed that in the bulk gouge the finite shear strain γ was typically < 2-2.5, while most of the shear strain ($\gamma > 10^3$) was localized in a < 100 μm thick slip zone at the gouge layer-sample holder contact (Smith et al., 2015; Rempe et al., 2017). Moreover, the area analyzed in this study was located at distances greater than 400-500 μm from the gouge layer boundary, where most of the strain was accommodated and, for high-velocity experiments (i.e., V ≥ 0.1 ms^{-1}), a PSS formed and high temperature achieved. Therefore, given the short duration of the experiments (< 0.5 s) and the distance from the PSS, this allowed us to exclude the possibility that the temperature rise along the PSS during intermediate- to high-velocity experiments promoted the activation of thermally-dependent deformation mechanisms in the bulk gouge. This is also supported by microstructural observations showing that the bulk gouge remains brittle and granular, with no evidence for recrystallization, porosity reduction by grain growth or thermal decomposition (see

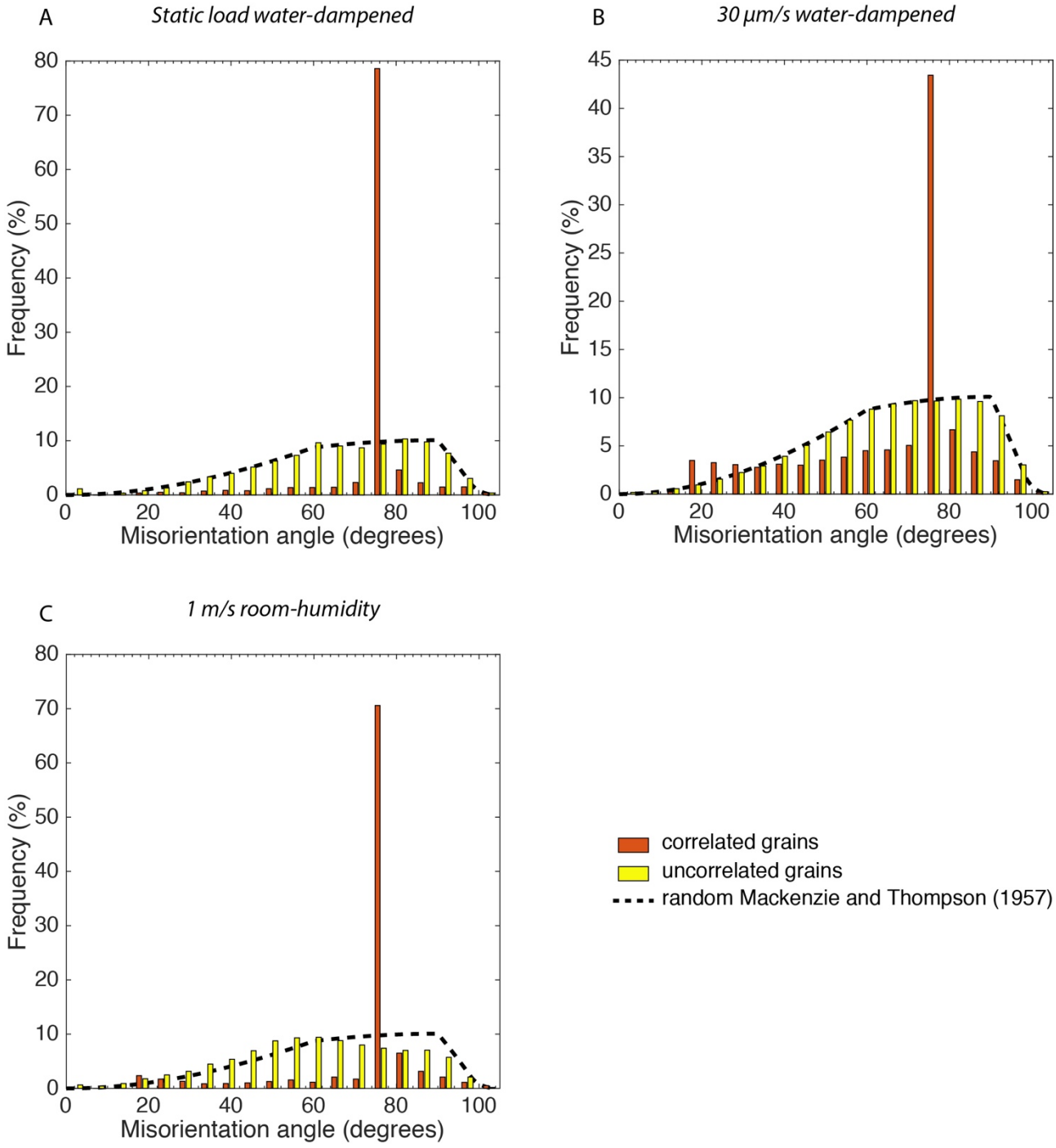


Fig. 8. Misorientation analysis. Misorientation angle distribution analysis on the a) undeformed and b) – c) sheared samples evidenced the occurrence of a random misorientation distribution, with the exception of a clear peak around ca. 70-80°. This misorientation angle is associated to the formation of *e*-twins in calcite.

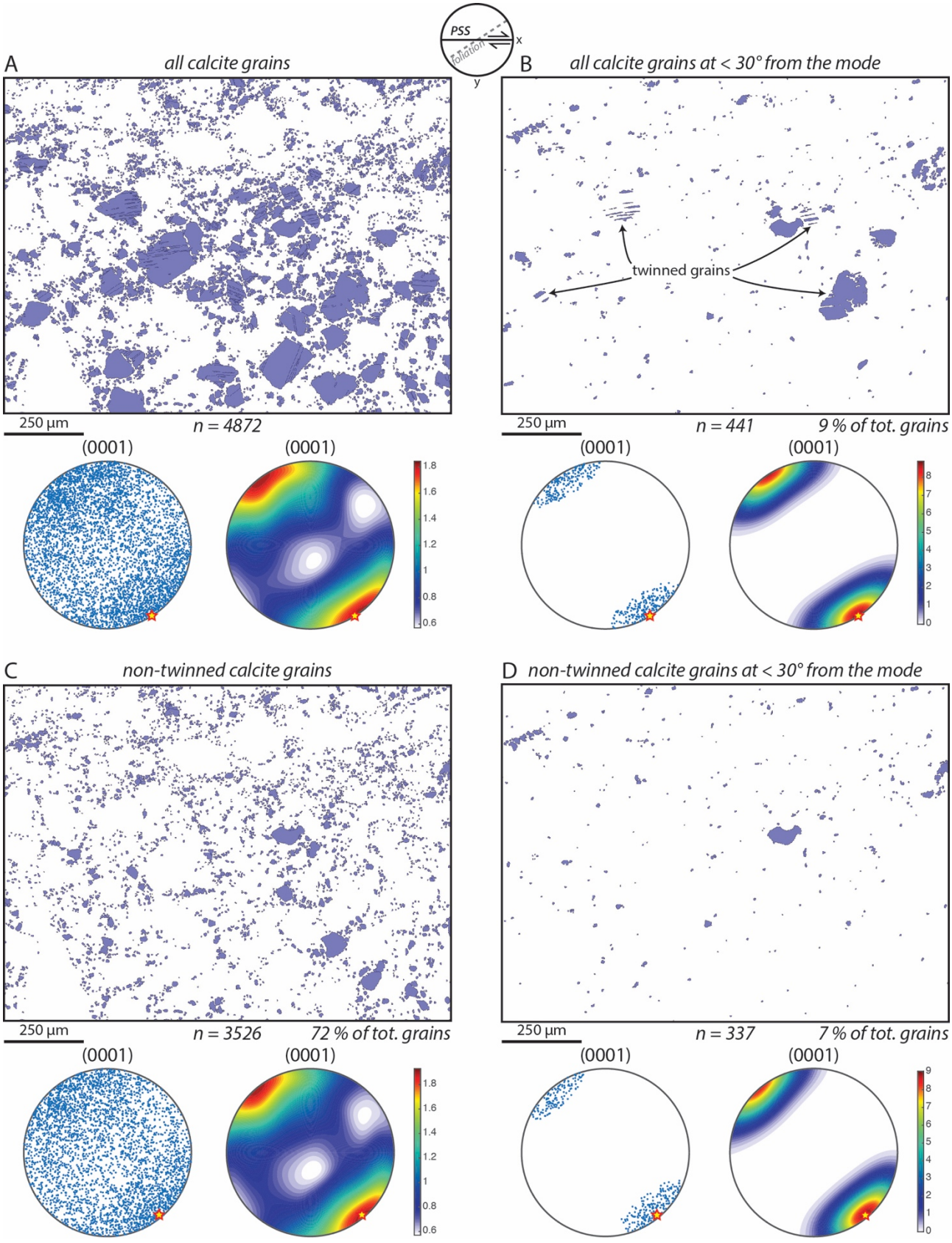


Fig. 9. See next page for caption.

Fig. 9. (previous page) Contribution of calcite grains to the CPO. a) All the calcite grains showed the development of a CPO with the c-axes oriented sub-parallel to the instantaneous shortening direction. b) The grains composing the CPO within a 30° radius cone from the mode were ca. 9% of the total grains and consisted in both small grains from the matrix and twinned grains. c) Orientation data from non-twinned grains showed no sensible changes in both the geometry and the intensity of the CPO. d) Non-twinned grains composing the CPO within a 30° radius cone from the mode consisted in small grains dispersed in the matrix and being ca. 7% of the total number of grains.

Fig. 10. (next page) Fracture and calcite twin planes orientation analysis. a) Under static load conditions, fractures were typically oriented sub-parallel to the vertical normal load. Calcite twins were few in number and scattered in orientation. b)–e) In sheared samples, fractures had a preferred orientation sub-parallel to the instantaneous shortening direction. Conversely, newly formed twins were oriented consistently with the dextral shear sense, being oriented sub-perpendicular to the instantaneous shortening direction.

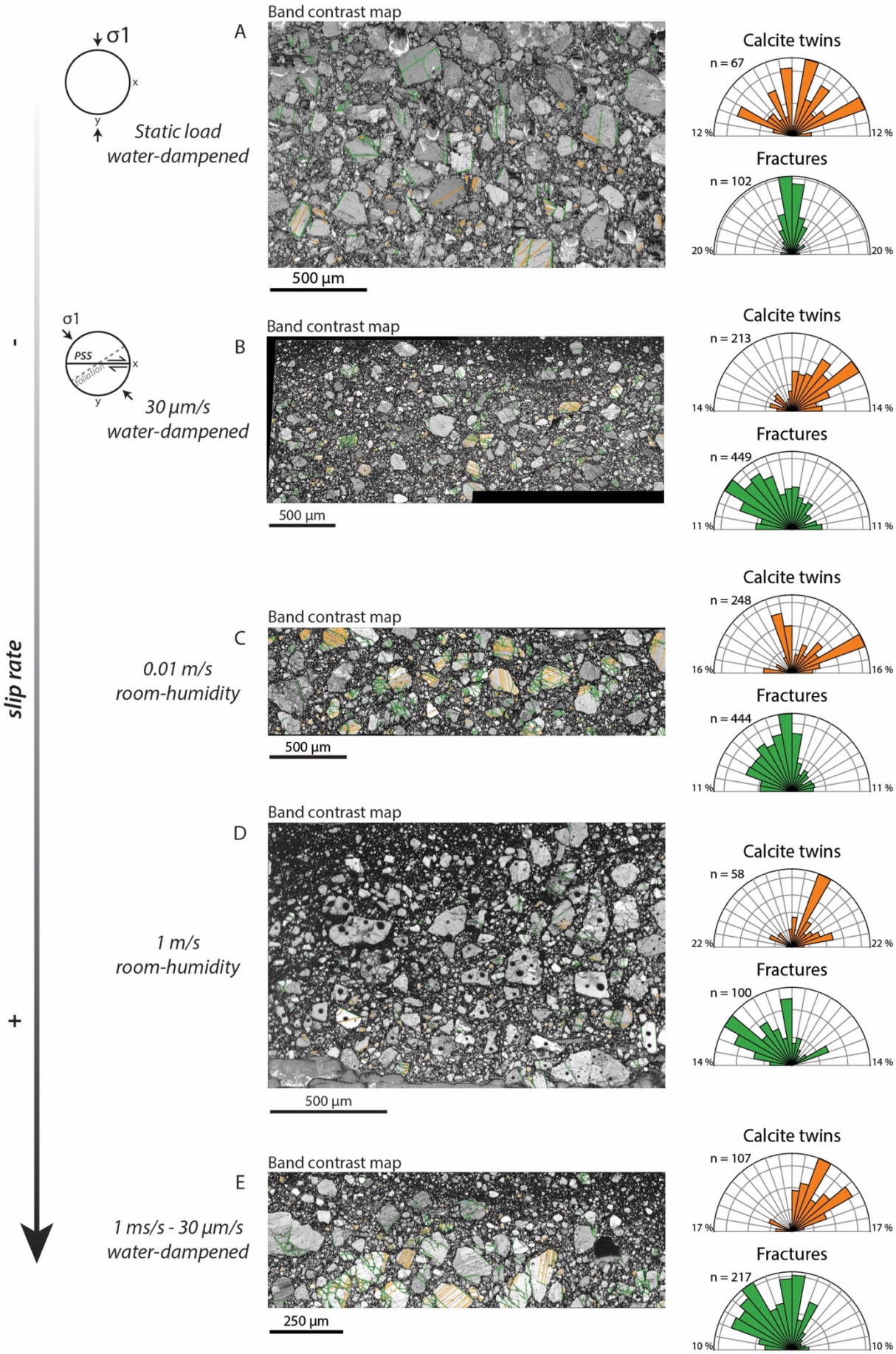


Fig. 10. See previous page for caption.

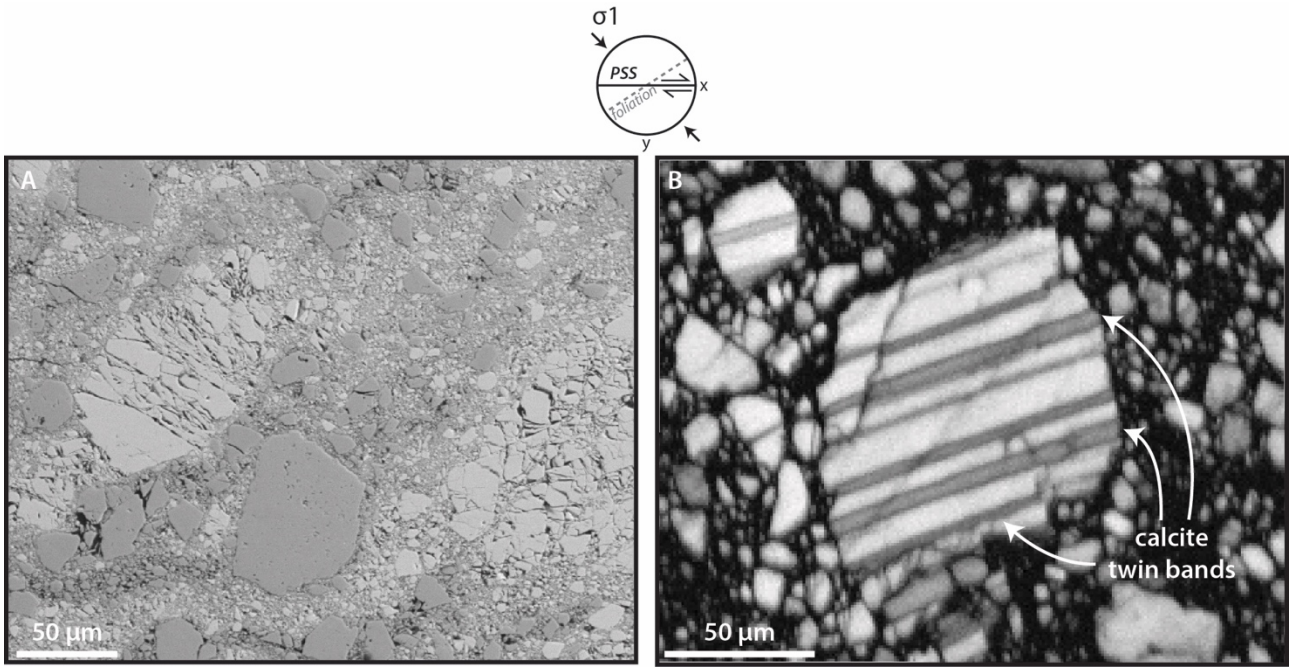


Fig. 11. Fracturing and twinning in calcite grains. a) Fractures in calcite typically exploited cleavage planes and were oriented sub-parallel to the instantaneous shortening direction. b) Conversely, *e*-twins were oriented consistently with the shear sense and almost sub-perpendicular to instantaneous shortening direction.

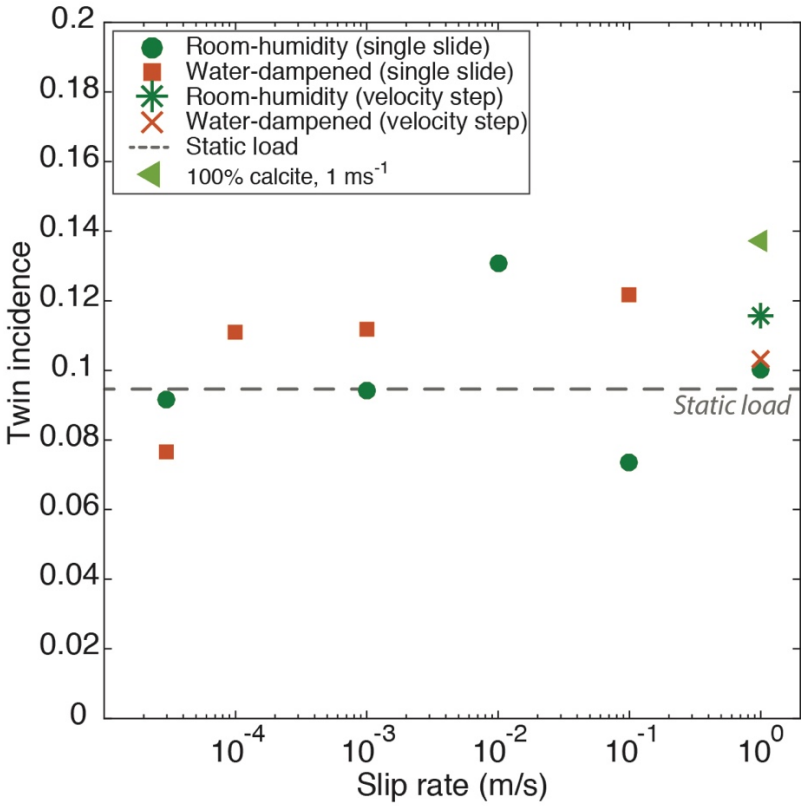


Fig. 12. Twin incidence vs. slip rate in calcite grains. Twin incidence analysis shows no clear dependence with the imposed slip rate. Moreover, there were no evident differences in the twin incidence between room-humidity and water-dampened experiments.

detailed microstructural characterization in Chapter II).

However, despite the negligible temperature rise, our analysis showed that a well-defined CPO developed in the gouge layers at all tested conditions, with the c-axes of the calcite grains oriented sub-parallel to the instantaneous shortening direction ($\sigma 1$) (Fig. 4). Moreover, the CPO was typically weaker in the case of water-dampened experiments (Fig. 7). No low misorientation angles (<20-30°) were observed in the gouges that underwent both static loading or shearing (Fig. 8), suggesting that dislocation activity and recrystallization were negligible in the bulk gouge. Instead, only twinning and brittle fracturing were identified as the active deformation mechanisms in calcite far from the principal slip zone (Fig. 8).

Therefore, we interpret the development of a CPO in the gouge experiments as the result of mechanical rotation and fracturing of grains along cleavage planes during the early stages of shearing, when strain and cataclasis occurred within the bulk gouge layer (Fig. 13). During static loading the calcite grains in the matrix are randomly oriented (Fig. 13a). Fracturing in the larger clasts occurs mainly sub-parallel to the vertical normal load applied, whilst calcite twins are few and scattered (Fig. 13a). At the initiation of shearing, calcite grains in the gouge matrix are interpreted to rotate until a population of grains have their c-axes oriented sub-parallel to the instantaneous shortening direction $\sigma 1$ (Fig 13b). At this stage, the grains in such an orientation would fracture relatively easily along cleavage planes (i.e., the rhomb planes) oriented sub-parallel to the c-axes. This is predicted to lead to the formation of a shape-preferred orientation, with elongate grains oriented sub-parallel to $\sigma 1$ (Fig 13b). This process may be capable of keeping the grains in a "stable" orientation within the deforming matrix. Although this process would ideally promote the development of a SPO, no evidence for a SPO was observed in the EBSD maps. One reason could reside in the way grains were defined in MTEX during data processing. Since we accounted also for the porosity within the gouge, we took care in avoiding MTEX to create fake contacts between the grains at the expenses of the real grain shape. High resolution grain shape analysis on SEM images will be needed to verify the possible development of a SPO in the bulk gouge. Finally, the weaker CPO in the case of the water-dampened experiments (Figs. 4-7) could be explained, with respect to the experiments conducted under room humidity conditions, by the more efficient stress corrosion and subcritical crack growth in the presence of liquid water (Atkinson and Meredith, 1987; Røyne et al., 2011). Efficient subcritical crack growth would result in faster fracturing, without the need for the calcite grains to rotate until they achieve the ideal orientation for failure under the applied stress. In addition, previous investigations on the mechanical role of water in cohesive and non-

cohesive calcite-built rocks during shearing showed, with respect to the experiments performed under room humidity conditions, a shorter strengthening phase at the initiation of slip in the presence of liquid water (Violay et al., 2014; Rempe et al., 2017). The shorter strengthening phase in the presence of liquid water was also concomitant to faster strain localization in the gouge layer (Violay et al., 2014; Rempe et al., 2017). Clearly, the latter would imply that less strain is accommodated in the bulk gouge prior to the onset of dynamic weakening, resulting in less grains having the possibility to rotate in an orientation optimal for fracturing. Furthermore, the presence of liquid water within the gouge would also inhibit, at least partially, the development of force chains by reducing the effective stress carried by grain bridges.

Our interpretation for the development of a CPO within granular materials during shearing can result in important implications for the investigation of deformation mechanisms in natural and experimental fault products. In fact, if previous studies (e.g., Smith et al., 2011, 2013; Verberne et al., 2013b) ascribed the occurrence of a CPO to temperature-dependent intracrystalline deformation during shearing, our results suggest that similar crystallographic orientations can be obtained through purely brittle deformation (i.e., fracturing) and minimum intracrystalline strain accommodation (i.e., twinning). Therefore, the identification of a CPO within gouges and cataclasites composed by mineral phases owing strong crystallographic anisotropies cannot be used as a reliable indicator for temperature-dependent deformation processes during seismic sliding. The integration of CPO data with microstructural observations on grain and grain boundary shapes is thus required to constrain the deformation conditions (seismic vs. aseismic) in gouges and cataclasites.

4.2. Applicability of paleopiezometry to granular materials

Twinning in calcite is a very common microstructural feature associated with low temperature (i.e., T < 400 °C) intracrystalline strain accommodation (Turner, 1953; Carter and Raleigh, 1969; Groshong, 1988; De Bresser and Spiers, 1997). In particular, calcite *e*-twinning has been largely studied as a very promising paleopiezometer (e.g., Turner et al., 1954; Jamison and Spang, 1976; Rowe and Rutter, 1990; Lacombe and Laurent, 1996; Laurent et al., 2000). As a result, applications of the calcite paleopiezometer to natural samples helped to estimate paleostresses in field-related studies (e.g., Lacombe, 2007; Rutter et al., 2007; Rybacki et al., 2011; Beaudoin et al., 2016). However, the empirical relationships obtained between twinning and the applied stresses

(Eqs. 1 and 2) were obtained from experiments performed with triaxial or torsion apparatuses and on marbles, mainly composed by calcite (e.g., Rowe and Rutter, 1990; Ferrill et al., 1998; Rybacki et al., 2013). To our knowledge, attempts to evaluate the influence of other phases on the relationships between mechanical twinning in calcite and applied stress have not been made yet. Moreover, paleopiezometry has been applied almost exclusively on crystalline calcite-bearing rocks. To date, only one attempt has been made of applying the calcite twin analysis to infer the stresses experienced in granular materials (Sakaguchi et al., 2011). Sakaguchi et al. (2011) examined and modelled the feasibility of inferring the paleo-elastic strain experienced in a granular material, by the plastic strain accommodated within calcite grains through mechanical twinning. Their results showed that for the case of rocks composed of mineral phases with various strengths, and thus an inhomogeneous internal distribution of the stresses, a statistical analysis of calcite twins could help estimate the paleo-elastic stress (Sakaguchi et al., 2011), even for calcite contents as low as ~ 5 %.

In our samples, calcite composed half of the deformed gouge. Mechanical *e*-twinning occurred mainly in the larger grains (ca. ≥ 100 μm in diameter) within the gouge. Only occasionally twins were detected in the grains composing the matrix (grain size < 20 μm). Paleopiezometry analysis resulted in estimated $\Delta\sigma$ of ca. 129 MPa for the static load, and higher differential stresses in the case of the sheared gouges (ca. 152 – 175 MPa). Such estimates are about one order of magnitude higher than the load applied in the experiments. An intuitive explanation for these unexpectedly high values might reside in the fact that larger calcite grains "feel" the local stresses associated with the development of force chains within the gouge layers during shearing and cataclasis. Force chains have been described in micromechanical models for fault friction evolution and comminution within gouge (e.g., Sammis et a., 1987; Sammis and Steacy, 1994; Cates et al., 1998; Sammis and King, 2007). Within a granular material with a non-homogeneous grain size distribution undergoing shear, the stress distribution is heterogeneous. The applied load at any given time is carried by a network of constantly evolving grain bridges spanning the gouge layer thickness (e.g., Sammis and Steacy, 1994). As a result, those grains bridges will be likely to experience greater stresses than the external stresses, while the other grains in the gouge layer will act as "spectators", sustaining very low stresses (even lower that the remotely applied). The overall (frictional) behavior of the gouge will be controlled by the process of dismembering and reforming such grain bridges through fracturing and grain rearrangement. (e.g., Mair et al., 2002).

In our experiments, calcite grains tend to act as the "soft" phase with respect to dolomite. This is evidenced by the more intense development of twins and fractures in calcite, resulting in a

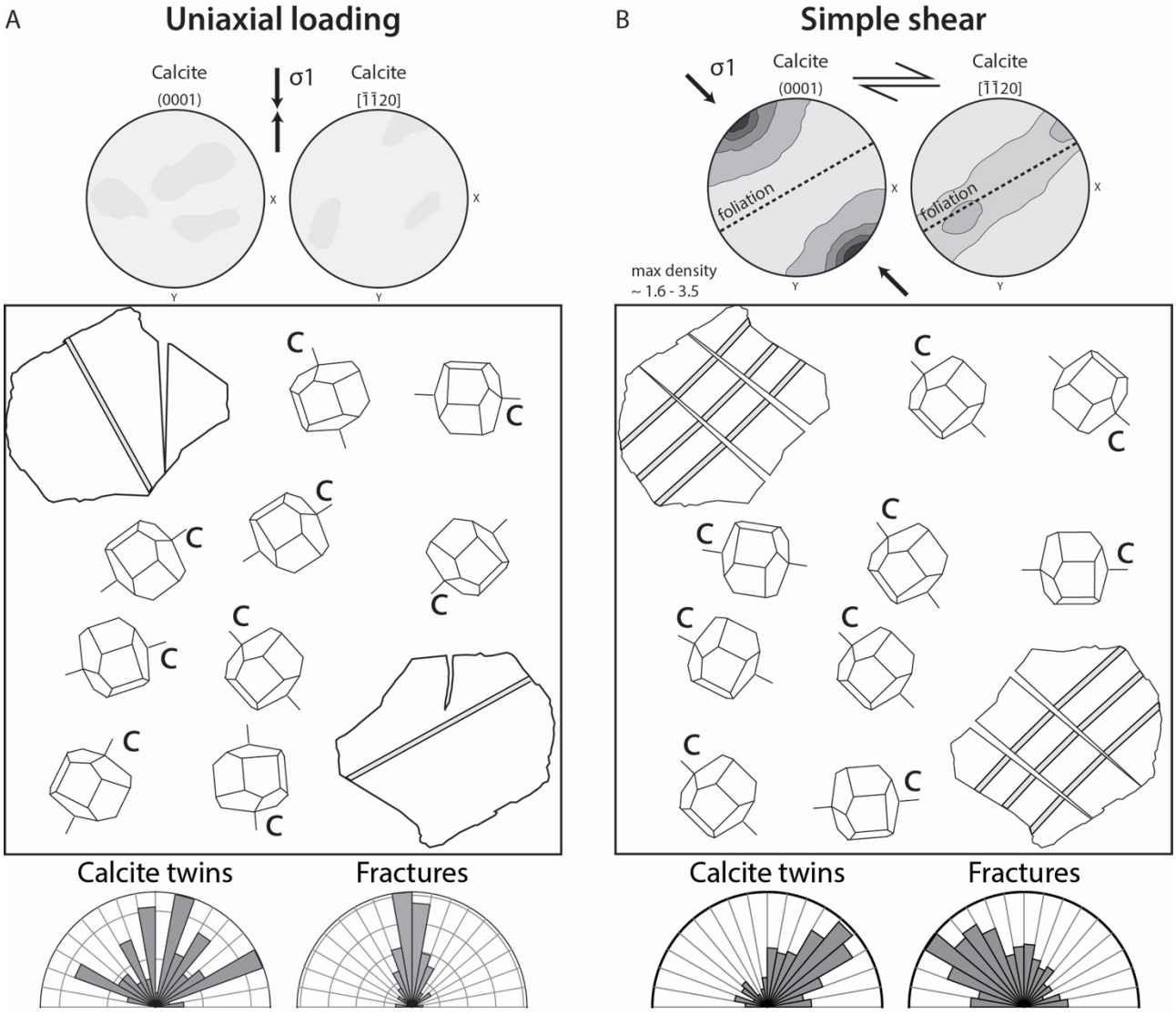


Fig. 13. Diagram showing CPO development in a granular material. a) During static (uniaxial) load, the gouge has a random orientation for calcite grains. Intragranular fractures are few and mainly oriented sub-parallel to the vertical normal applied load. Conversely, twin planes have a scattered orientation. b) Once the gouges are sheared, calcite develops a CPO in the grains of the matrix consisting in the c-axes clustered near the circumference of the pole figure and oriented sub-parallel to the shortening direction. Larger clasts (ca. > 100 μm in size) are commonly twinned, with twins being oriented consistent with the shear sense and roughly perpendicular to $\sigma 1$. Fractures are again found to be mainly parallel to $\sigma 1$.

relatively rapid grain size reduction in calcite compared to dolomite (Smith et al., 2017). The occurrence of fracturing sub-parallel to the instantaneous shortening direction has been interpreted as tensile fracturing due to failing of the grain bridges supporting the load (e.g., Mair and Hazzard, 2007; Sammis and Ben-Zion, 2008; Smith et al., 2017). Prior to fracturing, calcite grains within those grain bridges will be likely to have undergone much higher stresses than the applied 17.5 MPa. Moreover, in our case, the presence of a bimaterial system (i.e., calcite and dolomite) would promote concentration of stresses into the strong "skeleton", here represented by the dolomite grains. Therefore, for calcite grains surrounded by dolomite grains, the stress carried would be intuitively higher than in the case of a pure calcite gouge. As a conclusion, the high $\Delta\sigma$ estimates obtained from the calcite twin paleopiezometer could be an indication of the magnitude of the stresses that developed along grain bridges during cataclasis. An investigation of the magnitude of the force chains that develop during cataclasis through numerical models could support our interpretation and the feasibility of applying the calcite twin paleopiezometer as an indicator for stress distribution within granular materials during deformation.

4.3. Implications for natural faults

Our experiments demonstrate that crystallographic preferred orientations can develop in granular fault rocks over a wide range of deformation conditions. The development of a CPO in the gouges was interpreted as the result of mechanical grain rotation and subsequent fracturing exploiting the strong calcite crystal anisotropies (i.e., cleavage planes). We suggest that CPO development in the bulk gouge is mainly influenced by the characteristic anisotropies of calcite. This suggests that cataclasis and the evolution of gouge grain size distribution in the shallowest portions of the crust (e.g., < 2-3 km) could be strongly influenced by the occurrence of mineral phases with strong anisotropies. This includes calcite, but also other common gouge-forming phases such as phyllosilicates, amphiboles, and feldspars.

Twins are a common occurrence within calcite-bearing rocks (e.g., Fernández et al., 2004; Smith et al., 2013; Collettini et al., 2014). Our investigation suggests that calcite twin paleopiezometry in fault gouges and cataclasites could record the stress distribution during force chain development in the early stages of cataclasis (e.g., Mair and Hazzard, 2007). However, prolonged cataclasis, and related grain size reduction, would likely progressively hinder the ability

and reliability of the analysis. Finally, incorporation of CPO development by mechanical grain rotation and preferred fracture and twin alignments in calcite, together with other physico-chemical processes active during deformation, could provide a more complete model for gouge friction evolution in carbonate rocks.

5. Conclusions

Electron backscatter diffraction (EBSD) analysis was performed on calcite-dolomite gouges deformed in rotary-shear experiments at slip rates of 30 μms^{-1} – 1 ms^{-1} under a normal load of 17.5 MPa and both room-humidity and water-dampened conditions.

Under all tested conditions, calcite in the bulk gouge layers developed a well-defined crystallographic preferred orientation (CPO), consisting of c-axes oriented sub-parallel to the instantaneous shortening direction, and poles to the a-axes direction forming a girdle sub-perpendicular to the c-axes cluster. The formation of a CPO was interpreted to reflect mechanical grain rotation and subsequent fracturing along cleavage planes oriented sub-parallel to the instantaneous shortening direction. Water-dampened gouges showed a weaker CPO than gouge deformed at room-humidity, likely due to easier and faster fracturing of calcite (Røyne et al., 2011) during cataclasis, faster strain localization and partial inhibition of force chain development.

Calcite twin analysis showed a systematic preferred orientation for calcite twin planes consistent with the shear sense and sub-perpendicular to the instantaneous shortening direction. Fracturing occurred mostly in the larger grains and with an orientation sub-parallel to $\sigma 1$. Calcite twin paleopiezometry analysis resulted in differential stress estimates of ca. 152-175 MPa, roughly one order of magnitude higher than the applied load. Such high values were interpreted as a record by calcite grains of the maximum magnitude of stresses carried by grain bridges that formed within the gouge during cataclasis.

Overall, our experiments show that well-defined CPOs can develop by brittle mechanisms in granular fault rocks over a wide range of conditions. This has important implications for the interpretation of CPOs in the fault record and the understanding of frictional and mechanical properties of gouge during shear.

6. Tables

	Experiment	*Target slip rate* ms^{-1}	*Displacement* *m*	*EBSD analysis*	*Eigenvalue texture analysis*	*Twins/fracture analysis*	*Calcite twin paleopiezometry*
Room-humidity							
	s1322	0.00003	0.1	x	x		
	s1323	0.001	0.1	x	x		
	s1217	0.01	0.4	x	x	x	x
	s1218	0.1	0.4	x	x		
	s1221	1	0.4	x	x	x	
	s1223	0.00003 – 1	0.1 – 0.3	x	x		x
Water-dampened							
	s1327	0.00003	0.05	x	x		
	s1329	0.00003	0.1	x	x		
	s1328	0.00003	0.2	x	x		
	s1214	0.00003	0.4	x	x	x	
	s1330	0.00003	0.4	x	x		
	s1215	0.0001	0.4	x	x		
	s1213	0.001	0.4	x	x		
	s1220	0.1	0.4	x	x		
	s1226	1 – 0.00003	0.3 – 0.1	x	x	x	x
Static load water-dampened	slw			x	x	x	x
Calcite Room-humidity	s269	1	2.61	x	x	*Note: normal load of 8.5 MPa*	
Dolomite Room-humidity	s525	0.1	0.86	x	x		

Table 1. Summary of texture and fabric analysis.

Experiment		*Twin density* mm^{-1}	*n Grains*	$\Delta\sigma$ *Rybacki* *MPa*	$\Delta\sigma$ *R&R* *MPa*
s1217	range	14 – 150	65	**156 ± 39**	**248 ± 43**
	average	**64 ± 32**			
s1223	range	12 – 128	36	**152 ± 37**	**245 ± 43**
	average	**60 ± 25**			
s1226	range	22 – 119	20	**175 ± 45**	**266 ± 43**
	average	**78 ± 27**			
slw	range	7 – 92	28	**129 ± 30**	**217 ± 43**
	average	**45 ± 23**			

Table 2. Results of calcite twins analysis.

Chapter IV

Transmission Kikuchi Diffraction nanoscale investigation of experimental seismic faults in carbonates

This study was performed with the collaboration of Steven A.F. Smith, David J. Prior, Frank E. Brenker and Giulio Di Toro. I performed all the work described in this chapter. Sample preparation was carried out in collaboration with Frank E. Brenker. I was assisted (but not continuously) during TKD analysis by Steven A.F. Smith and David J. Prior. The material presented here was discussed with Steven A.F. Smith and Giulio Di Toro.

Abstract

In the last decade, nanoparticles (<< 1 µm) have been reported along the localized slip zones of both natural and experimental faults. Although various deformation processes have been implicated in their formation, their origin (seismic vs. aseismic) and mechanical behaviour on fault slip surfaces is still poorly understood. Understanding the deformation processes that produce nanoparticles and nanoparticle aggregates in faults requires an understanding of their grain sizes, shapes, crystallographic orientations and grain boundary structures. However, to understand the crystallographic characteristics of nanograins over reasonable sample areas (i.e., 10^{3-4} µm^2), higher spatial resolution than is currently possible using standard EBSD techniques is required. Transmission Kikuchi Diffraction (TKD) in the SEM is a newly developed microanalytical technique that allows orientation mapping to be performed on electron transparent foils with a standard EBSD system. TKD can achieve a resolution of 1-2 nm and thus opens a new door to studying deformation processes and crystallographic orientations in nanoparticles.

We present results of TKD analysis performed on large electron-transparent foils (foil area of ca. 10^4 µm^2) prepared from gouges composed of a mixture of 50 wt% calcite and 50 wt% dolomite. The gouges were deformed at coseismic slip rate (i.e., 1 m^{-1}) for a total displacement of 0.4 m, under a normal load of 17.5 MPa and at room-humidity conditions. Coupled TKD-EDS analysis allowed visualization of Ca distribution in the principal slip zone at a scale of tens of nanometers. Preliminary results show a principal slip zone composed of nanograins ranging in size from 100-2068 nm, with two population centered around grain sizes of ca. 100 nm and 250 nm. Nanograins were equant and showed quadruple and ca. 120° triple junctions. Smaller grains (< 700 nm) were characterized by low internal misorientation suggesting low dislocation density, whilst larger grains (> 800) showed higher values of internal misorientation, as well as development of sub-grains of approximately the same size as recrystallized grains in the matrix. A weak crystallographic preferred orientation was observed that progressively disappeared moving along the principal slip zone. These observations suggest the activation of grain-size sensitive deformation mechanisms within the nanoparticles in the principal slip zone, which accommodated coseismic strain by grain-boundary sliding aided by diffusion creep (i.e., superplastic flow).

1. Introduction

In the last decade, nanoparticles (<< 1 μm) have being widely reported along both natural (e.g., Chester et al., 2005; Wilson et al., 2005; Ma et al., 2006; Pittarello et al., 2008; Siman-Tov et al., 2013; Fondriest et al., 2015; Demurtas et al., 2016; Smeraglia et al., 2017a) and experimental fault slip zones (e.g., Han et al., 2007b, 2010; Reches and Lockner, 2010; De Paola et al., 2011b; Han et al., 2011; Tisato et al., 2012; Chen et al., 2013; Verberne et al., 2013b, 2014; De Paola et al., 2015; Green et al., 2015; Spagnuolo et al., 2015; Yao et al., 2016; Aretusini et al., 2017; Smeraglia et al., 2017b). Some hypotheses have been proposed regarding their formation, which include (i) thermal decomposition (e.g., Han et al., 2007b; Green et al., 2015), (ii) shock loading (Wilson et al., 2005; Spagnuolo et al., 2015), (iii) subcritical crack growth in compression (Sammis and Ben-Zion, 2008), (iv) high tensile strain rates (Sammis and Ben-Zion, 2008) or (v) mechanical milling (Siman-Tov et al., 2013). However, the role of nanograins during frictional sliding remains poorly understood. This is because (i) their physical properties, size and texture can highly influence the effect on the fault mechanical properties (e.g., grain size dependent processes), (ii) the commonly used microanalytical techniques fail to allow us a complete characterization of such materials and (iii) their very small grain size makes them extremely reactive. In the latter case, the shape, size and often the mineral composition of the particles during shearing might be different from those achieved during deformation. This, for instance, resulted in contrasting interpretations of the deformation mechanisms activated in the experiments reproducing seismic slip conditions (see below). Additionally, because nanoparticles were found both in experiments simulating aseismic and seismic deformation conditions and slip rates (e.g., Han et al., 2010; Tisato et al., 2012; Verberne et al., 2013b; Spagnuolo et al., 2015; Smeraglia et al., 2017b), it is still doubtful whether there is a peculiar microstructural feature in nanoparticles that would ascribe their formation to a specific fault slip behavior (seismic vs. aseismic).

Perhaps more relevant, the role of the presence of nanoparticles on the frictional and rheological properties of fault zones during the seismic cycle is also debated. High-velocity rock friction studies aimed at reproducing seismic slip deformation conditions, introduced the term “powder lubrication” to describe the process responsible for dynamic fault weakening concomitant to the production of nanoparticulate aggregates in the slip zone (e.g., Han et al., 2010; Reches and Lockner, 2010; Han et al., 2011; Tisato et al., 2012). However, the dynamic fault weakening itself may not be directly related to the formation of nanograins. Some studies have interpreted dynamic weakening as the result of a switch from high sliding friction to low rolling friction, with

nanoparticles that start to roll along the fault slip surface instead of sliding (Han et al., 2011). More recent experimental studies performed at high-velocity (slip rate V = 1 ms^{-1}) have explored the possibility that nanoparticles could influence fault rheological properties due to the activation of "viscous" deformation mechanisms. In particular, the production of nanoparticles coupled with temperature rise due to frictional heating could promote grain-size sensitive deformation mechanisms such as grain boundary sliding (GBS) aided by dislocation- or diffusion creep (i.e., superplastic flow *lato-sensu*), leading to efficient strain accommodation and dynamic weakening (De Paola et al., 2015; Green et al., 2015; Spagnuolo et al., 2015). The evidence of the possible activation of these deformation mechanisms was supported by Scanning- (SEM) and Transmission Electron Microscope (TEM) observations. High magnification microstructural investigation showed the presence in the experimental slip zones of equant nanograins (from 10 to 600 nm in size) forming a foam-like fabric with 120° triple junctions and with a low density of dislocations (De Paola et al., 2015; Green et al., 2015; Spagnuolo et al., 2015). Such microstructures are typically associated to superplastic flow (Poirier, 1985).

Regarding the low-velocity regime (V ≤ 100 μms^{-1}), microstructural observations on calcite gouges produced at V = 1-10 μms^{-1} suggest that they also deformed by grain boundary sliding (GBS) aided by dislocation- or diffusion creep (Verberne et al., 2014). Verberne et al. (2014) suggested that sintering occurred between the nanograins, leading to the development of nanofibers that deformed by a granular flow mechanism similar to the one proposed by Niemeijer and Spiers (2007). According to the authors, this micro-physical mechanism involves the competition between dilation caused by grain-neighbor swapping and compaction due to active diffusive mass transfer (Verberne et al., 2014). Moreover, the presence of a crystallographic preferred orientation (CPO) within shear bands cutting the gouge was interpreted as the result of cataclastic flow aided by shear-induced dislocation glide at the grain contacts (Verberne et al., 2013b).

To date, the investigation of deformation mechanisms active within nanoparticle aggregates has been performed mainly by SEM and TEM analyses. Limitations to the spatial resolution of conventional electron backscatter diffraction (EBSD) analysis (ca. 300-500 nm; Prior et al 1999) has hindered the application of this technique to the study of nanoparticles in natural and experimental slip zones. Because of this, no data are currently available to quantify the crystallographic preferred orientation (CPO) of nanograins and nanograin aggregates, grain boundary misorientations, internal lattice distortions and slip systems activity. Although some of these information can be obtained through TEM analysis, the latter typically lack of statistical significance (i.e., large data collection

would be highly time and money consuming) and, more relevant, loss of the overall microstructural context given the extremely limited volume of the analyzed sample. Clearly, robust statistical analysis of significant volumes of nanogranular aggregates would allow us to test the hypotheses regarding the mechanisms that control deformation in natural and experimental slip zones.

In the last few years, a novel technique called Transmission Kikuchi Diffraction (TKD) has been developed and applied in material science studies (e.g., Trimby, 2012; Trimby et al., 2014). The TKD allows the investigator to obtain the same type of information as in conventional EBSD analysis, but with the advantage of a significantly higher spatial resolution (i.e., 1-2 nm; Trimby, 2012). Application of TKD to geological problems is in its infancy, and, to our knowledge, there is currently only one published paper where TKD data collected from geological materials are discussed (i.e., diamonds: Piazolo et al., 2016).

The overall aim of this chapter is to apply the TKD technique to study nanomaterials produced in high-velocity deformation experiments performed on carbonate gouges, and to use the new nano-structural observations to test hypotheses regarding the deformation mechanisms active during seismic faulting in experiments and, possibly, in nature.

2. Methods

2.1. Starting materials and sample preparation

The TKD analysis was performed on a sample of gouge composed of 50 wt.% calcite and 50 wt.% dolomite after being sheared at a peak slip rate of 1 ms^{-1} for 40 cm of slip in room-humidity conditions and under a normal stress of 17.5 MPa (for a complete microstructural and mechanical characterization see sample s1221 in Chapter II).

Sample preparation for TKD analysis was carried out by Argon Ion Slicing (ArIS) following the methods outlined in Stojic and Brenker (2010). One of the main advantages of the ArIS technique is that very large (in the range of 2-4*10^4 μm2) electron-transparent sample areas can be obtained, much larger than the foils produced with Focused Ion Beam (FIB) technique (i.e., ca.

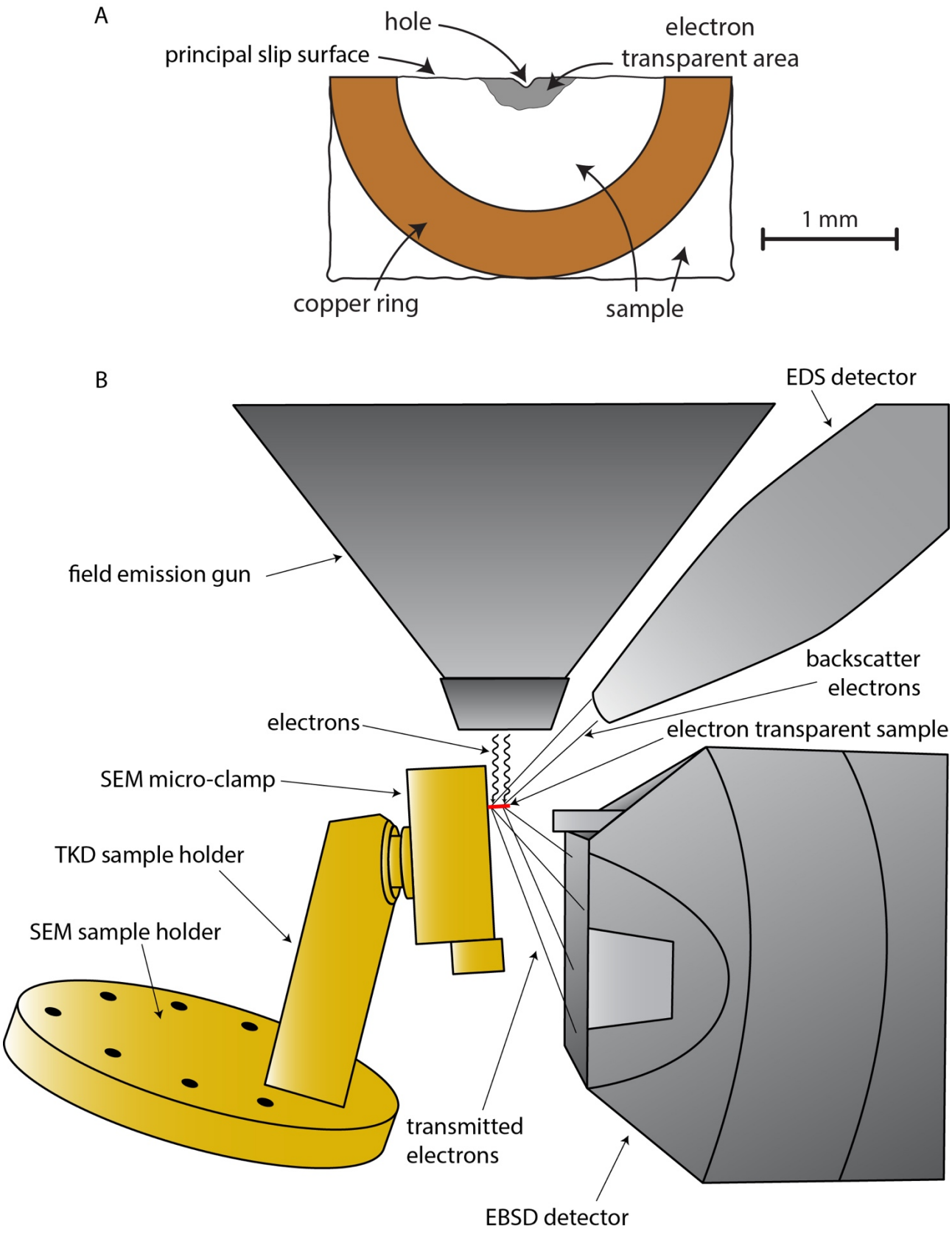


Fig. 1. See next page for caption.

Fig. 1. (previous page) Transmission Kikuchi Diffraction (TKD) in the SEM setup. a) The sample thinned through the ArIS technique was typically characterized by a lagoon-shaped electron transparent area, surrounding a hole, as a result of the argon beam hitting the sample. b) Conversely to standard EBSD analysis, the thinned sample was mounted on an ad-hoc sample holder and back-tilted of 3.3° in respect to the horizontal (compare the diagram with Fig. 1 in Chapter III). The EBSD detector was kept at a position of 211.6 mm and the working distance was typically ca. 8 mm. The SEM was operated at an accelerating voltage of 30 kV and a beam aperture of 120 µm. The diffraction patterns collected by the EBSD detector came from the lowermost part of the electron transparent area.

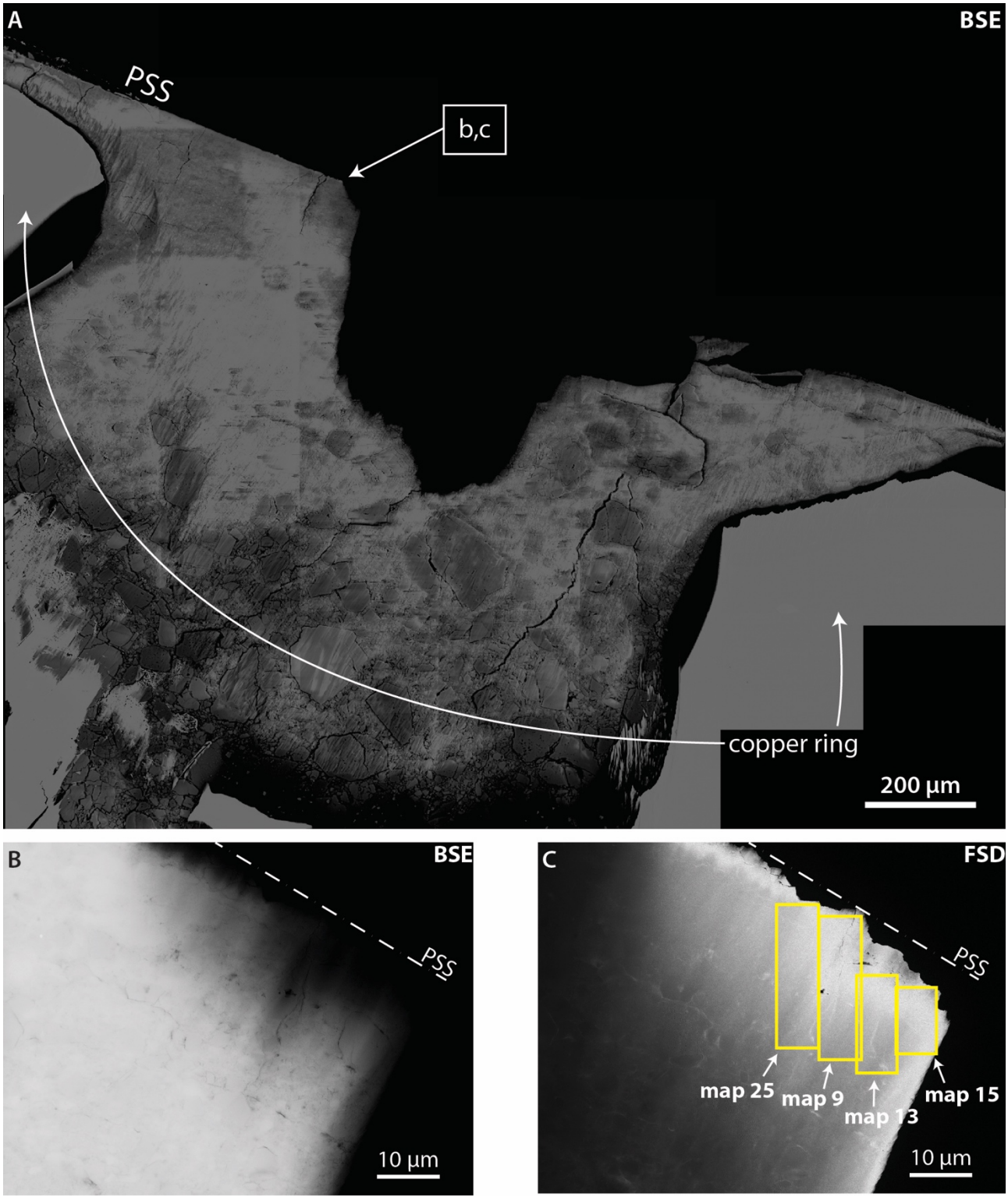


Fig. 2. Experimental sample analyzed. a) Backscatter electron montage of experiment s1221. b) Detail on BSE of the analyzed area. c) Images with the forescatter detector (FSD) allowed to see electron transparent areas, where the TKD analysis focused. Areas analyzed are depicted in yellow rectangles.

250 μm^2). Moreover, since the thin film produced during ArIS is oriented sub-parallel to the argon beam propagation direction, the sample is almost unaffected by irradiation damage, which is a common issue when performing argon ion milling.

A petrological thin section 100 µm thick was prepared from the recovered experimental sample. The thin section was cut at high angles to the slip vector (i.e., tangential cut) and attached to the glass with superglue. The area of interest on the experimental slip surface was then identified and a rectangle of dimension 3 X 2 mm was removed by means of an ultrasonic drill ("sample" in Fig 1a). Half of a circular TEM grid was glued on to the sample (Fig 1a), and everything was immersed in acetone to remove the glass slide. The sample was then mounted inside a JEOL SM – 09010 Cross Section Polisher to polish the sample edges. Finally, the sample was inserted in a JEOL EM-09100IS argon ion slicer. The duration of the thinning procedure varied greatly depending on the sample, with run times typically > 4-5 hours. The ArIS procedure produces an elongate electron-transparent area along the leading edge of the sample, corresponding in this case to the position of the experimental slip surface (Fig 1a). The sample described in this chapter contained an electron transparent area that was c. 900 µm long along the experimental slip surface and c. 450 µm in width away from the slip surface (Fig 2a).

2.2. Transmission Kikuchi Diffraction analysis

The TKD in the SEM is a microanalytical technique that has only recently been developed and successfully applied in material science studies (Trimby, 2012). One of the main advantages of the TKD technique resides in the very high spatial resolution (i.e., ca. 2 nm) at which the orientation analyses can be performed. This significant improvement in the spatial resolution with respect to conventional EBSD analysis is achieved by the use of an electron transparent sample that is mounted nearly horizontally in the SEM (Fig 1b; compare to the 70° tilt in conventional EBSD analysis, e.g., Fig. 1 in Chapter III).

The TKD analysis was performed on a Zeiss Sigma VP Field-Emission-Gun Scanning Electron Microscope equipped with a NordlysF EBSD camera from Oxford Instruments, located at the Otago Centre for Electron Microscopy, University of Otago (New Zealand). Raw data were collected and processed using AZtec software (Oxford Instruments). The sample was mounted on a micro-clamp

SEM sub-stage that was fixed to a standard SEM sample holder and back-tilted 3.3° from horizontal (Fig. 1b). The sample was kept at a working distance of ca. 8 mm and the EBSD detector was kept at a position of 211.6 mm. The SEM was operated with an accelerating voltage of 30 kV and a beam aperture of 120 µm. Since the electron transparent sample was not carbon-coated, the analysis was performed under variable pressure conditions: charging on the sample surface was avoided thanks to small quantities (a few tens of Pa) of nitrogen being kept inside the chamber.

Before the analysis, identification of the electron transparent area immediately beneath the principal slip surface (PSS) was done by imaging the sample both with backscattered electrons (BSE; Fig. 2a-b) and forescattered electrons (FSD; Fig. 2c). Given the extremely sensitivity of the TKD technique to sample thickness, several tests had to be performed to determine the most suitable electron-transparent area for analysis. For high-quality diffraction patterns the sample should be around 100 nm thick or less (Trimby, 2012). The TKD data were collected at a step size ranging from 20 nm - 50 nm (Table 1). In one case, coupled EDS-TKD analysis was performed with a step size of 35.3 nm (map 15). During the analysis, the Transmission Kikuchi Diffraction patterns were stored, allowing the quality of indexing to be improved in the post-processing stage.

The TKD analysis was focused on an electron transparent area located between 1.2 µm and 21.75 µm beneath the experimental PSS (Figs. 2c, 3). Previous microstructural observations (see Chapter II) indicated that this part of the sample likely accommodated most of the strain during deformation and underwent thermal decomposition of the dolomite. Four adjacent maps were obtained from this area allowing analysis of a total sample area of c. 30 µm x 30 µm (Figs. 2c, 3; Table 1).

2.3. Data cleaning and processing

Raw TKD maps were typically characterized by indexing rates between 13-33 % (that is the percentage of indexed pixels). These rates are substantially lower than in polycrystalline metals and alloys (indexing > 60 % on raw TKD maps; Trimby, 2012), mainly due to the geological samples having variable thickness and a high number of mineralogically-similar phases included in the analysis (i.e., calcite, dolomite, lime and periclase). Reanalysis of the stored TKD patterns was done by assuming that calcite was the only phase present. This is due to the fact that the processing of the Kikuchi

bands from the automated band detector algorithm decreases the reliability of the solutions if the system comprises similar mineral phases, resulting in low indexing rates. This simple step improved the overall indexing (30-40%). Further data cleaning was performed through the EBSDinterp 1.0 software (Pearce, 2015), a MATLAB program developed to perform microstructurally-constrained interpolation of non-indexed EBSD points. The software allows grains to be "grown" while taking in to account the pattern quality of the band contrast image, and thus not interpolating orientation data in to areas with no data. This further cleaning process allowed the TKD maps to have an overall indexing rate between 51-96%.

During the TKD analysis, the AZtec software interpreted the orientation of the patterns as if the sample was oriented like a conventional EBSD analysis (i.e., 70° tilt towards the EBSD detector). Therefore, before performing any type of orientation analysis, TKD data had to be rotated to match the exact orientation of the sample during the analysis (i.e., back-tilt of 3.3°). This step was performed in the CHANNEL5 software (from HKL Technology, Oxford Instruments). Once rotated, TKD data were processed in MTEX, using the same grain reconstruction approach described in Chapter III. Grain boundaries were hand-traced from the band contrast images (Fig 3b) and grain size analysis was performed in Image SXM (Fig. 4; Barrett, 2015). The band contrast map (or pattern quality map) gives an indication of the quality of the diffraction patterns: high quality patterns would result in bright areas, whilst dark or black pixels would indicate low quality pattern (e.g., grain boundaries or pores). Grain size was calculated as the diameter of an equivalent circle. Grains touching the border of the maps were not included in the analysis.

3. Results

3.1. Grain size analysis of the experimental slip zone

Figure 4 shows the result of the grain size analysis performed on the four band contrast maps (Fig. 3). A lower grain size cut off was set at 100 nm due to limits of the resolution at which the TKD analysis was performed (i.e., 20 to 50 nm). The very large grains that can be seen in Fig. 3 were not included in the grain size analysis as they were touching the map borders. Overall, the grain size distribution shows a range up to 2068 nm and a median value of 252 nm. However, the

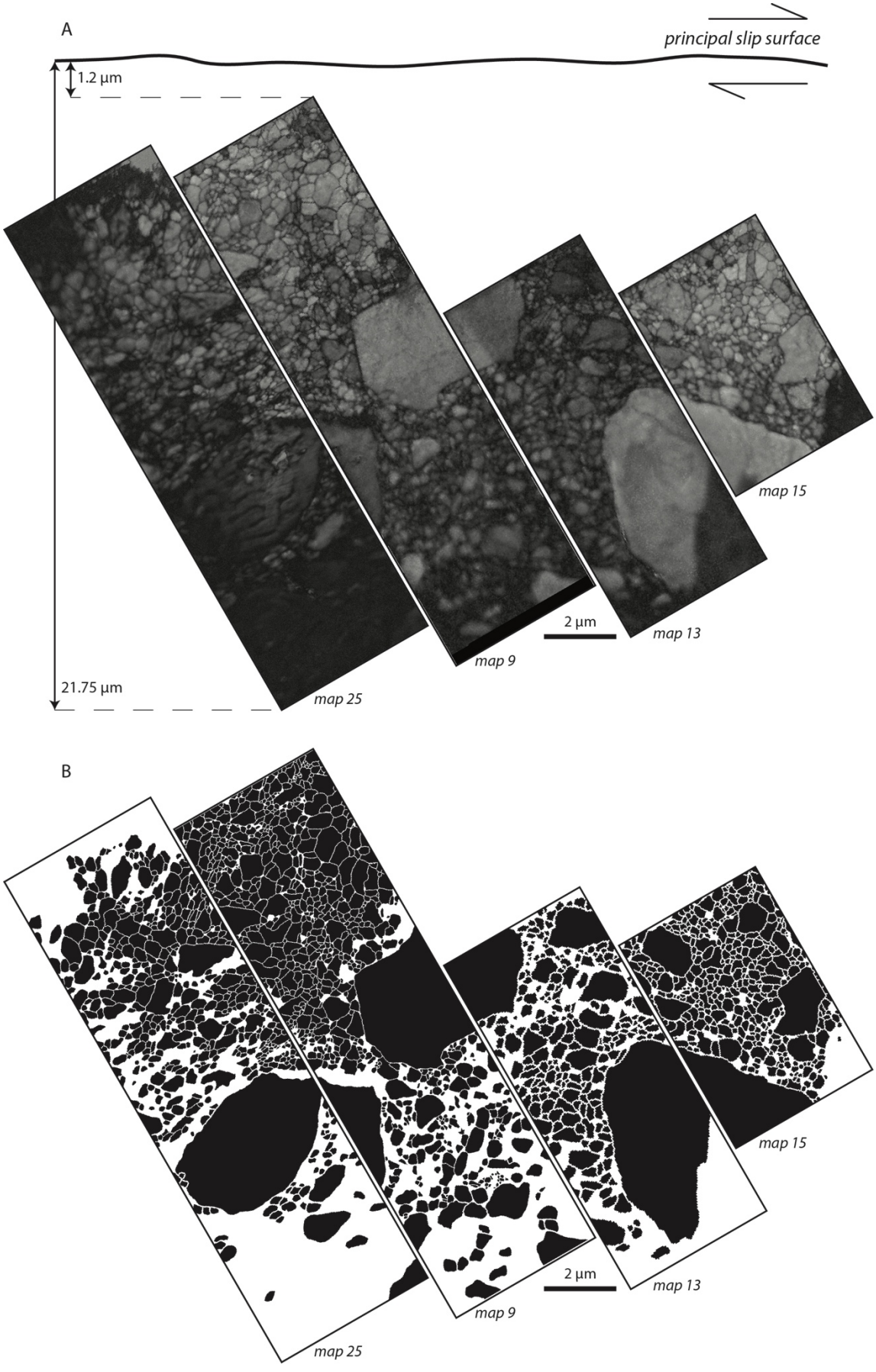


Fig. 3. See next page for caption.

Fig. 3. (previous page) Band contrast maps and hand-traced grains. a) TKD band contrast maps and relative location to the PSS. The area analyzed ranged from 1.2 µm up to 23.75 µm from the PSS. Darker areas (i.e., poor quality data to no data) indicate thickness variations in the sample probably not transparent to electrons anymore. b) Grains (in black) were hand-traced from the band contrast images. Grains touching the edges of the maps were not accounted during the grain size analysis.

Fig. 4. (next page) Grain size analysis. a) Grain size analysis showed the presence of a bimodal distribution, with a population being around 100 nm and a second one at about 250 nm. A lower bound was set at 100 nm due to the resolution of the TKD maps (i.e., 20 to 50 nm). b) Aspect ratio vs. grain size. Grains were equiaxed, with the aspect ratio being typically < 2.5. c) Orientation of the long axis of the fitted ellipse for grains with an aspect ratio > 1.3. No clear development of a shape preferred orientation was observed.

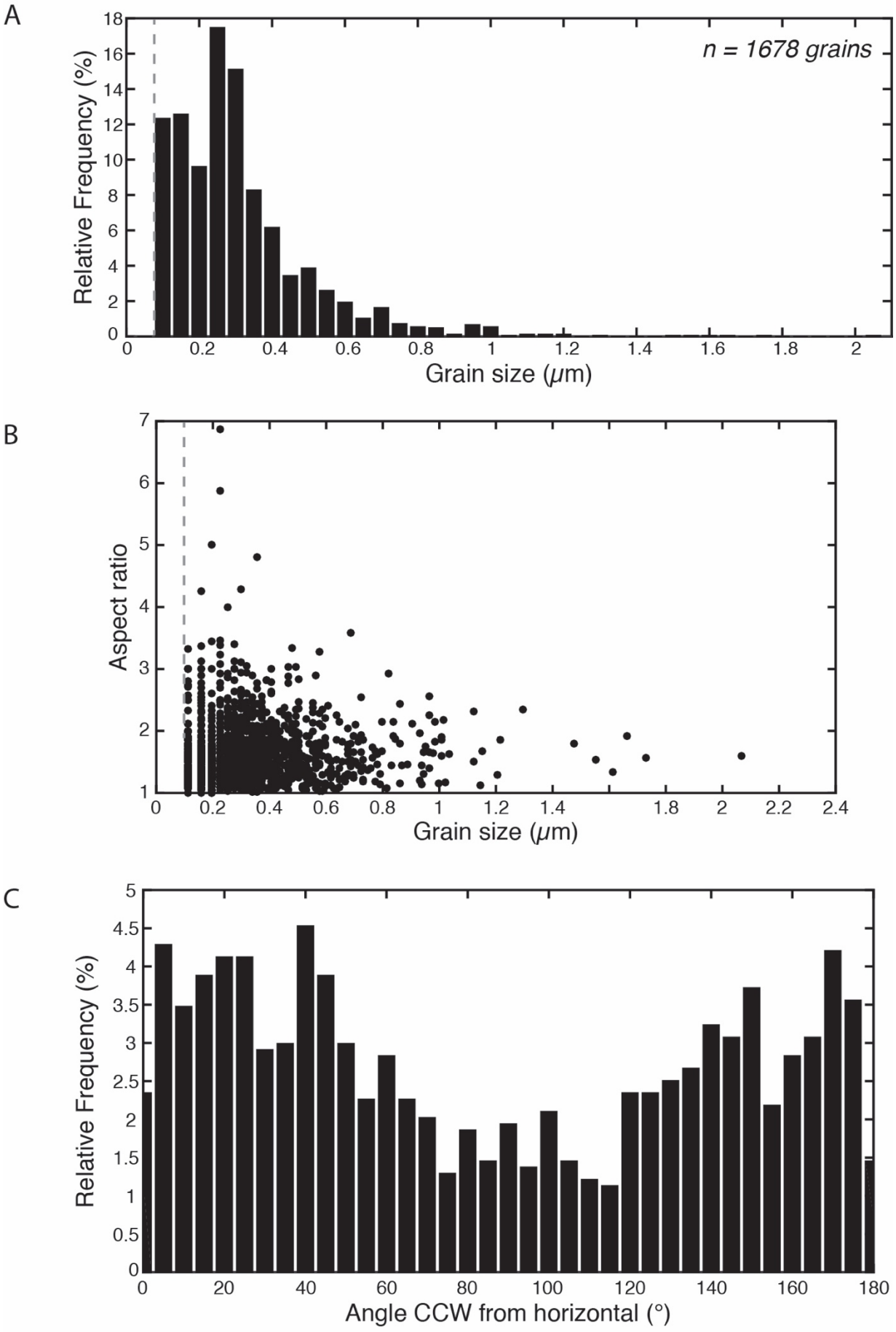


Fig. 4. See previous page for caption.

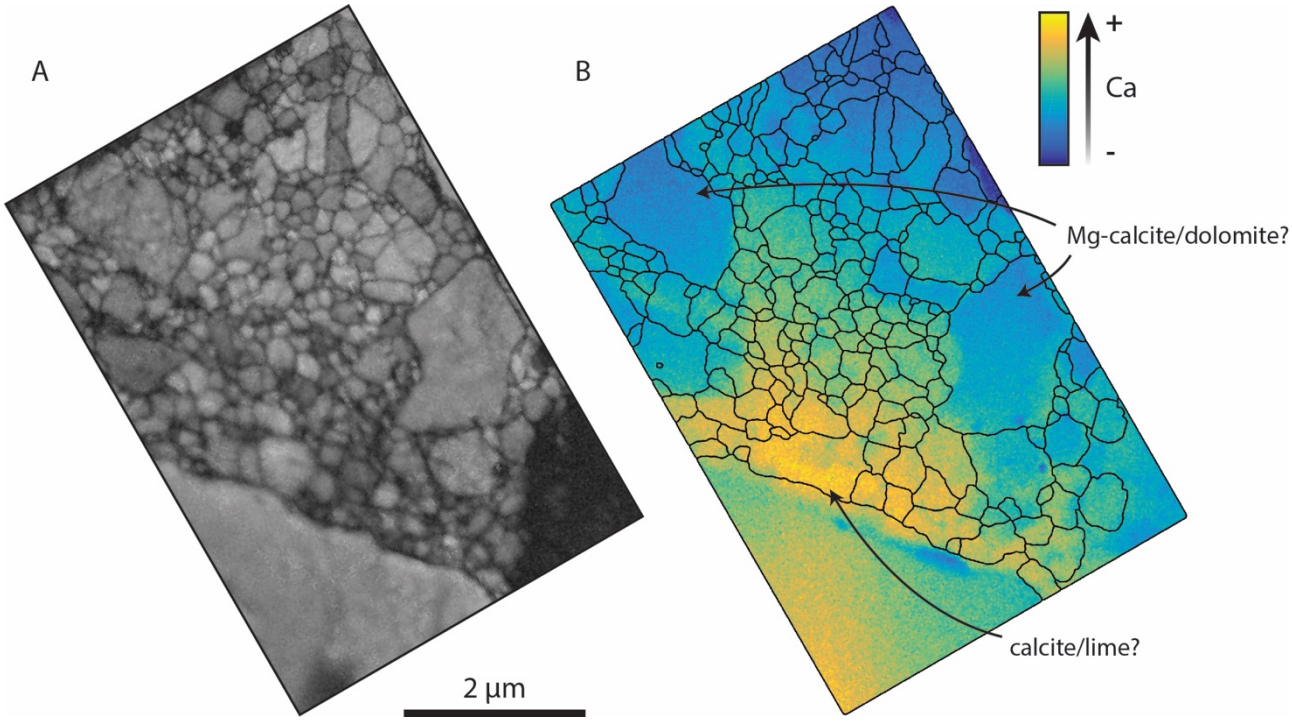


Fig. 5. Map 15 band contrast and EDS analysis. a) Band contrast map of map 15. b) EDS Ca map with superimposed grain boundaries. Grains with very high presence of Ca could suggest the presence of lime (CaO, a decarbonation product of calcite). A gradual enrichment in Ca is observed moving far from the PSS. Blue colors indicate minor Ca abundance and yellow colors higher presence of Ca.

prominent maxima at values between 100-300 nm contains two distinct sub-populations with peaks at c. 100 nm and c. 250 nm.

3.2. Grain shapes

Grains were typically polygonal and equant in shape and characterized by relatively low aspect ratios (< 2.5; Fig. 4b). Grain boundaries are straight to slightly curved (Figs. 5, 6). Grains met at c. 120° triple junctions, with quadruple junctions being also common (Fig. 6). The grain aggregates did not display a shape-preferred orientation (SPO) (Fig. 4c).

3.3. Chemical analysis

EDS data showing the distribution of Ca were collected for map 15 during the TKD analysis (Fig. 5). However, due to the resolution of the EDS map and the relatively minor variation in Ca between calcite, Mg-calcite and dolomite, it was not possible to identify whether the bimodal grain size distribution described in section 3.1 correlates with chemical differences in the PSZ. Unfortunately, we lack a Mg chemical map due to a setting error during data collection. Areas characterized by relatively high concentration of Ca suggest that lime (CaO, a decarbonation product of calcite) could be present, at least locally, within the PSZ.

3.4. Crystallographic preferred orientation and intragranular misorientations

Figure 7 summarizes the crystallographic orientation data for calcite collected with the TKD technique. Although the four TKD maps were collected adjacent to each other, significant variation in the CPO is observed in the different maps. In particular, it is to note that while maps 25 and 9 cover almost all the distance from the PSS investigate (1.2 to 21.75 µm), maps 13 and 15 include areas ca. > 10 µm from the PSS. In maps 25 and 9, calcite shows a weak CPO consisting of a clustering of c-axes at 20-45° to the y-axis (Fig. 7). No clear CPO was observed on the a-axis direction and along the r- and e- rhomb planes. In map 13, c-axes are organized in two weak clusters located near the circumference of the pole figures and aligned subparallel to the y-axis (Fig. 7). Again, no CPO was observed along the other crystal planes and directions. Map 15 was characterized by a random orientation (Fig. 7).

Grains ca. < 700 nm in size are typically characterized by very low to negligible intragranular misorientation (< 1-2°), defined as the misorientation angle of a pixel with respect to the mean orientation of the grain it belongs to (Figs. 6, 8a). Grains larger than about 800 nm (Figs. 6, 8b) show the development of internal low-angle boundaries and sub-grains (Fig. 8b). The threshold for the minimum misorientation angle that defines a grain boundary was set at 10°.

4. Discussion

4.1. Deformation mechanisms active in the PSZ

In experiments performed on calcite-dolomite gouges deformed at a target slip rate of 1 ms^{-1} for 0.4 m of displacement under room-humidity conditions (i.e., samples 1221 and s1324, see Chapter II), a discrete, mirror-like PSS cutting the gouge was observed (Chapter II). The PSZ was ca. 15-20 µm thick and consisted of calcite, periclase and Mg-calcite, the latter two being a decarbonation product of dolomite (i.e., $MgCa(CO_3)_2 \implies MgO + (Ca,Mg)CO_3 + CO_2$; Samtani et al., 2002). Microstructural investigation of the PSS with secondary electrons (SE) at the SEM showed a very compact structure composed of nanograins with sizes down to ca. 100 nm (Fig. 9a). The TKD analysis of the PSZ in cross-section shows a foam-like polygonal texture with equant nanograins having 120° triple junctions and recurrent quadruple junctions (e.g., Fig. 5a). Such microstructures have been suggested as diagnostic of grain-boundary sliding (GBS) aided by diffusion creep, which can lead to superplastic flow (Ashby and Verrall, 1973; Verberne et al., 2013b, 2014; De Paola et al., 2015; Green et al., 2015).

Starting from their microstructural observations and estimates of temperature rise during rotary-shear deformation experiments in calcite gouges, De Paola et al. (2015) performed flow stress calculations to test their hypothesis that the observed drop in the friction coefficient at coseismic slip rates (i.e., V = 1 ms^{-1}) could be driven by the activation of grain-size sensitive deformation mechanisms, namely GBS aided by diffusion creep. Their results showed that during the initial strengthening and successive dynamic weakening phase, cataclasis and dislocation creep were the main active deformation mechanisms. Only when friction dropped to a steady-state value, with temperature rising up to ca. 1000 °C, nanograins (D < 100 nm) were able to accommodate coseismic strain through GBS aided by diffusion creep (De Paola et al., 2015). Transmission electron

microscope (TEM) observations showed a low density of dislocations in the calcite nanograins, with larger grains typically exhibiting development of sub-grain boundaries (De Paola et al., 2015).

In our case, the temperature rise within the PSZ was estimated to be ca. 600 °C, although this should be considered a lower bound (see Chapter II). Image analysis on the TKD maps highlighted the presence of two nanograin populations at c. 100 nm and c. 250 nm in size (Fig. 4a). Because grains likely experience some static growth during cooling at the end of the experiment, the grain sizes estimated from TKD analysis (Fig. 4) can be interpreted as an upper bound to the actual grain sizes that were present during the deformation. Smaller grains (D ca. < 700 nm) showed little to no internal misorientation while larger grains (D ca. > 800 nm) showed the development of sub-grain boundaries. The magnitude of intragranular misorientation is related to the internal strain in the grains, hence the occurrence and density of dislocations, with dislocations being more abundant in grains with higher internal misorientations. In the case of diffusion-creep, strain-free grains are expected (Fig. 8a; Poirier, 1985). On the other hand, development of sub-grain boundaries suggests that larger grains were deforming by dislocation creep (Fig. 8b; Rutter, 1995). Both processes were probably active simultaneously in grain population with different grain sizes. However, diffusion-accommodated deformation mechanisms might have played a major role in controlling strain accommodation, hence the rheology of the PSZ. It is to note that the size of the sub-grains appears to be similar to that of the strain-free matrix, suggesting that at least part of the latter formed by sub-grain rotation recrystallization. Following this, the sub-grains size could help estimate the “coseismic” grain size, since it is unlikely that they underwent significant coarsening during annealing at the end of the experiment.

Our TKD observations offer a new perspective on the coseismic deformation mechanisms within calcite gouges and complement the studies of De Paola et al. (2015) that focused their attention on the deformation mechanisms active in natural and experimental faults (e.g., Verberne et al., 2013b, 2014; Green et al., 2015). Our observations indicate that during deformation and once the steady-state friction was attained, dislocation- and diffusion creep might have been active at the same time within the deforming slip zone. However, a progressive

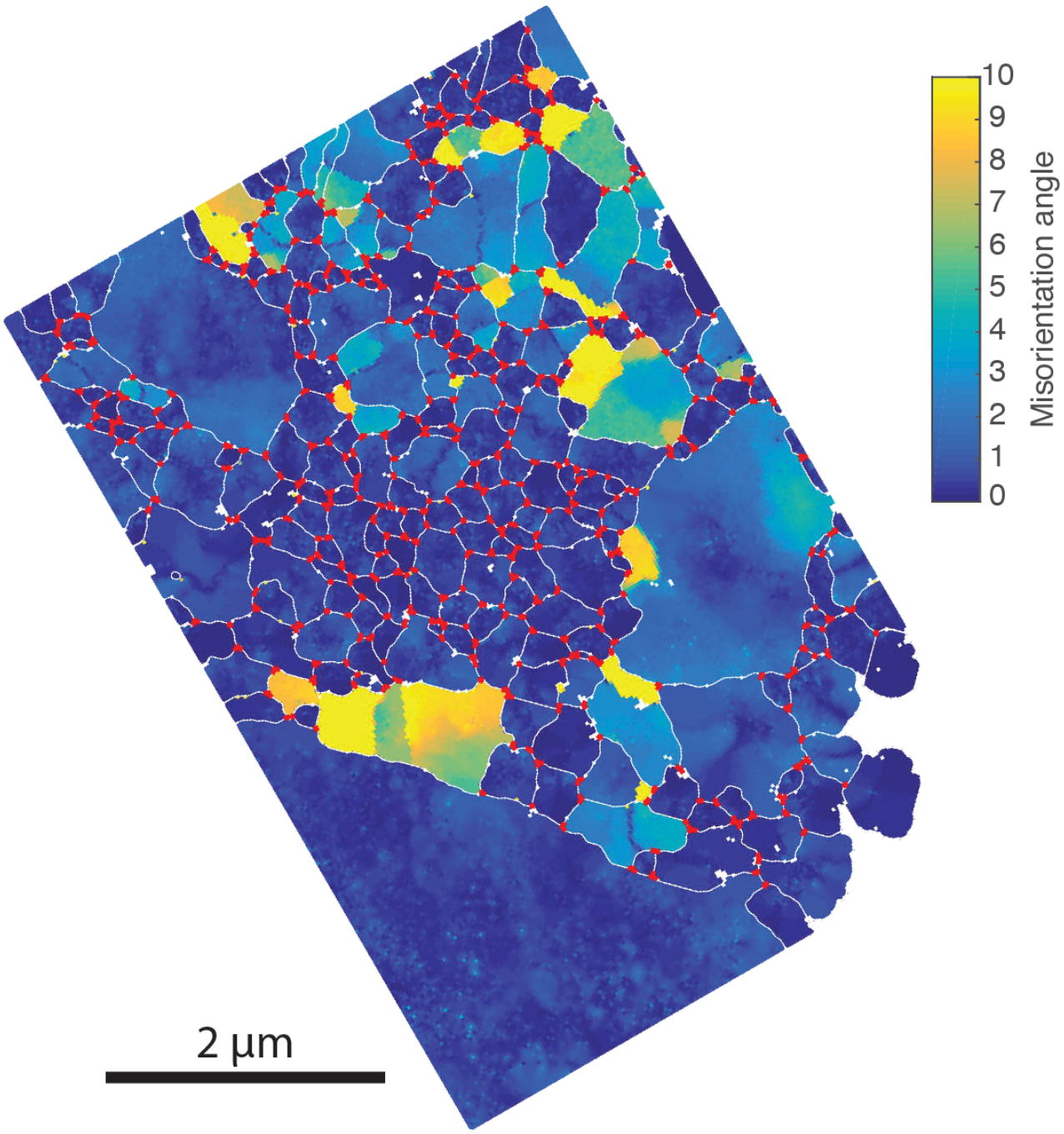


Fig. 6. Map 15 intragranular misorientation and triple points. Grain are characterized by straight grain boundaries (white lines) and triple point junctions (red lines). Occurrence of quadruple points is also commonly observed. Grains smaller than ca. 700 nm are typically characterized by very low internal misorientation (< 2 °) with respect to the mean grain orientation. This suggests that such grains are relatively strain free.

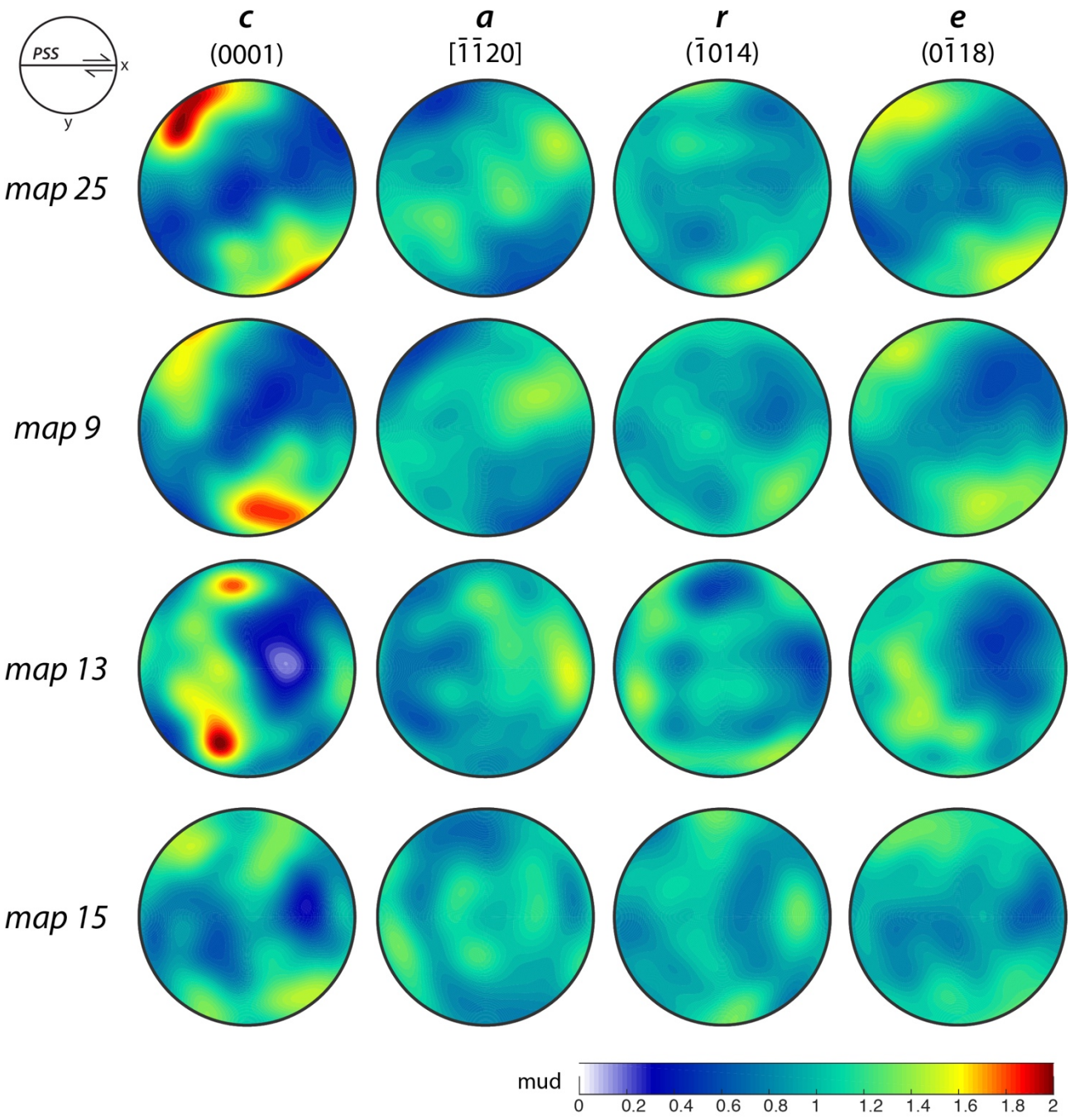


Fig. 7. Calcite crystallographic preferred orientation. Calcite showed the development of a weak CPO that progressively disappeared moving parallel to the principal slip surface (map 25 to map 15). The CPO consisted of a clustering of c-axes inclined of ca. 30° to the y axis. No CPO development was observed on the a-axis direction and r- and e-rhomb planes.

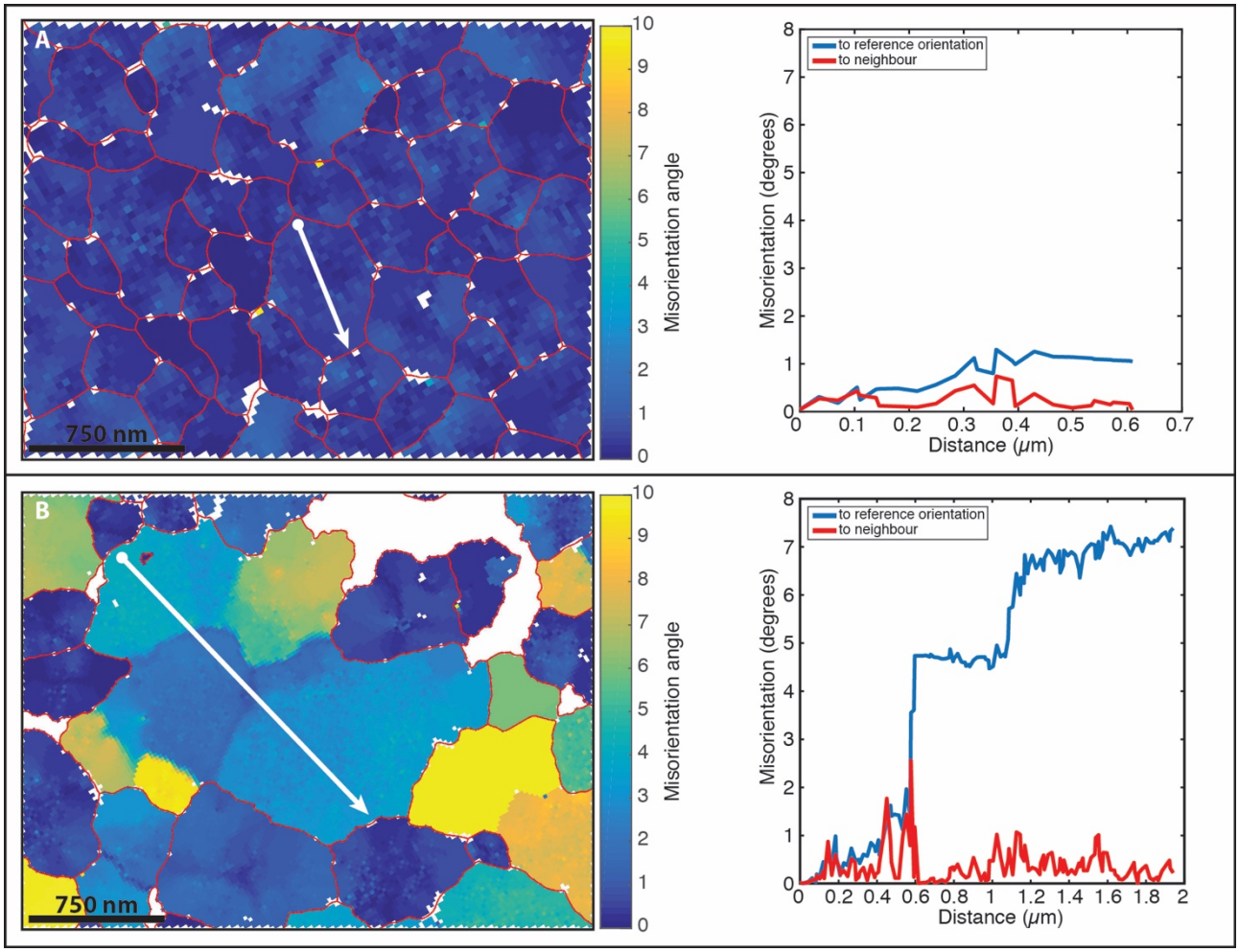


Fig. 8. Intragranular misorientation profiles. Depending on the grain size, calcite showed (a) low to no intragranular misorientation for grains ca. < 700 nm, and (b) the development of sub-grains in larger grains (> 800 nm). The white line shows the location of the misorientation profiles and the red line the grain boundaries (defined as having a misorientation angle > 10°). In the misorientation profiles are shown both the angles in respect to the first point in the profile (blue line) and the misorientation angle in respect to the previous point (red line). Grains are from (a) map 15 and (b) map 25.

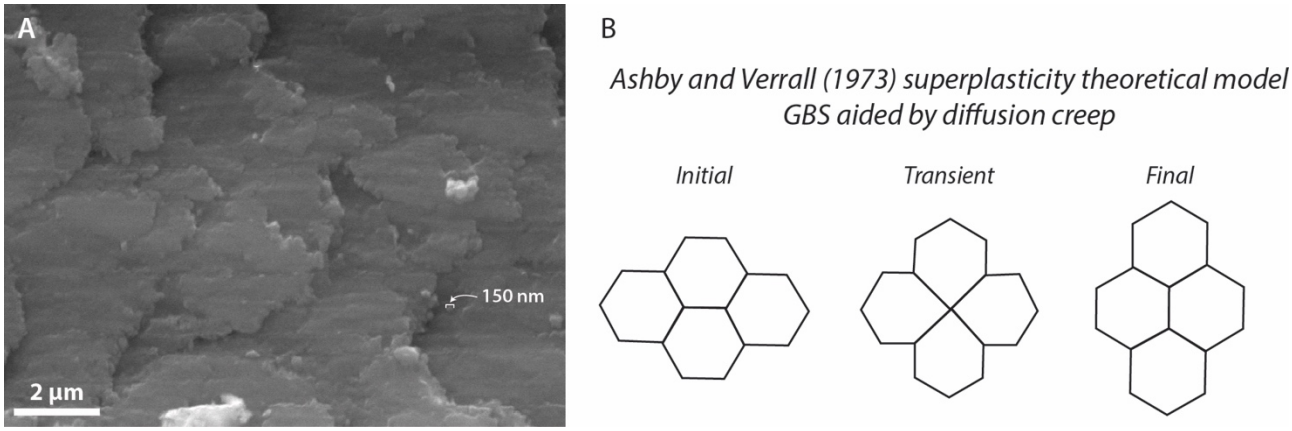


Fig. 9. Experimental microstructures diagnostic of superplastic flow within the PSZ. a) View from the top of the mirror-like PSS of experiment s1221, that slid for 0.4 m at 1 ms^{-1} under room-humidity conditions. The PSS was composed of a pavement of nanograins with negligible porosity. The image was taken with the secondary electron detector in the SEM. b) Diagram showing the theoretical model developed by Ashby and Verrall for neighbor switching during superplastic flow accommodated by grain boundary sliding (GBS) aided by diffusion creep.

decrease in the grain size in the PSZ favored deformation of the nanograins by diffusion-accommodated mechanisms, with dislocation creep being confined to the larger remnant grains. The occurrence of a weak CPO that progressively disappears moving either along the PSZ or further from the PSS (increasing distance from the PSS in maps from 25 to 15, Fig. 7) is consistent with a PSZ mainly deforming through GBS aided by diffusion creep. In fact, GBS has been demonstrated to be accompanied by a rotation of grains leading to weakening and eventual randomization of any starting texture (Taplin et al., 1979). The starting CPO would likely form due to dislocation activity prior the onset of more efficient diffusive processes. It has to be noted that the observed CPO could also be influenced by the small area investigated (i.e., statistical significance) and by later preferential grain growth of the nanograins during fast cooling at the end of the experiment.

The EDS measurements coupled with TKD analysis showed a heterogeneous distribution of Ca in the PSZ (Fig. 5). The larger grains exhibited typically have lower content in Ca, with slightly higher concentration at the grain boundary, suggesting that they may have been dolomite grains undergoing decarbonation. A distinct area characterized by higher concentrations of Ca might suggest the occurrence of lime (CaO, one of the decarbonation products of calcite), and thus local temperatures as high as ca. 800 °C. Unfortunately, the lack of a Mg map and the knowledge of the noise in the analysis limit our interpretation of the EDS data. However, a general trend of increase in Ca moving away from the PSS was clear. Similar behavior has been observed in rotary-shear experiments on solid cylinders performed on calcitic- and dolomitic-marble and deformed at very high slip rates ($V = 6\ ms^{-1}$) for large displacements ($d > 10$ m) (Di Toro, personal communication). Here, a clear chemical banding was observed, with the PSZ showing an enrichment of Mg and depletion of Ca, and progressive depletion of Mg and enrichment in Ca moving away from the PSS. This has been interpreted as a pore-controlled diffusive process enhanced by the production of CO_2 due to the ongoing decarbonation, which allowed a very efficient vapor mass transfer for GBS during sliding and sintering of grains at the end of the experiment. In our case, the lack of diffuse porosity observed could be only representative of a final stage during which static growth of the grains at the end of the experiment progressively occluded the voids.

4.2. The role of nanoparticles in fault lubrication

The nature of the nanoparticles observed in the PSZ and their influence on the frictional evolution of gouges is still not well understood. Occurrence of sub-micron grains (D < 1 μm) has been documented in experiments performed at lower slip rates (V << 1 ms^{-1}) and both in the presence and absence of water (see microstructural characterization in Chapter II). The production of nanoparticles consisting of thermal decomposition products (e.g., Mg- calcite and periclase in the case of decarbonation of the dolomite) has been inferred to be responsible for the dynamic weakening observed during coseismic sliding (Green et al., 2015). However, De Paola et al. (2015) suggested that thermally activated grain-size sensitive GBS could be responsible for fault lubrication and the measured drop in the friction coefficient. Their hypothesis was supported by the presence of nanoparticles before the onset of the dynamic weakening when the gouge still showed Byerlee friction values (μ =0.68-0.80), as well as little evidence of phase transformation at the end of the experiment, not enough to justify the mechanical evolution of the gouge.

Our observations seem to validate the interpretations of De Paola et al. (2015). In our experiments, a layer of ca. 15-20 μm composed of sub-micrometric particles of calcite, Mg-calcite and periclase was produced after 0.4 m of slip at 1 ms^{-1}, showing that decarbonation of dolomite was proceeding. However, according to microstructural observations of experiments performed at lower slip rates (V << 1 ms^{-1}), nanoparticles were also likely to be formed due to intense comminution in the PSZ at deformation conditions where the temperature rise was much less than that required for decarbonation of dolomite (i.e., ca. 550 °C, Samtani et al., 2002). Therefore, the occurrence of nanoparticles in the PSZ was likely to be a precursor to the onset of dynamic weakening. However, significant temperature rise due to frictional heating was needed in order to activate grain-size sensitive GBS leading to fault lubrication and a drop in the friction coefficient. Further investigation of deformation mechanisms active in nanoparticles also produced at slip rates at which weakening was not observed (V < 1 ms^{-1}) might result in a better understanding of the mechanical influence of nanoparticles during fault slip.

5. Conclusions

The TKD analysis was performed on electron-transparent foils prepared from gouges composed of a mixture of 50 wt% calcite and 50 wt% dolomite. The gouges were deformed at

seismic slip rates (i.e., 1 m^{-1}) for a total displacement of 0.4 m, under a normal load of 17.5 MPa and at room-humidity conditions.

The PSZ was composed of nanograins with a wide range of sizes between 100-2068 nm, though in one main population of nanoparticles two subsidiary peaks with grain sizes of c. 100 nm and c. 250 nm were present. Individual nanograins were equant and showed 120° triple junctions as well as frequent quadruple junctions. Grains smaller than ca. 700 nm commonly showed very low to no internal misorientation, implying a low dislocation density, while larger grains (> 800 nm) were characterized by the development of sub-grains and low-angle boundaries. The CPO analysis showed the presence of a weak CPO that progressively disappeared moving parallel to the PSS. These observations are consistent and complementary to previous studies suggesting that the activation of grain-size sensitive deformation mechanisms such as superplastic flow (i.e., GBS aided by diffusion creep) during frictional heating could be a lubrication mechanism leading to dynamic weakening (De Paola et al., 2015).

Finally, although geological applications are currently rare, this preliminary study shows that the TKD analysis is a powerful tool to investigate at very high spatial resolution (i.e., here 20 nm, but potentially only few nm; Trimby, 2012) and over relatively large areas (compared to typical TEM analyses) common geological materials. In this particular case, TKD analysis allowed us to investigate the deformation mechanisms active in faults where nanoparticles might play an important role in the fault slip behavior.

6. Tables

Map	*Step size* *nm*	*Map width* *µm*	*Map height* *µm*	*Raw indexing* *%*	*Processed indexing* *%*	*EDS map*
9	50	6.60	23.06	31.3	75	
13	50	6.50	15.50	21.9	94	
15	35.3	6.53	9.71	33.1	96	x
25	20	7.00	23.00	13.5	51	

Table 1. TKD maps acquired on sample s1221.

Chapter V

Discussion and future work

The studies presented in this thesis dealt with the characterization of the structure and deformation processes active in fault zones cutting carbonate rocks, with observations spanning over more than ten orders of magnitude (from 10^{3-4} m in Chapter I to 10^{-9} m in Chapter IV). In particular, the main questions here addressed regard (i) the quantification of the structural complexity of active fault zones (Chapter I), (ii) the frictional and microstructural evolution of carbonate mixes gouges (Chapter II) and (iii) the deformation processes that are active during fault slip in carbonate gouges (Chapter III and IV).

The structure of fault zones has a major influence on their mechanics and seismogenic behavior, and more broadly on the earthquakes distribution during seismic sequences. Therefore, the investigation of the structures that control present day seismicity is of great importance for seismic hazard studies and for understanding of the seismic cycle. In Chapter I, the internal structure of the Vado di Corno Fault Zone (VCFZ), an exhumed active fault zone outcropping in the Italian Central Apennines, was mapped in detail. The resulting map highlighted the interplay between the inherited compressional structures related to compression during thrusting in the Pliocene, and the newly formed normal faults during Present extension. Consequently, the fault network described in the VCFZ compared well with the fault geometry inferred from hypocenter relocation during the L'Aquila 2009 seismic sequence (Valoroso et al., 2013, 2014). This geometrical similarity may result in a better understanding of the active buried seismic structures controlling the present seismicity in the Central Apennines. To better quantify the structural complexity documented in Chapter I, current work regarding the VCFZ (mainly carried out by Michele Fondriest) is focused on the construction of a three-dimensional (3D) model starting from the detailed field surveys. A comparison of the 3D architecture of the VCFZ with the one documented for the seismic source of the L'Aquila 2009 seismic sequence could improve our understanding of the structures responsible for the seismic sequences in the Central Apennines for seismic hazard studies. Moreover, the detailed 3D characterization of the fault network within an active fault zone could be used in numerical models of earthquake dynamic rupture propagation. The additional characterization of the described structural units with their physical properties (e.g., porosity, permeability, stiffness, velocity anisotropy) might help understanding how such properties influence rupture propagation,

off-fault damage and aftershock evolution in space and time. Finally, a comparison between our 3D fault zone model and results from geophysical investigations (e.g., Pischiutta et al., 2017) could be used as a benchmark for the characterization of fault zones and their monitoring in other areas worldwide.

Motivated by their widespread occurrence in the VCFZ, Chapter II focused on the frictional and microstructural evolution of calcite-dolomite mixed gouges. This topic was addressed by performing a series of rotary shear experiments on the mixed gouges over a wide range of slip rates (30 μms^{-1} to 1 ms^{-1}), deformation conditions (room-humidity vs. water-dampened) and deformation history (single slide vs. slide-hold-slide). The addition of small percentages of dolomite in pure calcite gouges, as low as 15 wt%, showed already a significant change in the frictional behavior of the gouge, with less displacement required to achieve dynamic weakening. The presence of liquid water had also a strong influence on the frictional evolution of the mixed gouge by "stabilizing" the gouge up to slip rates of 1 ms^{-1}, when dynamic weakening was observed. Moreover, water-dampened experiments resulted in a minor microstructural variation with increasing slip rate with respect to the gouge layers sheared under room humidity conditions. The results presented in this chapter aim to address a new insight in the mechanical behavior of faults putting in contact limestone-dolostone sequences as in the case of major thrust and normal faults in mountain belts (e.g., Apennines) and of basin-bounding faults. Following the study of Smith et al. (2017), in this thesis the development of a foliation was observed solely when the gouge was sheared at seismic slip rates (i.e., 1 ms^{-1}) under room-humidity conditions, suggesting that the occurrence of foliations in nature, associated with other peculiar microstructures such as mirror-like slip surfaces with truncated clasts, could be interpreted as an indicator of seismic slip in the rock record. However, in the experiments presented in this thesis the lower imposed slip rate was 30 μms^{-1}, which is still too high to be considered aseismic (Rowe and Griffith, 2015). Moreover, for $V \leq 10$ μms^{-1} other deformation mechanisms such as pressure solution are active in carbonate-bearing gouges. An extended investigation of both the frictional and microstructural evolution of calcite-dolomite mixtures for $V \leq 10$ μms^{-1} would allow us to obtain a more complete understanding of the slip rate dependent behavior of the carbonate gouges and, possibly, to attribute (or not) the formation of a foliation in calcite-dolomite gouges to seismic faulting. Moreover, due to technical limitations, in this study it was not possible to control and monitor the pore fluid pressure during the experiments. The development of a dedicated gouge holder capable of performing fluid-controlled experiments, would allow us to investigate

differences in both the frictional and microstructural evolution of calcite-dolomite mixtures under different pore-fluid factors.

Chapter III and IV focused on the physical processes associated to strain accommodation in the calcite-dolomite mixed gouge layers sheared in the experiments discussed in Chapter II. Chapter III, by means of standard electron backscatter diffraction (EBSD) microanalysis, addressed the deformation mechanisms operating in the gouge (micrometric in size) sandwiching the slip zone, while Chapter IV, thanks to the dataset acquired by means of a novel nano-analytical technique (Transmission Kikuchi Diffraction, TKD), focused on the deformation mechanisms operating in the experimental slip zone (sub-micrometric to nanometric in size). In Chapter III, EBSD data showed the development of a weak crystallographic preferred orientation (CPO) in calcite during shearing. The formation of a CPO was suggested to be controlled by the strong anisotropy in calcite (cleavage planes), mechanical grain rotation towards the direction of the maximum compressive stress and subsequent fracturing, rather than an evidence of dislocation mobility activity. The calcite twin paleopiezometry was also performed. High differential stress estimates were interpreted as the consequence of the formation and dismembering of grain bridges (also called *force chains*) in the gouge during shearing. To date and to our knowledge, there is not a method to directly measure the magnitude of the stress concentration along such grain bridges. Further work will be aimed at trying to include mineral anisotropy (i.e., cleavage planes) in 3D gouge deformation models (e.g., Mair and Hazzard, 2007). If successful, this will allow us to calculate (i) development of grain shape preferred orientations, (ii) grain crystallographic preferred orientations and (iii) magnitude of stresses along grain bridges. The latter, in particular, will allow us to test the applicability of the calcite twin paleopiezometry in granular materials.

Lastly, in Chapter IV, the experimental slip zone of a calcite-dolomite gouge mixture slid at seismic slip rate (i.e., 1 ms^{-1}) was investigated with the Transmission Kikuchi Diffraction (TKD) technique. TKD is a newly developed technique, and its application has been mainly confined to material science studies so far (only two papers have been published with TKD application on geological materials, Piazolo et al., 2016; Delle Piane et al., 2018). The very high resolution of the TKD (down to 20 nm compared to the ca. 500 nm of the standard EBSD) and the wealth of data obtained (i.e., crystallographic preferred orientations, grain boundary misorientation, elemental analysis, internal lattice distortion) allowed us to strongly support the activation of grain boundary sliding aided by diffusion creep (i.e., occurrence of a very weak CPO in the nanoparticle aggregates) in the slip zone at seismic deformation conditions. Clearly, the next step is to investigate the natural

slip zones with this technique to check if the processes activated in the laboratory in carbonates do occur in nature. Moreover, though geological materials resulted to be by far more technically challenging to study with the TKD with respect to metals and alloys (e.g., sample preparation, indexing) the encouraging results obtained in this thesis will be the starting point for future work making the TKD nano-analysis an easier technique for the study of nanoparticles in nature.

Overall, the observations regarding the deformation processes documented in the bulk gouge and the principal slip surface in carbonate gouges (Chapter III and IV, respectively) suggest that the crystallographic properties of gouge-forming minerals have a major control on cataclasis, and hence friction, in the early stages of deformation when bulk temperature rise is minimum and strain accommodated throughout the gouge layer. However, as strain localizes, along the principal slip zone mean grain size decreases and temperature increases, and deformation is more efficiently accommodated through the activation of temperature-dependent intra-crystalline mechanisms, such as dislocation creep and grain-boundary sliding aided by diffusion creep. This switch between "brittle" to more "ductile" strain accommodation mechanisms relates with the onset of dynamic weakening during seismic slip, raising the question whether shallow earthquakes can be considered "brittle" or "ductile" (Di Toro et al., 2016).

References

Abe, S., Mair, K., 2005. Grain fracture in 3D numerical simulations of granular shear. Geophys. Res. Lett. 32, 1–4. doi:10.1029/2004GL022123.

Abe, S., Mair, K., 2009. Effects of gouge fragment shape on fault friction: New 3D modelling results. Geophys. Res. Lett. 36, 2–5. doi:10.1029/2009GL040684.

Aben, F. M., Doan, M.-L., Mitchell, T. M., Toussaint, R. Reuschlé, T., Fondriest, M., Gratier, J.-P., Renard, F., 2016. Dynamic fracturing by successive coseismic loadings leads to pulverization in active fault zones. J. Geophys. Res., 121, 2338–2360.

Adamoli, L., Calamita, F., Pelorosso, M., 2003. Itinerario N° 2 - Gran Sasso d'Italia: dai Prati di Tivo ai Prati di Tivo attraverso il ghiacciaio del Calderone, il Corno Grande, Campo Pericoli e la Val Maone. In: Guide Geologiche Regionali, Abruzzo: 102-112, BE-MA ed., Lodi (MI).

Adamoli, L., Calamita, F., Pizzi, A., 2012. Note Illustrative del Foglio 349 "G. Sasso" della Carta Geologica d'Italia alla scala 1 : 50.000. ISPRA, Roma.

Agosta, F., Aydin, A., 2006. Architecture and deformation mechanism of a basin-bounding normal fault in Mesozoic platform carbonates, central Italy. J. Struct. Geol. 28 (8), 1445–1467.

Agosta, F., Kirschner, D., 2003. Fluid conduits in carbonate-hosted seismogenic normal faults of central Italy. J. Geophys. Res. 108 (B4), 2221. http://dx.doi.org/10.1029/2002JB002013.

Al-Anzi, E., Al-Mutawa, M., Al-Habib, N., Al-Mumen, A., Nasr-El-Din, H., Alvarado, O., Brady, M., Davies, S., Fredd, C., Fu, D., Lungwitz, B., Chang, F., Huidobro, E., Jemmali, M., Samuel, M., Sandhu, D., 2003. Positive Reactions in Carbonate Reservoir Stimulation. Oilf. Rev. Winter, 28–45.

Allam, A. A., Ben-Zion, Y., 2012. Seismic velocity structures in the Southern California plate-boundary environment from double-difference tomography. Geophys. J. Int. 190, 1181-1196.

Allègre, C.J., Le Mouel, J.L., Provost, A., 1982. Scaling rules in rock fracture and possible implications for earthquake prediction. Nature 297, 47–49. doi:10.1038/297047a0.

Alvarez, W., Engelder, T., Geiser, P. A., 1978. Classification of solution cleavage in pelagic limestones. Geology, 6(5), 263-266.

Aretusini, S., Mittempergher, S., Plümper, O., Spagnuolo, E., Gualtieri, A.F., Di Toro, G., 2017. Production of nanoparticles during experimental deformation of smectite and implications for seismic slip. Earth Planet. Sci. Lett. 463, 221–231. doi:10.1016/j.epsl.2017.01.048.

Ashby, M.F., Verrall, R.A., 1973. Diffusion-accommodated flow and superplasticity. Acta Metall. 21, 149–163.

Atkinson, B.K., and Meredith, P.G., 1987, The theory of subcritical crack growth with applications to minerals and rocks, in Atkinson, B.K., ed., Fracture mechanics of rock: London, Academic Press, p. 111–166.

Austin, N. J., and Kennedy, L. A., 2005, Textural controls on the brittle deformation of dolomite: variations in peak strength: Geological Society Special Publication, no. 243, p. 37-49.

Aydin, A., Antonellini, M., Tondi, E., Agosta, F., 2010. Deformation along the leading edge of the Maiella thrust sheet in Central Italy. J. Struct. Geol. 32, 1291-1304.

Bachmann, F., Hielscher, R., Schaeben, H., 2010. Texture Analysis with MTEX – Free and Open Source Software Toolbox. Solid State Phenom. 160, 63–68. doi:10.4028/www.scientific.net/SSP.160.63.

Bachmann, F., Hielscher, R., Schaeben, H., 2011. Ultramicroscopy Grain detection from 2d and 3d EBSD data — Specification of the MTEX algorithm. Ultramicroscopy 111, 1720–1733. doi:10.1016/j.ultramic.2011.08.002.

Bai, T., Pollard, D. D., 2000. Fracture spacing in layered rocks: a new explanation based on the stress transition. J. Struct. Geol. 22 (1), 43-57.

Barber, D. J., Heard, H. C., and Wenk, H. R., 1981, Deformation of dolomite single-crystals from 20-800 degrees-C: Physics and Chemistry of Minerals, v. 7, no. 6, p. 271-286.

Barrett, S., 2015. Image SXM, http://www.ImageSXM.org.uk.

Beaudoin, N., Koehen, D., Lacomobe, O., Lecouty, A., Billi, A., Aharonov, E., Parlangeau, C., 2016. Fingerprinting stress: Stylolite and calcite twinning paleopiezometry revealing the complexity of progressive stress patterns during folding—The case of the Monte Nero anticline in the Apennines, Italy. Tectonics 35, 1687–1712. doi:10.1002/2016TC004128.

Beeler, N. M., Tullis, T. E., Blanpied, M. L., and Weeks, J. D., 1996. Frictional behavior of large displacement experimental faults. Journal of Geophysical Research: Solid Earth (1978–2012), 101(B4), 8697-8715.

Ben-Zion, Y., Shi, Z., 2005. Dynamic rupture on a material interface with spontaneous generation of plastic strain in the bulk. Earth Planet. Sci. Lett. 236, 489–496.

Bestmann, M., Kunze, K., Matthews, A., 2000. Evolution of a calcite marble shear zone complex on Thassos Island, Greece: Microstructural and textural fabrics and their kinematic significance. J. Struct. Geol. 22, 1789–1807. doi:10.1016/S0191-8141(00)00112-7.

Bestmann, M., Prior, D.J., Grasemann, B., 2006. Characterisation of deformation and flow mechanics around porphyroclasts in a calcite marble ultramylonite by means of EBSD analysis. Tectonophysics 413, 185–200. doi:10.1016/j.tecto.2005.10.044.

Billi, A., Salvini, F., Storti, F., 2003. The damage zone-fault core transition in carbonate rocks: implications for fault growth, structure and permeability. J. Struct. Geol. 25 (11), 1779-1794.

Billi, A., Storti, F., 2004. Fractal distribution of particle size in carbonate cataclastic rocks from the core of a regional strike-slip fault zone. Tectonophysics 384 (1), 115-128.

Bistacchi, A., Massironi, M., Menegon, L., 2010. Three-dimensional characterization of a crustal-scale fault zone: The Pusteria and Sprechenstein fault system (Eastern Alps). J. Struct. Geol. 32, 2022-2041.

Boccaletti, M., Elter, P., Guazzone, G., 1971. Plate tectonic models for the development of the Western Alps and Northern Apennines. Nature, 234 (49), 108-111.

Bons, P.D., Elburg, M.A., Gomez-Rivas, E., 2012. A review of the formation of tectonic veins and their microstructures. J. Struct. Geol. 43, 33–62. doi:10.1016/j.jsg.2012.07.005.

Bonson, C. G., Childs, C., Walsh, J. J., Schöpfer, M. P., Carboni, V., 2007. Geometric and kinematic controls on the internal structure of a large normal fault in massive limestones: the Maghlaq Fault, Malta. J. Struct. Geol. 29 (2), 336-354.

Borradaile, G.J., 1981. Particulate flow of rock and the formation of cleavage. Tectonophysics 72, 305–321.

Bos, B., Peach, C.J., Spiers, C.J., 2000. Frictional-viscous flow of simulated fault gouge caused by the combined effects of phyllosilicates and pressure solution. Tectonophysics 327, 173–194.

Bos, B., Spiers, C.J., 2002. Frictional-viscous flow of phyllosilicate-bearing fault rock: Microphysical model and implications for crustal strength profiles. J. Geophys. Res. 107, 2028. doi:10.1029/2001JB000301.

Bouchon, M., Vallee, M., 2003. Observation of Long Supershear Rupture During the Magnitude 8.1 Kunlunshan Earthquake. Science, 301, 824-826.

Boullier, A.M., Yeh, E.C., et al., 2009. Microscale anatomy of the 1999 Chi-Chi earthquake fault zone. Geochem. Geophys. Geosyst. 10.

Boulton, C., Yao, L., Faulkner, D.R., Townend, J., Toy, V.G., Sutherland, R., Ma, S., Shimamoto, T., 2017. High-velocity frictional properties of Alpine Fault rocks: Mechanical data, microstructural analysis, and implications for rupture propagation. J. Struct. Geol. 97, 71–92. doi:10.1016/j.jsg.2017.02.003.

Brodsky, E.E., Rowe, C.D., Meneghini, F., Moore, J.C., 2009. A geological fingerprint of low-viscosity fault fluids mobilized during an earthquake. J. Geophys. Res. Solid Earth 114, 1–14. doi:10.1029/2008JB005633.

Brune, J. N., 2001. Fault normal dynamic loading and unloading: an explanation for ‘‘non-gouge’’rock powder and lack of fault-parallel shear bands along the San Andreas fault. Eos Trans. AGU 82 (47). Fall Meet. Suppl., Abstract S22B-0655.

Buiter, S. J. H., Wortel, M. J. R., Govers, R., 1998. The role of subduction in the evolution of the Apennines foreland basin. Tectonophysics 296 (3), 249-268.

Bullock, R. J., De Paola, N., Holdsworth, R. E., Trabucho-Alexandre, J., 2014. Lithological controls on the deformation mechanisms operating within carbonate-hosted faults during the seismic cycle. J. Struct. Geol. 58, 22-42.

Bullock, R.J., De Paola, N., Holdsworth, R.E., 2015. An experimental investigation into the role of phyllosilicate content on earthquake propagation during seismic slip in carbonate faults. J. Geophys. Res. Solid Earth 120, 3187–3207. doi:10.1002/2015JB011914.

Bunge, H.J., 1982. Fabric analysis by orientation distribution functions. Tectonophysics, 78, 1.

Burchfiel, B. C., Nakov, R., Dumurdzanov, N., Papanikolaou, D., Tzankov, T., Serafimovski, T., King, R. W., Kotzev, V., Todosov, A., Nurce, B., 2008. Evolution and dynamics of the Cenozoic tectonics of the South Balkan extensional system. Geosphere, 4(6), 919-938.

Burkhard, M., 1993. Calcite twins, their geometry, appearance and significance as stress-strain markers and indicators of tectonic regime: a review. J. Struct. Geol. 15, 351–368.

Busch, J.P., van der Pluijm, B.A., 1995. Calcite textures, microstructures and rheological properties of marble mylonites in the Bancroft shear zone, Ontario, Canada. J. Struct. Geol. 17, 677–688. doi:10.1016/0191-8141(94)00092-E.

Caine, J. S., Evans, J. P., Forster, C. B., 1996. Fault zone architecture and permeability structure. Geology, 24 (11), 1025-1028.

Calamita, F., Di Domenica, A., Viandante, M.G., Tavarnelli, E., 2008. Sovrascorrimenti younger on older o faglie normali ruotate: la linea Vallepietra-Filettino-Monte Ortara (Appennino centrale laziale-abruzzese). Rend. Online SGI, 1, Note Brevi, p. 43-47, 5 figg.

Calamita, F., Paltrinieri, W., Pelorosso, M., Scisciani, V., Tavarnelli, E., 2003b. Inherited Mesozoic architecture of the Adria continental palaeomargin in the Neogene central Apennines orogenic system, Italy, Boll. Soc. Geol. Ital. 122, 307–318.

Calamita, F., Pelorosso, M., Satolli, S., 2003a. The role of the Adria Mesozoic paleomargin architecture on the Gran Sasso d'Italia orogenic system (central Apennines), Boll. Soc. Geol. Ital. 122, 337–349.

Cardello, G., Doglioni, C., 2014. From Mesozoic rifting to Apennine orogeny: The Gran Sasso range (Italy). Gondwana Res. doi:10.1016/j.gr.2014.09.009.

Carminati, E., Lustrino, M., Doglioni, C., 2012. Geodynamic evolution of the central and western Mediterranean: Tectonics vs. igneous petrology constraints. Tectonophysics 579, 173-192.

Carter, N.L., Raleigh, C.B., 1969. Principal stress directions from plastic flow in crystals. Bulletin of the Geological Society of America 80, 1231–1264.

Cates, M.E., Wittmer, J., Bouchaud, J.P., Claudin, P., 1998. Jamming, Force Chains and Fragile Matter. Phys. Rev. Lett. 81, 1841–1844. doi:10.1103/PhysRevLett.81.1841.

Chen, X., Madden, A.S., Bickmore, B.R., Reches, Z., 2013. Dynamic weakening by nanoscale smoothing during high-velocity fault slip. Geology 41, 739–742. doi:10.1130/G34169.1.

Chen, J., Spiers, C.J., 2016. Rate and state frictional and healing behavior of carbonate fault gouge explained using microphysical model 1–42. doi:10.1002/2016JB013470.

Chen, J., Niemeijer, A., Yao, L., Ma, S., 2017. Water vaporization promotes coseismic fluid pressurization and buffers temperature rise. Geophys. Res. Lett. 1–9. doi:10.1002/2016GL071932.

Chester, F.M., Friedman, M., Logan, J.M., 1985. Foliated Cataclasite. Tectonophysis 111, 139–146.

Chester, F., Logan, J., 1986. Implications for mechanical properties of brittle faults from observations of the Punchbowl fault zone, California. Pure and Applied Geophysics, 124(1-2), 79-106.

Chester, F.M., Chester, J.S., 1998. Ultracataclasite structure and friction processes of the Punchbowl fault, San Andreas system, California. Tectonophysics 295, 199–221. doi:10.1016/S0040-1951(98)00121-8.

Chester, J.S., Chester, F.M., Kronenberg, A.K., 2005. Fracture surface energy of the Punchbowl fault, San Andreas system. Nature 437, 133–136. doi:10.1038/nature03942.

Chiarabba, C., Amato, A., Anselmi, M., Baccheschi, P., Bianchi, I., Cattaneo, M., Cecere, G., Chiaraluce, L., Ciaccio, M.G., De Gori, P., De Luca, G., Di Bona, M., Di Stefano R., Faenza, L., Govoni, A., Improta, L., Lucente, F.P., Marchetti, A., Margheriti, L., Mele, F., Michelini, A., Monachesi, G., Moretti, M., Pastori, M., Piana Agostinetti, N., Piccinini, D., Roselli, P., Seccia, D., Valoroso, L., 2009. The 2009 L'Aquila (central Italy) Mw6. 3 earthquake: Main shock and aftershocks. Geophys. Res. Lett. 36 (18), L18308. http://dx.doi.org/10.1029/2009GL039627.

Chiaraluce, L., 2012. Unravelling the complexity of Apenninic extensional fault systems: A review of the 2009 L'Aquila earthquake (Central Apennines, Italy). J. Struct. Geol. 42, 2–18. doi:10.1016/j.jsg.2012.06.007.

Chiaraluce, L., Valoroso, L., Piccinini, D., Di Stefano, R., De Gori, P., 2011. The anatomy of the 2009 L'Aquila normal fault system (central Italy) imaged by high resolution foreshock and aftershock locations. J. Geophys. Res. 116 (B12). http://dx.doi.org/10.1029/2011JB008352.

Childs, C., Manzocchi, T., Walsh, J. J., Bonson, C. G., Nicol, A., Schöpfer, M. P., 2009. A geometric model of fault zone and fault rock thickness variations. J. Struct. Geol. 31 (2), 117-127.

Ciamarra, M. P., M. D. De Vizia, A. Fierro, M. Tarzia, A. Coniglio, and N. Nicodemi, 2006. Granular species segregation under vertical tapping: Effects of size, density, friction, and shaking amplitude. Phys. Rev. Lett., 96, 058001, doi:10.1103/PhysRevLett.96.058001.

Cladouhos, TT, 1999. Shape preferred orientations of survivor grains in fault gouge. J. Struct. Geol. 21, 419-436.

Clemenzi, L., Storti, F., Balsamo, F., Molli, G., Ellam, R., Muchez, P., Swennen, R., 2015. Fluid pressure cycles, variations in permeability, and weakening mechanisms along low-angle normal faults: The Tellaro detachment, Italy. Geological Society of America Bulletin, 127(11-12), 1689-1710.

Collettini, C., Holdsworth, R.E., 2004. Fault zone weakening and character of slip along low-angle normal faults: insights from the Zuccale fault, Elba, Italy. J. Geol. Soc. London. 161, 1039–1051.

Collettini, C., Viti, C., Tesei, T., Mollo, S., 2013. Thermal decomposition along natural carbonate faults during earthquakes. Geology, 41(8), 927-930.

Collettini, C., Carpenter, B. M., Viti, C., Cruciani, F., Mollo, S., Tesei, T., Trippetta, F., Valoroso, L., Chiaraluce, L., 2014. Fault structure and slip localization in carbonate-bearing normal faults: An example from the Northern Apennines of Italy. J. Struct. Geol. 67, 154-166.

Cottle, J.M., Jessup, M.J., Newell, D.L., Searle, M.P., Law, R.D., Horstwood, M.S.A., 2007. Structural insights into the early stages of exhumation along an orogen-scale detachment: The South Tibetan Detachment System, Dzakaa Chu section, Eastern Himalaya. J. Struct. Geol. 29, 1781–1797. doi:10.1016/j.jsg.2007.08.007.

D'Agostino, N., Chamot-Rooke, N., Funiciello, R., Jolivet, L., Speranza, F., 1998. The role of pre-existing thrust faults and topography on the styles of extension in the Gran Sasso range (central Italy). Tectonophysics 292, 229-254.

Davis, N. E., Kronenberg, A. K., and Newman, J., 2008, Plasticity and diffusion creep of dolomite: Tectonophysics, no. 456, p. 127-146.

De Bresser, J. H. P., and Spiers, C. J., 1990, High-temperature deformation of calcite single crystals by r+ and f+ slip, in Knipe, R. J., and Rutter, E. H., eds., Deformation Mechanisms, Rheology and Tectonics, Volume 54, Geological Society Special Publication, p. 285-298.

De Bresser, J.H.P., Spiers, C.J., 1997. Strength characteristics of the r, f, and c slip systems in calcite. Tectonophysics 272, 1–23. doi:10.1016/S0040-1951(96)00273-9.

De Paola, N., Mirabella, F., Barchi, M.R., Burchielli, F., 2006. Early orogenic normal faults and their reactivation during thrust belt evolution: the Gubbio Fault case study, Umbria-Marche Apennines (Italy). J. Struct. Geol. 28, 1948–1957. doi:10.1016/j.jsg.2006.06.002.

De Paola, N., Collettini, C., Faulkner, D.R., Trippetta, F., 2008. Fault zone architecture and deformation processes within evaporitic rocks in the upper crust. Tectonics 27, 1–21. doi:10.1029/2007TC002230.

De Paola, N., Chiodini, G., Hirose, T., Cardellini, C., Caliro, S., Shimamoto, T., 2011a. The geochemical signature caused by earthquake propagation in carbonate-hosted faults. Earth Planet. Sci. Lett. 310, 225–232. doi:10.1016/j.epsl.2011.09.001.

De Paola, N., Hirose, T., Mitchell, T., Di Toro, G., Viti, C., Shimamoto, T., 2011b. Fault lubrication and earthquake propagation in thermally unstable rocks. Geology 39, 35–38. doi:10.1130/G31398.1.

De Paola, N., Holdsworth, R.E., Viti, C., Collettini, C., Bullock, R., 2015. Can grain size sensitive flow lubricate faults during the initial stages of earthquake propagation? Earth Planet. Sci. Lett. 431, 48–58. doi:10.1016/j.epsl.2015.09.002.

Delle Piane, C., Burlini, L., and Grobety, B., 2007, Reaction-induced strain localization: Torsion experiments on dolomite: Earth and Planetary Science Letters, v. 256, no. 1-2, p. 36-46.

Delle Piane, C., Burlini, L., Kunze, K., Brack, P., and Burg, J. P., 2008, Rheology of dolomite: Large strain torsion experiments and natural examples: Journal of Structural Geology, v. 30, p. 767-776.

Delle Piane, C., Burlini, L., Kunze, K., 2009. The influence of dolomite on the plastic flow of calcite. Rheological, microstructural and chemical evolution during large strain torsion experiments. Tectonophysics 467, 145–166. doi:10.1016/j.tecto.2008.12.022.

Delle Piane, C., Clennell, M. Ben, Keller, J.V.A., Giwelli, A., Luzin, V., 2017. Carbonate hosted fault rocks: A review of structural and microstructural characteristic with implications for seismicity in the upper crust. J. Struct. Geol. 103, 17–36. doi:10.1016/j.jsg.2017.09.003.

Delle Piane, C., Piazolo, S., Timms, N.E., Luzin, V., Saunders, M., Bourdet, J., Giwelli, A., Clennell, M. Ben, Kong, C., Rickard, W.D.A., Verrall, M., 2018. Generation of amorphous carbon and crystallographic texture during low-temperature subseismic slip in calcite fault gouge. Geology 2–5.

Demurtas, M., Fondriest, M., Balsamo, F., Clemenzi, L., Storti, F., Bistacchi, A., Di Toro, G., 2016. Structure of a normal seismogenic fault zone in carbonates: The Vado di Corno Fault, Campo Imperatore, Central Apennines (Italy). J. Struct. Geol. 90, 185–206. doi:10.1016/j.jsg.2016.08.004.

den Hartog, S.A.M., Spiers, C.J., 2014. A microphysical model for fault gouge friction applied to subduction megathrusts. J. Geophys. Res. Solid Earth 119, 1510–1529. doi:10.1002/2013JB010580.

Dershowitz, W.S., Herda, H.H., 1992. Interpretation of fracture spacing and intensity. In:Tillerson, J.R., Wawersik, W.R. (Eds.), Proceedings of the 33rd U.S. Symposium on Rock Mechanics. Balkema, Rotterdam, Sante Fe, New Mexico, 757-766.

Destro, N., 1995. Release fault: A variety of cross fault in linked extensional fault systems, in the Sergipe-Alagoas Basin, NE Brazil. J. Struct. Geol. 17 (5), 615-629.

Dieterich, J. H., 1979. Modeling of rock friction: 1. Experimental results and constitutive equations. Journal of Geophysical Research: Solid Earth (1978–2012), 84(B5), 2161-2168.

Di Bucci, D., Mazzoli, S., 2003. The October–November 2002 Molise seismic sequence (southern Italy): an expression of Adria intraplate deformation. Journal of the Geological Society, 160(4), 503-506.

Di Stefano, R., Chiarabba, C., Chiaraluce, L., Cocco, M., De Gori, P., Piccinini, D., Valoroso, L., 2011. Fault zone properties affecting the rupture evolution of the 2009 (Mw 6.1) L'Aquila earthquake (central Italy): Insights from seismic tomography. Geophys. Res. Lett. 38 (10). doi:10.1029/2011GL047365.

Di Toro, G., Pennacchioni, G., Teza, G., 2005. Can pseudotachylytes be used to infer earthquake source parameters? An example of limitations in the study of exhumed faults. Tectonophysics 402, 3–20. doi:10.1016/j.tecto.2004.10.014.

Di Toro, G., Pennacchioni, G., 2005. Fault plane processes and mesoscopic structure of a strong-type seismogenic fault in tonalites (Adamello batholith, Southern Alps). Tectonophysics 402, 55–80. doi:10.1016/j.tecto.2004.12.036.

Di Toro, G., Niemeijer, A., Tripoli, A., Nielsen, S., Di Felice, F., Scarlato, P., Spada, G., Alessandroni, R., Romeo, G., Di Stefano, G., Smith, S., Spagnuolo, E., Mariano, S., 2010. From field geology to earthquake simulation: A new state-of-The-art tool to investigate rock friction during the seismic cycle (SHIVA). Rend. Lincei 21, 95–114. doi:10.1007/s12210-010-0097-x.

Di Toro, G., Han, R., Hirose, T., De Paola, N., Nielsen, S., Mizoguchi, K., Ferri, F., Cocco, M., Shimamoto, T., 2011. Fault lubrication during earthquakes. Nature 471, 494–498. doi:10.1038/nature09838.

Di Toro, G., Spagnuolo, E., Violay, M., Rempe, M., Smith, S.A.F., Nielsen, S., Fondriest, M., Plümper, O., 2015. “Frictional processes” in carbonate-bearing rocks at seismic deformation conditions. American Geophysical Union Annual Meeting, AGU2015 Abstracts with Programme MR31B-01.

Di Toro, G., Spagnuolo, E., Fondriest, M., Passelegue, F., Aretusini, S., Demurtas, M., Murphy, S., Nielsen, S., Plümper, O., Kuo, L.W., 2016. Shallow earthquakes: are they “brittle” or “ductile”?, Congresso della Società Geologica Italiana, Napoli, September 2016.

Doan, M.-L., d’Hour, V., 2012. Effect of initial damage on rock pulverization along faults. J. Struct. Geol. 45, 113-124.

Doan, M.-L., Gary, G., 2009. Rock pulverization at high strain rate near the San Andreas Fault. Nat. Geosci. 2, 709–712.

Dor, O., Ben-Zion, Y., Rockwell, T.K., Brune, J., 2006b. Pulverized rocks in the Mojave section of the San Andreas fault zone. Earth Planet. Sci. Lett. 245, 642–654.

Dor, O., Rockwell, T.K., Ben-Zion, Y., 2006a. Geological observations of damage asymmetry in the structure of the San Jacinto, San Andreas and Punchbowl faults in Southern California: a possible indicator for preferred rupture propagation direction. Pure Appl. Geophys. 163, 301-349. http://dx.doi.org/10.1007/s00024-005-0023-9.

Edwards, M. A., Ratschbacher, L., 2005. Seismic and aseismic weakening effects in transtension: field and microstructural observations on the mechanics and architecture of a large fault zone in SE Tibet. Special Publication - Geological Society of London, 245, 109.

Elter, P., Giglia, G., Tongiorni, M., Trevisan, L. 1975. Tensional and compressional areas in recent (Tortonian to present) evolution of Northern Apennines. Boll. Geofis. Teor. Appl. 42, 3-18.

Fang, Z., Dunham, E.M., 2013. Additional shear resistance from fault roughness and stress levels on geometrically complex faults. J. Geophys. Res. Solid Earth 118, 3642–3654. doi:10.1002/jgrb.50262.

Faulkner, D. R., Lewis, A. C., Rutter, E. H., 2003. On the internal structure and mechanics of large strike-slip fault zones: field observations of the Carboneras fault in southeastern Spain. Tectonophysics 367 (3), 235-251. http://dx.doi.org/10.1016/S0040-1951(03)00134-3.

Faulkner, D., Jackson, C., Lunn, R., Schlische, R., Shipton, Z., Wibberley, C., Withjack, M., 2010. A review of recend development concerning the structure, mechanics and fluid flow properties of fault zones. J. Struct. Geol. 32(11), 1557-1575.

Fernández, F.J., Brown, D., Álvarez-Marrón, J., Prior, D.J., Pérez-Estaún, A., 2004. Microstructure and lattice preferred orientation of calcite mylonites at the base of the southern Urals accretionary prism. J. Geol. Soc. London. 161, 67–79. doi:10.1144/0016-764903-027.

Ferrill, D.A., 1998. Critical re-evaluation of differential stress estimates for calcite twins in coarse-grained limestone. Tectonophysics 285, 77–86.

Ferrill, D.A., Morris, A.P., Evans, M.A., Burkhard, M., Groshong, R.H., Onasch, C.M., 2004. Calcite twin morphology: A low-temperature deformation geothermometer. J. Struct. Geol. 26, 1521–1529. doi:10.1016/j.jsg.2003.11.028.

Fondriest, M., Smith, S.A.F., Di Toro, G., Zampieri, D., Mittempergher, S., 2012. Fault zone structure and seismic slip localization in dolostones, an example from the Southern Alps, Italy. J. Struct. Geol. 45, 52–67.

Fondriest, M., Smith, S.A.F., Candela, T., Nielsen, S.B., Mair, K., Toro, G. Di, 2013. Mirror-like faults and power dissipation during earthquakes. Geology 41, 1175–1178. doi:10.1130/G34641.1.

Fondriest, M., Aretusini, S., Di Toro, G., Smith, S.A.F., 2015. Fracturing and rock pulverization along an exhumed seismogenic fault zone in dolostones: The Foiana Fault Zone (Southern Alps, Italy). Tectonophysics 654, 56–74. doi:10.1016/j.tecto.2015.04.015.

Fossen, H., Schultz, R. A., Shipton, Z. K., Mair, K., 2007. Deformation bands in sandstone: a review. J. Geol. Soc. 164 (4), 755-769.

Fukuyama, E., Mizoguchi, K., 2010. Constitutive parameters for earthquake rupture dynamics based on high-velocity friction tests with variable sliprate 15–26. doi:10.1007/s10704-009-9417-5.

Fynn, G.W., Powell, W.J.A., 1979. The cutting and polishing of electro-optic materials. 216 p. Adams Hilger, London.

Galadini, F., 1999. Pleistocene changes in the central Apennine fault kinematics: a key to decipher active tectonics in central Italy. Tectonics 18 (5), 877-894.

Galadini, F, Galli, P, Moro, M, 2003. Paleoseismology of silent faults in the central Apennines (Italy): the Campo Imperatore fault (Gran Sasso Range fault system). Ann. Geophys. 46 (5), 793-813.

Galli, P., Galadini, F., Moro, M., Giraudi, C., 2002. New paleoseismological data from the Gran Sasso d'Italia area (central Apennines). Geophys. Res. Lett. 29 (7), 38-1.

Ghisetti, F., Vezzani, L., 1981. Contribution of structural analysis to understanding the geodynamic evolution of the Calabrian Arc (Southern Italy). J. Struct. Geol. 3 (4), 371-381.

Ghisetti, F., Vezzani, L., 1991. Thrust belt development in the central Apennines (Italy): Northward polarity of thrusting and out-of-sequence deformations in the Gran Sasso Chain. Tectonics 10, 904–919.

Ghisetti, F., Vezzani, L., 1999. Depth and modes of Pliocene-Pleistocene crustal extension of the Apennines (Italy). Terra Nova 11, 67–72.

Ghisetti, F., Vezzani, L., 2002. Normal faulting, transcrustal permeability and seismogenesis in the Apennines (Italy). Tectonophysics 348, 155–168. doi:10.1016/S0040-1951(01)00254-2.

Giraudi, C., Frezzotti, M., 1995. Palaeoseismicity in the Gran Sasso Massif (Abruzzo, central Italy). Quaternary Int. 25, 81-93.

Giraudi, C., Frezzotti, M., 1997. Late Pleistocene glacial events in the central Apennines, Italy. Quaternary Res. 48 (3), 280-290.

Goldsby, D. L., Tullis, T. E., 2011. Flash heating leads to low frictional strength of crustal rocks at earthquake slip rates. Science, 334(6053), 216-218.

Govoni, A., Marchetti, A., De Gori, P., Di Bona, M., Lucente, F.P., Improta, L., Chiarabba, C., Nardi, A., Margheriti, L., Agostinetti, N.P., Di Giovambattista, R., Latorre, D., Anselmi, M., Ciaccio, M.G., Moretti, M., Castellano, C., Piccinini, D., 2014. The 2012 Emilia seismic sequence (Northern Italy): Imaging the thrust fault system by accurate aftershock location. Tectonophysics 622, 44–55. doi:10.1016/j.tecto.2014.02.013.

Gratier, J. P., Gamond, J. F., 1990. Transition between seismic and aseismic deformation in the upper crust. Geological Society, London, Special Publications, 54(1), 461-473.

Green, H.W., Shi, F., Bozhilov, K., Xia, G., Reches, Z., 2015. Phase transformation and nanometric flow cause extreme weakening during fault slip. Nat. Geosci. 8, 484–489. doi:10.1038/ngeo2436.

Groshong, R.H. Jr, 1988. Low-temperature deformation mechanisms and their interpretation. Bulletin of the Geological Society of America 100, 1329–1360.

Han, R., Shimamoto, T., Ando, J.I., Ree, J.H., 2007a. Seismic slip record in carbonate-bearing fault zones: An insight from high-velocity friction experiments on siderite gouge. Geology 35, 1131–1134. doi:10.1130/G24106A.1.

Han, R., Shimamoto, T., Hirose, T., Ree, J.-H., Ando, J., 2007b. Ultralow Friction of Carbonate Faults Caused by Thermal Decomposition. Science (80-.). 316, 878–881. doi:10.1126/science.1139763.

Han, R., Hirose, T., Shimamoto, T., 2010. Strong velocity weakening and powder lubrication of simulated carbonate faults at seismic slip rates. J. Geophys. Res. Solid Earth 115. doi:10.1029/2008JB006136.

Han, R., Hirose, T., Shimamoto, T., Lee, Y., Ando, J.I., 2011. Granular nanoparticles lubricate faults during seismic slip. Geology 39, 599–602. doi:10.1130/G31842.1.

Hansen, L.N., Zimmerman, M.E., Kohlstedt, D.L., 2011. Grain boundary sliding in San Carlos olivine : Flow law parameters and crystallographic - preferred orientation. J. Geophys. Res. 116. doi:10.1029/2011JB008220.

Hausegger, S., Kurz, W., Rabitsch, R., Kiechl, E., Brosch, F.J., 2010. Analysis of the internal structure of a carbonate damage zone: Implications for the mechanisms of fault breccia formation and fluid flow. J. Struct. Geol. 32, 1349–1362. doi:10.1016/j.jsg.2009.04.014.

Heaton, T.H., 1990. Evidence for and implications of self-healing pulses of slip in earthquake rupture. Phys. Earth Planet. Inter. 64, 1–20.

Hirose, T., Shimamoto, T., 2005. Growth of molten zone as a mechanism of slip weakening of simulated faults in gabbro during frictional melting. J. Geophys. Res. Solid Earth 110 (B5).

Holdsworth, R., N. De Paola, I. Faoro, R. Bullock, C. Viti, and C. Collettini, 2013. Nano-scale diffusion-accommodated weakening triggered by frictional sliding during earthquakes in carbonate rocks, Geol. Soc. Am. Abstr. Programs, 45, 679.

Holyoke, C.W., Kronenberg, A.K., Newman, J., 2014. Microstructural evolution during strain localization in dolomite aggregates. J. Struct. Geol. 69, 449–464. doi:10.1016/j.jsg.2014.04.008.

ISIDe Working Group, 2010. Italian Seismological Instrumental and parametric database. http://iside.rm.ingv.it/iside/standard/index.jsp.

Ispra, 2012. Carta Geologica d'Italia, sheet 349 "Gran Sasso d'Italia". APAT, Servizio Geologico d'Italia. S.EL.CA., Florence, Italy. http://www.isprambiente.gov.it/Media/carg/349_GRANSASSO/Foglio.html.

Jamison, W.R., Spang, J.H., 1976. Use of calcite twin lamellae to infer differential stress. Geol. Soc. Am. Bull. 87, 868–872.

Jefferies, S.P., Holdsworth, R.E., Shimamoto, T., Takagi, H., Lloyd, G.E., Spiers, C.J., 2006. Origin and mechanical significance of foliated cataclastic rocks in the cores of crustal-scale faults: Examples from the Median Tectonic Line, Japan. J. Geophys. Res. Solid Earth 111, 1–17. doi:10.1029/2005JB004205.

Jolivet, L., Faccenna, C., 2000. Mediterranean extension and the Africa-Eurasia collision. Tectonics 19 (6), 1095-1106.

Jolivet, L., Faccenna, C., Goffé, B., Mattei, M., Rossetti, F., Brunet, C., Storti, F., Funiciello, R., Cadet, J.P., D'Agostino, N., Parra, T., 1998. Midcrustal shear zones in postorogenic extension: example from the northern Tyrrhenian Sea. J. Geophys. Res. 103 (B6), 12123-12160.

Kanamori, H., Brodsky, E., 2004. The physics of earthquakes. Reports on Progress in Physics, v. 67, p. 1429–1496, doi:10.1088/0034-4885/67/8/R03.

Kanamori, H., Rivera, L., 2006. Energy Partitioning During an Earthquake Hiroo Kanamori and Luis Rivera, in: Earthquakes: Radiated Energy and the Physics of Faulting. Geophysical Monograph Series 170, pp. 3–13.

Karato, S., 2008. Deformation of earth materials, An Introduction to the Rheology of Solid Earth. doi:10.1007/s00024-009-0536-8.

Kennedy, L. A., and Logan, J. M., 1997, The role of veining and dissolution in the evolution of fine-grained mylonites: the McConnell thrust, Alberta: Journal of Structural Geology, v. 19, no. 6, p. 785-797.

Kennedy, L. A., and White, J. C., 2001, Low-temperature recrystallization in calcite: Mechnisms and consequences: Geology, v. 29, no. 11, p. 1027-1030.

Kitajima, H., Chester, J.S., Chester, F.M., Shimamoto, T., 2010. High-speed friction of disaggregated ultracataclasite in rotary shear: Characterization of frictional heating, mechanical behavior, and microstructure evolution. J. Geophys. Res. Solid Earth 115, 1–21. doi:10.1029/2009JB007038.

Kushnir, A.R.L., Kennedy, L.A., Misra, S., Benson, P., White, J.C., 2015. The mechanical and microstructural behaviour of calcite-dolomite composites: An experimental investigation. J. Struct. Geol. 70, 200–216. doi:10.1016/j.jsg.2014.12.006.

Lacombe, O., Laurent, P., 1996. Determination of deviatoric stress tensors based on inversion of calcite twin data from experimentally deformed monophase samples: preliminary results. Tectonophysics, 25, 189-202.

Lacombe, O., 2007. Comparison of paleostress magnitudes from calcite twins with contemporary stress magnitudes and frictional sliding criteria in the conti- nental crust: mechanical implications. J. Struct. Geol. 29 (1), 86-99.

Laurent, P., Kern, H., Lacombe, O., 2000. Determination of deviatoric stress tensors based on inversion of calcite twin data from experimentally deformed monophase samples. II: Uniaxial and triaxial stress experiments. Tectonophysics, 327, 131–148.

Lavecchia, G., 1985. Il sovrascorrimento dei Monti Sibillini; analisi cinematica e strutturale. Bollettino della Società Geologica Italiana, 104(1), 161-194.

Lavecchia, G., de Nardis, R., Cirillo, D., Brozzetti, F., Boncio, P., 2012. The May-June 2012 Ferrara Arc earthquakes (northern Italy): Structural control of the spatial evolution of the seismic sequence and of the surface pattern of coseismic fractures. Ann. Geophys. 55, 533–540. doi:10.4401/ag-6173.

Li, T., Sui, F., Li, F., Cai, Y., Jin, Z., 2014. Effects of dry grinding on the structure and granularity of calcite and its polymorphic transformation into aragonite. Powder Technol. 254, 338–343. doi:10.1016/j.powtec.2014.01.043.

Lin, A., 2001. S-C fabrics developed in cataclastic rocks from the Nojima fault zone, Japan and their implications for tectonic history. J. Struct. Geol. 23, 1167–1178. doi:10.1016/S0191-8141(00)00171-1.

Liu, J., Walter, J.M., Weber, K., 2002. Fluid-enhanced low-temperature plasticity of calcite marble: Microstructures and mechanisms. Geology 30, 787–790. doi:10.1130/0091-7613(2002)030<0787:FELTPO>2.0.CO;2.

Logan, J. M., Friedman, M., Higgs, N., Dengo, C., Shimamoto, T., 1979. Experimental studies of simulated gouge and their application to studies of natural fault zones, Proceedings of Conference VIII on Analysis of Actual Fault Zones in Bedrock, U.S. Geological Survey Open-File Report 79–1239.

Ma, K.-F., Tanaka, H., Song, S.-R., Wang, C.-Y., Hung, J.-H., Tsai, Y.-B., Mori, J., Song, Y.-F., Yeh, E.-C., Soh, W., Sone, H., Kuo, L.-W., Wu, H.-Y., 2006. Slip zone and energetics of a large earthquake from the Taiwan Chelungpu-fault Drilling Project. Nature 444, 473–476. doi:10.1038/nature05253.

Ma, S., Andrews, D.J., 2010. Inelastic off-fault response and three-dimensional dynamics of earthquake rupture on a strike-slip fault. J. Geophys. Res. 115. http://dx.doi.org/10.1029/2009JB006382.

Ma, S., Shimamoto, T., Yao, L., Togo, T., Kitajima, H., 2014. A rotary-shear low to high-velocity friction apparatus in Beijing to study rock friction at plate to seismic slip rates. Earthq. Sci. 27, 469–497. doi:10.1007/s11589-014-0097-5.

Mackenzie, J. K., Thomson, M. J., 1957. Some statistics associated with the random disorientation of cubes. Biometrika, 44(1-2), 205-210.

Mair, K., Frye, K.M., Marone, C., 2002. Influence of grain characteristics on the friction of granular shear zones. J. Geophys. Res. Solid Earth 107, 2219. doi:10.1029/2001JB000516.

Mair, K., Hazzard, J.F., 2007. Nature of stress accommodation in sheared granular material: Insights from 3D numerical modeling. Earth Planet. Sci. Lett. 259, 469–485. doi:10.1016/j.epsl.2007.05.006.

Mair, K., Abe, S., 2008. 3D numerical simulations of fault gouge evolution during shear: Grain size reduction and strain localization. Earth Planet. Sci. Lett. 274, 72–81. doi:10.1016/j.epsl.2008.07.010.

Malinverno, A., Ryan, W. B., 1986. Extension in the Tyrrhenian Sea and shortening in the Apennines as result of arc migration driven by sinking of the lithosphere. Tectonics 5 (2), 227-245.

Marone, C., 1998. Laboratory-derived friction laws and their application to seismic faulting. Annu. Rev. Earth Planet. Sci. 26, 643–696.

Marone, C., Raleigh, C. B., and Scholz, C. H., 1990. Frictional behavior and constitutive modeling of simulated fault gouge. Journal of Geophysical Research: Solid Earth (1978–2012), 95(B5), 7007-7025.

Micarelli, L., Benedicto, A., Wibberley, C. A. J., 2006. Structural evolution and permeability of normal fault zones in highly porous carbonate rocks. J. Struct. Geol. 28 (7), 1214-1227.

Michie, E. A. H., Haines, T. J., Healy, D., Neilson, J. E., Timms, N. E., Wibberley, C. A. J., 2014. Influence of carbonate facies on fault zone architecture. J. Struct. Geol. 65, 82-99.

Miller, S.A., Collettini, C., Chiaraluce, L., Cocco, M., Barchi, M., Kaus, B.J.P., 2004. Aftershocks driven by a high-pressure CO2 source at depth. Nature 427, 724–727. doi:10.1038/nature02251.

Miller, J.A., Viola, G., Mancktelow, N.S., 2008. Oxygen, carbon and strontium isotope constraints on the mechanisms of nappe emplacement and fluid-rock interaction along the subhorizontal Naukluft Thrust, central Namibia. J. Geol. Soc. London. 165, 739–753. doi:10.1144/0016-76492007-079.

Mirabella, F., Barchi, M. R., Lupattelli, A., Stucchi, E., Ciaccio, M. G., 2008. Insights on the seismogenic layer thickness from the upper crust structure of the Umbria-Marche Apennines (central Italy). Tectonics, 27(1), 1–15, doi:10.1029/2007TC002134.

Mitchell, T. M., Faulkner, D. R., 2009. The nature and origin of off-fault damage surrounding strike-slip fault zones with a wide range of displacements: a field study from the Atacama fault system, northern Chile. J. Struct. Geol. 31 (8), 802-816. http://dx.doi.org/10.1016/j.jsg.2009.05.002.

Mitchell, T. M., Ben-Zion, Y., Shimamoto, T., 2011. Pulverized fault rocks and damage asymmetry along the Arima-Takatsuki Tectonic Line, Japan. Earth Planet. Sci. Lett. 308, 284-297. http://dx.doi.org/10.1016/j.epsl.2011.04.023.

Mitchell, T.M., Smith, S.A.F., Anders, M.H., Di Toro, G., Nielsen, S., Cavallo, A., Beard, A.D., 2015. Catastrophic emplacement of giant landslides aided by thermal decomposition: Heart Mountain, Wyoming. Earth Planet. Sci. Lett. 411, 199–207. doi:10.1016/j.epsl.2014.10.051.

Mollema, P. N. and Antonellini, M., (1999). Development of strike-slip faults in the dolomites of the Sella Group, Northern Italy. Journal of Structural Geology, 21, 273-292.

Molli, G., Cortecci, G., Vaselli, L., Ottria, G., Cortopassi, A., Dinelli, E., Mussi, M., Barbieri, M., 2010. Fault zone structure and fluid-rock interaction of a high angle normal fault in Carrara marble (NW Tuscany, Italy). J. Struct. Geol. 32, 1334–1348. doi:10.1016/j.jsg.2009.04.021.

Molli, G., Malavieille, J., 2011. Orogenic processes and the Corsica/Apennines geodynamic evolution: insights from Taiwan. Int. J. Earth Sci. 100 (5), 1207-1224.

Molli, G., White, J. C., Kennedy, L. A., and Taini, V., 2011, Low-temperature deformation of limestone, Isola Palmaria, northern Apennine, Italy - The role of primary textures, precursory veins and intracryatlline deformation in localization: Journal of Structural Geology, no. 33, p. 225-270.

Monzawa, N., Otsuki, K., 2003. Comminution and fluidization of granular fault materials: Implications for fault slip behavior. Tectonophysics 367, 127–143. doi:10.1016/S0040-1951(03)00133-1.

Mort, K., Woodcock, N. H., 2008. Quantifying fault breccia geometry: Dent fault, NW England. J. Struct. Geol. 30, 701-709. http://dx.doi.org/10.1016/j.jsg.2008.02.005.

Muto, J., Nakatani, T., Nishikawa, O., Nagahama, H., 2015. Fractal particle size distribution of pulverized fault rocks as a function of distance from the fault core. Geophys. Res. Lett. 42, 3811–3819. doi:10.1002/2015GL064026.

Niemeijer, A.R., Spiers, C.J., 2006. Velocity dependence of strength and healing behaviour in simulated phyllosilicate-bearing fault gouge. Tectonophysics 427, 231–253. doi:10.1016/j.tecto.2006.03.048.

Niemeijer, A.R., Spiers, C.J., 2007. A microphysical model for strong velocity weakening in phyllosilicate-bearing fault gouges. J. Geophys. Res. Solid Earth 112, 1–12. doi:10.1029/2007JB005008.

Niemeijer, A., G. Di Toro, S. Nielsen, and F. Di Felice, 2011. Frictional melting of gabbro under extreme experimental conditions of normal stress, acceleration, and sliding velocity, J. Geophys. Res., 116, B07404, doi:10.1029/2010JB008181.

Niemeijer, A.R., Di Toro, G., Griffith, A.W., Bistacchi, A., Smith, S.A.F., Nielsen, S., 2012. Inferring earthquake physics and chemistry using an integrated field and laboratory approach. J. Struct. Geol. 39, 2–36. doi:10.1016/j.jsg.2012.02.018.

Oesterling, N., Heilbronner, R., Stünitz, H., Barnhoorn, A., Molli, G., 2007. Strain dependent variation of microstructure and texture in naturally deformed Carrara marble. J. Struct. Geol. 29, 681–696. doi:10.1016/j.jsg.2006.10.007.

Parotto, M., Praturlon, A., 1975. Geological summary of the Central Apennines. Quaderni della Ricerca Scientifica 90, 257-300.

Passchier, C.W., Trouw, R.A.J., 2005. Microtectonics, 2nd edition. Springer-Verlag, Berlin.

Patacca, E., Sartori, R., Scandone, P., 1990. Tyrrhenian basin and Apenninic arcs: kinematic relations since late Tortonian times. Mem. Soc. Geol. It. 45 (1), 425-451.

Paterson, M. S., 1958. Experimental deformation and faulting in Wombeyan marble. Geological Society of America Bulletin, 69(4), 465-476.

Paterson, M. S., and Olgaard, D. L., 2000. Rock deformation tests to large shear strains in torsion: Journal of Structural Geology, v. 22, p. 1341-1358.

Pearce, M.A., Timms, N.E., Hough, R.M., Cleverley, J.S., 2013. Reaction mechanism for the replacement of calcite by dolomite and siderite: Implications for geochemistry, microstructure and porosity evolution during hydrothermal mineralisation. Contrib. to Mineral. Petrol. 166, 995–1009. doi:10.1007/s00410-013-0905-2.

Pearce, M.A., 2015. EBSDinterp 1.0: A MATLAB ® Program to Perform Microstructurally Constrained Interpolation of EBSD Data. Microsc. Microanal. 21, 985–993. doi:10.1017/S1431927615000781.

Piazolo, S., Kaminsky, F. V., Trimby, P., Evans, L., Luzin, V., 2016. Carbonado revisited: Insights from neutron diffraction, high resolution orientation mapping and numerical simulations. Lithos 265, 244–256. doi:10.1016/j.lithos.2016.09.011.

Pischiutta, M., Fondriest, M., Demurtas, M., Magnoni, F., Di Toro, G., Rovelli, A., 2017. Structural control on the directional amplification of seismic noise (Campo Imperatore, central Italy). Earth Planet. Sci. Lett. 471, 10–18. doi:10.1016/j.epsl.2017.04.017.

Pittarello, L., Di Toro, G., Bizzarri, A., Pennacchioni, G., Hadizadeh, J., Cocco, M., 2008. Energy partitioning during seismic slip in pseudotachylyte-bearing faults (Gole Larghe Fault, Adamello, Italy). Earth Planet. Sci. Lett. 269, 131–139. doi:10.1016/j.epsl.2008.01.052.

Poirier, J.-P., 1985. Creep of Crystals: High-Temperature Deformation Processes in Metals, Ceramics and Minerals. Cambridge Univ. Press.

Prior, D.J., Boyle, A.P., Brenker, F., Cheadle, M.C., Day, A., Lopez, G., Peruzzo, L., Potts, G.J., Reddy, S., Spiess, R., Timms, N.E., Trimby, P.W., Wheeler, J., Zetterström, L., 1999. The application of electron backscatter diffraction and orientation constrast imaging in th SEM to textural problems in rocks. Am. Mineral. 84, 1741–1759. doi:10.2138/am-1999-11-1204.

Proctor, B.P., Mitchell, T.M., Hirth, G., Goldsby, D., Zorzi, F., Platt, J.D., Di Toro, G., 2014. Dynamic weakening of serpentinite gouges and bare surfaces at seismic slip rates. J. Geophys. Res. Solid Earth 119, 8107–8131. doi:10.1002/ 2014JB011057.

Rathbun, A.P., Marone, C., 2010. Effect of strain localization on frictional behavior of sheared granular materials. J. Geophys. Res. 115, 1–16. doi:10.1029/2009JB006466.

Reches, Z. E., Lockner, D. A., 2010. Fault weakening and earthquake instability by powder lubrication. Nature, 467(7314), 452.

Rempe, M., 2015. Frictional behavior and microstructures of calcite-bearing fault gouges. Phd thesis.

Rempe, M., Smith, S., Mitchell, T., Hirose, T., Di Toro, G., 2017. The effect of water on strain localization in calcite fault gouge sheared at seismic slip rates. J. Struct. Geol. 97, 104–117. doi:10.1016/j.jsg.2017.02.007.

Rice, J.R., 2006. Heating and weakening of faults during earthquake slip. J. Geophys. Res. Solid Earth 111, 1–29. doi:10.1029/2005JB004006.

Rosenbaum, G., Lister, G.S., 2004. Neogene and Quaternary rollback evolution of the Tyrrhenian Sea, the Apennines, and the Sicilian Maghrebides. Tectonics 23 (1), TC1013. doi:1010.1029/2003TC001518.

Røyne, A., Bisschop, J., and Dysthe, D. K., 2011. Experimental investigation of surface energy and subcritical crack growth in calcite. Journal of Geophysical Research: Solid Earth (1978 – 2012), 116(B4).

Rowe, K.J., Rutter, E.H., 1990. Palaeostress estimation using calcite twinning. Experimental calibration and application to nature. J. Struct. Geol. 12, 1–17. doi:10.1016/0191-8141(90)90044-Y.

Rowe, C.D., Moore, J.C., Meneghini, F., McKeirnan, A.W., 2005. Large-scale pseudotachylytes and fluidized cataclasites from an ancient subduction thrust fault. Geology 33, 937–940. doi:10.1130/G21856.1.

Rowe, C.D., Fagereng, A., Miller, J.A., Mapani, B., 2012. Signature of coseismic decarbonation in dolomitic fault rocks of the Naukluft Thrust, Namibia. Earth Planet. Sci. Lett. 333-334, 200-210.

Rowe, C.D., Griffith, W.A., 2015. Do faults preserve a record of seismic slip: A second opinion. J. Struct. Geol. 78, 1–26. doi:10.1016/j.jsg.2015.06.006.

Ruina, A., 1983. Slip instability and state variable friction laws. Journal of Geophysical Research: Solid Earth (1978–2012), 88(B12), 10359-10370.

Rutter, E. H., 1972, The Effects of Strain-Rate Changes on the Strength and Ductility of Solenhofen Limestone at Low Temperatures and Confining Pressures: International Journal of Rock Mechanics and Mining Sciences and Geomechanics Abstracts, v. 1972, p. 183-189.

Rutter, E. H., 1983. Pressure solution in nature, theory and experiment. Journal of the Geological Society, 140(5), 725-740.

Rutter, E.H., Maddock, R.H., Hall, S.H., White, S.H., 1986. Comparative microstructures of natural and experimentally produced clay-bearing fault gouges. Pure Appl. Geophys. PAGEOPH 124, 3–30. doi:10.1007/BF00875717.

Rutter, E.H., 1995, Experimental study of the influence of stress, temperature, and strain on the dynamic recrystallization of Carrara marble: Journal of Geophysical Research, v. 100, No. B12, p. 24651-24663.

Rutter, E.H., Faulkner, D.R., Brodie, K.H., Phillips, R.J., Searle, M.P., 2007. Rock deformation processes in the Karakoram fault zone, Eastern Karakoram, Ladakh, NW India. J. Struct. Geol. 29, 1315–1326. doi:10.1016/j.jsg.2007.05.001.

Rybacki, E., Janssen, C., Wirth, R., Chen, K., Wenk, H.R., Stromeyer, D., Dresen, G., 2011. Low-temperature deformation in calcite veins of SAFOD core samples (San Andreas Fault) - Microstructural analysis and implications for fault rheology. Tectonophysics 509, 107–119. doi:10.1016/j.tecto.2011.05.014.

Rybacki, E., Evans, B., Janssen, C., Wirth, R., Dresen, G., 2013. Influence of stress, temperature, and strain on calcite twins constrained by deformation experiments. Tectonophysics 601, 20–36. doi:10.1016/j.tecto.2013.04.021.

Sakaguchi, A., Sakaguchi, H., Nishiura, D., Nakatani, M., Yoshida, S., 2011. Elastic stress indication in elastically rebounded rock. Geophys. Res. Lett. 38, L09316. doi:10.1029/2011GL047055.

Sammis, C., King, G., Biegel, R., 1987. The kinematics of gouge deformation. Pure Appl. Geophys. 125, 777–812. doi:10.1007/BF00878033.

Sammis, C.G., Steacy, S.J., 1994. The micromechanics of friction in a granular layer. Pure Appl. Geophys. 142, 777–794. doi:10.1007/BF00876064.

Sammis, C.G., King, G.C.P., 2007. Mechanical origin of power law scaling in fault zone rock. Geophys. Res. Lett. 34, 2–5. doi:10.1029/2006GL028548.

Sammis, C.G., Ben-Zion, Y., 2008. Mechanics of grain-size reduction in fault zones. J. Geophys. Res. Solid Earth 113, 1–12. doi:10.1029/2006JB004892.

Samtani, M., Dollimore, D., Alexander, K.S., 2002. Comparison of dolomite decomposition kinetics with related carbonates and the effect of procedural variables on its kinetic parameters. Thermochim. Acta 393, 135–145.

Sani, F., Ventisette, C., Montanari, D., Coli, M., Nafissi, P., Piazzini, A., 2004. Tectonic evolution of the internal sector of the Central Apennines, Italy. Mar. Pet. Geol. 21, 1235-1254.

Santantonio, M., Carminati, E., 2011. Jurassic rifting evolution of the Apennines and Southern Alps (Italy): parallels and differences. Geol. Soc. Am. Bull. 123 (3-4), 468-484.

Schaff, D. P., Bokelmann, G. H., Beroza, G. C., Waldhauser, F., Ellsworth, W. L., 2002. High-resolution image of Calaveras Fault seismicity. J. Geophys. Res. 107 (B9), ESE-5.

Schmid, S. M., Paterson, M. S., and Boland, J. N., 1980, High temperature flow and dynamic recrystallization in Carrara marble Tectonophysics, v. 65, p. 245-280.

Schmid, S. M., Panozzo, R., and Bauer, S., 1987, Simple shear experiments on calcite rocks: rheology and microfabric: Journal of Structural Geology, v. 9, no. 5/6, p. 747-778.

Scholz, C.H., 2002. The mechanics of earthquakes and faulting. Cambridge Univer- sity Press, Cambridge, p. 471.

Schröckenfuchs, T., Bauer, H., Grasemann, B., Decker, K., 2015. Rock pulverization and localization of a strike-slip fault zone in dolomite rocks (Salzach–Ennstal–Mariazell–Puchberg fault, Austria). J. Struct. Geol. 78, 67-85.

Shipton, Z. K., Soden, A. M., Kirkpatrick, J. D., Bright, A. M., Lunn, R. J., 2006. How thick is a fault? Fault displacement-thickness scaling revisited. Geophysical Monograph Series, 170, 193-198.

Sibson, R.H., 1973. Interactions between Temperature and Pore-Fluid Pressure during Earthquake Faulting and a Mechanism for Partial or Total Stress Relief. Nature 243, 66–68. doi:10.1038/physci243066a0.

Sibson, R. H., 1975. Generation of pseudotachylyte by ancient seismic faulting. Geophysical Journal International, 43(3), 775-794.

Sibson, R.H., 1977. Fault rocks and fault mechanisms. J. Geol. Soc. London. 133, 191–213. doi:10.1144/gsjgs.133.3.0191.

Sibson, R.H., 1985. Stopping of earthquake ruptures at dilational fault jogs. Nature 316, 248–251. doi:10.1038/316248a0.

Sibson, R. H., 1989. Earthquake faulting as a structural process. J. Struct. Geol. 11(1), 1-14. http://dx.doi.org/10.1016/0191-8141(89)90032-1.

Sibson, R. H., 1990. Conditions for fault-valve behaviour. In: Knipe, R.J., Rutter, E.H. (Eds.), Deformation Mechanisms, Rheology and Tectonics. Geological Society London, Special Publications 54 (1), 15-28.

Sibson, R.H., 2003. Thickness of the seismic slip zone. Bull. Seismol. Soc. Am. 93 (3), 1169e1178.

Siman-Tov, S., Aharonov, E., Sagy, A., Emmanuel, S., 2013. Nanograins form carbonate fault mirrors. Geology 41, 703–706. doi:10.1130/G34087.1.

Siman-Tov, S., Aharonov, E., Boneh, Y., & Reches, Z. E., 2015. Fault mirrors along carbonate faults: Formation and destruction during shear experiments. Earth Planet. Sci. Lett. 430, 367-376.

Smeraglia, L., Aldega, L., Billi, A., Carminati, E., Doglioni, C., 2016. Phyllosilicate injection along extensional carbonate-hosted faults and implications for co-seismic slip propagation: Case studies from the central Apennines, Italy. J. Struct. Geol. 93, 29–50. doi:10.1016/j.jsg.2016.10.003.

Smeraglia, L., Billi, A., Carminati, E., Cavallo, A., Doglioni, C., 2017a. Field- to nano-scale evidence for weakening mechanisms along the fault of the 2016 Amatrice and Norcia earthquakes, Italy. Tectonophysics 712–713, 156–169. doi:10.1016/j.tecto.2017.05.014.

Smeraglia, L., Bettucci, A., Billi, A., Carminati, E., Cavallo, A., Di Toro, G., Natali, M., Passeri, D., Rossi, M., Spagnuolo, E., 2017b. Microstructural evidence for seismic and aseismic slips along clay-bearing, carbonate faults. J. Geophys. Res. Solid Earth 122, 1–21. doi:10.1002/2017JB014042.

Smith, S.A.F., Billi, A., di Toro, G., Spiess, R., 2011. Principal Slip Zones in Limestone: Microstructural Characterization and Implications for the Seismic Cycle (Tre Monti Fault, Central Apennines, Italy). Pure Appl. Geophys. 168, 2365–2393. doi:10.1007/s00024-011-0267-5.

Smith, S.A.F., Di Toro, G., Kim, S., Ree, J.H., Nielsen, S., Billi, A., Spiess, R., 2013. Coseismic recrystallization during shallow earthquake slip. Geology 41, 63–66. doi:10.1130/G33588.1.

Smith, S.A.F., Nielsen, S., Di Toro, G., 2015. Strain localization and the onset of dynamic weakening in calcite fault gouge. Earth Planet. Sci. Lett. 413, 25–36. doi:10.1016/j.epsl.2014.12.043.

Smith, S.A.F., Griffiths, J.R., Fondriest, M., Di Toro, G., 2017. “Coseismic Foliations” in Gouge and Cataclasite: Experimental Observations and Consequences for Interpreting the Fault Rock Record 81–102.

Snoke, A.W., Tullis, J., Todd, V.R., 1998. Fault-Related Rocks: a Photographic Atlas. Princeton Univ. Press, Princeton, N.J.

Sone, H., Shimamoto, T., 2009. Frictional resistance of faults during accelerating and decelerating slip Frictional resistance of faults during accelerating and decelerating earthquake slip. Nat. Geosci. 2, 705–708. doi:10.1038/ngeo637.

Spagnuolo, E., Plümper, O., Violay, M.E.S., Cavallo, A., Di Toro, G., 2015. Fast-moving dislocations trigger flash weakening in carbonate-bearing faults during earthquakes. Sci. Rep. 5, 16112. doi:10.1038/srep16112.

Speranza, F., 2003. Passive-margin heritage on thrust-system development: evidence from Corno Grande (Gran Sasso range, Italy). Boll. Soc. Geol. It. 122, 233-249, 13 ff.

Speranza, F., Adamoli, L., Maniscalco, R., Florindo, F., 2003. Genesis and evolution of a curved mountain front: paleomagnetic and geological evidence from the Gran Sasso range (central Apennines, Italy). Tectonophysics 362, 183–197.

Speranza, F., Minelli, L., 2014. Ultra-thick Triassic dolomites control the rupture behavior of the central Apennine seismicity: Evidence from magnetic modeling of the L'Aquila fault zone. J. Geophys. Res. 119, 6756–6770.

Stein, R.S., 1999. The role of stress transfer in earthquake occurrence. Nature 402, 605–609. doi:10.1038/45144.

Stojic, A.N., Brenker, F.E., 2010. Argon ion slicing (ArIS): a new tool to prepare super large TEM thin films from Earth and planetary materials. Eur. J. Mineral. 22, 17–21. doi:10.1127/0935-1221/2009/0022-2004.

Storti, F., Aldega, L., Balsamo, F., Corrado, S., Del Monaco, F., Di Paolo, L., Mastalerz, M., Monaco, P., Tallini, M., 2013. Evidence for strong middle Pleistocene earthquakes in the epicentral area of the 6 April 2009 L'Aquila seismic event from sediment paleofluidization and overconsolidation. J. Geophys. Res. 118 (7), 3767-3784.

Storti, F., Balsamo, F., Salvini, F., 2007. Particle shape evolution in natural carbonate granular wear material. Terra Nova 19 (5), 344-352.

Taplin, D.M.R., Dunlop, G.L., Langdon, T.G., 1979. Flow and failure of superplastic materials. Annu. Rev. Mater. Sci. 9, 151–189.

Tesei, T., Collettini, C., Viti, C., Barchi, M. R., 2013. Fault architecture and deformation mechanisms in exhumed analogues of seismogenic carbonate-bearing thrusts. J. Struct. Geol. 55, 167-181.

Tesei, T., Collettini, C., Barchi, M.R., Carpenter, B.M., Di Stefano, G., 2014. Heterogeneous strength and fault zone complexity of carbonate-bearing thrusts with possible implications for seismicity. Earth Planet. Sci. Lett. 408, 307–318. doi:10.1016/j.epsl.2014.10.021.

Tesei, T., Carpenter, B.M., Giorgetti, C., Scuderi, M.M., Sagy, A., Scarlato, P., Collettini, C., 2017. Friction and scale-dependent deformation processes of large experimental carbonate faults. J. Struct. Geol. 100, 12–23. doi:10.1016/j.jsg.2017.05.008.

Tinti, E., Fukuyama, E., Piatanesi, A., Cocco, M., 2005. A Kinematic Source Time Function Compatible With Earthquake Dynamics. Bull. Seismol. Soc. Am. 1–39.

Tisato, N., Di Toro, G., De Rossi, N., Quaresimin, M., Candela, T., 2012. Experimental investigation of flash weakening in limestone. J. Struct. Geol. 38, 183–199. doi:10.1016/j.jsg.2011.11.017.

Trimby, P.W., 2012. Orientation mapping of nanostructured materials using transmission Kikuchi diffraction in the scanning electron microscope. Ultramicroscopy 120, 16–24. doi:10.1016/j.ultramic.2012.06.004.

Trimby, P.W., Cao, Y., Chen, Z., Han, S., Hemker, K.J., Lian, J., Liao, X., Rottmann, P., Samudrala, S., Sun, J., Wang, J.T., Wheeler, J., Cairney, J.M., 2014. Characterizing deformed ultrafine-grained and nanocrystalline materials using transmission Kikuchi diffraction in a scanning electron microscope. Acta Mater. 62, 69–80. doi:10.1016/j.actamat.2013.09.026.

Trouw, R. A., Passchier, C. W., Wiersma, D. J., 2009. Atlas of Mylonites-and related microstructures. Springer Science & Business Media.

Turcotte, D.L., 1986. Fractals and Fragmentation. J. Geophys. Res. 91, 1921–1926.

Turner, F.J., 1953. Nature and dynamic interpretation of deformation lamellae in calcite of three marbles. Am. J. Sci. 251, 276–298. doi:10.2475/ajs.251.4.276.

Turner, F. J., Griggs, D. T., Heard, H., 1954. Experimental deformation of calcite crystals. Geol. Soc. Am. Bull., 65, 883–934, doi:10.1130/0016- 606(1954)65[883:EDOCC]2.0.CO;2.

Udías, A., Madariaga, R., Buforn, E., 2014. Source Mechanisms of Earthquakes: Theory and Practice. Cambridge University press.

Ujiie, K., Tsutsumi, A., Kameda, J., 2011. Reproduction of thermal pressurization and fluidization of clay-rich fault gouges by high-velocity friction experiments and implications for seismic slip in natural faults. In: Fagereng, Á., Toy, V.G., Rowland, J.V. (Eds.), Geology of the Earthquake Source: a Volume in Honour of Rick Sibson, Geol. Soc. London Special Pub, vol. 359, pp. 267e285.

Valoroso, L., Chiaraluce, L., Collettini, C., 2014. Earthquakes and fault zone structure. Geology 42, 343-346.

Valoroso, L., Chiaraluce, L., Piccinini, D., Stefano, R., Schaff, D., Waldhauser, F., 2013. Radiography of a normal fault system by 64,000 high-precision earthquake locations: The 2009 L'Aquila (central Italy) case study. J. Geophys. Res. 118, 1156–1176.

Verberne, B. A., He, C., Spiers, C. J., 2010. Frictional properties of sedimentary rocks and natural fault gouge from the Longmen Shan fault zone, Sichuan, China. Bulletin of the Seismological Society of America, 100(5B), 2767-2790.

Verberne, B., Spiers, C., Niemeijer, A., De Bresser, J., De Winter, D., Plumper, O., 2013a. Frictional properties and microstructure of calcite-rock fault gouges sheared at sub-seismic velocites. Pure Appl. Geophys. 31, 1–45. doi:10.1007/s00024-013-0760-0.

Verberne, B.A., de Bresser, J.H.P., Niemeijer, A.R., Spiers, C.J., de Winter, D.A.M., Plümper, O., 2013b. Nanocrystalline slip zones in calcite fault gouge show intense crystallographic preferred orientation: Crystal plasticity at subseismic slip rates at 18-150 °C. Geology 41, 863–866. doi:10.1130/G34279.1.

Verberne, B.A., Plümper, O., de Winter, M.D.A., Spiers, C.J., 2014. Superplastic nanofibrous slip zones control seismogenic fault friction. Science (80-.). 346, 1342–1344. doi:10.1126/science.1259003.

Vezzani, L., Festa, A., Ghisetti, F.C., 2010. Geology and tectonic evolution of the Central-Southern Apennines, Italy. Geol. Soc. Am. Special Papers 469, 1-58.

Viganò, A., Tumiati, S., Recchia, S., Martin, S., Marelli, M., Rigon, R., 2011. Carbonate pseudotachylytes: Evidence for seismic faulting along carbonate faults. Terra Nov. 23, 187–194. doi:10.1111/j.1365-3121.2011.00997.x.

Viola, G., Mancktelow, N.S., Miller, J.A., 2006. Cyclic frictional-viscous slip oscillations along the base of an advancing nappe complex: Insights into brittle-ductile nappe emplacement mechanisms from the Naukluft Nappe Complex, central Namibia. Tectonics 25, 1–20. doi:10.1029/2005TC001939.

Violay, M., Nielsen, S., Spagnuolo, E., Cinti, D., Di Toro, G., Di Stefano, G., 2013. Pore fluid in experimental calcite-bearing faults: Abrupt weakening and geochemical signature of co-seismic processes. Earth Planet. Sci. Lett. 361, 74–84. doi:10.1016/j.epsl.2012.11.021.

Violay, M., Nielsen, S., Gibert, B., Spagnuolo, E., Cavallo, A., Azais, P., Vinciguerra, S., Di Toro, G., 2014. Effect of water on the frictional behavior of cohesive rocks during earthquakes. Geology 42, 27–30. doi:10.1130/G34916.1.

Viti, C., Collettini, C., Tesei, T., 2014. Pressure solution seams in carbonatic fault rocks: mineralogy, micro/nanostructures and deformation mechanism. Contribution to Mineralogy and Petrology, 167(2), 1-15.

Waldhauser, F., Ellsworth, W.L., 2000. A double-difference earthquake location algorithm: Method and application to the northern Hayward fault, California. Bull. Seismol. Soc. Am. 90 (6), 1353-1368.

Weeks, J.D., Tullis, T.E., 1985. Frictional sliding of dolomite: A variation in constitutive behavior. J. Geophys. Res. 90, 7821. doi:10.1029/JB090iB09p07821.

Wesnousky, S.G., 1988. Seismological and structural evolution of strike-slip faults. Nature. doi:10.1038/335340a0.

Wesnousky, S.G., 2006. Predicting the endpoints of earthquake ruptures. Nature 444, 358–360. doi:10.1038/nature05275.

Wheeler, J., Prior, D.J., Jiang, Z., Spiess, R., Trimby, P.W., 2001. The petrological significance of misorientations between grains. Contrib. to Mineral. Petrol. 141, 109–124. doi:10.1007/s004100000225.

Wibberley, C.A., Shimamoto, T., 2003. Internal structure and permeability of major strike-slip fault zones: the Median Tectonic Line in Mie Prefecture, Southwest Japan. J. Struct. Geol. 25 (1), 59-78.

Wibberley, C. A., Yielding, G., Di Toro, G., 2008. Recent advances in the understanding of fault zone internal structure: a review. Geological Society, London, Special Publications, 299(1), 5-33.

Willemse, E. J., Peacock, D. C., Aydin, A., 1997. Nucleation and growth of strike-slip faults in limestones from Somerset, UK. Journal of Structural Geology, 19(12), 1461-1477.

Wilson, B., Dewers, T.A., Reches, Z., Brune, J., 2005. Particle size and energetics of gouge from earthquake rupture zones. Nature 434, 749–752. doi:10.1038/nature03433.

Woodcock, N.H., 1977. Specification of fabric shapes using an eigenvalue method. Bull. Geol. Soc. Am. 88, 1231–1236. doi:10.1130/0016-7606(1977)88<1231:SOFSUA>2.0.CO;2.

Wojtal, S., Mitra, G., 1986. Strain hardening and strain softening in fault zones from foreland thrusts. Geological Society of America Bulletin, 97(6), 674-687.

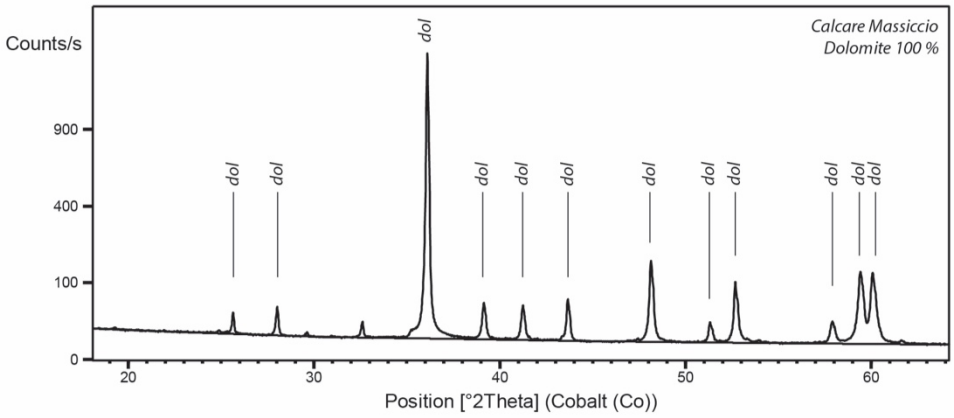
Yao, L., Ma, S., Niemeijer, A.R., Shimamoto, T., Platt, J.D., 2016. Is frictional heating needed to cause dramatic weakening of nanoparticle gouge during seismic slip? Insights from friction experiments with variable thermal evolutions. Geophys. Res. Lett. 43, 6852–6860. doi:10.1002/2016GL069053.

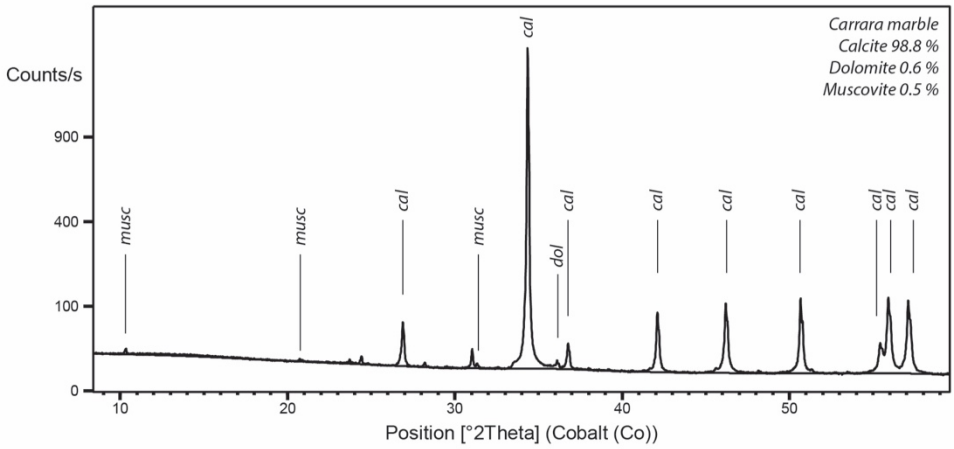
Yuan, F., Prakash, V., Tullis, T., 2011. Origin of pulverized rocks during earthquake fault rupture. J. Geophys. Res. 116, B06309. http://dx.doi.org/10.1029/2010JB007721.

Appendix A

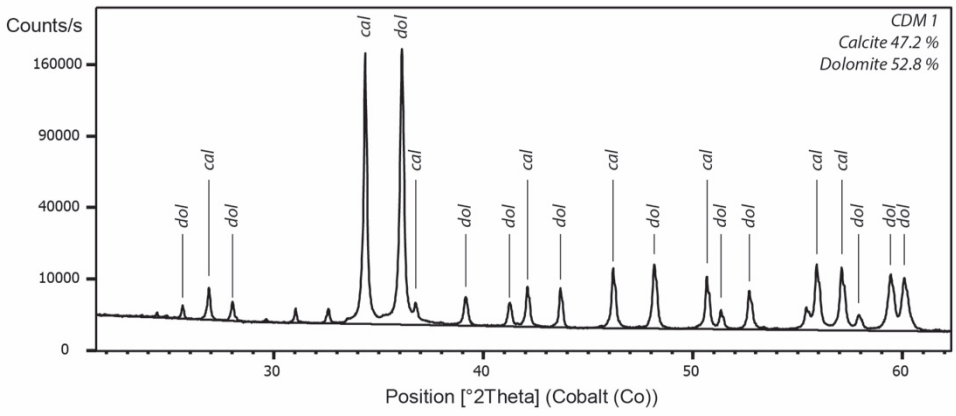
All X-ray Powder Diffraction results presented in Chapter II.

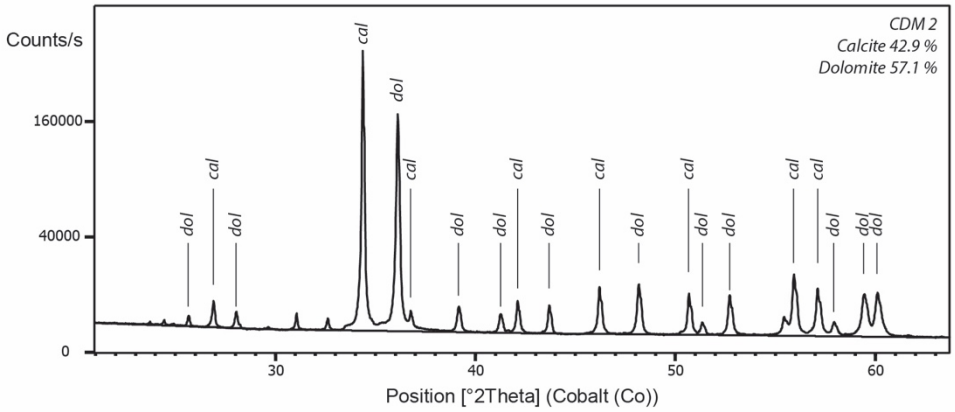
Starting materials



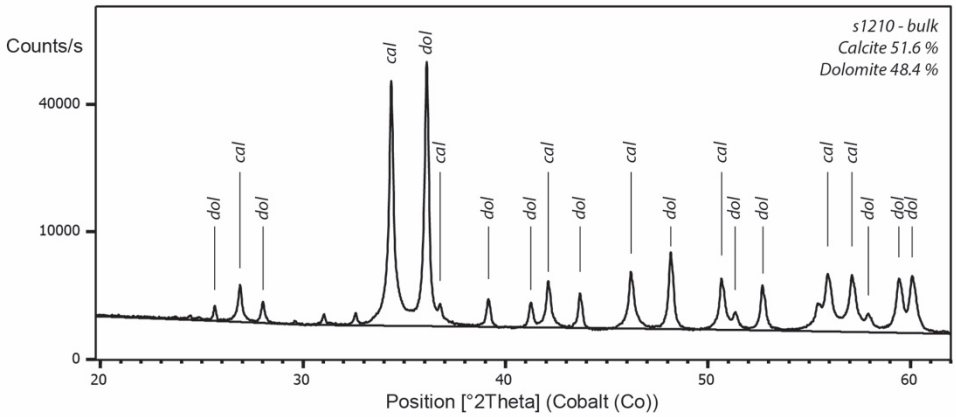


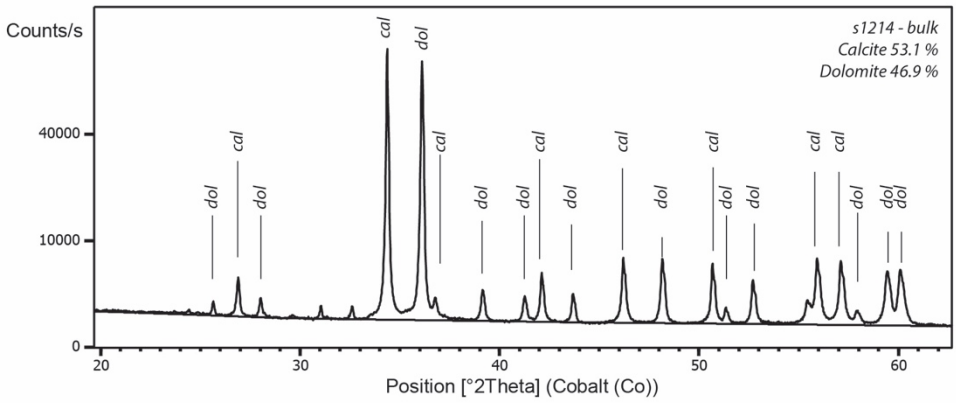
Calcite-dolomite mixture batches

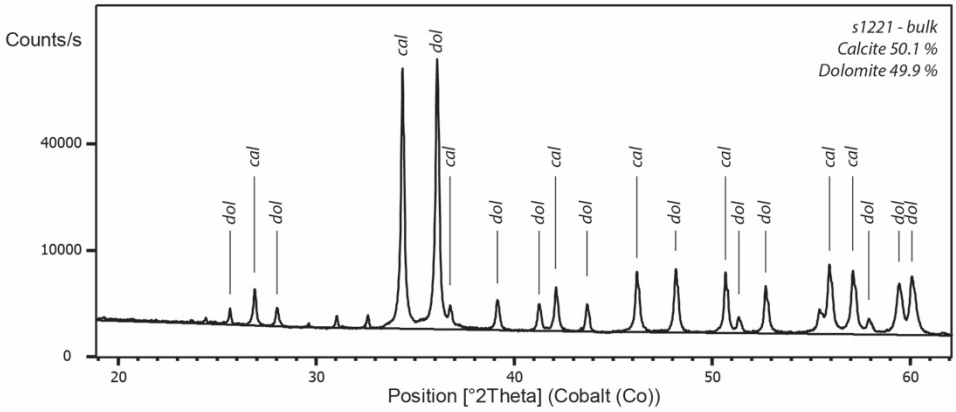


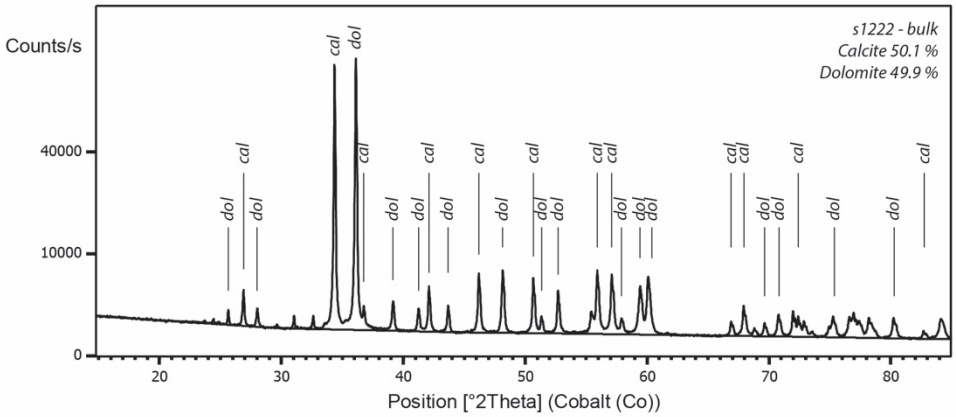


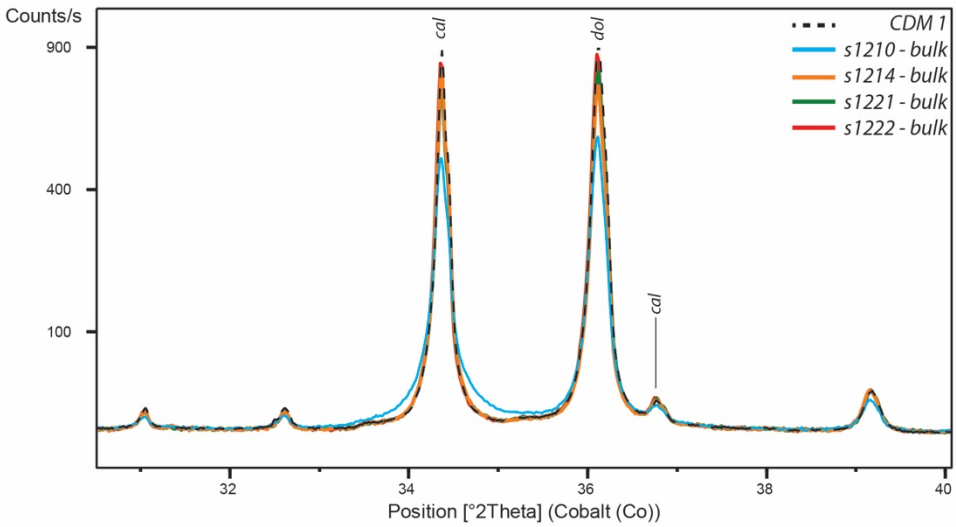
Bulk gouge analysis



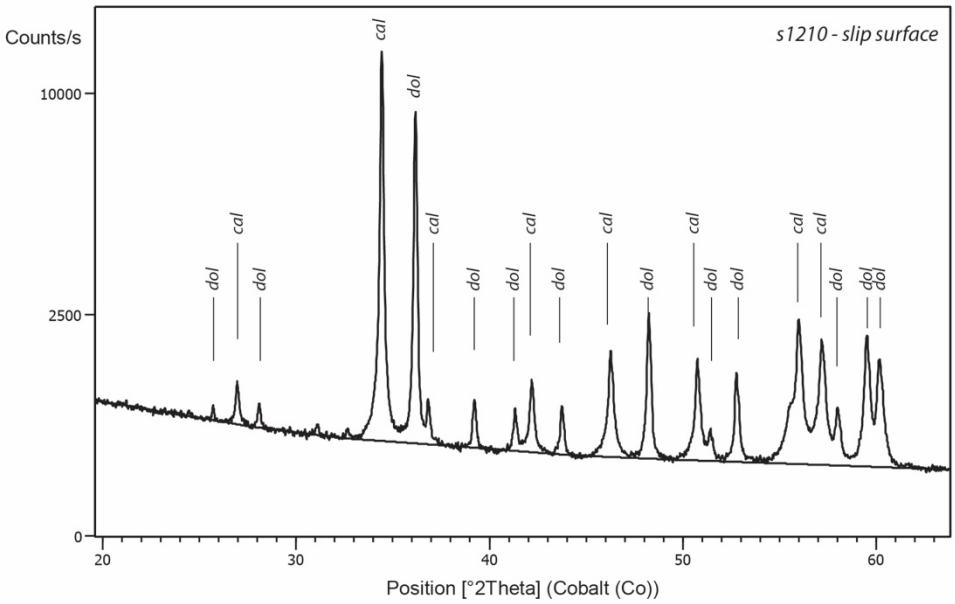


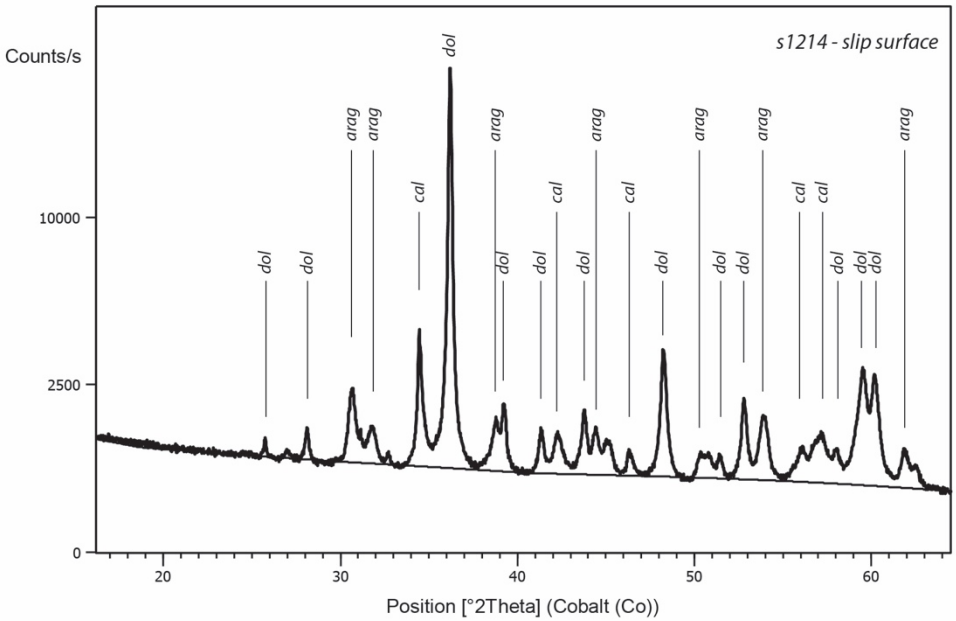

Counts/s
s1221 - bulk
Calcite 50.1 %
Dolomite 49.9 %
cal
dol
Position [°2Theta] (Cobalt (Co))

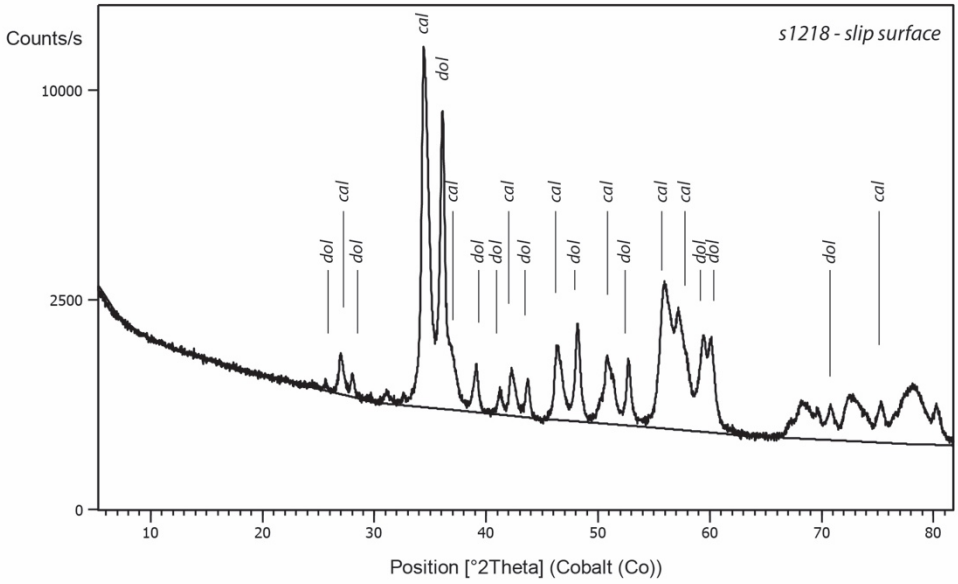

Counts/s
s1222 - bulk
Calcite 50.1 %
Dolomite 49.9 %
cal
dol
Position [°2Theta] (Cobalt (Co))

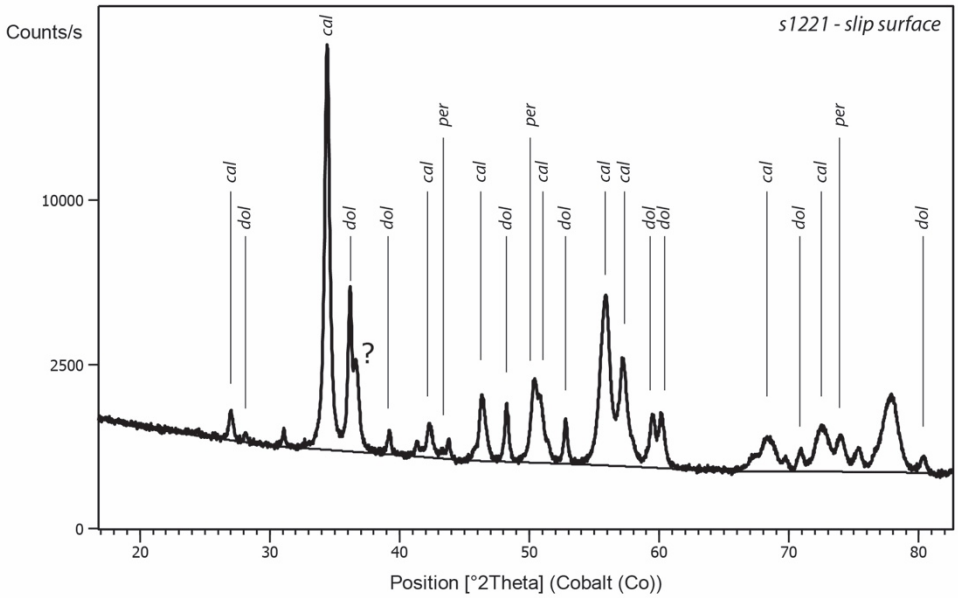

Counts/s
CDM 1
s1210 - bulk
s1214 - bulk
s1221 - bulk
s1222 - bulk
cal
dol
Position [°2Theta] (Cobalt (Co))

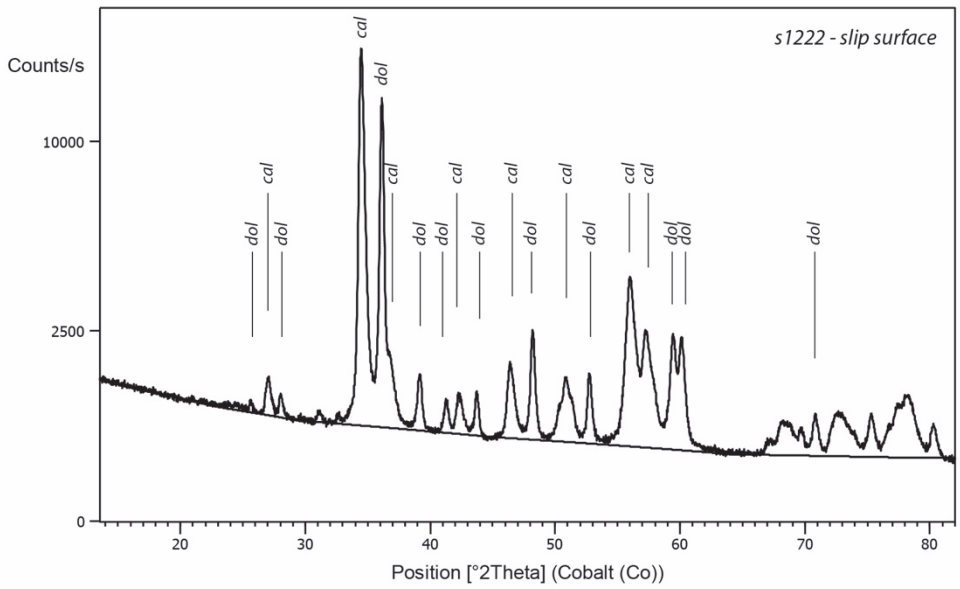
Slip surface analysis






Counts/s
s1218 - slip surface
10000
2500
0
cal
dol
10
20
30
40
50
60
70
80
Position [°2Theta] (Cobalt (Co))


Counts/s
s1221 - slip surface
10000
2500
0
cal
dol
per
?
20
30
40
50
60
70
80
Position [°2Theta] (Cobalt (Co))

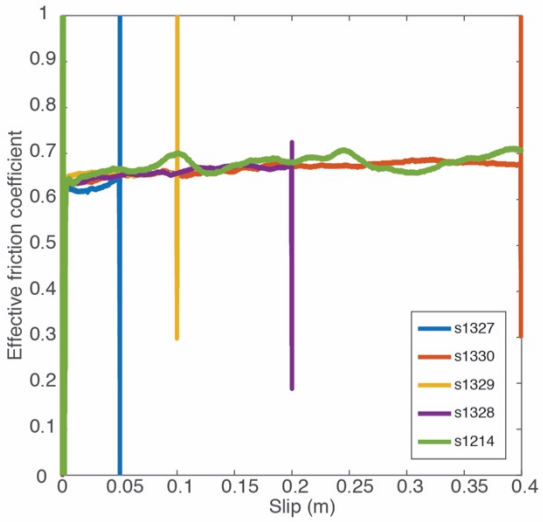

s1222 - slip surface
Counts/s
10000
2500
0
20
30
40
50
60
70
80
Position [°2Theta] (Cobalt (Co))
cal
dol

Appendix B

Raw mechanical data and additional microstructures from all the experiments presented in this thesis.

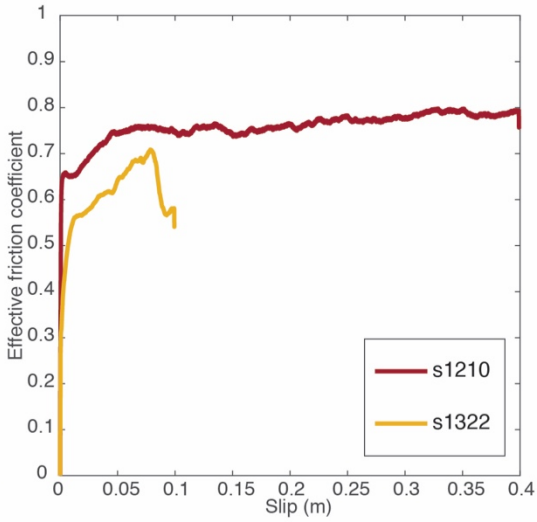
Experiments with increasing displacement

30 µm/s - water dampened



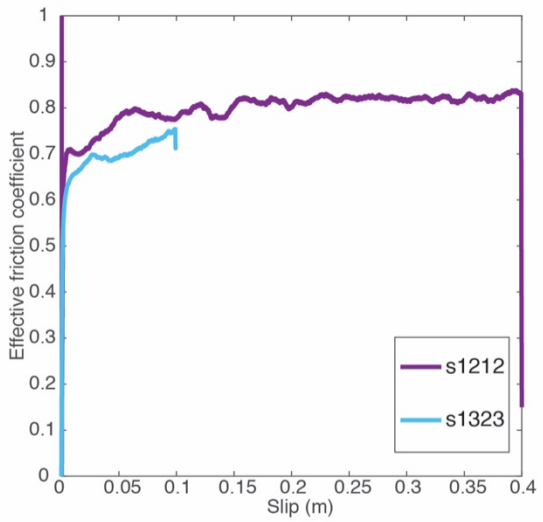
s1327: test of a prototype for water saturated experiments

30 µm/s - room humidity

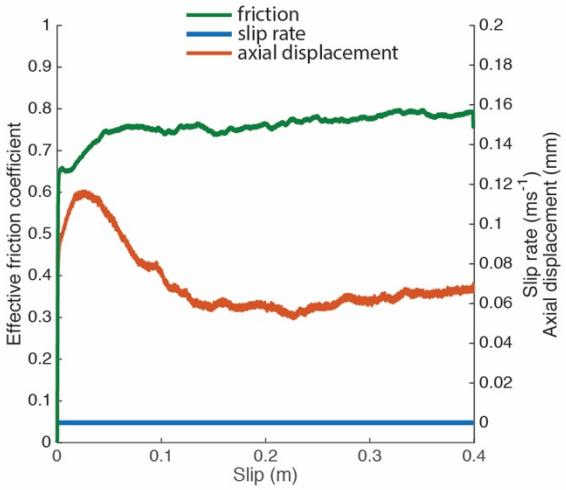


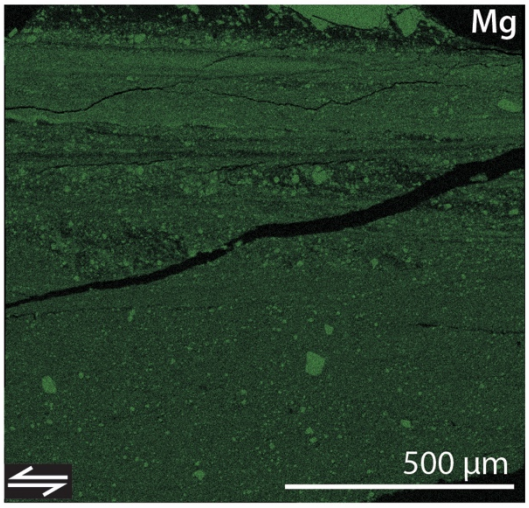
s1322: presence of some smeared grease on the slip surface

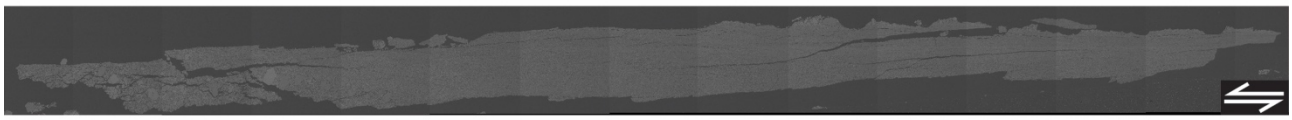
1 mm/s - room humidity



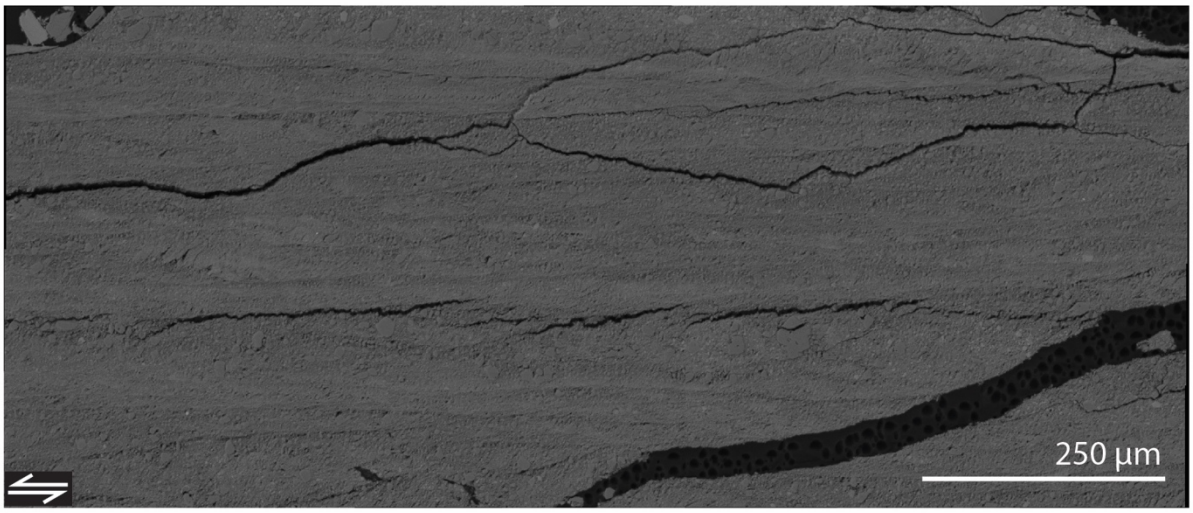
s1210
30 µms^{-1} - 40 cm - 17.5 MPa Room humidity

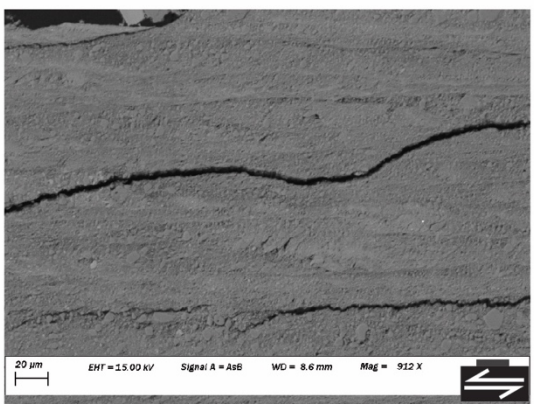


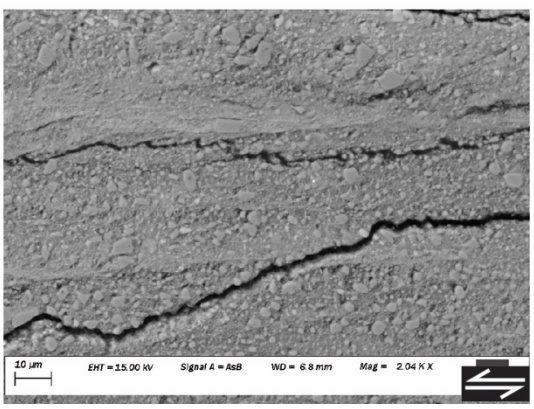




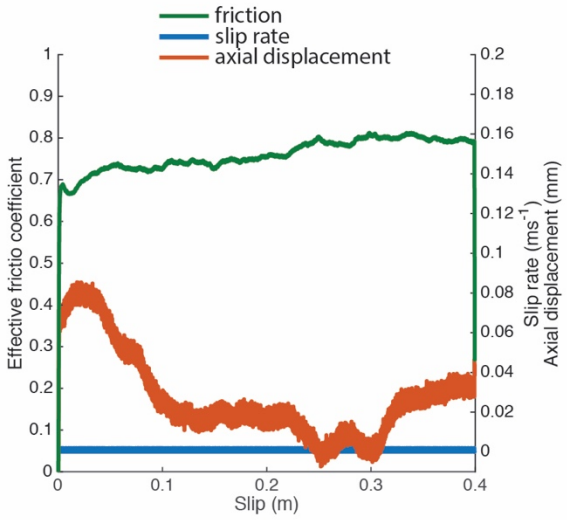
2 mm

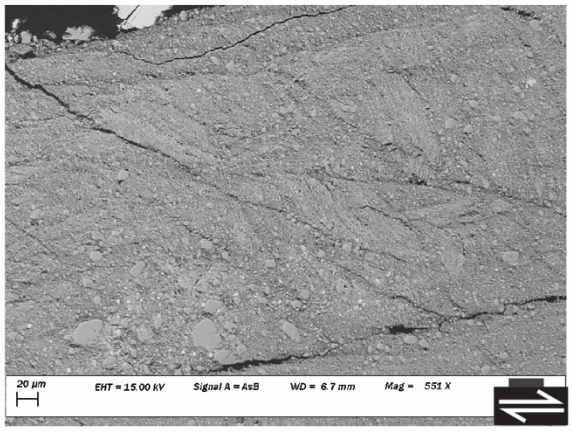


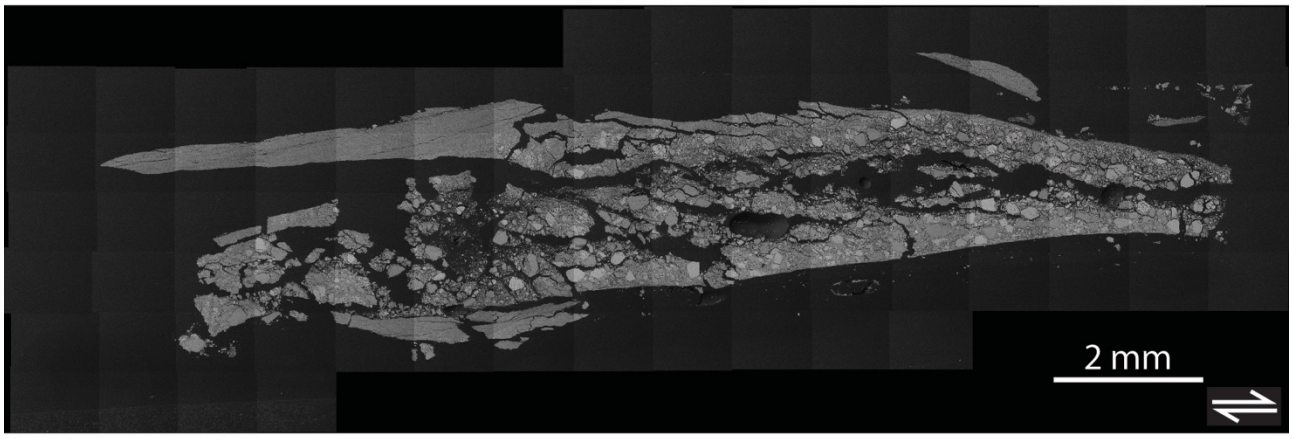


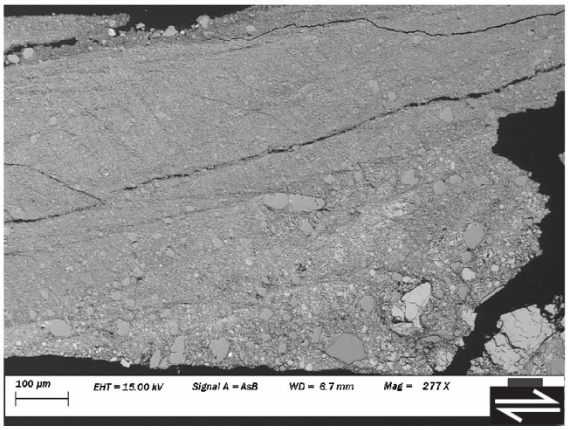


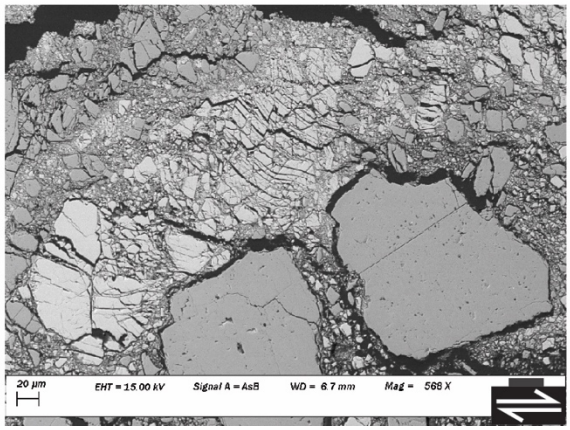
s1211
100 µms^{-1} - 40 cm - 17.5 MPa Room humidity



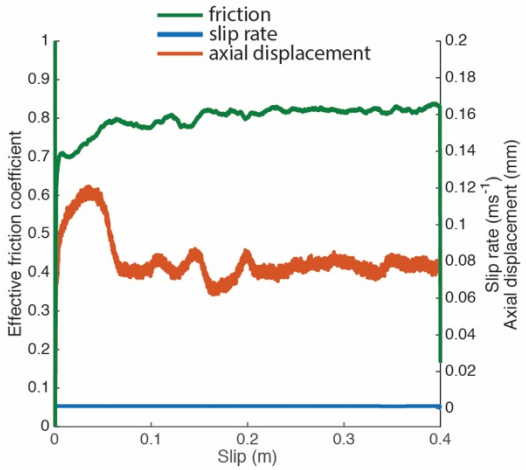


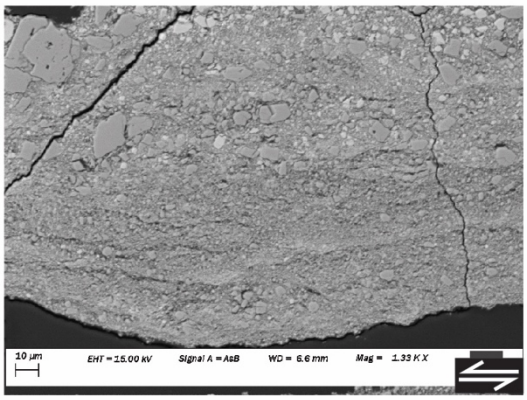


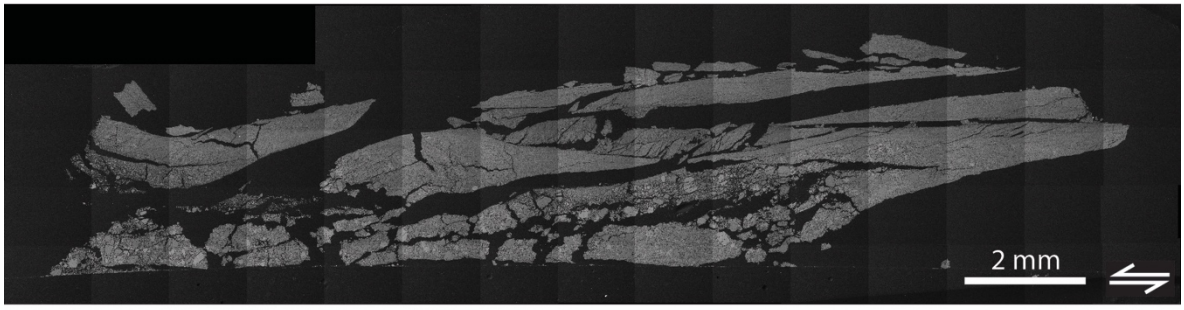


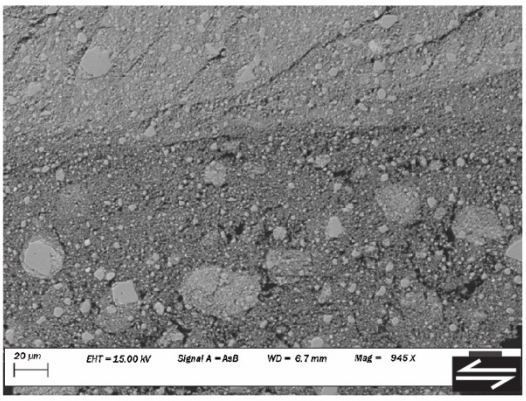


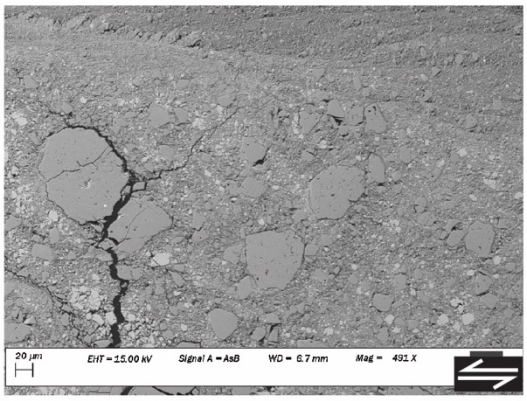
s1212
0.001 ms^{-1} - 40 cm - 17.5 MPa Room humidity

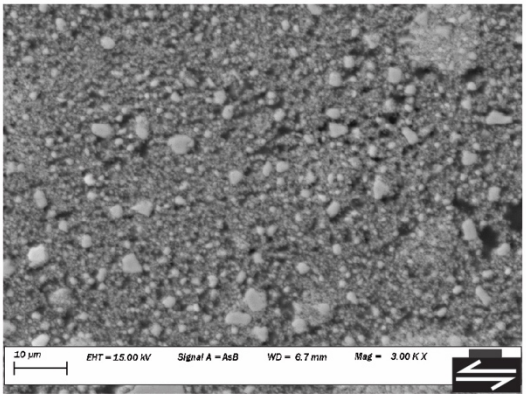




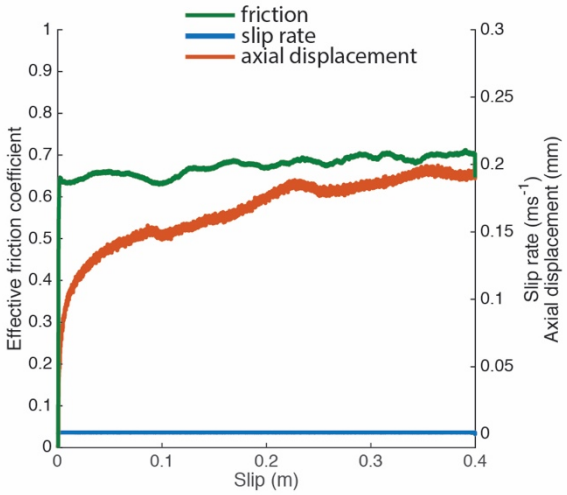


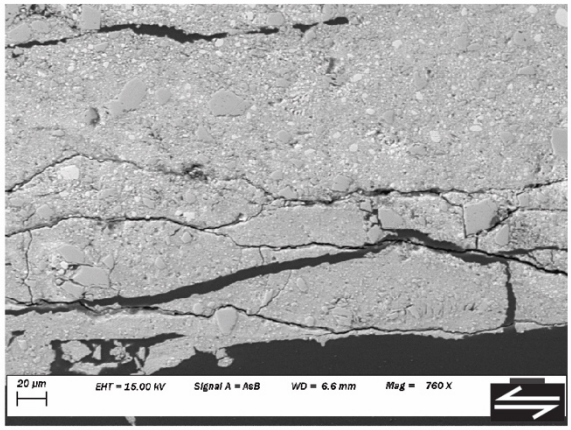


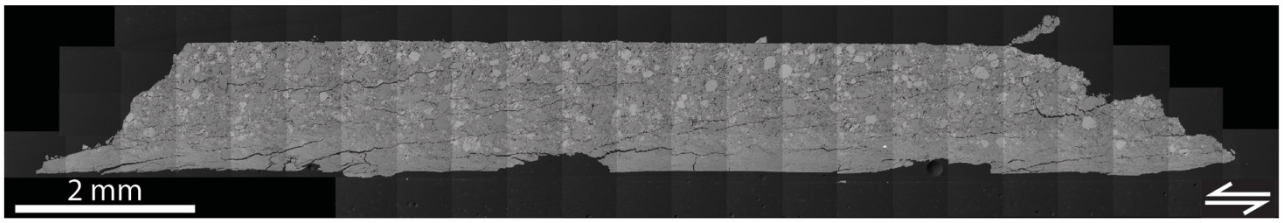


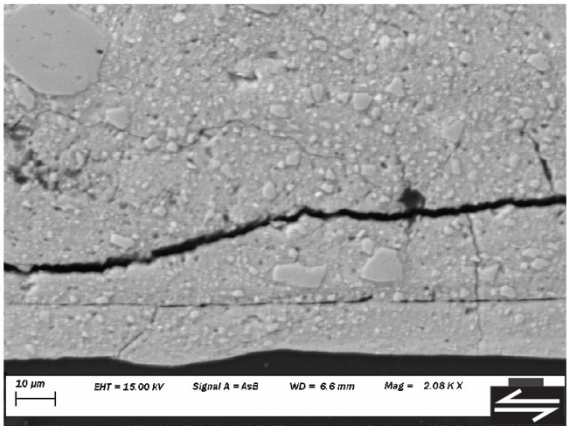


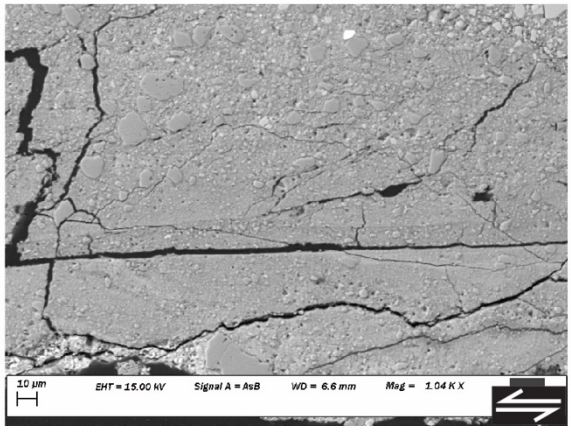
s1213
0.001 ms^{-1} - 40 cm - 17.5 MPa Water dampened



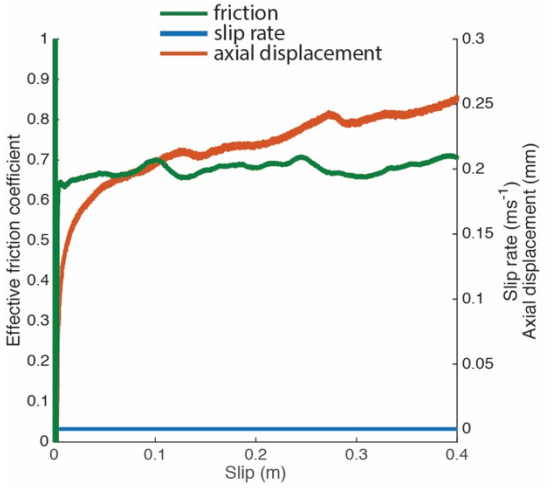


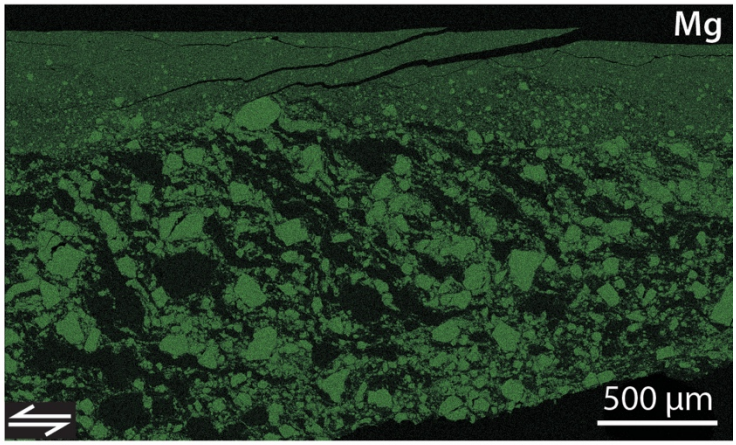


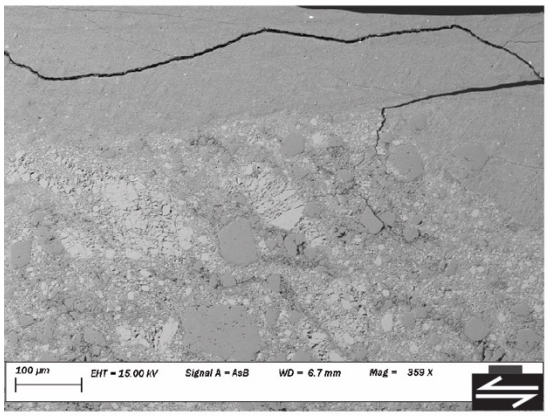


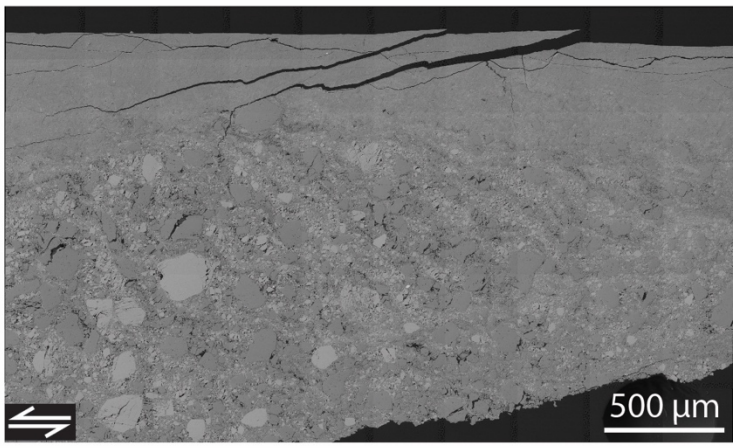


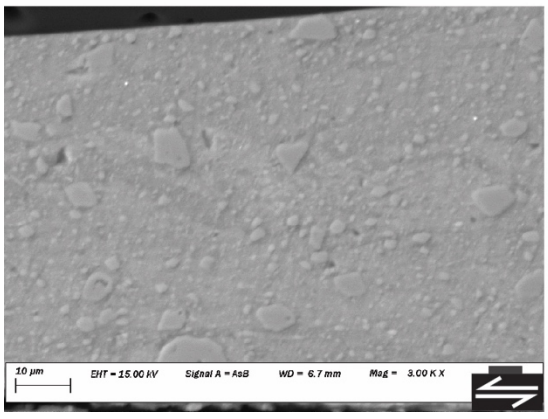
s1214
30 µms^{-1} - 40 cm - 17.5 MPa Water dampened

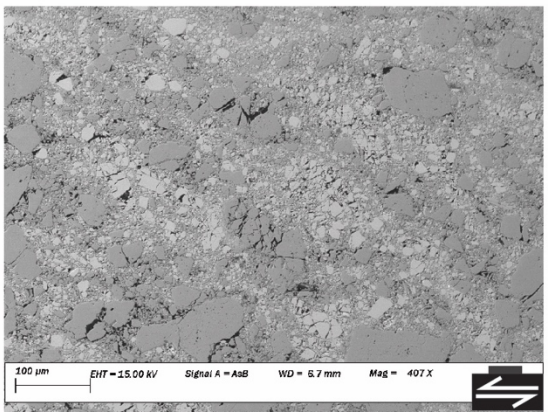




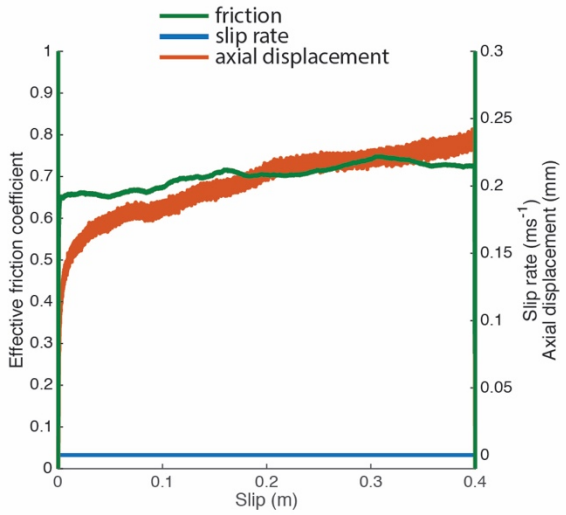


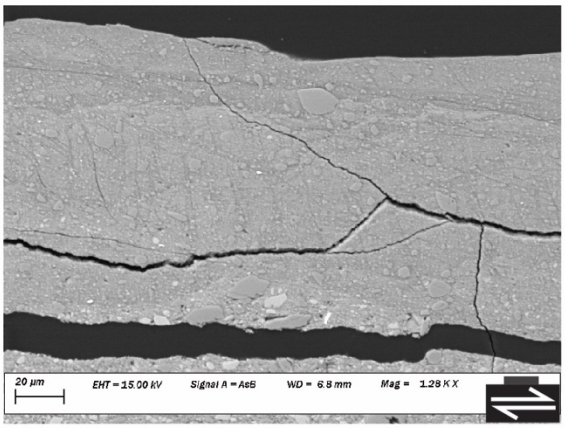


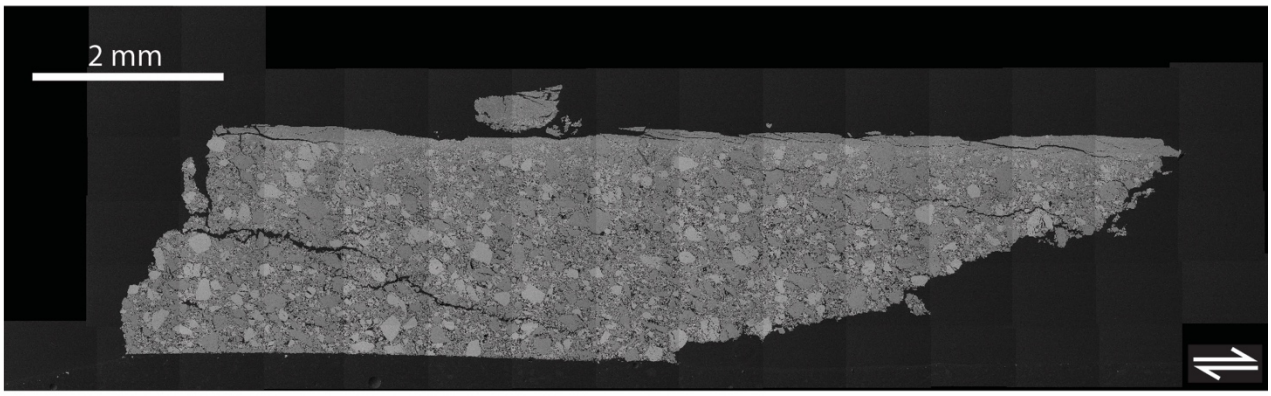


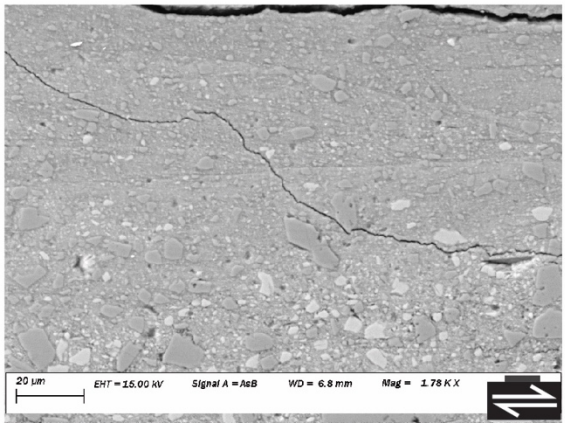


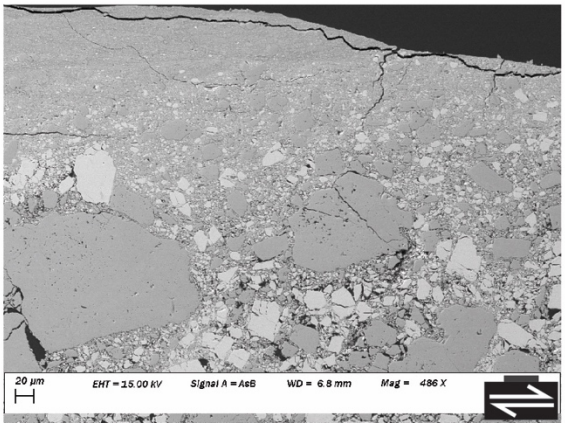
s1215
100 µms^{-1} - 40 cm - 17.5 MPa Water dampened



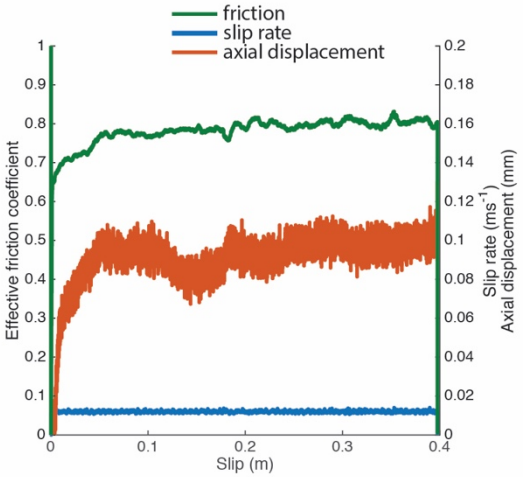


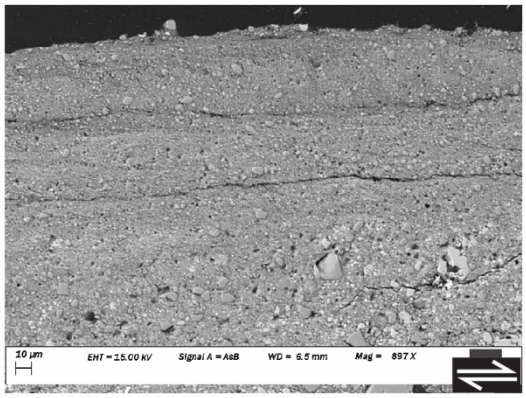


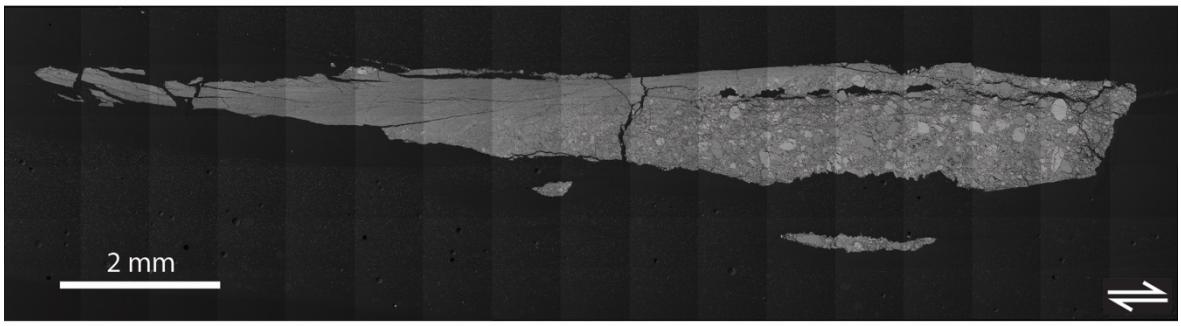


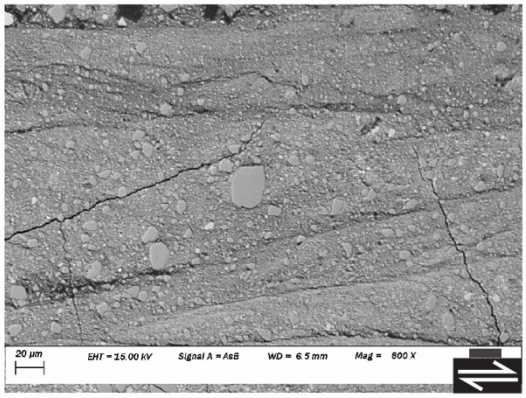


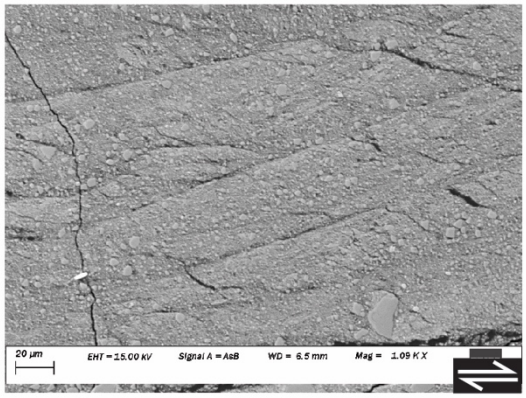
s1217
0.01 ms^{-1} - 40 cm - 17.5 MPa Room humidity

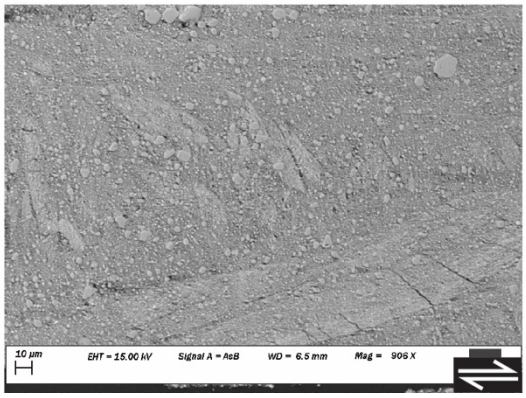




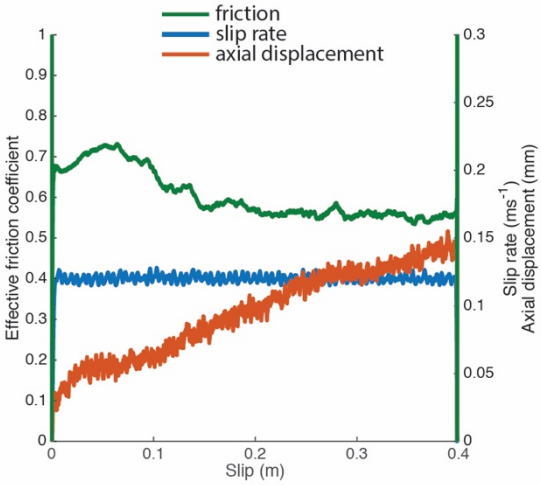


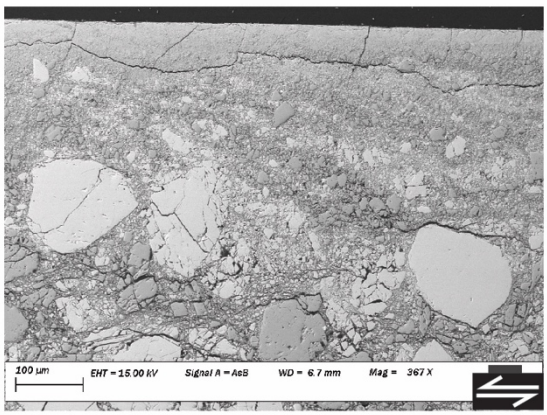


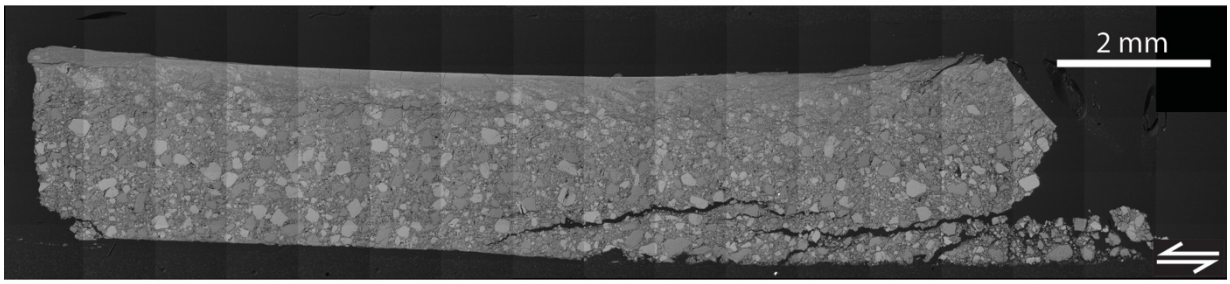


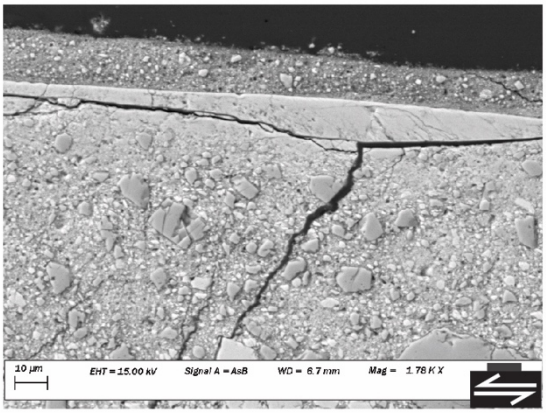


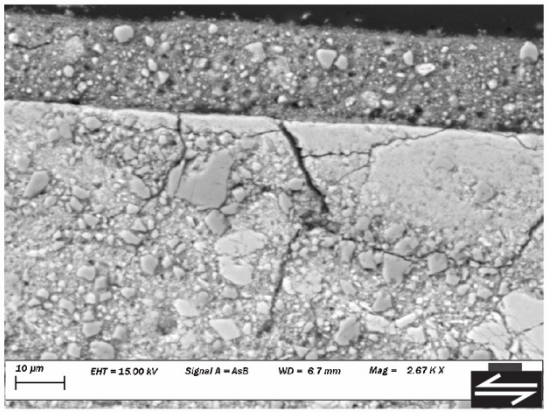
s1218
0.1 ms^{-1} - 40 cm - 17.5 MPa Room humidity

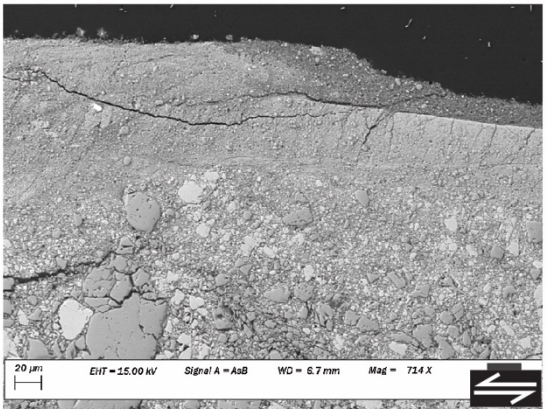


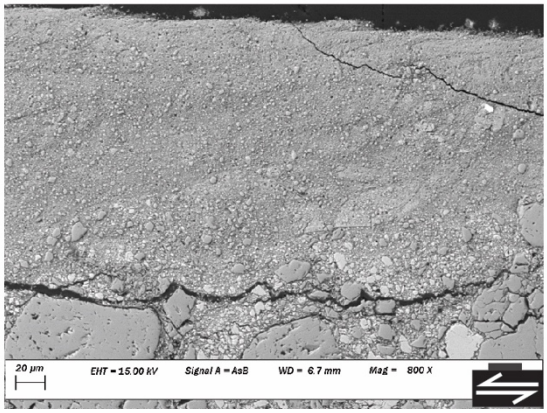




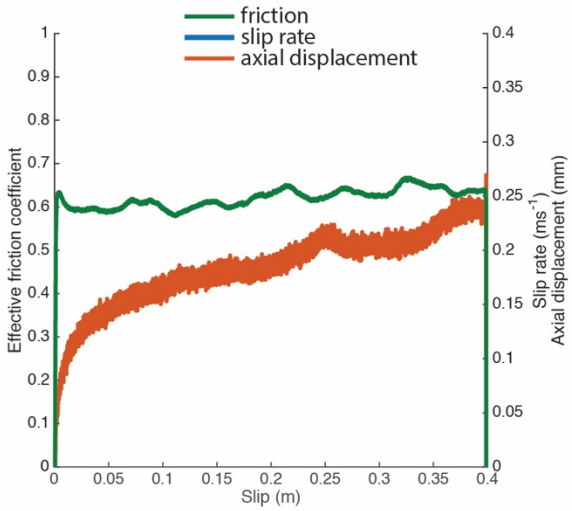


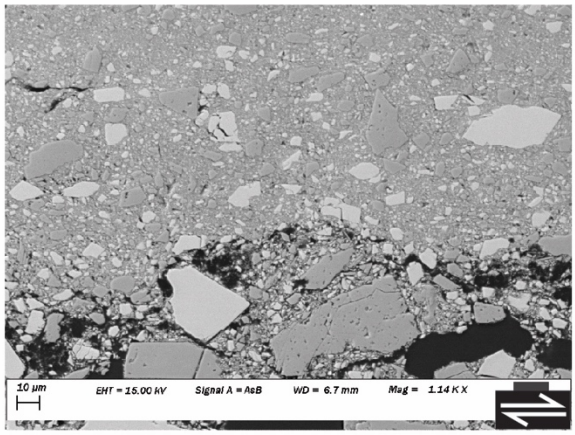


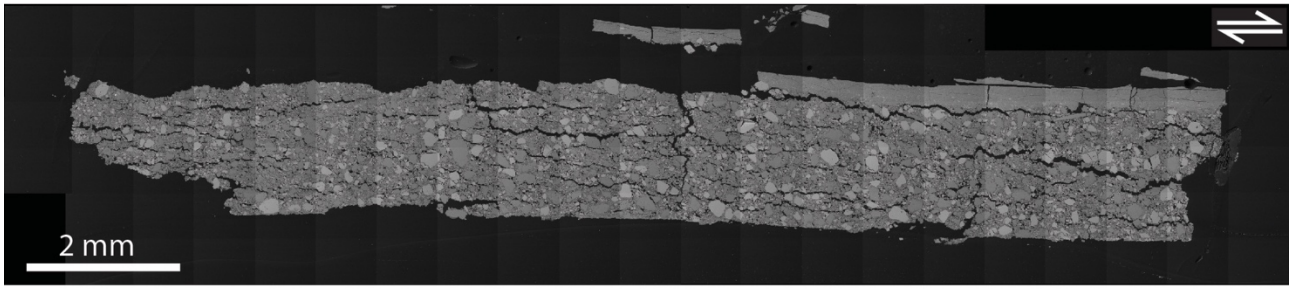


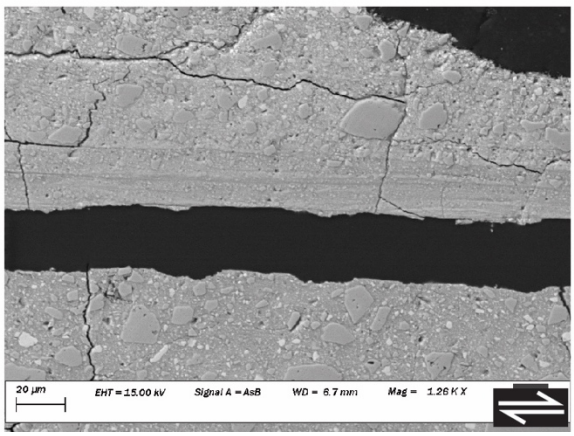


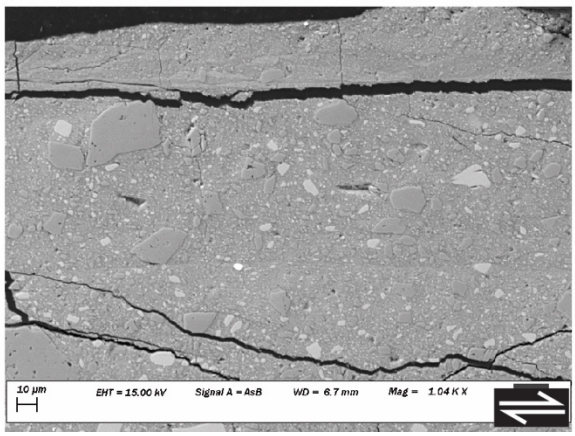
s1219
0.01 ms^{-1} - 40 cm - 17.5 MPa Water dampened



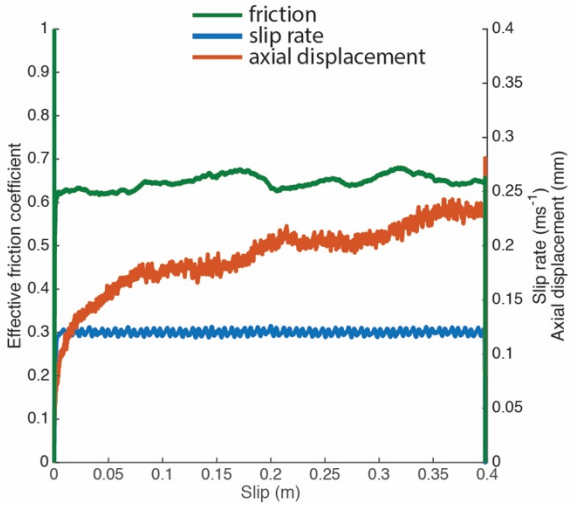


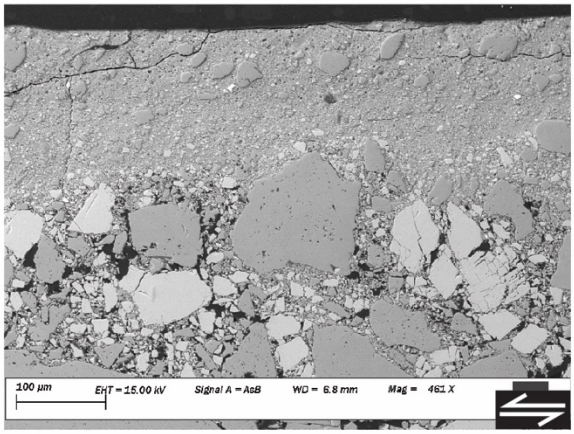


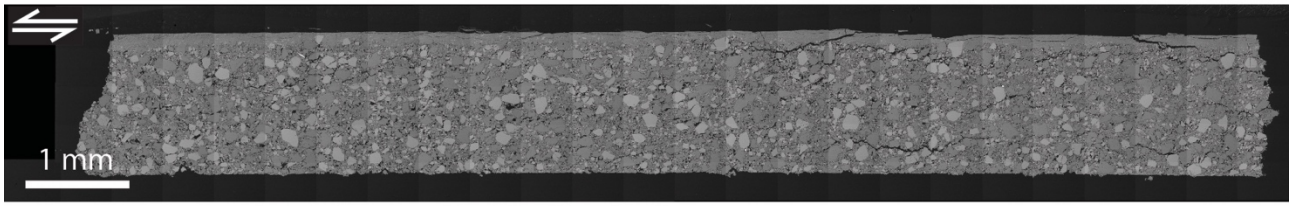


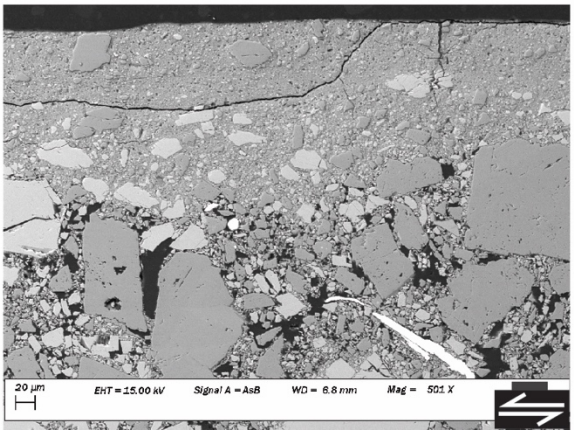


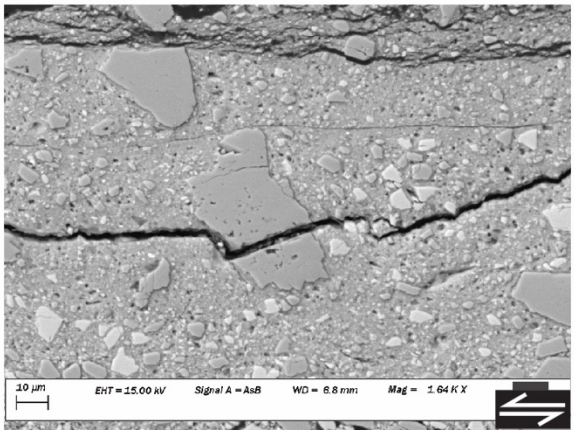
s1220
0.1 ms^{-1} - 40 cm - 17.5 MPa Water dampened



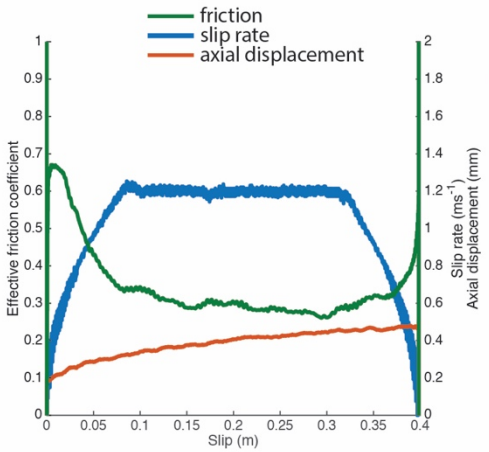


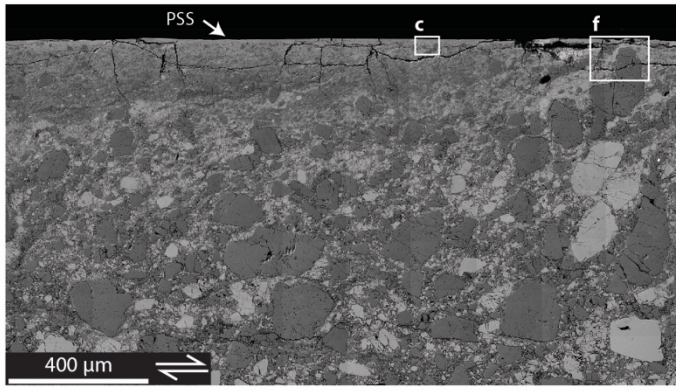


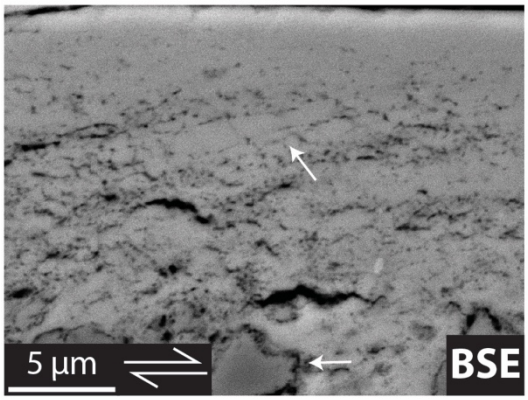


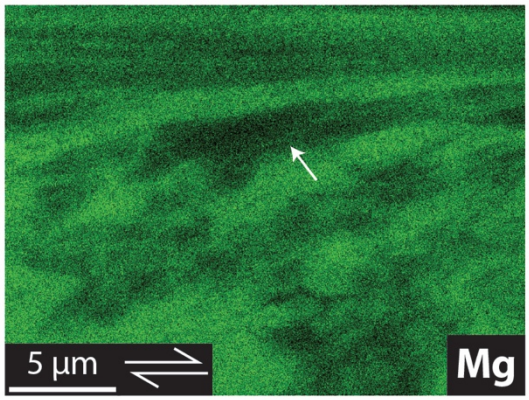


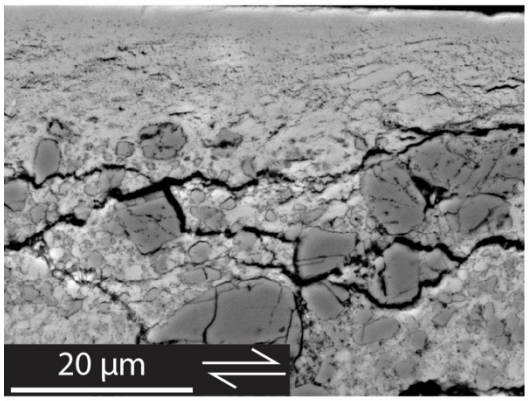
s1221
1 ms^{-1} - 40 cm - 17.5 MPa Room humidity

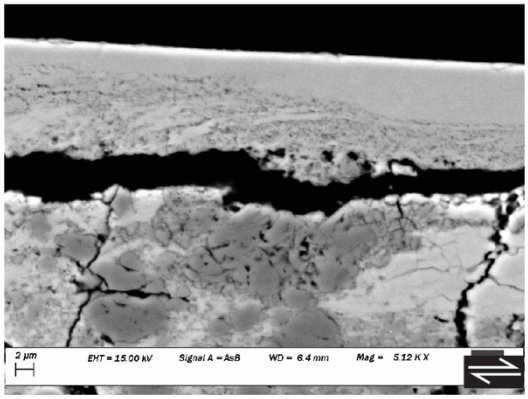


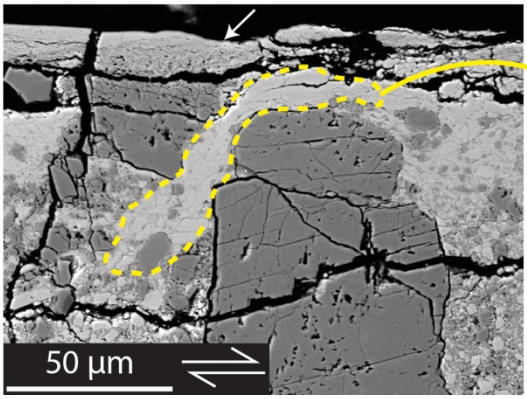


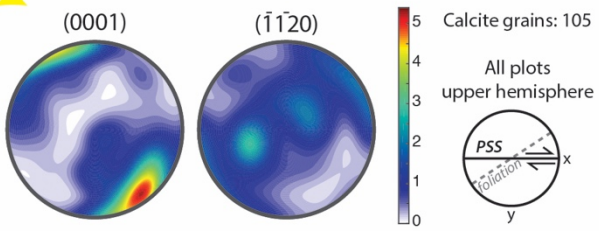




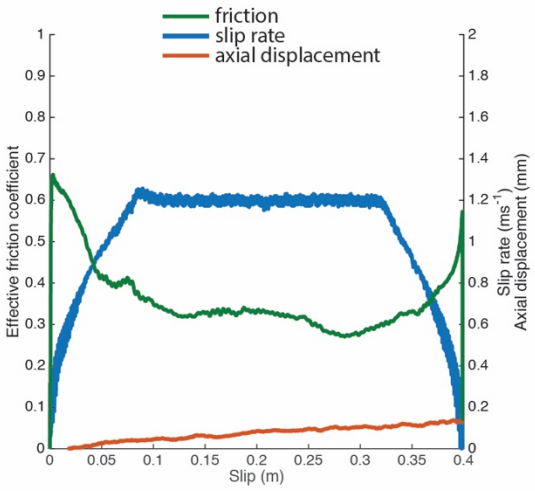


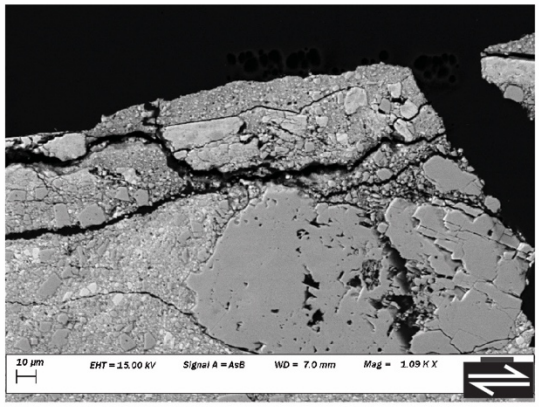


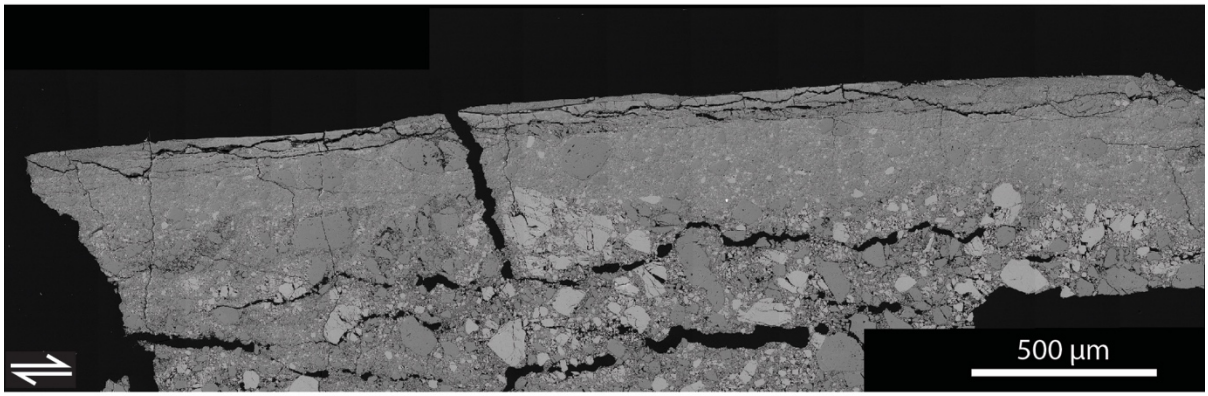


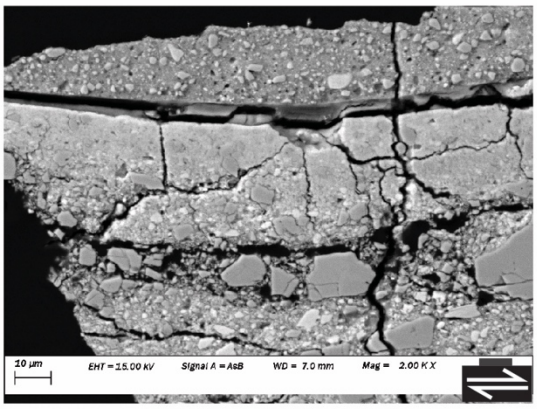


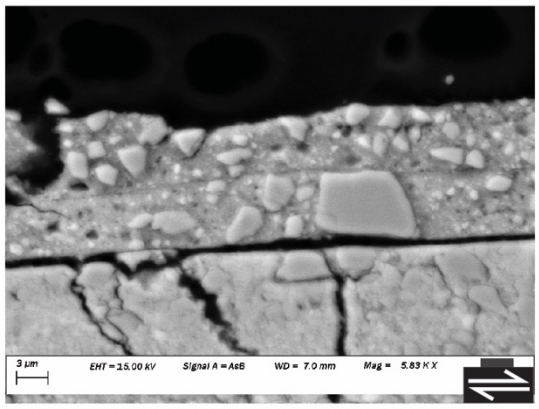
s1222
1 ms^{-1} - 40 cm - 17.5 MPa Water dampened

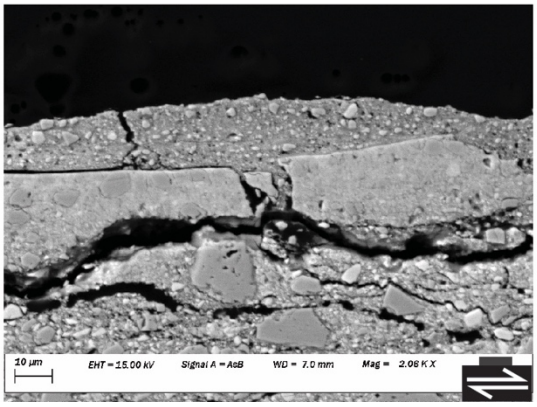


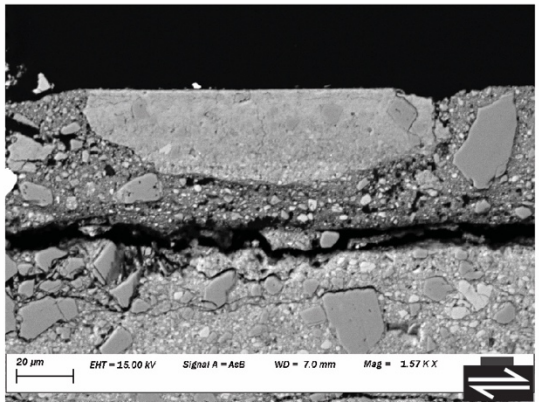






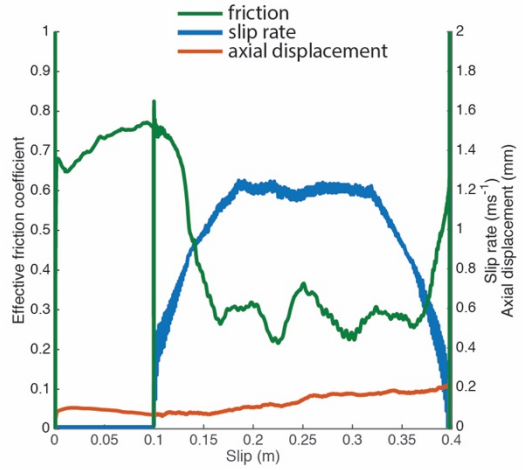


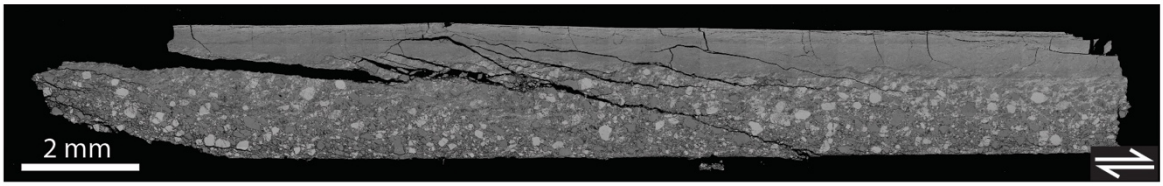


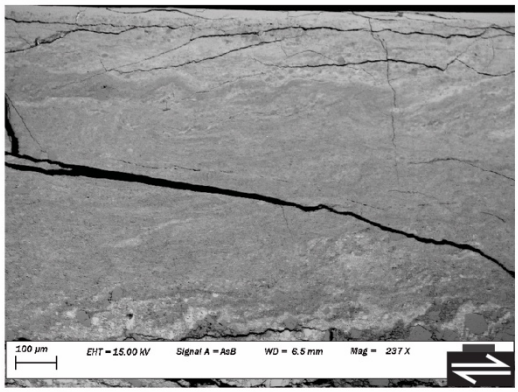


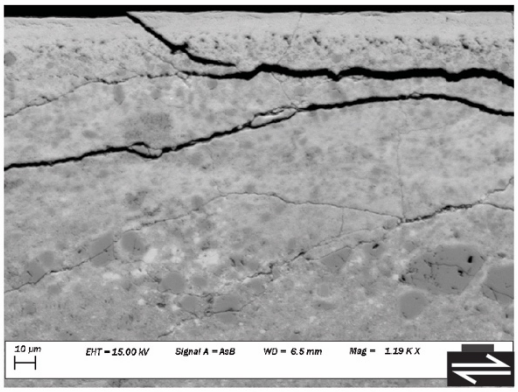
s1223

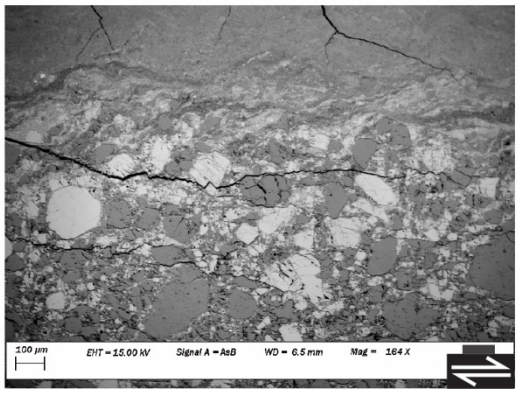
30 µms^{-1} ->1 ms^{-1} - 40 cm - 17.5 MPa Room humidity

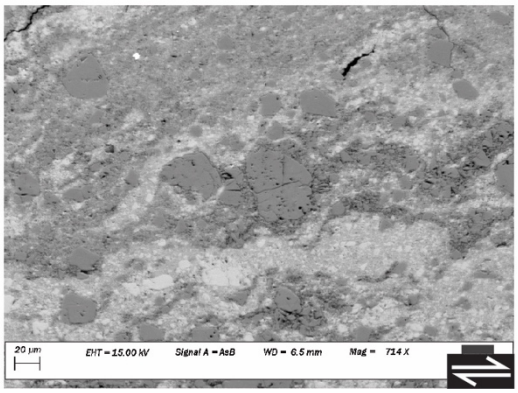






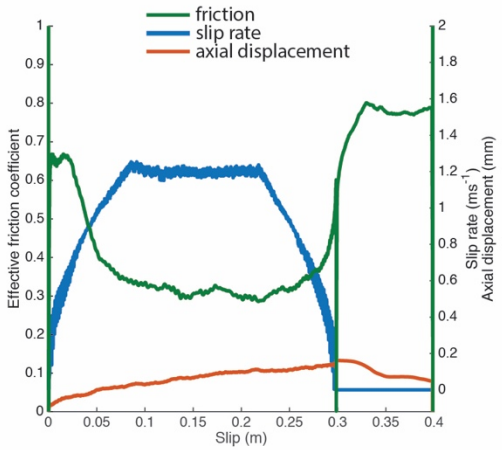


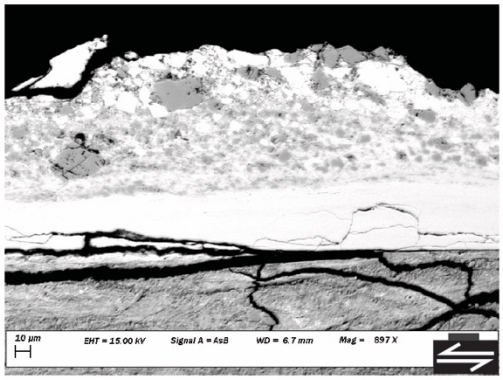


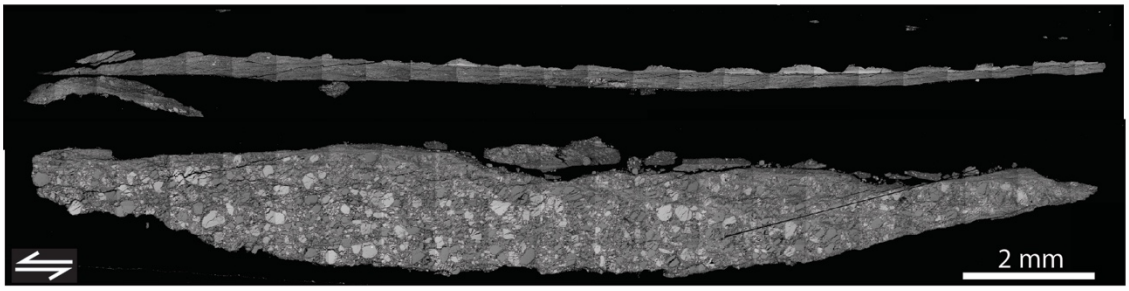


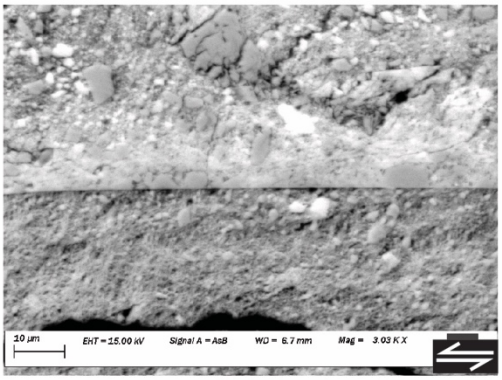
s1224

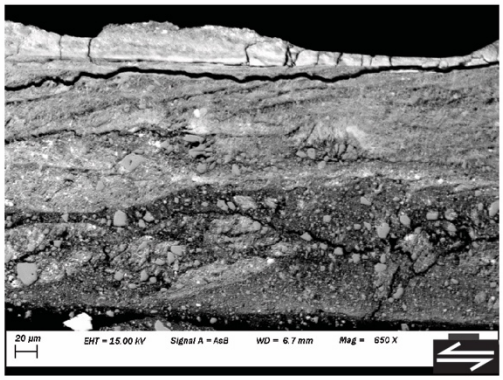
1 ms^{-1} -> 30 μms^{-1} - 40 cm - 17.5 MPa Room humidity

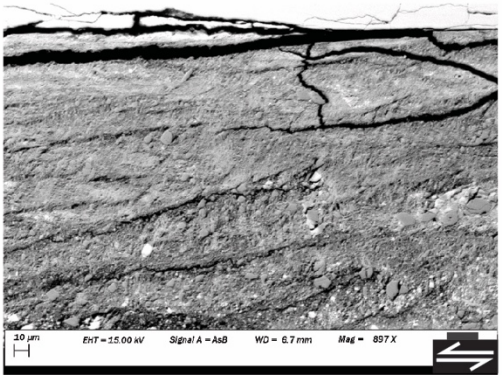


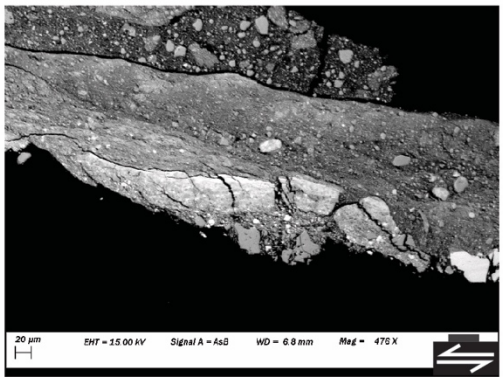






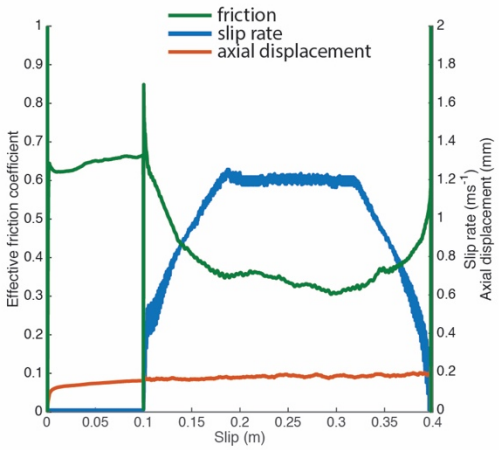


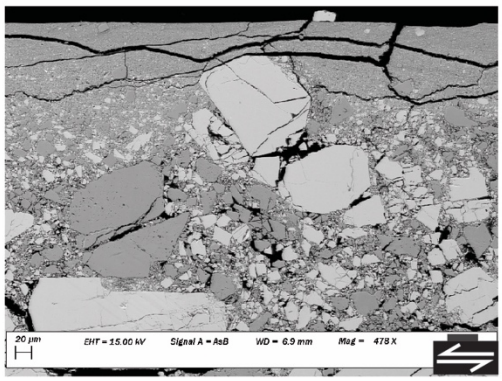


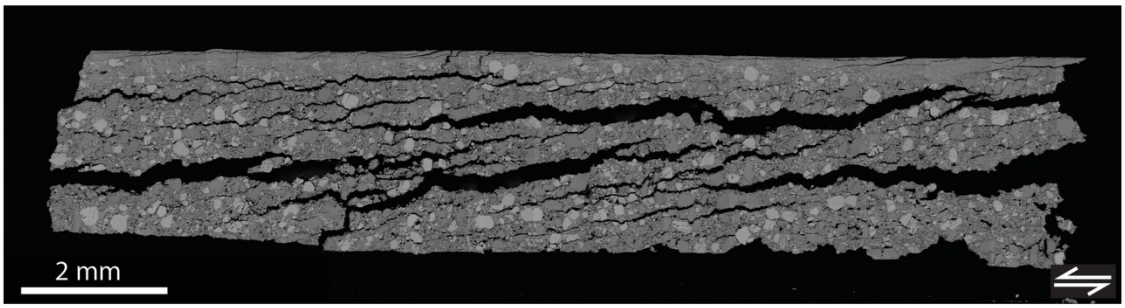


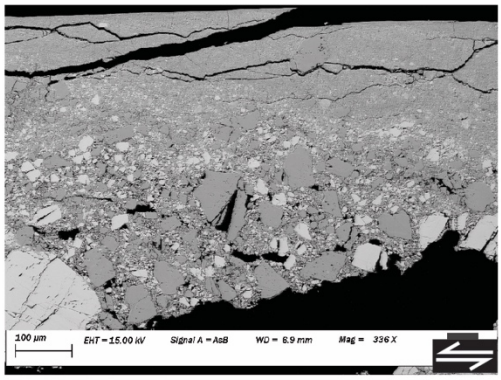
s1225

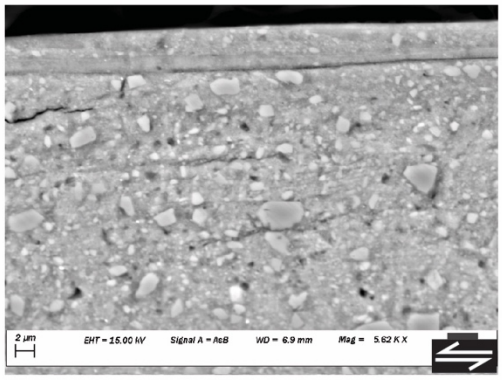
30 µms^{-1} ->1 ms^{-1} - 40 cm - 17.5 MPa Water dampened

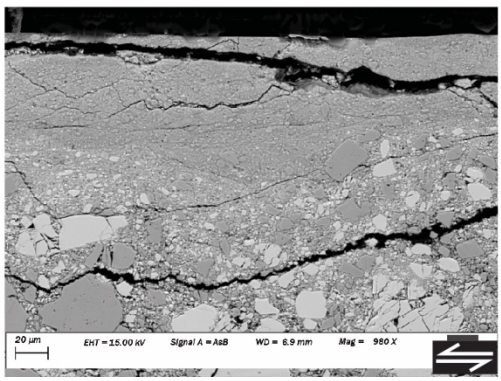


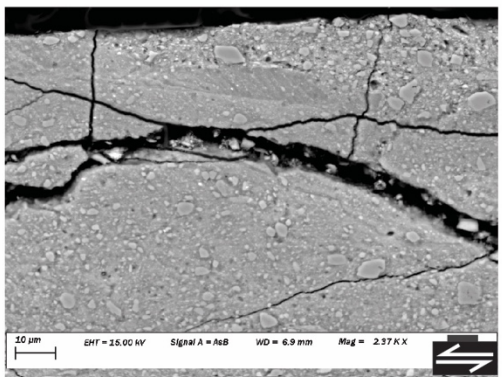






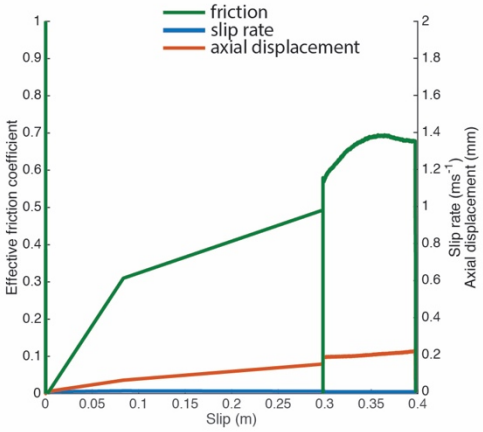


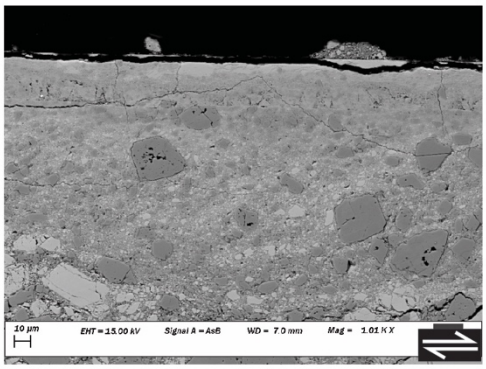


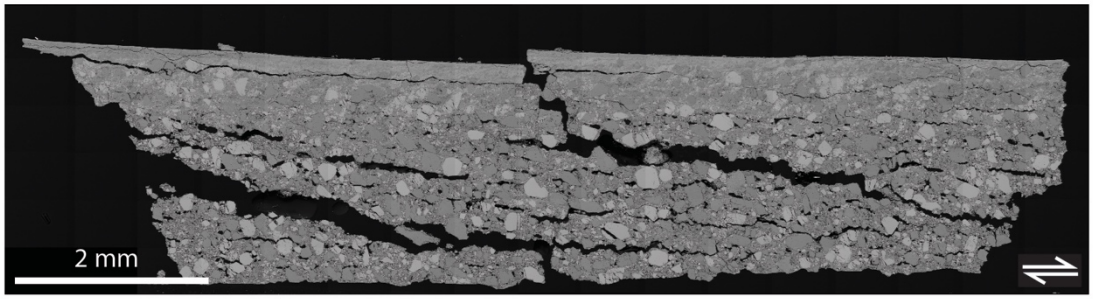


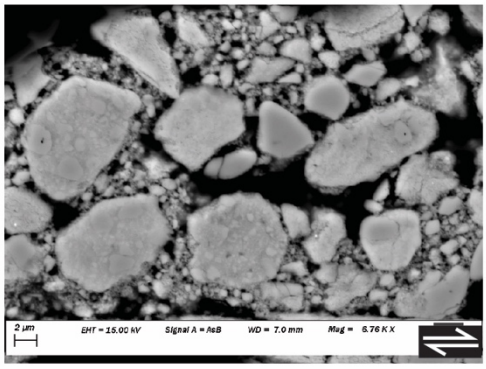
s1226

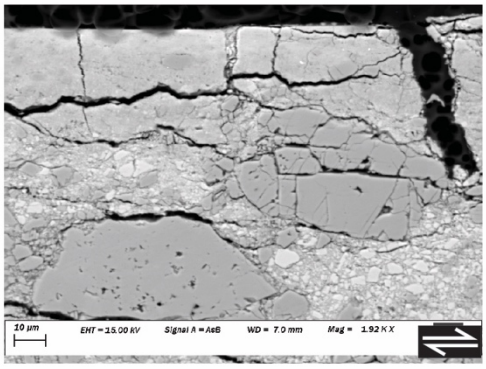
1 ms^{-1} -> 30 μms^{-1} - 40 cm - 17.5 MPa Water dampened

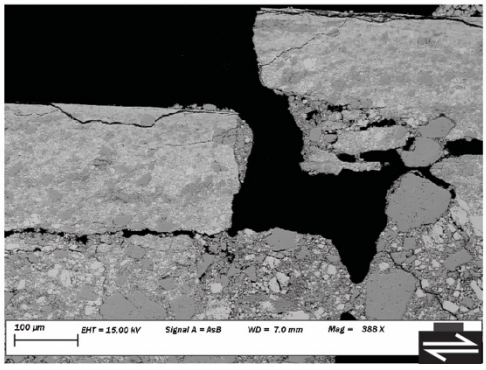


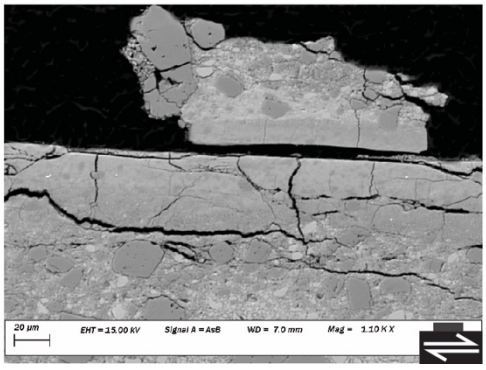




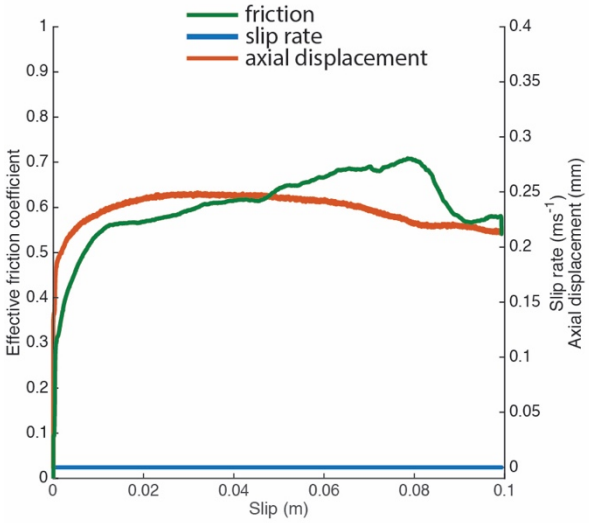


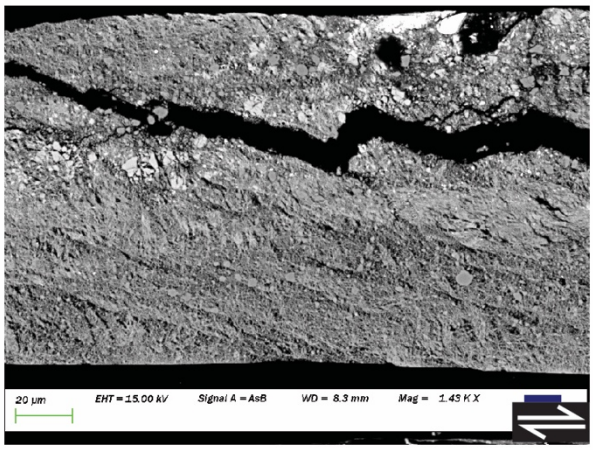


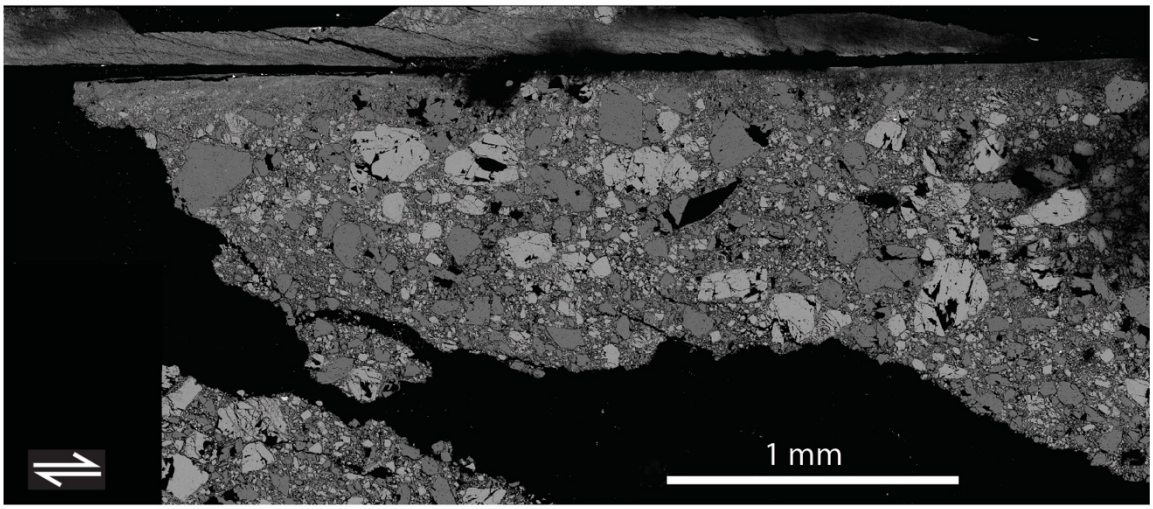


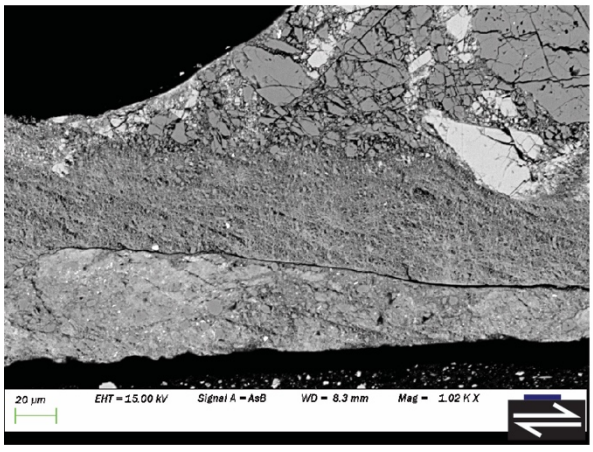


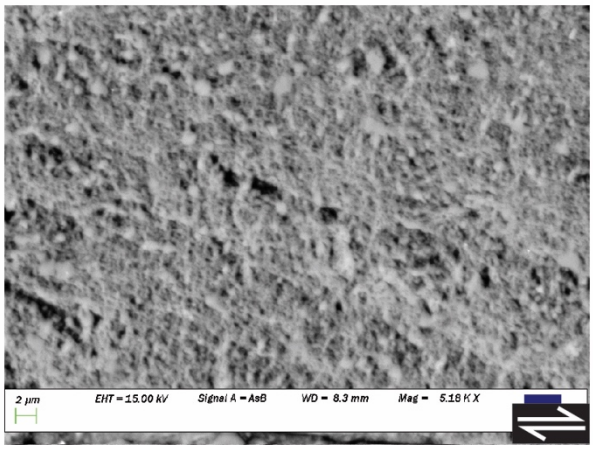
s1322
30 µms^{-1} - 10 cm - 17.5 MPa Room humidity



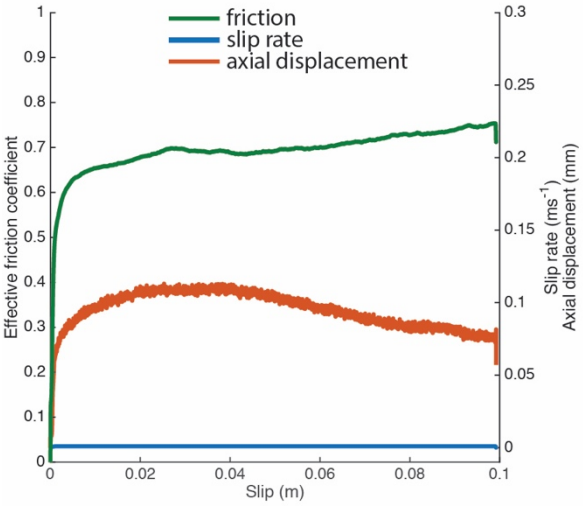


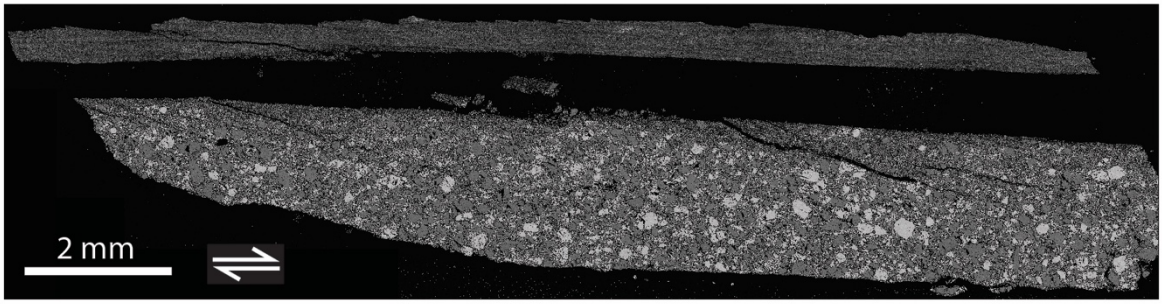


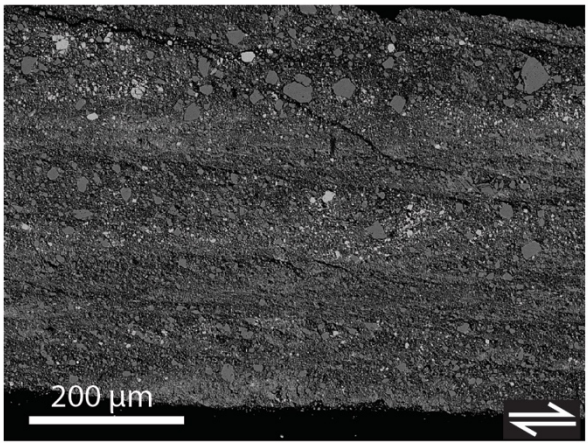


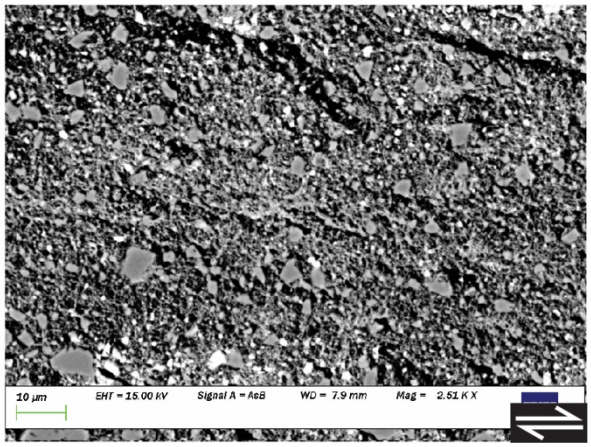


s1323
0.001 ms^{-1} - 10 cm - 17.5 MPa Room humidity

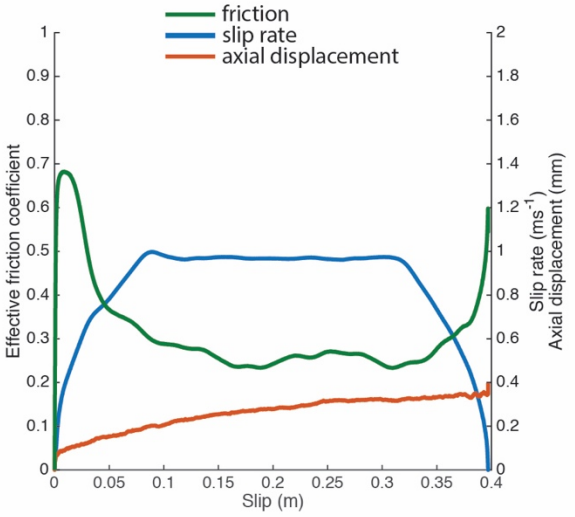


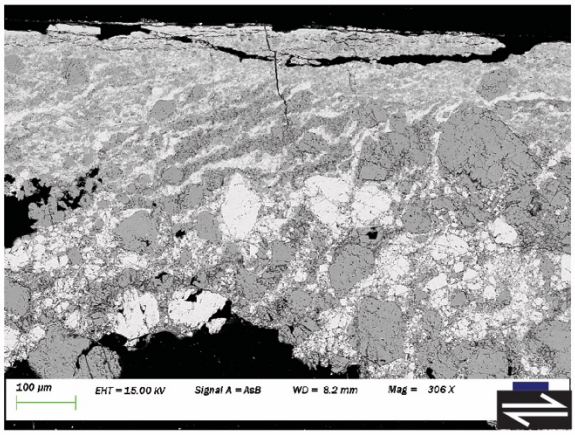


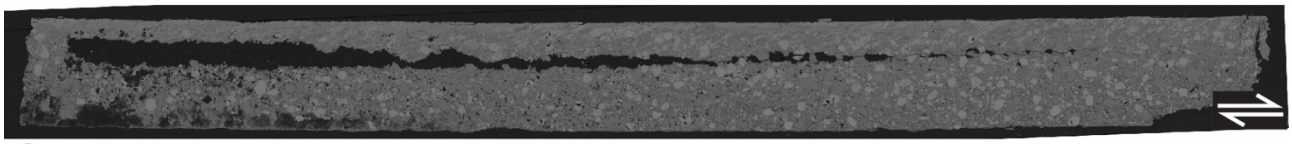


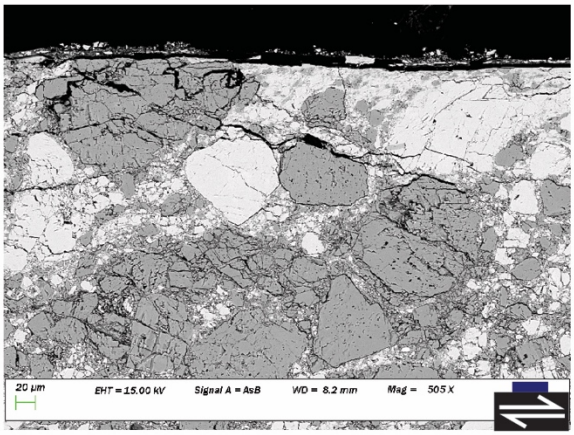


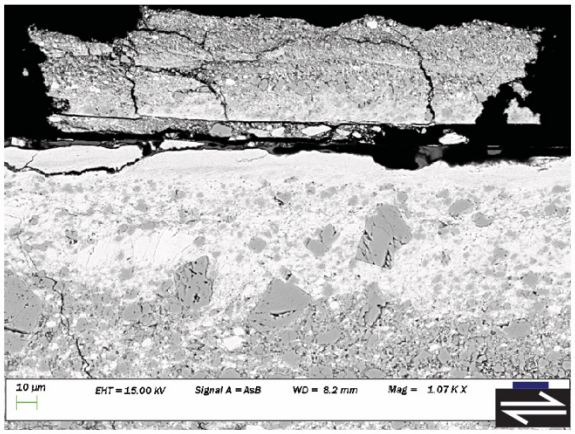
s1324
1 ms^{-1} - 40 cm - 26 MPa Room humidity

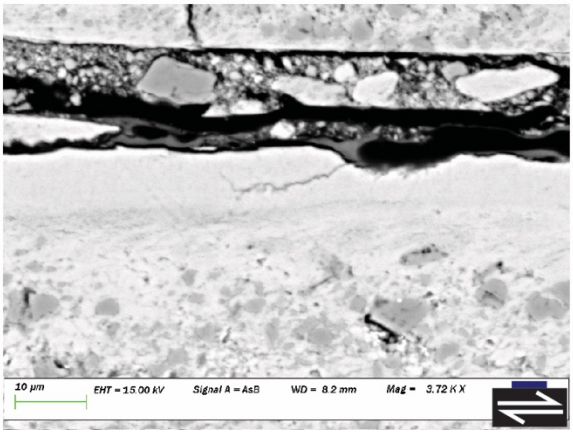






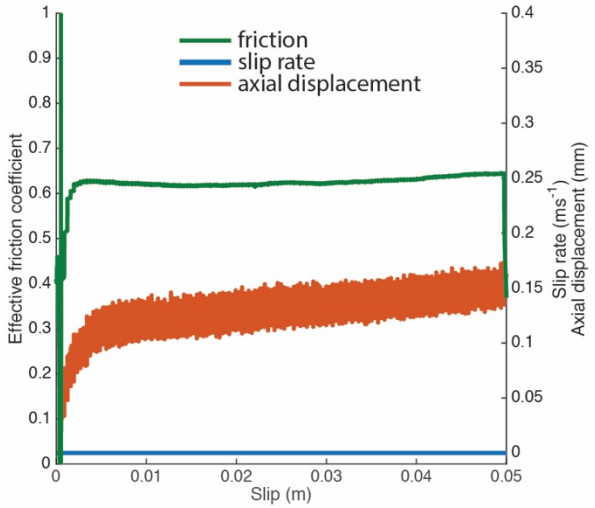


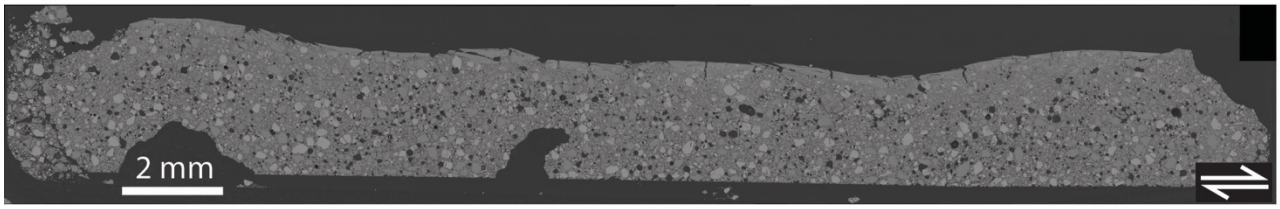


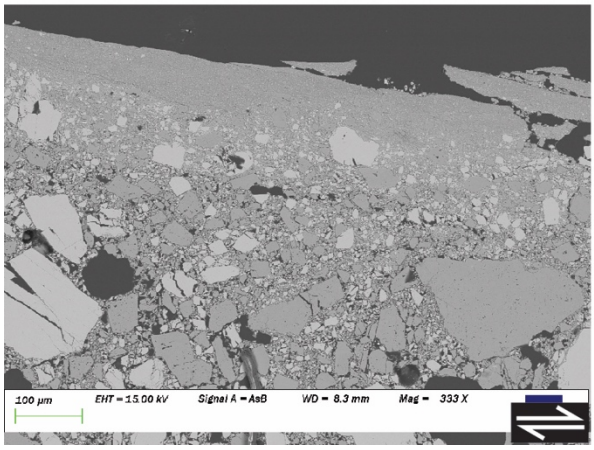


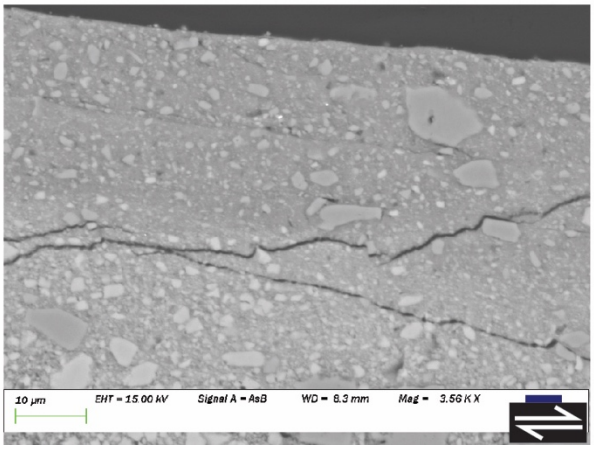
s1327

30 µms^{-1} - 5 cm - 17.5 MPa Water dampened



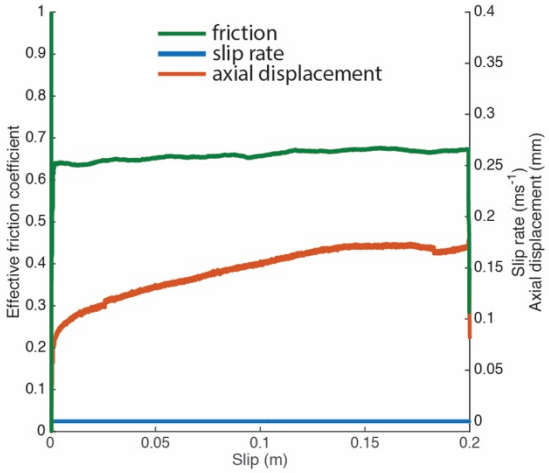


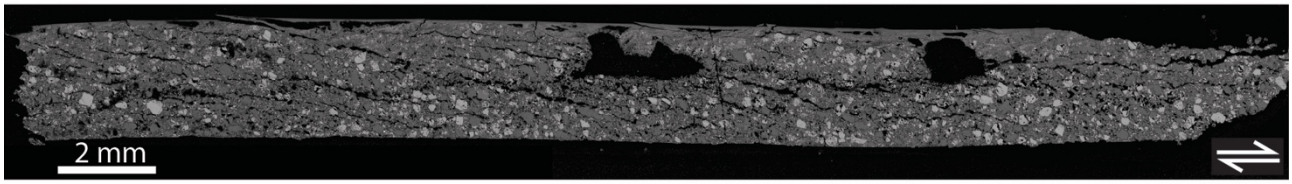


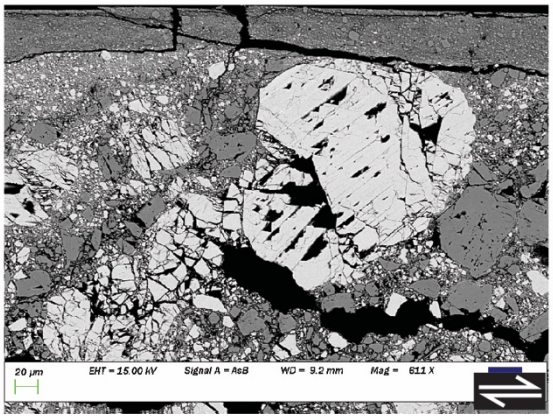


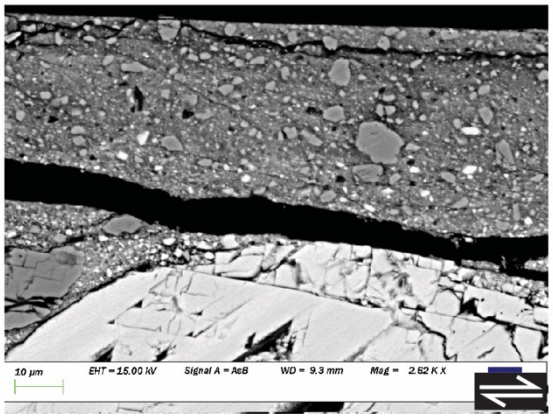
s1328

30 µms^{-1} - 20 cm - 17.5 MPa Water dampened



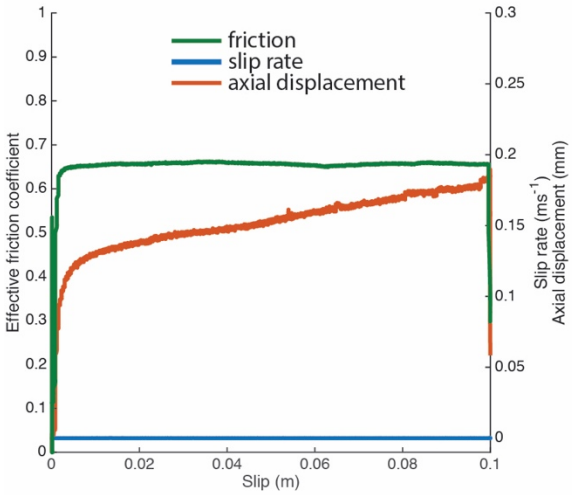


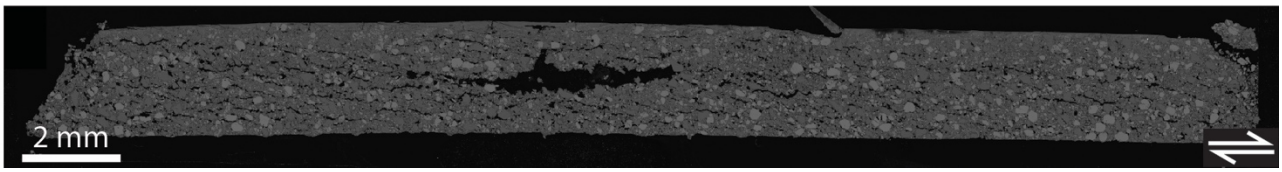




s1329

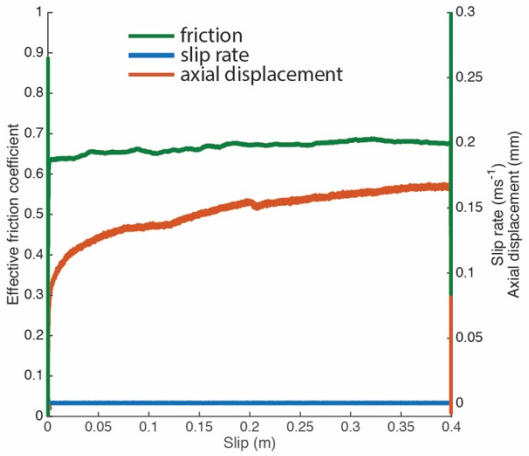
30 µms^{-1} - 10 cm - 17.5 MPa Water dampened

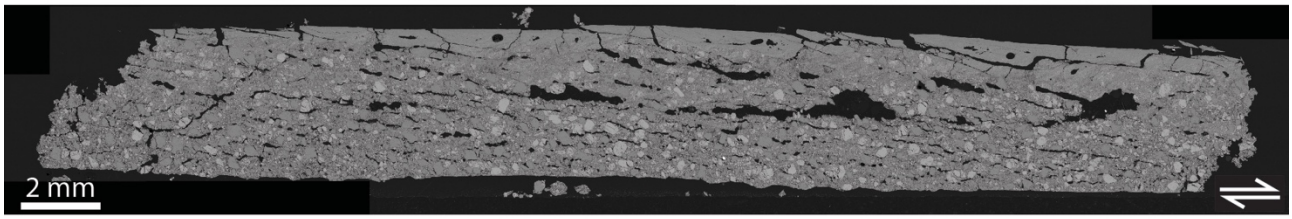


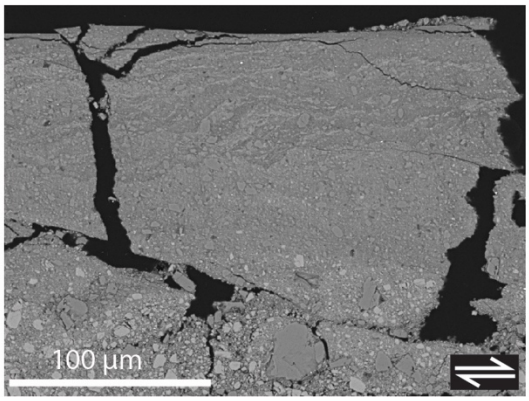


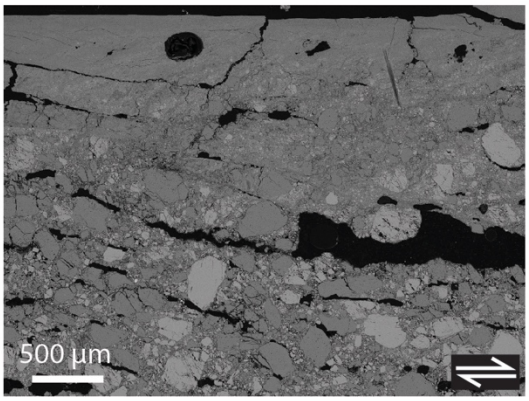
s1330

30 µms^{-1} - 40 cm - 17.5 MPa Water dampened









Acknowledgements

I would like to thank my supervisor Giulio Di Toro and my co-tutors Steven A.F. Smith and Michele Fondriest for their extensive support throughout the last three years, the fruitful and enlightening discussions and the inspiring enthusiasm they provided.

Special thanks to the “Campo Imperatore” crew for the great months spent in the field, in particular, Fabrizio Storti, Fabrizio Balsamo, Michele Fondriest, Giulio Di Toro, Alessio Lucca, Harold Leah, Matteo Massironi and Anna Traforti. The “Ente Parco Nazionale del Gran Sasso e Monti della Laga” is thanked for allowing us to conduct field work in the Campo Imperatore area, the Regione Abruzzo for providing the aerial photographs for the mapping and the Hotel Campo Imperatore staff for support during field work.

Thanks to Elena Spagnuolo for the help and assistance during the experimental part and fruitful discussions. Stefano Aretusini is also acknowledged for discussions and help on the experimental mechanical data and thermal modelling.

People at the University of Otago are thanked for the access to their facilities, their support during the many hours spent at the SEM, fruitful discussions and the overall great time: Rosie Cole, Martina Kirilova, Loren Mathewson, Arran Murch, Marianne Negrini, David J. Prior, Kat Sauer, Matthew Tarling, Jack Williams.

Frank E. Brenker is warmly thanked for his time during sample preparation for TKD analysis, Leonardo Tauro for help during thin sections preparation and Federico Zorzi for XRPD analysis.

Lastly, many thanks to my family for their continuous support during the whole Ph.D.